Title

Earth versus Neutrinos: Measuring the total muon-neutrino-to-nucleon cross section at ultra-high energies through differential Earth absorption of muon neutrinos from cosmic rays using the IceCube Detector

Author

Miarecki, Sandra C.

Publication Date

2016

Peer reviewed|Thesis/dissertation

Earth versus Neutrinos: Measuring the total muon-neutrino-to-nucleon cross section at ultra-high energies through differential Earth absorption of muon neutrinos from cosmic rays using the IceCube Detector

By

Sandra Christine Miarecki

A dissertation submitted in partial satisfaction of the

requirements for the degree of

Doctor of Philosophy

in

Physics

in the

Graduate Division

of the

University of California, Berkeley

Committee in charge:

Professor Marjorie D. Shapiro, Co-chair
Doctor Spencer R. Klein, Co-chair
Professor Robert G. Jacobsen
Professor Karl A. van Bibber

Fall 2016

Earth versus Neutrinos: Measuring the total muon-neutrino-to-nucleon cross section at ultra-high energies through differential Earth absorption of muon neutrinos from cosmic rays using the IceCube Detector

Abstract

Earth versus Neutrinos: Measuring the total muon-neutrino-to-nucleon cross section at ultra-high energies through differential Earth absorption of muon neutrinos from cosmic rays using the IceCube Detector

by

Sandra Christine Miarecki

Doctor of Philosophy in Physics

University of California, Berkeley

Professor Marjorie D. Shapiro, Co-chair
Doctor Spencer R. Klein, Co-chair

The IceCube Neutrino Detector at the South Pole was constructed to measure the flux of high-energy neutrinos and to try to identify their cosmic sources. In addition to these astrophysical neutrinos, IceCube also detects the neutrinos that result from cosmic ray interactions with the atmosphere. These atmospheric neutrinos can be used to measure the total muon neutrino-to-nucleon cross section by measuring neutrino absorption in the Earth. The measurement involves isolating a sample of 10,784 Earth-transiting muons detected by IceCube in its 79-string configuration. The cross-section is determined using a two-dimensional fit in measured muon energy and zenith angle and is presented as a multiple of the Standard Model expectation as calculated by Cooper-Sarkar, Mertsch, and Sarkar in 2011. A multiple of 1.0 would indicate agreement with the Standard Model. The results of this analysis find the multiple to be 1.30 (+0.21 -0.19 statistical) (+0.40 -0.44 systematic) for the neutrino energy range of 6.3 to 980 TeV, which is in agreement with the Standard Model expectation.

To all the people who have been a part of my life, both good and bad,
because we are all influenced by those that we meet,
and everything in life happens for a reason.

Contents

Acknowledgments

I graciously thank the following individuals and organizations for all their support:

My dissertation advisor, Dr. Spencer Klein, for giving me the opportunity to complete this research project and for his extreme patience during the hard times. Many thanks for your advice, instruction, and overall guidance during my many years of research with the Lawrence Berkeley National Laboratory (LBNL) IceCube group.

My faculty advisor, Professor Marjorie Shapiro, for keeping me on the correct path toward PhD completion and encouraging me when my energy was low.

The remaining two members of my committee, Professor Bob Jacobsen and Professor Karl van Bibber, for "volunteering" to be on my committee and for working with me near the end when crunch time was occurring.

The IceCube Collaboration, for allowing me to join their ranks and to use their data.

The Diffuse group, a subgroup of IceCube that was responsible for keeping my analysis on track.

The University of California-Berkeley Department of Physics, for accepting an older but wiser non-traditional student into their program, and for their support (both financial and otherwise) throughout my studies.

The Department of Defense, for awarding me one of their National Defense Science and Engineering Graduate Fellowships (NDSEG), which allowed me to focus full-time on my studies and research.

Bob Stokstad, an IceCube scientist at LBNL, who sat next to me on an airline flight before I arrived in Berkeley and invited me to visit the IceCube group during my first semester. If this random-chance meeting had not taken place, I would not have known about the IceCube Detector at all, and my dissertation would have been written on a completely different subject.

Lisa Gerhardt and Chang Hyon Ha, post-doctoral scientists at LBNL, for helping me to learn just about everything in IceCube that I needed to learn to complete this research.

Mariola Lesiak-Bzdak, a post-doctoral scientist at LBNL, and Don van der Drift, a visiting graduate student, for helping me learn about Root, Python, and other computer languages that I had never worked with before.

Tomasz Palczewski, the most recent LBNL post-doctoral scientist, whose assistance was critical during my battle with LaTex while formatting this dissertation.

Gary Binder, a fellow Berkeley graduate student in IceCube, whose knowledge of statistics and least likelihood fitters was critical to my learning about these subjects, and for being the man with the answers on almost any subject.

Kotoyo Hoshina, an IceCube scientist, for her superb help with simulation and processing,

and understanding the Earth composition model.

Wolfgang Rhode, an IceCube scientist at the Technische Universitat Dortmund, for his generous hospitality, and Florian Scheriau and Martin Schmidt, for their patient instruction in the methods of RapidMiner, a data mining program that originally functioned as the event selection method until problems arose. Special thanks also to Mathis Bonner and Tomasz Fuchs for their help in trouble-shooting the method.

Christopher Weaver, a graduate student in IceCube at the University of Wisconsin-Madison, who was extremely helpful in teaching me about his event selection method when my first method had problems.

Sebastian Euler and Carlos de los Heros, IceCube scientists who were my analysis reviewers for unblinding, making sure that the analysis was thorough and scientific.

Thorsten Stezelberger, an LBNL engineer whose friendship and encouragement helped me through the tough times to finish this dissertation and PhD.

United States Air Force Academy Department of Physics, for their support while I completed my dissertation.

This work was partially supported by the National Defense Science and Engineering Graduate Fellowship program and by a grant from the National Science Foundation.

Chapter 1

Introduction

Neutrino astrophysics is a relatively new field of study with vast potential for discovery. Neutrinos have very small masses and are neutral in charge. This means that they are almost unaffected by gravity and are completely unaffected by electromagnetic fields. Neutrinos can travel very long distances in the universe and, when detected, point back towards their sources.

The IceCube Neutrino Detector was built to find the sources of these high-energy neutrinos, from 10 GeV to 10 EeV. Since neutrinos are very non-interactive particles, a very large detector had to be built in order to observe enough interactions to make discoveries. From 2005-2010, IceCube was constructed in stages from 1 "string" of sensors in the first year to the final 86-string configuration. A large international collaboration was involved in every aspect of the design, testing, construction, and data analysis of the multi-year results of the completed detector.

In addition to the search for neutrino point sources, the data can be used for many other studies, such as the search for new supernovae, dark matter, magnetic monopoles, and more. In this research, the data are used to determine the cross section of the muon neutrino during its interactions with nucleons. Before this work, the highest neutrino energy available for a measurement of the muon neutrino-to-nucleon cross section was approximately 340 GeV. This analysis examines the total muon neutrino-to-nucleon cross section for neutrino energies between $\sim$6 TeV and 1 PeV, or $\sim$20 to 3,000 times higher than previous results. This is possible because the neutrinos do not come from a terrestrial accelerator but instead from high-energy cosmic rays.

Standard accelerator particle physics experiments are characterized by three things: the particle source, the target for interactions, and the detector. In the case of this research, the source is the constant barrage of cosmic rays interacting with the Earth's atmosphere to create the stream of high-energy neutrinos for the analysis. The target is the Earth itself, using variations in rock density versus zenith angle to measure high-energy neutrino absorption by the Earth for the first time. The detector is the IceCube Neutrino Detector at the South Pole, which uses a cubic kilometer of clear Antarctic ice and over 5,000 sensors to detect incoming charged particles from any direction.

The research strategy is to examine the number of muon neutrinos from cosmic rays that interact with nucleons to form muons, which are then detected at various angles during one year of data in the 79-string configuration. The neutrinos that come from the horizon

(which corresponds to 90 degrees zenith angle) travel through a minimal amount of rock and ice before reaching the detector. The neutrinos that come through the Earth's core, or directly upwards through the detector (which corresponds to 180 degrees zenith angle), travel through the densest region of the Earth. As the zenith angle varies from 90 and 180 degrees, the neutrinos would encounter an increasing amount of matter.

By comparing the expected numbers of muons from simulation to the actual numbers of muons observed from the interactions of the muon neutrinos with the nucleons of the rock and ice, the cross section of the muon neutrino with nucleons as a multiple of the Standard Model expectation can be determined. This analysis is a "first look" at the neutrino cross section above 1 TeV. The result is important because some theories beyond the Standard Model predict an increase in the neutrino-nucleon cross section at higher energies. If the increase is seen, then the alternate theories may have merit.

This dissertation is organized into chapters that are intended to explain the theoretical concepts and to describe the unique aspects of this research. Chapter 2 describes the concepts of neutrino physics and muon detection. Chapter 3 describes the cosmic rays, which provide the source of the high-energy neutrinos used in this research. Chapter 4 covers the IceCube Neutrino Detector and how the particles are detected. Chapter 5 describes the simulation that is used for comparisons to data. Chapter 6 covers the standardized data analysis. Chapter 7 describes the event selection methods that isolate the sample of events that result in the measurement. Chapter 8 covers the analysis procedures, putting all the pieces together to find the best-fit result. Chapter 9 describes the actual result, with relevant systematic errors. Chapter 10 summarizes the analysis and proposes future research in this area.

Chapter 2

Neutrinos and Interactions

2.1 Introduction

The neutrino was first postulated by Wolfgang Pauli in a letter dated 4 December 1930 to the attendees of a physics conference in Tübingen, Germany [1]. He proposed the existence of a tiny neutral particle (given the name "neutrino" by Enrico Fermi in 1933) to explain the apparent violation of energy conservation in radioactive decays. His famous quote about the neutrino summarizes its elusive nature: "I have done a terrible thing, I have postulated a particle that cannot be detected." The neutrino would remain undiscovered until 1956 when Cowan and Reines first detected the antineutrino [2]. The first neutrino experiments used reactors as the sources of neutrinos. Later experiments used neutrinos from the Sun or from accelerators to measure the cross sections of the muon neutrino (and the muon antineutrino) at energies up to 340 GeV [3]. The cross sections for higher-energy neutrinos have not been possible due to energy limitations of the accelerators. Cosmic rays can be used as the source of high-energy neutrinos, and this approach will be the subject of Chapter 3.

This chapter reviews the relevant concepts of neutrino physics, including the cross section and calculations of the cross section, followed by previous experimental results, Earth absorption of neutrinos, the creation of muons, and muon energy loss processes.

2.2 Neutrino basics

The Standard Model of particle physics (SM) describes the fundamental particles and their interactions. The SM accounts for the existence of neutrinos, but it does not currently account for their masses, and thus the model is incomplete. Neutrinos are in a class of particles called leptons. There are three lepton "flavors" (with their matching anti-particles): the electron, the muon, and the tau. For each of these particles (and anti-particles), there are matching neutrinos. The existence of the first two neutrino flavors was demonstrated in 1962 by scientists at Columbia University and Brookhaven National Laboratory (BNL) [4]. For the third flavor, the tau was discovered at the Stanford Linear Accelerator Center in 1975 [5]. While indirect evidence for the tau neutrino existed earlier, it was first observed by the DONUT collaboration in 2000 [6]. The neutrino has left-handed helicity, while the anti-neutrino has right-handed helicity, as shown at BNL in 1958 [7].

2.3 Neutrino oscillations

Neutrinos must have mass because neutrinos can oscillate between flavors as they travel through space, as was first proposed by Bruno Pontecorvo in 1957 [8]. Oscillations are apparent when counting the neutrinos created by the Sun during nuclear fusion. These neutrinos are entirely electron neutrinos in the ratio of 1:0:0 (for ν_e:ν_μ:ν_τ). By the time the neutrinos arrive at the Earth, their ratio is roughly 1:1:1 [9]. This phenomenon explains the solar neutrino deficit that was seen in 1968, when neutrinos from the Sun were first observed using a detector deep underground in the Homestake mine in South Dakota [10]. IceCube has also seen this oscillation of neutrinos at higher energies [11].

The probability P that a neutrino of energy E, originally in state A, is instead in state B after a distance L from its generation point, can be given by [12]:

$$P(\nu_A \rightarrow \nu_B) = \sin^2(2\theta)\sin^2\left(1.27\delta m^2 \frac{L}{E}\right) \tag{2.1}$$

where $\delta m^2 = (m_B^2 - m_A^2)$ is the difference in the squared masses of the neutrino mass eigenstates in units eV^2, $\sin^2(2\theta)$ is the mixing parameter, and $\frac{L}{E}$ is in units km/GeV.

One question is whether the high-energy neutrinos that form in the atmosphere have enough time to oscillate during their transit of the Earth before reaching the detector, therefore changing the available neutrino spectrum for this analysis. If oscillations are not important, $\sin^2(1.27\delta m^2 L/E)$ will be near 0, which implies that the value of the variables within the parentheses would be near 0. The $\frac{L}{E}$ term needs to balance the small δm^2 term, which is on order of 10^{-3} eV^2. For this analysis, L is in thousands of kilometers, and E is on the order of a TeV. Therefore, $\frac{L}{E}$ is $\sim$1. Even when using the full Earth diameter (12,720 kilometers from pole to pole) at the lowest energy, $\frac{L}{E}$ becomes $\sim$12 at its highest value. A higher neutrino energy would make $\frac{L}{E}$ smaller. The value of the variables within the parentheses for the energy range of this analysis will be on order 0.01 or lower, which results in a very small chance of oscillation. In reality, a neutrino energy of less than $\sim$100 GeV is needed for any reasonable oscillation measurement in the Earth [11]. Therefore, oscillations are not a factor in this analysis for the neutrinos created in cosmic ray interactions.

2.4 Neutrino interactions and cross sections

The neutrinos interact weakly, and the neutrino-to-nucleon interaction can be approximated as that of the neutrino with one of the quarks (or antiquarks) inside the nucleon. The most important interaction for this analysis is deep inelastic scattering (DIS) due to the larger cross sections. Neutrinos participate in both types of DIS: neutral current (NC) interactions (where the Feynman diagram includes the exchange of a virtual Z boson) and charged current (CC) interactions (with the exchange of a virtual W boson). In 1973, the first NC event was observed by an international team working at the Conseil Européen pour la Recherche Nucléaire (CERN) in Geneva, Switzerland, using a bubble chamber [13]. This observation provided strong support to a unified theory of weak and electromagnetic interactions that had been proposed earlier by Sheldon Glashow and collaborators [14], Abdus Salam [15], and Steven Weinberg [16]. The combination of this model with that of the quark

sector comprises the SM. Figure 2.1 shows the general Feynman diagrams of the NC and CC interactions. The CC interaction is the dominant one in this analysis, but both NC and CC interactions for ν and $\bar{\nu}$ are relevant.

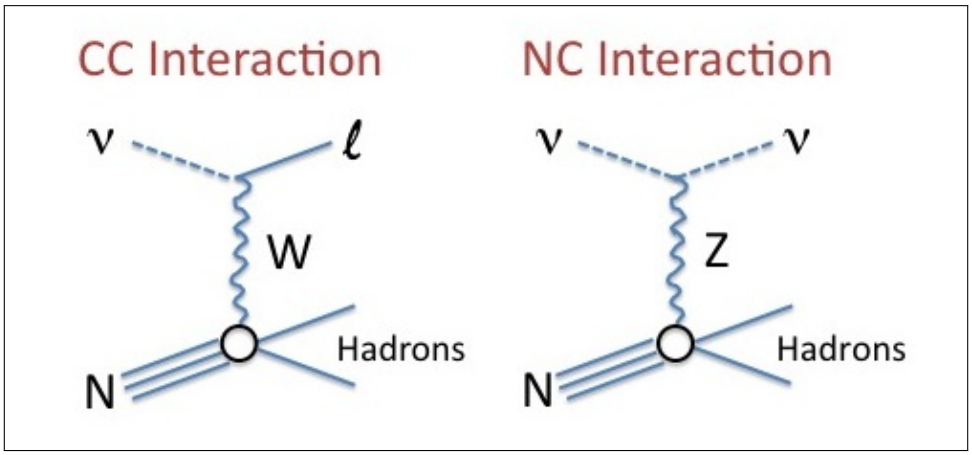

Figure 2.1: Feynman diagrams showing the general form of the different types of interactions, including a charged-current (CC) interaction, which produces a lepton, and a neutral-current (NC) interaction, where the neutrino is unchanged except for the loss of energy. In both cases, energy will be transferred to the quark in the nucleon, which recoils and produces a shower of hadronic particles.

The initial formalism for the calculation of the neutrino cross section was developed in the 1960's to describe the scattering of charged leptons with nucleons. Later, the calculations were expanded to include the scattering of neutrinos. The formalism used "structure functions" to provide the most general, Lorentz-invariant parameterization of the lepton-hadron vertex of the Feynman diagrams. These structure functions were later associated with "parton distribution functions" or PDFs, where the partons are the constituents of the nucleons. For lepton interactions, the quarks and the antiquarks are the partons that can be accessed directly by using lepton interactions.

The generalized Feynman CC diagram from Figure 2.1 has been specialized for the muon neutrino and labeled with the particle four-momenta in Figure 2.2. The four-momenta are defined as $p_1 = (E_1, \boldsymbol{p}_1)$, where $\boldsymbol{p}_1$ is the three-momentum, with p_1 assigned to the neutrino, p_2 to the nucleon, p_3 to the outbound muon, and p_4 to all the hadrons. The variable q is assigned to the transfer of four-momentum by the W boson. From these quantities, we can construct new variables which are invariant under Lorentz transformations:

$$s = (p_1 + p_2)^2 \tag{2.2}$$

$$Q^2 = -q^2 \tag{2.3}$$

$$y = \frac{p_2 \cdot q}{p_2 \cdot p_1} \tag{2.4}$$

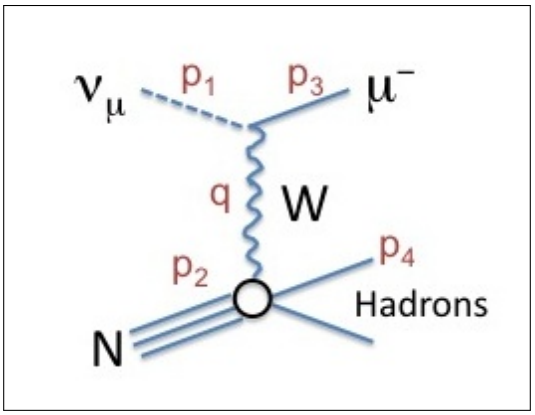

Figure 2.2: Four-momenta for the specific CC interaction of ν_μ on a nucleon.

where s is the square of the center of mass energy, Q^2 is the square of the four-momentum transfer, and y is the inelasticity. In the target's rest frame, the inelasticity can be written:

$$y = \frac{E_1 - E_3}{E_1} \tag{2.5}$$

The inelasticity can be interpreted as the fraction of the neutrino's initial energy transferred by the interaction. Lastly, we define the Bjorken scaling variable, x, which is roughly equivalent to the fraction of the target nucleon's momentum carried by the quark:

$$x = \frac{Q^2}{2p_2 \cdot q} \tag{2.6}$$

The variables $[x, y, Q^2]$ fully define the kinematics to parameterize unpolarized cross sections. A simpler interaction mechanism than DIS is $e\ p$ elastic scattering, which has been well studied in accelerator experiments. The Rosenbluth formula for the cross section of this interaction at q^2 is [17]:

$$\left(\frac{d\sigma}{d\Omega}\right) = \frac{\alpha^2}{4E_1^2 \sin^4(\theta/2)} \left(\frac{E_3}{E_1}\right) \left(\frac{q^2}{2M_p^2} G_M^2 \sin^2(\theta/2)\right) \tag{2.7}$$

where σ is the cross section, Ω is the solid angle, α is the structure constant $= \frac{e^2}{\hbar \cdot c} = \frac{1}{137}$, θ is the scattering angle, M_p is the mass of the proton, and G_M is the proton magnetic form factor, all assuming natural units where $\hbar = c = 1$. In the case of inelastic scattering, the proton does not remain intact, and the mass of the proton is replaced with the mass of the hadrons that form in the jet. This jet must contain at least one baryon, and the total mass is represented by $M_X^2 = p_4^2$. Using the invariant quantities, this equation becomes:

$$M_X^2 = (q + p_2)^2 = -Q^2 + 2p_2 \cdot q + M_p^2 \tag{2.8}$$

Defining one more variable $\tau = Q^2/4M^2$, the Rosenbluth formula can be rewritten in the lab frame as:

$$\left(\frac{d\sigma}{d\Omega}\right) = \frac{\alpha^2}{4E_1^2 \sin^4(\theta/2)} \left(\frac{E_3}{E_1}\right) \left(\frac{G_E^2 + \tau G_M^2}{(1+\tau)} cos^2(\theta/2) + 2\tau G_M^2 \sin^2(\theta/2)\right) \tag{2.9}$$

Changing to a derivative in Q^2, the formula becomes:

$$\left(\frac{d\sigma}{dQ^2}\right) = \frac{4\pi\alpha^2}{Q^4}\left[\frac{G_E^2 + \tau G_M^2}{(1+\tau)}\left(1 - y - \frac{M_p^2 y^2}{Q^2}\right) + \frac{1}{2}y^2 G_M^2\right] \tag{2.10}$$

This can be simplified by substituting form functions $f(Q^2)$ for the magnetic form factors:

$$\left(\frac{d\sigma}{dQ^2}\right) = \frac{4\pi\alpha^2}{Q^4}\left[f_2(Q^2)\left(1 - y - \frac{M_p^2 y^2}{Q^2}\right) + \frac{1}{2}y^2 f_1(Q^2)\right] \tag{2.11}$$

This formula is a first-order derivative in Q^2 alone because $x = 1$ for elastic scattering. For deep inelastic scattering, $0 < x < 1$, and the cross section formula becomes a second-order derivative in Q^2 and x:

$$\left(\frac{d^2\sigma}{dx\ dQ^2}\right) = \frac{4\pi\alpha^2}{Q^4}\left[\left(1 - y - \frac{M_p^2 y^2}{Q^2}\right)\frac{F_2(x,Q^2)}{x} + y^2 F_1(x,Q^2)\right] \tag{2.12}$$

where the structure functions $F(x, Q^2)$ describe the momentum distribution of the quarks within the proton as the most general Lorentz-invariant form of the kinematic dependence. In the limit of high $Q^2 \gg M_p^2 y^2$, the equation becomes:

$$\left(\frac{d^2\sigma}{dx\ dQ^2}\right) = \frac{4\pi\alpha^2}{Q^4}\left[(1-y)\frac{F_2(x,Q^2)}{x} + y^2 F_1(x,Q^2)\right] \tag{2.13}$$

This is the general form of the equation describing the differential cross section for $e\ p$ inelastic interactions at high energy [18]. The $(1 - y)$ term stems from the "V-A interaction law," which is a generalization of Fermi's interaction theory to address parity violation for polar vector (V) and axial vector (A) currents [19]. The determination of the structure functions for a given x and Q^2 requires measurements of the differential cross section at several different scattering angles and incoming electron beam energies.

For DIS of neutrinos with nucleons, the main difference is that the propagator is not a photon as in $e\ p$ scattering, but a W boson. There are only 2 polarizations for photons but 3 possible polarizations for bosons, which then requires the structure function F_L for the longitudinal mode. A similar procedure to that described above is followed to produce the differential DIS cross section for neutrinos on nucleons [20]:

$$\frac{d^2\sigma(\nu(\bar{\nu})N)}{dx\ dQ^2} = \left[\frac{G_F^2 M_W^4}{4\pi(Q^2 + M_W^2)^2 x}\right]\sigma(\nu(\bar{\nu})N) \tag{2.14}$$

where G_F is the Fermi constant, M_W is the W mass, x, y, and Q^2 are the invariant variables already defined, and $\sigma(\nu N)$ and $\sigma(\bar{\nu}N)$ are the cross sections defined as (using $Y_\pm = 1 \pm (1-y)^2$):

$$\sigma(\nu N) = \left[Y_+ F_2^\nu(x,Q^2) - y^2 F_L^\nu(x,Q^2) + Y_- x F_3^\nu(x,Q^2)\right] \tag{2.15}$$

$$\sigma(\bar{\nu}N) = \left[Y_+ F_2^{\bar{\nu}}(x,Q^2) - y^2 F_L^{\bar{\nu}}(x,Q^2) - Y_- x F_3^{\bar{\nu}}(x,Q^2)\right] \tag{2.16}$$

For leading order interactions, the structure function F_L is equal to zero, and the structure functions F_2 and xF_3 for CC interactions on isoscalar targets can be identified with quark distributions as follows [21]:

$$F_2^{\nu} = x(u + d + 2s + 2b + \bar{u} + \bar{d} + 2\bar{c}) \tag{2.17}$$

$$xF_3^{\nu} = x(u + d + 2s + 2b - \bar{u} - \bar{d} - 2\bar{c}) \tag{2.18}$$

$$F_2^{\bar{\nu}} = x(u + d + 2c + \bar{u} + \bar{d} + 2\bar{s} + 2\bar{b}) \tag{2.19}$$

$$xF_3^{\bar{\nu}} = x(u + d + 2c - \bar{u} - \bar{d} - 2\bar{s} - 2\bar{b}) \tag{2.20}$$

where each quark is represented (up, down, strange, bottom, charm) except top. The sea quarks only account for about 10% of the hadrons' momentum at high Q^2. Since the sea quarks are made up of $q\,\bar{q}$ pairs emitted by gluons, the lighter pairs are more readily produced than the heavier pairs. This is why the quark contributions from charm and strange are small compared to the others [20].

The quark PDFs (u, d, etc.) are determined by assuming a parameterization in x at a starting value of $Q^2 = Q_0^2$. The parameterization for the lighter quarks is of the form $Ax^B(1-x)^C P(x)$, where $P(x)$ is some smooth function of x. These equations are fit to the DIS data over the range of the (x, Q^2) plane [21].

The equations for the differential cross section for NC interactions have the same general form as Equation 2.14 but with M_W changed to M_Z for the mass of the Z boson. With the change in propagators, the structure functions to leading order are [21]:

$$F_2^{\nu,\bar{\nu}} = x\left[\frac{1}{2}(a_u^2 + v_u^2 + a_d^2 + v_d^2)(u + \bar{u} + d + \bar{d}) + (a_d^2 + v_d^2)(s + b + \bar{s} + \bar{b}) + (a_u^2 + v_u^2)(c + \bar{c})\right] \tag{2.21}$$

$$xF_3^{\nu,\bar{\nu}} = x\left[(u - \bar{u} + d - \bar{d})(v_u a_u + v_d a_d)\right] \tag{2.22}$$

where v_u, v_d, a_u, and a_d are the neutral-current-vector and axial-vector couplings for u and d type quarks.

In order to integrate the differential cross section equations to get the total cross section, the quark distributions above need to be determined. At lowest order, the cross sections exhibit scaling in x, making it possible to describe them in terms of PDFs. The proton and neutron structures have been thoroughly examined in a variety of atomic and nuclear experiments, and this knowledge can be used to create the necessary PDFs. For fixed x and y, e p collider experiments can reach much large values in Q^2. In addition, for fixed y and Q^2, the same experiments can reach much smaller values in x.

The parton model assumes that each nucleon is composed of point-like constituents called partons, including valence quarks (3), sea quarks, and gluons. There are separate PDFs for the proton and the neutron. For neutrino interactions, the relevant partons are the valence quarks and sea quarks, but not the gluons because the neutrinos are colorless with respect to quantum chromodynamics (QCD). A PDF gives the probability that the struck quark

carries a specific fraction of the nucleon's momentum. The simple parton model does a fair job at lowest order, but more precise measurements see violations from scaling, which are predicted by QCD corrections to the simple model.

If the PDFs are known, then the SM allows the cross sections to be calculated. These calculations include next-to-next-to-leading order (NNLO) contributions in QCD. However, the PDFs cannot be calculated from first principles in QCD when α_s becomes large. The PDFs must be measured by experiment.

For many years, the PDFs used by many experiments were derived from the results of the CTEQ collaboration (Coordinated Theoretical/Experimental Project on QCD Phenomenology and Tests of the Standard Model) [22]. The PDFs have evolved over the years, hence the numerical designation attached to the CTEQ acronym. For example, the CTEQ5 PDFs [23] were used by IceCube until 2013. However, the CTEQ PDF energies did not extend above 1 TeV ($0.005 < x < 0.4$), and a rough (i.e., linear) extrapolation of the PDFs to higher energies was necessary for use in IceCube simulation.

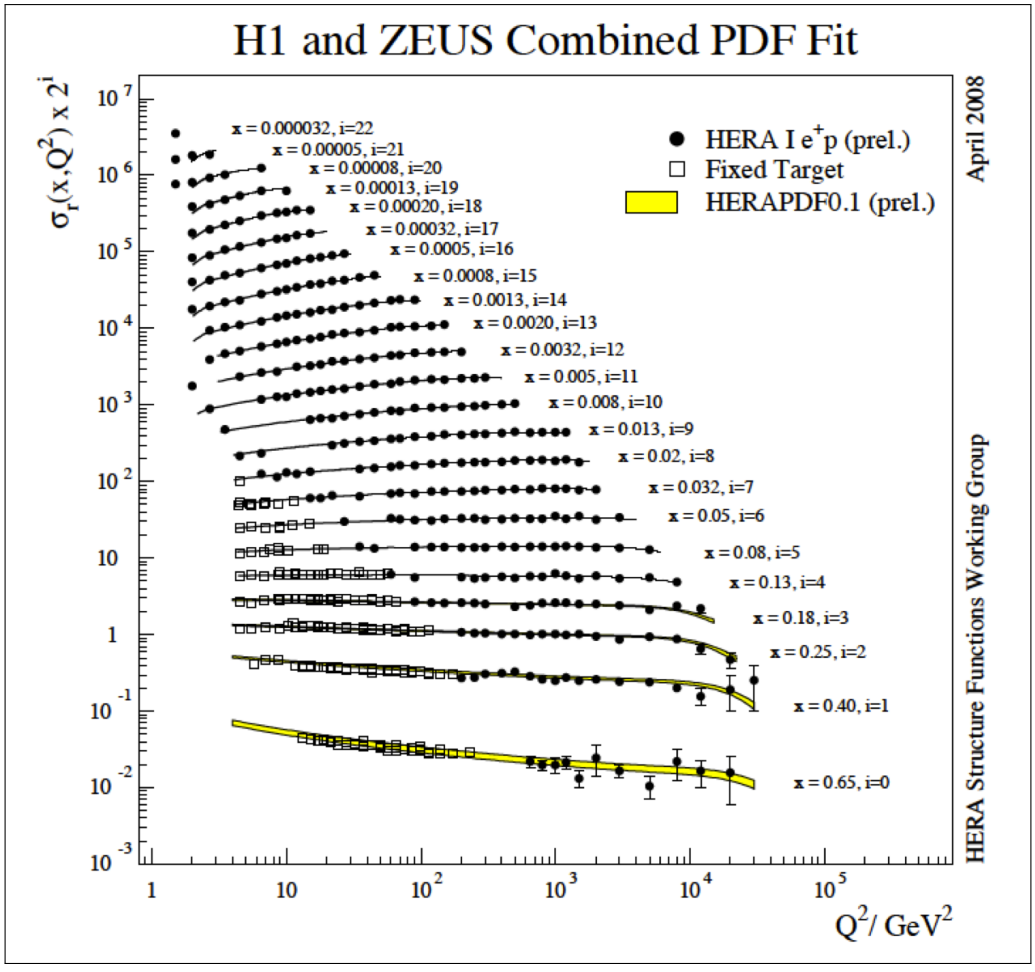

Figure 2.3: Ranges of x and Q^2 represented by the combined H1 and ZEUS data, which are used to form the HERAPDF1.5. Low x and high Q^2 are represented but not simultaneously. The DGLAP formalism is used to extrapolate the data to higher energies represented by low x and high Q^2. The yellow lines compare the data to an earlier HERAPDF. From [24].

There are many collaborations that combine experimental measurements to produce parameterizations of the PDFs and their uncertainties. Each one uses a variety of functional forms and makes different choices about which data to include and how to handle the uncertainties in the data. There are a number of newer parameterizations available from experiments, and each analysis needs to choose the most appropriate one. In the case of this analysis, only one cross section calculation extends into the relevant neutrino energy range, making the choice simple. That calculation uses the HERAPDF1.5 fit to the most recent HERA data [25]. In this PDF, the inclusive cross section data from the HERA-I and HERA-II running period of 1992-2007 for e^+p and e^-p scattering are combined. The combination procedure accounts for the correlated systematic uncertainties of the data sets, resulting in benefits from the best features of each detector. The combined data set has systematic uncertainties which are smaller than its statistical errors, and the total uncertainties are small (1-2%) over a large portion of the kinematic range. Figure 2.3 shows the ranges of x and Q^2 that are represented by the data. The ranges are 6 x $10^{-7} < x < 0.65$ and $0.045 < Q^2 <$ 30,000 GeV^2 [25].

The values of x and Q^2 pertinent to this analysis will be discussed in detail below, but a rough order of magnitude estimation is possible. Using Equation 2.2 for s, and by using energy-momentum conservation, $Q^2 = sxy$. For $y \sim 1$, $x = Q^2/s$. For a nucleon at rest in the lab frame, $s \simeq 2M_N E_\nu$ [26]. Also, Q^2 is restricted to values near $M_W^2 \sim 6 \cdot 10^3$ GeV^2 (for CC interactions), due to the gauge boson propagator above a neutrino energy of ~1 TeV. At ultra-high energies, the largest contributions to the cross section occur for the values of x in the region near $M_W^2/2M_qE_\nu$ [27]. This expression gives a rough order of magnitude for $x \simeq 5{\cdot}10^{-3}\,(E_\nu/PeV)^{-1}$. For a neutrino energy ~10 PeV, this gives x of $\sim 10^{-4}$ [26]. However, x cannot be greater than 1 by definition, and at low energies this method for a rough estimate will fail, as Figure 2.4 shows the relative actual importance of x values for different neutrino energies. Putting all this together, the estimates for x and Q^2 for the energy range of this analysis are $10^{-4} < x < 0.5$, and $10^3 < Q^2 < 10^5$ GeV^2.

The shape of the cross section versus energy curve is influenced by the W propagator. At low neutrino energies ($E_\nu \ll M_W^2/M$, where M_W is the W boson mass and M is the nucleon mass), the differential and total cross sections for neutrinos with nucleons are proportional to the neutrino energy. For $E_\nu \gtrsim 1$ TeV, the W propagator restricts Q^2 to values near M_W^2 and damps the cross section such that the cross section no longer rises linearly with energy [27].

Individually, the estimated ranges of x and Q^2 above agree fairly well with the HERAPDF1.5 ranges, but not when paired. In other words, H1 and ZEUS were able to probe high Q^2 and low x but not at the same time. Since this analysis requires PDFs utilizing a combination of x and Q^2 not directly measured, an extrapolation formalism is required. The conventional PDF uses the Dokshitzer-Gribov-Lipatov-Altarelli-Parisi (DGLAP) formalism [29; 30; 31] of next-to-leading-order (NLO) QCD. In the DGLAP formalism, a QCD analysis is performed using the equations from the references listed. The DGLAP equations yield PDFs at all values of Q^2 if they are provided as functions of x at some input scale Q_o^2. In essence, the DGLAP formalism theoretically extrapolates experimental results to all combinations of x and Q^2. The formalism allows the momentum distribution in the nucleon to be determined for a much wider range than with experiment alone, which then results in the individual quark distributions needed for Equations 2.17 through 2.22.

The interaction amplitudes can be calculated exactly by using simple Feynman diagrams

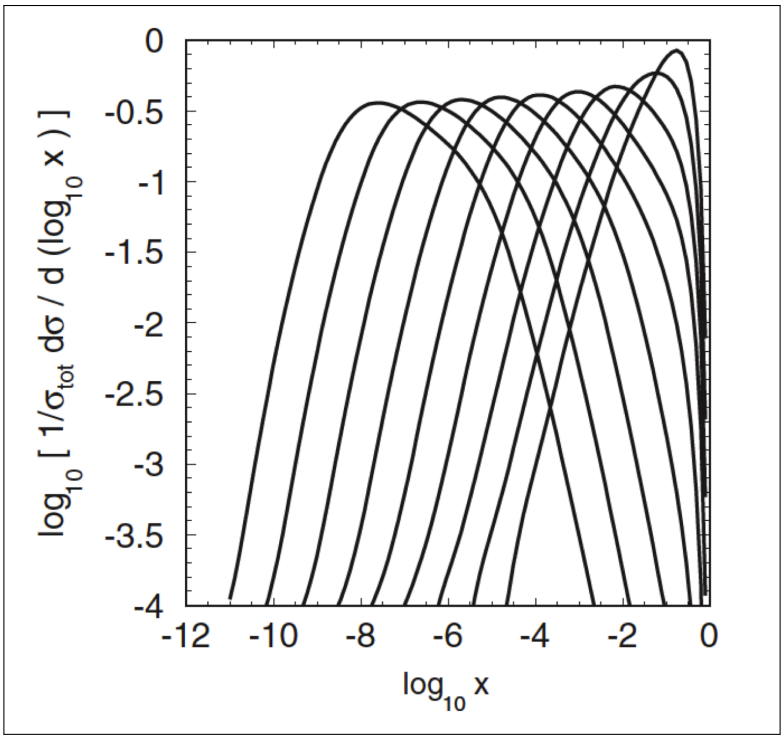

Figure 2.4: Normalized x distributions for neutrino interactions for each energy decade from $E_\nu = 10^4$ to 10^{12} GeV. As neutrino energy increases, the mean value of $\log_{10}(x)$ decreases. For this analysis, the first four lines from the right are the most relevant, representing neutrino energies from 10 TeV to 10 PeV. From [28].

called tree-level, or lowest order (LO), diagrams. NLO diagrams are called loop-level diagrams and lead to quantum corrections [32]. The relative contribution of LO versus NLO is discussed below. Modern PDFs use NLO QCD. In order to calculate the cross section, one must integrate the PDF over x (from 0 to 1) and Q^2. This calculation gives the probability that the parton is carrying a specific amount of the nucleon's momentum.

In 2008, these procedures were used in a cross section calculation published by Cooper-Sarkar and Sarkar of the ZEUS collaboration and designated CSS [33]. They used the conventional DGLAP formalism of NLO QCD using a modern PDF fit to the HERA data called HERAPDF1.0 [34]. They extended the PDF to lower values of x, which allowed a more robust extrapolation of the neutrino cross section to higher energies. However, the calculation overlooked some of the b-quark and t-quark contributions at low x values [21], and the calculation did not include updated x and y tables. In order to use the CSS PDFs in simulation, one had to use an existing set of tables, such as the CTEQ tables.

In 2011, Cooper-Sarkar, Mertsch, and Sarkar [21] completely revised the previous calculation but this time included x and y tables with the PDFs. They updated the calculations for high-energy neutrino and antineutrino CC and NC cross-sections within the conventional DGLAP formalism of NLO QCD but this time using the HERAPDF1.5. The cross section calculation, designated as CSMS, covers the energy range up to 10^{12} GeV and includes new x and y tables that are three times more refined than the old tables. This calculation became the new standard in the simulation of the IceCube collaboration in 2013.

The CSMS calculation examined three different sets of PDFs before choosing the final one, namely CT10 [35], Martin et al. (MSTW) [36], and HERAPDF1.5. The relevant variable ranges for CT10 are the same as HERAPDF1.5 (since they also used the updated HERA data), and for MSTW are $10^{-4} < x < 0.9$ and $4 < Q^2 < 10{,}000$ GeV^2. CSMS examined the differences due to the three PDFs at $Q^2 = 10{,}000$ GeV^2 and found very little effect on the total cross section. These uncertainties were on the order of a few percent for all neutrino energies in this analysis, regardless of the PDF choice. The authors chose HERAPDF1.5 because of the small errors inherent from the combined data and the large range of x and Q^2 values. Since the overall systematic uncertainty in this analysis is ∼30% (discussed in Chapter 9), the CSMS calculation uncertainties are considered negligible.

Figure 2.5 depicts the upper and lower limits of x and Q^2 relevant for the neutrino energies in this analysis from the CSMS calculation, which are $50 < Q^2 < 100{,}000$ GeV^2 and $10^{-5} < x < 0.6$. The contours in the figure show the contributions to the cross section for the paired values of x and Q^2. The dominant contributions to the cross section do not come from the kinematic regions with the greatest uncertainty in the PDFs, which occur at low x with low Q^2. Although the relevant values of Q^2 for this analysis are a bit higher than that probed by the HERA data, these values are covered by the DGLAP formalism. Fortunately, events with $Q^2 > 10{,}000$ GeV^2 are rare in this analysis, on order of a few per 10,000 events in a data year, and uncertainties due to the extrapolation should have minimal impact on the overall analysis.

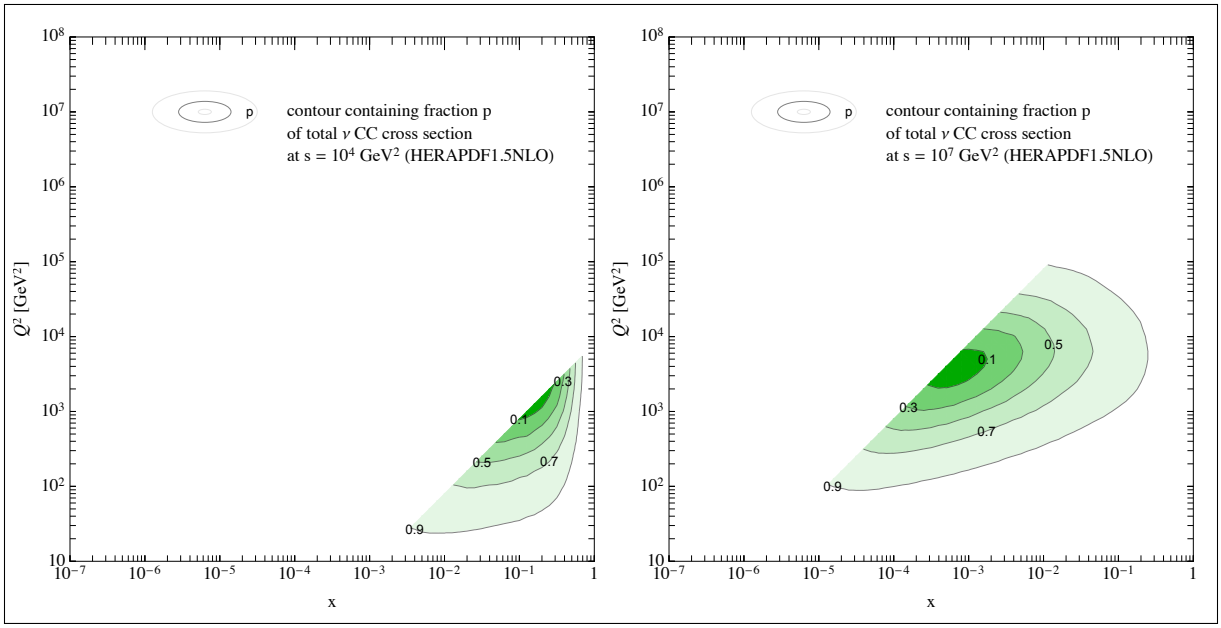

Figure 2.5: (left) Paired values of x and Q^2 for $s = 10^4$ GeV^2, or lab frame neutrino energy ∼5 x 10^3 GeV. The contours in the figure show the contributions to the cross section, with the 0.9 contour indicates that 90% of the contribution to the cross section originates from those values of x and Q^2. (right) Same plot for $s = 10^7$ GeV^2, or lab frame neutrino energy ∼5 x 10^6 GeV. The two plots show most of the x and Q^2 space relevant for this analysis. From [21; 37].

There are four cross sections that apply to this analysis: νN CC interactions, νN NC interactions, $\bar{\nu} N$ CC interactions, and $\bar{\nu} N$ NC interactions. Figure 2.6 shows their relative

values from the CSMS calculation. The dominant component is the νN CC cross section. The $\bar{\nu}N$ cross section is lower than the νN cross section because of helicity conservation. The left-handed ν interacts with a left-handed q or right-handed $\bar{q}$ via the exchange of a W^+. At energies above $\sim 10^6$ GeV (1 PeV), the $\bar{\nu}N$ cross section becomes nearly identical to the νN cross section, for both NC and CC interactions. This is due to the interaction contribution of sea quarks, which exist as equal proportions of q and $\bar{q}$.

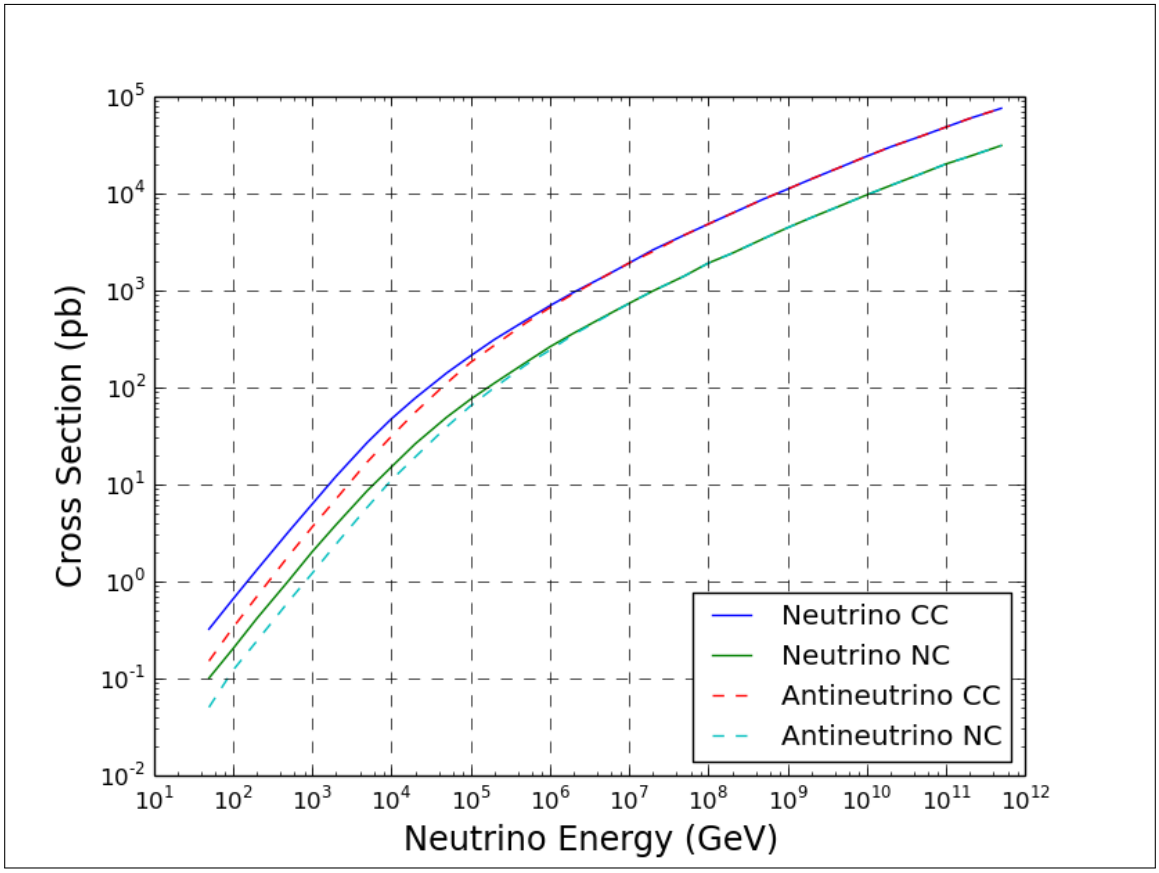

Figure 2.6: Theoretical predictions for $\nu_\mu N$ and $\bar{\nu}_\mu N$ cross sections for charged-current (CC) and neutral-current (NC) inelastic scattering. Data from [21].

The CSMS cross section calculation provides a table of the theoretical predictions of the cross sections using an "isoscalar target", for equal numbers of protons and neutrons in the material. The Earth is composed of iron (32.1%), oxygen (30.1%), silicon (15.1%), magnesium (13.9%), sulfur (2.9%), nickel (1.8%), calcium (1.5%), aluminum (1.4%), and other trace elements (1.2%) [38]. Other than iron, the majority of the elements that make up the Earth contain equal or nearly equal numbers of protons and neutrons (no more than one nucleon difference). In addition, iron has 26 protons and 30 neutrons and is not too far from being an isoscalar target, plus it is mostly concentrated in the core. Therefore, the assumption of an isoscalar target is adequate for this analysis.

Table 2.1 lists numerical values from the CSMS tables for the individual cross sections for muon neutrinos and muon antineutrinos with nucleons for ease of reference for the remainder of this analysis.

Table 2.1: Cross sections (in pb) for ν_μ and $\bar{\nu}_\mu$ with nucleons, for both charged-current (CC) and neutral-current (NC) interactions, for the energy range of this analysis. Data from [21].

E_ν (GeV)	ν_μ CC	ν_μ NC	$\bar{\nu}_\mu$ CC	$\bar{\nu}_\mu$ NC
1,000	6.2	2.0	3.6	1.2
2,000	12.	3.8	7.0	2.4
5,000	27.	8.6	17.	5.8
10,000	47.	15.	31.	11.
20,000	77.	26.	55.	19.
50,000	140.	49.	110.	39.
100,000	210.	75.	180.	64.
200,000	310.	110.	270.	99.
500,000	490.	180.	460.	170.
1,000,000	690.	260.	660.	240.
2,000,000	950.	360.	920.	350.
5,000,000	1400.	540.	1400.	530.
10,000,000	1900.	730.	1900.	730.

2.5 Neutrino cross section measurements

The neutrino cross section has been measured by a multitude of experiments over the years. The energies of these experiments are well below the energy range of this analysis, but the results are important nonetheless. Figure 2.7 shows a summary of accelerator experiments compiled by the Particle Data Group (PDG) [39]. In the figure, the values for the CC cross section divided by energy, for both $\nu_\mu N$ and $\bar{\nu}_\mu N$, are shown.

Differential cross sections for inclusive scattering processes at higher energies have been measured on iron by NuTeV [3]. At lower energies, the cross sections were measured on argon by ArgoNeuT [40] and on carbon by T2K [41]. Several high-energy neutrino experiments have measured the DIS cross sections for specific final states, such as opposite-sign dimuon production. Recent dimuon cross section measurements include those from CHORUS [42], NOMAD [43], and NuTeV [44]. These results are shown in Figure 2.7.

For the high-energy cross section, the predecessor to IceCube called AMANDA (Antarctic Muon And Neutrino Detector Array) collected data that set limits [45] based upon hypothetical neutrino sources. The reference cross section for the CC neutrino-nucleon interaction was from [46] using CTEQ4 PDFs [47]. The limits were based upon the numbers of events that were seen within the detector. The limits were set for $\sqrt{s} \sim 6$ TeV, which equates to a neutrino energy in the rest frame of $\sim$20 PeV. Figure 2.8 shows the values of cross section versus neutrino flux that were disfavored at more than 90% confidence level.

ANITA (ANtarctic Impulsive Transient Antenna) also set limits on the cross section, based upon hypothetical neutrino sources. ANITA was a balloon-based experiment that looked for the Cherenkov radio signals from ultra-high-energy neutrino interactions ($E_\nu > 10^{18.5}$ eV, or $10^{6.5}$ TeV) in the Antarctic ice. Their assumptions included a Greisen-Zatsepin-Kuzmin (GZK) neutrino spectrum from high-energy protons (where cosmic rays interact with the cosmic microwave background and are attenuated) [48; 49] and an equal scaling of

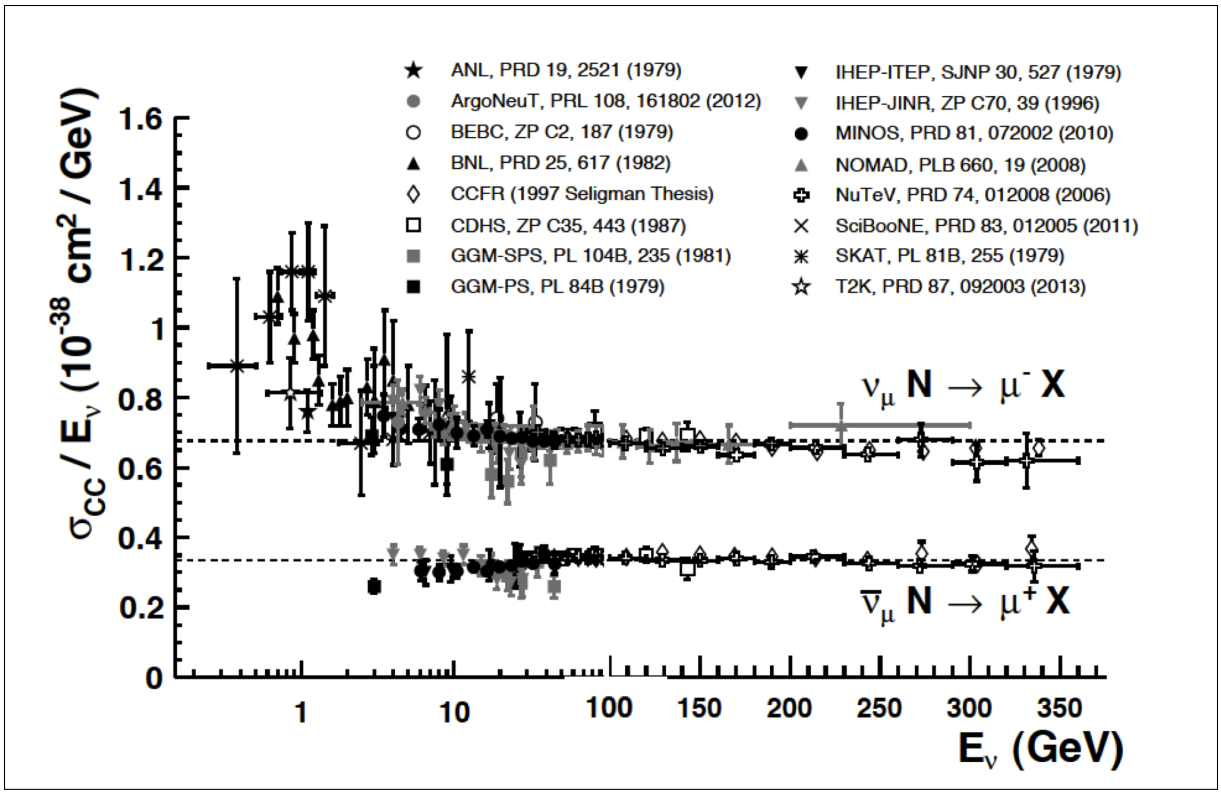

Figure 2.7: Measurements of the muon neutrino and muon antineutrino CC inclusive scattering cross sections divided by neutrino energy, as a function of neutrino energy (in units of 10^{-38} cm^2/GeV). The ratio equates to ∼0.68 for $\nu_\mu N$ and ∼0.34 for $\bar{\nu}_\mu N$ as shown by the dashed lines. Neutrino cross sections are typically twice as large as their corresponding antineutrino counterparts at the median energies of this plot, but the difference is larger at lower energies and smaller at higher energies. NC cross sections (not shown) are generally smaller but non-negligible when compared to the CC scattering case. Maximum energies for experimental measurements are ∼340 GeV. From [39].

the SM cross sections for both CC and NC interactions in the case of new physics. Because the experiment did not detect any neutrinos, the experiment set an upper limit on the cross section multiple for the energy range of $10^{6.5} < E_\nu < 10^9$ TeV. Their cross section upper limit is 18 times the SM expectation in this range [50; 51].

2.6 Earth absorption experiments

Assuming a SM cross section, neutrinos above ∼10 TeV will interact with the Earth in significant numbers. The energy of the neutrino where the North Pole to South Pole path is equivalent to an interaction length is ∼40 TeV [27]. There are two basic types of Earth absorption experiments: using the Earth's density profile to measure the neutrino-nucleon cross section, such as in this analysis, and the reverse idea of using the cross section to measure the Earth's density profile. The latter is called neutrino radiography or tomography and was first proposed by Volkova and Zatsepin in 1974 [52] using an Earth-bound accelerator.

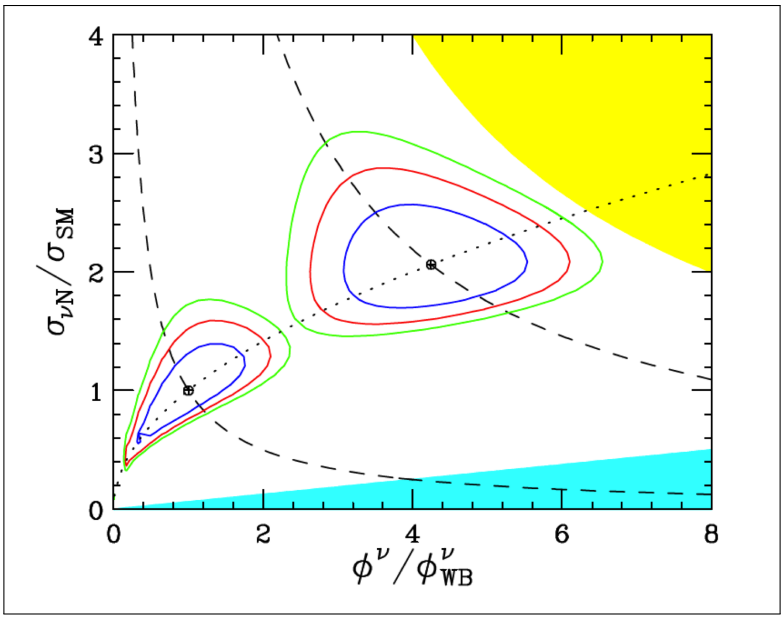

Figure 2.8: Neutrino fluxes ϕ_ν (in relation to the prediction by Waxman and Bahcall (WB)) versus cross sections (in relation to SM expectations), that are excluded by AMANDA data at 90% confidence level are indicated by the upper (yellow) shaded area for down-going events, and lower shaded area (aqua) for up-going events. Also included are projected results (for 90%, 99%, and 99.9% confidence level inclusion) on neutrino fluxes and cross sections at $\sqrt{s} \sim 6$ TeV for future IceCube data. Two cases are shown: a ratio of down-going to up-going events = 4:20 (right set of contours) and a ratio = 35:20 (left set of contours). From [45].

Previous scientific works discussing the two types of experiments have an intertwined history, but the initial proposed use of neutrino absorption in the Earth was for radiography.

Within the radiography subset, most papers discuss the use of neutrino oscillations to probe the Earth's density profile, such as Ohlsson and Winter in 2001 [53] and Rott et al. in 2015 [54]. They propose that the Earth's symmetric matter density profile could be reconstructed from a single neutrino baseline energy spectrum using two-flavor neutrino oscillations, in particular the core-mantle boundary, with a sufficiently high neutrino flux. However, these experiments would occur at energies much lower than this analysis and are not discussed further here.

In other papers, direct measurement of the absorption of neutrinos are also predicted to yield results. In 1983, de Rujula et al. [55] proposed using a multi-TeV proton synchrotron to probe the vertical density profile of the Earth, in addition to searching for oil and gas deposits or heavy-metal ores at large distances from the accelerator. Another paper in 2004 by Reynoso and Sampayo [56] proposed an improved technique for examining the change in neutrino flux that would reduce the statistical errors in the density profile calculation.

In 1984, Wilson [57] examined the feasibility of using a Tevatron-type accelerator to direct a stream of neutrinos through the Earth towards a detector to examine the density profile, but he was the first to examine the use of high-energy neutrinos from astrophysical point sources, although the fluxes would be low and would require a number of years of data and/or a large detector. His calculations used the newly-released Preliminary Reference

Earth Model [58] and the characteristics of the DUMAND detector [59].

The use of astrophysical neutrinos and/or cosmic rays as the sources were further explored by others. In 1995, Crawford et al. [60] proposed using neutrinos from extraterrestrial sources (possibly connected to gamma ray sources) with energies of 10 to 100 TeV to image the Earth's density boundaries by measuring the absorption of neutrinos with DUMAND or AMANDA. In 1999, Jain et al. [61] examined the feasibility of using an isotropic flux of cosmic neutrinos in the energy range from 10 to 10,000 TeV to study the interior structure of the Earth, where the angular distribution of events in a cubic-kilometer-scale neutrino telescope could yield information on the Earth's mass distribution that would be independent of other methods. In 2008, Gonzalez-Garcia et al. [62] determined that IceCube should be able to probe the density difference at the core-mantle boundary with significance and reject a homogeneous hypothesis with 10 years of data. Miele and Pisanti in 2011 [63] calculated the sensitivity to density differences to be 2% for the mantle and 5% for the core, with 10 years of data from a detector such as IceCube. In 2012, Hoshina and Tanaka [64] examined the use of atmospheric neutrinos from cosmic rays and the IceCube detector for performing a radiographic study of the Earth's interior using both oscillation and absorption methods.

The idea to calculate the neutrino-nucleon cross section by using neutrino absorption in the Earth in large neutrino detectors such as IceCube was explored by Dan Hooper in 2002 [65]. He realized that the high-energy cross section would be measurable by comparing the "up-going" to the "down-going" event rates to take into account the Earth's shielding effect. He showed that the method would be sensitive to neutrino energies ∼100 TeV to 10 PeV. In 2006, Winter proposed that the neutrino cross section could be determined by measuring absorption of neutrinos from a known flux (from a dedicated beam, or perhaps from high-energy cosmic rays or astrophysical sources) with energy above 1 TeV [66]. In 2008, Borriello et al. [67] also explored the idea of neutrino absorption by focusing on $E_\nu <$ 10 PeV. They recommended examining the neutrino flux in two-dimensions including zenith angle and energy to break the degeneracy between flux and cross section. In 2011, Connolly, Thorne, and Waters (CTW) [28] explored the idea of a measurement of the ultra-high-energy cross sections for $E_\nu > 100$ PeV that would be independent of the incident neutrino flux, using one of the future radio detection arrays. Experiments in this range include the proposed Askaryan Radio Array (ARA) [68] and the Antarctic Ross Ice Shelf Antenna Neutrino Array (ARIANNA) [69] radio Cherenkov detectors. In 2013, Klein and Connelly [70] proposed the use of a simple scaling of both the NC and CC SM cross sections as a probe of new physics above 1 TeV when measuring neutrino absorption.

2.7 Earth model

The first comprehensive Earth density model was published in 1981 and was called the Preliminary Reference Earth Model (PREM) [58]. The model was created using a detailed analysis of the reflections and refractions of years of seismic waves from earthquakes, volcanic eruptions, and nuclear testing. Although the model is over 30 years old, PREM remains essentially unchanged over time, despite many additional years of seismic data. Figure 2.9 shows a profile view of the variation in Earth's density with depth that comes from this model.

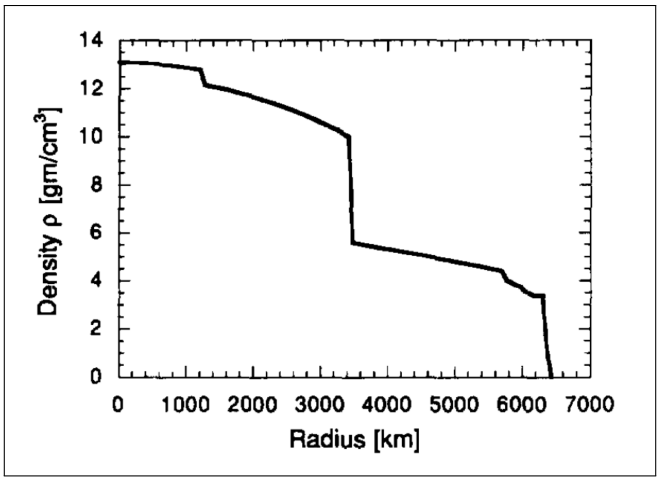

Figure 2.9: Density profile of the earth with respect to radius. The discontinuity at 3400 km is due to the core-mantle boundary. The discontinuity at 1200 km is due to the boundary between the inner core and outer core, but the composition of this boundary is still unknown. From [71].

The model is used to account for the effects of the changing density at various depths. The density (ρ) versus radius (r) relationship is represented by this set of equations [71]:

$$\rho = \begin{cases} 13.0885 - 8.8381a^2 & r < 1221.5 \\ 12.5815 - 1.2638a - 3.6426a^2 - 5.5281a^3 & 1221.5 < r < 3480 \\ 7.9565 - 6.4761a + 5.5283a^2 - 3.0807a^3 & 3480 < r < 5701 \\ 5.3197 - 1.4836a & 5701 < r < 5771 \\ 11.2494 - 8.0298a & 5771 < r < 5971 \\ 7.1089 - 3.8045a & 5971 < r < 6151 \\ 2.691 + 0.6924a & 6151 < r < 6346.6 \\ 2.9 & 6346.6 < r < 6356 \\ 2.6 & 6356 < r < 6368 \\ 1.02 & r \geq R_{Earth} \end{cases}$$

where the density is measured in g/cm^3, the distance r is measured from the center of the Earth in km, and the scaled radial variable $a \equiv \frac{r}{R_{Earth}}$, using an Earth radius $R_{Earth} = 6371$ km. Figure 2.10 shows the output of these equations for centimeters of water equivalent (cmwe) as a function of zenith angle for a spherically symmetric Earth. The plot shows how much material a particle would experience as it transited the Earth at that zenith angle.

Although PREM is an averaged Earth model, the variations due to location on the surface, such as the difference between being on the bottom of the ocean versus on top of Mt Everest, do not affect the absorption of neutrinos to a measurable degree. Chapter 9 includes a discussion about systematic uncertainties due to Earth model variations.

2.8 Muon interactions

The CC interaction of a ν_μ with matter forms a hadronic shower and μ^-. Conversely, when a $\bar{\nu}_\mu$ interacts with matter, it forms a hadronic shower and μ^+. Muons are also formed

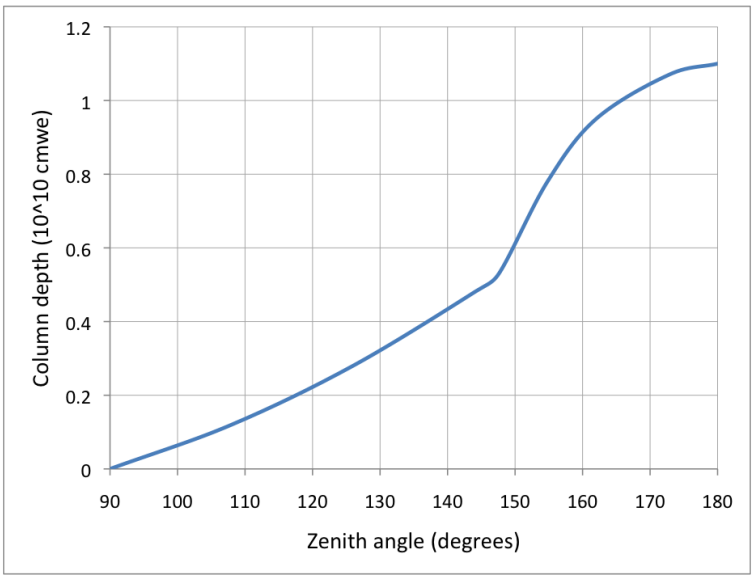

Figure 2.10: Effective column depth (in cm of water equivalent, cmwe) versus zenith angle for the Earth, based upon PREM. Zenith angle of 90 degrees is equivalent to the horizontal direction, and zenith angle of 180 degrees is equivalent to traveling directly through the Earth's core. The relationship is primarily linear until reaching the dense core ∼150 degrees. Equations from [71].

in the particle cascades from cosmic ray interactions at the top of the atmosphere (covered in Chapter 3). Many of these muons arrive at the surface of the Earth and are able to reach an underground detector, creating a formidable background. Muon energy losses are important in the detection of muons, which is the subject of the remainder of this chapter.

2.8.1 Cherenkov radiation

This radiation was first described by Pavel Cherenkov in 1934 [72] when studying solutions of uranium salts irradiated by gamma rays. He noticed a weak luminescence of the solution, which differed sharply from normal luminescence. A theoretical basis for the effect, analogous to Mach waves in hydrodynamics, was provided by Ilya Frank and Igor Tamm [73] and quantitatively verified by Cherenkov's further experiments in 1937 [74]. The radiation is formed in a completely different mechanism than bremsstrahlung (described below). This is apparent when a moving particle has a large mass, where bremsstrahlung disappears but Cherenkov radiation is unaffected.

Cherenkov radiation is perhaps best known as the cause of the deep blue glow that is seen in the pool of water surrounding the fuel rods of nuclear reactors. The light is emitted when the velocity of the charged particles exceeds the phase velocity of light in the medium. The polarized light forms a wave front at an angle that is determined by the particle's velocity and the refractive index of the medium. The particles lose energy continuously in this process. The number of photons N produced per unit path length x of a particle with charge ze, per unit wavelength λ of the photons, is [75]:

$$\left(\frac{d^2N}{dxd\lambda}\right) = \frac{2\pi\alpha z^2}{\lambda^2}\left(1 - \frac{1}{\beta^2 n^2(\lambda)}\right) \tag{2.23}$$

where α is the structure constant $= \frac{e^2}{\hbar \cdot c} = \frac{1}{137}$ and n is the refraction index of the medium as a function of the photon energy, or equivalently of λ.

At the high energies of this analysis, the Cherenkov radiation output by muons is dwarfed by the radiative processes described below. Cherenkov radiation is still included in simulation but is a minor contribution to the overall losses at high muon energies.

2.8.2 Muon energy loss processes

All charged particles, including muons, that transit the detector will lose energy through four main processes: (1) ionization, (2) bremsstrahlung, (3) pair production, and (4) photonuclear interactions [75]. These processes will be discussed in the next sections, with implementation of these energy-loss concepts discussed in Chapter 7. For a more detailed discussion of muon energy losses, see [76]. Figure 2.11 at the end of this discussion compares the magnitudes of the various energy loss mechanisms.

2.8.2.1 Ionization

The mean rate of ionization energy loss $\langle dE/dx \rangle$ by relativistic charged heavy particles is described by the relativistic equation by Hans Bethe [77], and in its modern form for relativistic particles in matter [78]:

$$-\left\langle \frac{dE}{dx} \right\rangle = \frac{4\pi}{m_e c^2} \frac{nz^2}{\beta^2} \left(\frac{e^2}{4\pi\epsilon_o} \right)^2 \left[\ln \left(\frac{2m_e c^2 \beta^2}{I \cdot (1-\beta^2)} \right) - \beta^2 \right] \tag{2.24}$$

for a material with electron number density n and mean excitation potential I, a particle with charge z (in multiples of the electron charge), speed v, and energy E, traveling a distance x into the target material. Other variables include c which is the speed of light, ϵ_o the vacuum permittivity, $\beta = \frac{v}{c}$, and e and m_e for the electron charge and electron rest mass, respectively. The electron number density n of the material is:

$$n = \frac{N_A Z \rho}{A M_u} \tag{2.25}$$

where Z is the atomic number, ρ is the mass density of the material, A is the relative atomic mass, N_A is Avogadro's number, and M_u is the molar mass constant. The mean ionization potential I can be estimated by the Bloch equation [79]:

$$I = (10\ eV)Z \tag{2.26}$$

The ionization effects represented by the Bethe formula are important only at lower energies because radiative effects become larger than ionization effects for muon energy $\gtrsim 1$ TeV.

2.8.2.2 Bremsstrahlung

While the ionization losses rise logarithmically with energy, bremsstrahlung losses rise nearly linearly [75]. Bremsstrahlung, from the German word meaning "braking radiation", is the electromagnetic radiation (i.e., photons) produced by the deceleration of a charged

particle when deflected by another charged particle. The energy losses are "stochastic" or random in nature. The spectrum of photons from bremsstrahlung is continuous, as opposed to other nuclear interactions [80].

The equation for $\langle dE/dx \rangle$ by bremsstrahlung (and other radiative processes) is given at high energy by the approximation [75]:

$$-\left\langle \frac{dE}{dx} \right\rangle \cong \frac{E}{X_o} \tag{2.27}$$

where X_o is the particle's radiation length, which depends upon the material. The radiation length is usually measured in g/cm^2 and is (a) the mean distance over which a high-energy particle loses all but $1/e$ of its energy by bremsstrahlung, and (b) 7/9 of the mean free path for pair production by a high-energy photon. For muons in clear ice, the radiation length is $\sim$36 g/cm^2 [75].

Cross sections for bremsstrahlung grow with energy, but the cross sections for electrons are reduced at high energies and/or matter densities by the Landau-Pomeranchuk-Migdal (LPM) effect [81; 82]. This causes the radiation length to increase greatly. The electron energy where the effect becomes important is above $\sim$300 TeV for ice and 100 TeV for rock. Muons with sufficient energy to create these high-energy electrons are rare, though.

Bremsstrahlung suppression for muons also occurs but at a much higher muon energy above 10^{11} TeV [83], well beyond the energy of this analysis, and is negligible. Since electrons are formed when a muon interacts with the detector medium, the LPM effect must be taken into account when simulating the propagation of these electrons through the IceCube detection volume, as explained in Chapter 5.

2.8.2.3 Pair production

Pair production processes are a larger contribution to the overall energy loss than bremsstrahlung at the muon energies of this analysis. High-energy photons interact with the electric fields of atoms in the medium to form electron-positron pairs. The electrons then lose energy mainly by bremsstrahlung. The pair production mechanism is also subject to the LPM effect described above. The equation for pair production is very similar to that of bremsstrahlung, and the cross section for pair production grows with energy like bremsstrahlung. In a way, pair production is the inverse of the bremsstrahlung process [75].

2.8.2.4 Photonuclear interactions

The photonuclear interaction of leptons is the process of the inelastic lepton-nucleon or lepton-nucleus scattering [84]. At high photon energies, this results in a stochastic hadronic cascade, in which the hadrons then decay or interact. The energy of the photon is divided into several particles that also interact to create photons of lesser energy [75]. This effect changes the spectrum of photons that are available to trigger the sensors and is dependent upon the distance from the sensors.

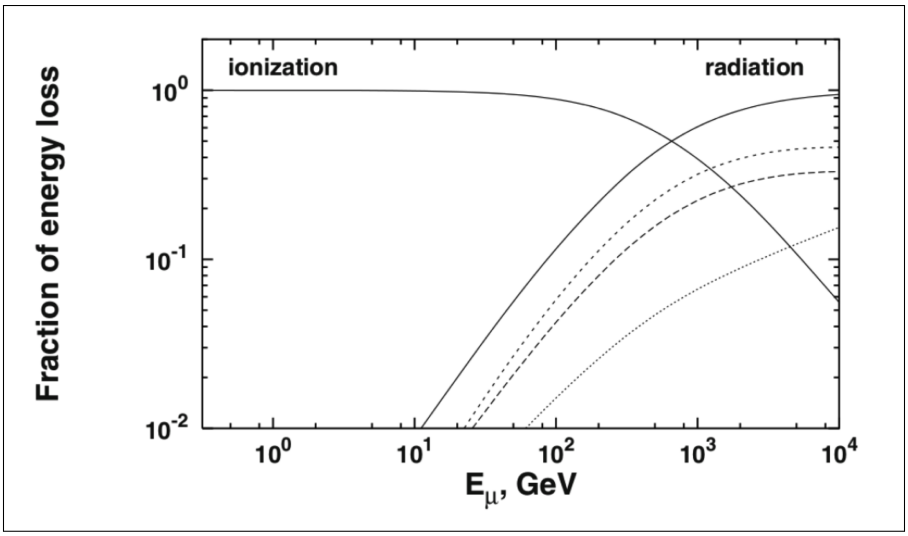

Figure 2.11: Relative importance of energy loss mechanisms for muons. Smaller dashed line represents pair production, while larger dashed line is for bremsstrahlung, which are almost the same in magnitude but with pair production being slightly higher. Dotted line is for photonuclear interactions, with the total radiative losses represented by the solid line increasing from left to right. Ionization is the solid line decreasing from left to right, which is overshadowed by the radiative processes above ∼1 TeV. From [85].

2.8.2.5 Overall muon energy loss

A comparison of the main energy loss mechanisms described above can be seen in Figure 2.11. Ionization is important at lower energies but becomes less important as the radiative effects dominate. The energy loss mechanisms can be combined into a general energy loss equation for muons in a medium. At high energies, an excellent approximation for the average energy loss, $\langle dE/dx \rangle$ is given by [76]:

$$-\left\langle \frac{dE}{dx} \right\rangle = a(E) + b(E)E \tag{2.28}$$

where E is the total energy, $a(E)$ is the electronic stopping power, and $b(E)$ is due to radiative processes (bremsstrahlung, pair production, photonuclear interactions) and is defined as:

$$b(E) = b_{brem} + b_{pair} + b_{photo} \tag{2.29}$$

The units of $a(E)$ are energy per unit distance, while the units of $b(E)$ are per unit distance. The term $a(E)$ can be estimated with Equation 2.24. The application of these concepts will be covered when discussing simulation (Chapter 5) and energy reconstructions (Chapter 7).

2.8.3 Muon range

The range of a typical muon with energy of ∼7 TeV is a few kilometers in rock, and even at 400 PeV, muons travel only ∼10 kilometers, on average [86]. Distances are slightly longer for muons in ice. Figure 4.7 compares the path length distributions for several muon

energies in ice. The muon travel distance is important for estimating the background from muons formed directly in the cosmic ray shower and also for calculating probabilities of survival when traversing both rock and ice after a neutrino interaction within the Earth. Both situations must be modeled correctly in simulation.

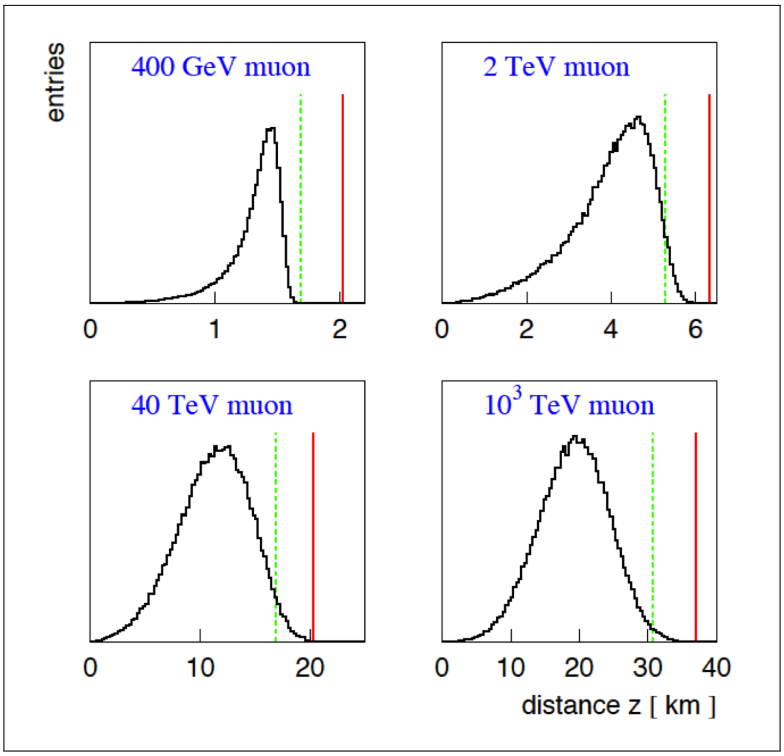

Figure 2.12: Comparison of the path length of a muon with different energies, in ice. The green and magenta lines are used in evaluating ice models and represent 99% and 99.9%, respectively, of all path length values. From [86].

Chapter 3

Cosmic Rays

3.1 Introduction

Cosmic rays are not rays at all, but high-energy particles traveling through space. When these particles collide with the atoms of our atmosphere, they create showers of collision products, one of which is a muon neutrino (or a muon antineutrino). The majority of the neutrinos that IceCube detects are created in this way, and they are called "atmospheric neutrinos." These neutrinos were first detected by two experiments in 1965, namely the Kolar Gold Mine experiment in South India [87] and the East Rand Gold Mine experiment in South Africa [88]. Some of the neutrinos come directly from their universal sources, since these particles are neutral and not deflected by magnetic fields. They are called "astrophysical neutrinos" but are considered separate from cosmic rays.

This chapter discusses the aspects of cosmic rays that are applicable to this analysis: the energy distribution of the cosmic rays; cosmic ray interactions with the atmosphere; the composition of the cosmic rays; origins of the neutrino flux; and models of the neutrino flux. Astrophysical neutrinos are also discussed.

3.2 Cosmic ray basics

Cosmic rays were first detected by Victor Hess in 1912 [89]. Cosmic rays are mostly energetic hydrogen nuclei (protons) hitting the Earth's atmosphere, although other particles (helium, heavier elements, electrons, neutrons) are also present. The interactions create showers of new particles, many of which reach the Earth's surface, particularly at high altitudes.

High-energy cosmic rays have been detected by various experiments since their discovery over 100 years ago. However, it is difficult to determine the sources because cosmic rays are charged particles, and their paths are bent when encountering the myriad of electromagnetic fields from our planet, solar system, galaxy, local cluster, etc. [90]. Once these cosmic rays arrive at the Earth, their trajectories no longer point back towards their origins.

3.3 Cosmic ray energy spectrum

Cosmic rays with energies up to ~300 EeV (3 x 10^{20} eV) have been found by HiRes [91; 92]. This energy is approximately 40 million times the energy of particles that have been accelerated by the Large Hadron Collider. Figure 3.1 summarizes the measured fluxes of cosmic rays versus energy from a number of experiments [93]. The curve has several

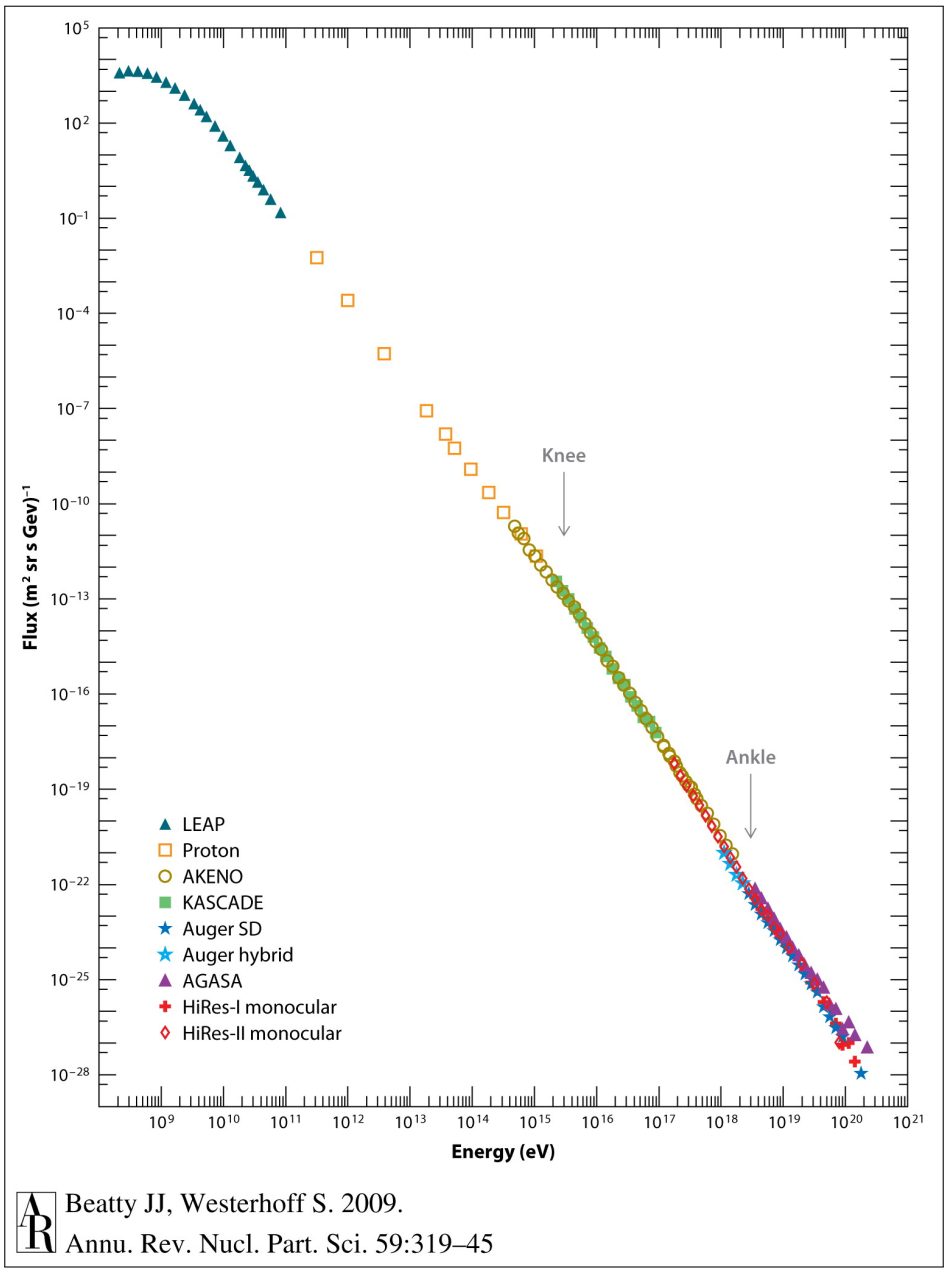

Figure 3.1: Overview of the cosmic ray spectrum from various experiments. The curve generally follows an $E^{-2.7}$ power law for nearly 10 orders of magnitude in energy. Approximate locations of the breaks in the spectrum, commonly referred to as the knee and the ankle, are indicated by arrows. From [93].

distinct features. The flux roughly follows an energy power law of $E^{-2.7}$. There are two breaks in the spectrum, defined as the "knee" and the "ankle." The knee occurs ∼4 PeV and is a "softening" of the spectrum, or where the curve becomes slightly more steep, to approximately an $E^{-3.0}$ power law. The ankle occurs ∼3 EeV and shows a slight hardening of the spectrum, or where it becomes slightly more shallow. The ankle may be an indication of the transition of cosmic rays from galactic to extra-galactic origins [90]. There is a spectral cutoff at ∼100 EeV due to the GZK effect [48; 49] above a threshold of ∼50 EeV.

The primary theoretical extra-galactic sources are active galactic nuclei (AGN) and gamma-ray bursts (GRB), although no experimental observations to-date support the theories. Galactic sources, such as supernova remnants (SNR), are most likely responsible for cosmic rays at energies lower than the knee. These cosmic rays are primarily protons, while the cosmic rays above the knee are generally heavier elements [93]. Additionally, at energies above 1 PeV, the number of arriving particles has dropped considerably to only about 1 per square meter per year. This is one of the main reasons why large-volume ground-based detectors are needed.

The baseline model of particle acceleration in most theories is the first-order Fermi process. Enrico Fermi first proposed a mechanism for acceleration [94], but this process is now considered second-order Fermi acceleration. In the first-order process, charged particles encounter an astrophysical shock front, which is formed when the moving material exceeds the speed of sound in that material (such as the ejected material from a supernova). The difference in velocity across the shock front results in the particle gaining energy with each crossing. There is a probability that the particle will escape the acceleration mechanism after each crossing. Because of this, the energy spectrum of accelerated particles follows a power law, which agrees with the cosmic-ray spectrum detected on Earth [95].

3.4 Cosmic ray interaction mechanisms

The interactions of cosmic rays with the atmosphere create kaons and pions in the upper atmosphere as part of the hadronic shower that is formed from the initial interaction. The neutral pions will decay to produce gamma rays and leptons, in what is referred to as the electromagnetic shower, but no neutrinos will be produced. The charged pions will decay to produce neutrinos. The energy of each particle will be divided amongst the products at each later stage until the average energy per particle becomes too low for further secondary particles. Then, the size of the shower will decrease as particles are absorbed by the medium, which is either the air or the Earth's surface if they reach that far.

The air shower that is induced by the cosmic ray interaction has three main components: electromagnetic, hadronic, and muonic. The electromagnetic component consists of high energy photons, electrons, and positrons. The hadronic component comprises the central part of the shower. Of these hadrons, the charged pions and kaons will decay to contribute to the muonic component, via the same processes where the neutrinos originate. The muonic component does not interact further [90].

The high-energy μ are relevant to this analysis because of their ability to penetrate the Earth and reach the detector as a formidable background. It is difficult for IceCube to determine if a lone muon came directly from a cosmic ray shower, or if it came from a

neutrino interaction. If the muon neutrino interaction occurred outside the fiducial volume of IceCube, the transiting muons look the same for both processes. One discriminating factor is the direction of the muon. Even the highest-energy muons have a range of only about 40 kilometers in rock and ice, as discussed in Chapter 2. Muons that arrive at the detector from below the horizon must be the products of nearby neutrino interactions because of the limited muon range.

3.5 Chemical composition of cosmic rays

Since each nucleon in a heavier element shares the total energy of the parent nucleus, the resulting pions from the interaction have lower energy, which means that they are more likely to decay. Thus, an iron nucleus produces more muons and neutrinos than a proton does [90]. The cosmic ray composition affects the overall spectrum of neutrinos that are available for this analysis, and composition effects must be incorporated into the neutrino-generation simulation. This subject will be covered in later sections.

For this analysis, the relevant cosmic ray energies are $\gtrsim$ 10 TeV because the higher-energy neutrinos formed in the secondary interactions only receive ∼5-10% of the original cosmic ray energy [96]. At ∼10 TeV, the distribution of cosmic ray particles is generally 35% protons, 25% helium, and 40% heavier nuclei [97], with higher percentages of heavier nuclei at higher energies. This subject will be discussed further in the models sections of this chapter.

3.5.1 Cosmic ray detection experiments

Experiments that have detected cosmic rays have provided hints about their composition and sources. The experiments can be classified into two main categories: space-based experiments and ground-based experiments. The space-based experiments include the Payload for Antimatter Matter Exploration and Light-nuclei Astrophysics (PAMELA) [98] and the Alpha Magnetic Spectrometer (AMS) [99]. PAMELA was primarily designed to measure the flux of anti-particles, namely antiprotons and positrons, in cosmic rays in the energy range of 60 MeV to 180 GeV. Their measurements are consistent with purely secondary production of antiprotons in the Galaxy [100]. AMS is an ongoing experiment on the International Space Station to measure the cosmic ray composition and the matter to anti-matter ratio for a variety of physics evaluations with particle energies up to ∼500 GeV.

Recent ground-based experiments include KASCADE in Germany [101] and Auger in Argentina [102]. KASCADE was designed to detect cosmic rays in the area of the knee (∼1-10 PeV) to determine any change in composition at that energy. Auger was designed to examine the ultra-high energy cosmic rays in the range from ∼1 to 100 EeV, near the GZK cutoff. The results of these experiments are shown in Figure 3.1.

3.6 Models of cosmic rays

In order to determine the incident neutrino flux from cosmic rays on the surface of the Earth for this analysis, a calculation of the incident cosmic ray flux as a function of composition, energy, and zenith angle from a cosmic ray model is required.

3.6.1 Gaisser et al. cosmic ray model with H3a modification

Because the composition of cosmic rays is not simply protons, a comprehensive model is needed for the flux calculation. The cosmic ray model by Thomas Gaisser has been in existence for many years and has undergone numerous modifications as new data and theories emerged [103; 104]. The version that is currently used by the majority of IceCube analyses, including this one, is the parametrization by Gaisser, Stanev, and Tilav [105]. This model is referred to as Gaisser et al.

The model has been modified in order to account for the effects of probable universal sources of cosmic rays and a variety of incident nuclei. In order to calculate the resulting lepton spectrum in the atmosphere, the model needs to account for the spectrum of incident nucleons. At the high energies of this analysis, the production of pions and kaons can be approximated by looking at the collisions of individual nucleons. This is the basis for the Gaisser et al. model.

The modification assumes a superposition of the energy spectra from five different mass groups (p, He, CNO, Mg-Si, Fe). Gaisser et al. grouped the measurements of the balloon-borne experiment called Cosmic-Ray Energetics And Mass (CREAM) [106; 107] into these mass groups. The direct measurements of primary nuclei only extended to a total particle energy of $\sim$100 TeV. In order to extend the lepton spectrum to more than a PeV, an extrapolation to higher energy was needed.

To achieve this, Gaisser et al. adopted the proposal of Hillas [108] to assume three source populations of cosmic rays. They expanded upon the idea of three versus four source populations [109]. In the Hillas parameterization, the change in spectral index at the knee represents the decreasing influence of cosmic rays accelerated by supernova remnants in the Milky Way Galaxy, and the ankle represents the transition to cosmic rays from extra-galactic sources. Gaisser et al.'s adaptations are called H3a and H4a, after Hillas [104]. In both adaptations, the nuclei are accelerated by three different source populations: galactic supernova remnants (lower energies), galactic sources of unknown origin (medium energies), and extragalactic sources (higher energies). In the H3a model, the extragalactic contribution is assumed to consist of a mixed composition of all five mass groups. In the H4a model, the extragalactic contribution assumes a proton-only composition. This analysis considers only the H3a modification.

The predictions of the Gaisser et al. H3a model are then compared to the combined cosmic ray flux data from 11 different analyses, shown in Figure 3.2. An equation for each component is then created. These equations represent the cosmic ray flux that arrives at the Earth [104].

3.6.2 Hörandel cosmic ray model

The Hörandel (or poly-gonato) model is based on a superposition of spectra for elements with atomic numbers from 1 to 92 (the stable elements). The model uses the measured spectra from lower-energy cosmic ray experiments, and these spectra are then extrapolated to higher energies but with distinct energy cut-offs [97]. The model is missing an extra-galactic component, which impacts predictions at IceCube particle energies. Because of this, an extra-galactic component is added before use in IceCube simulation, thus creating the

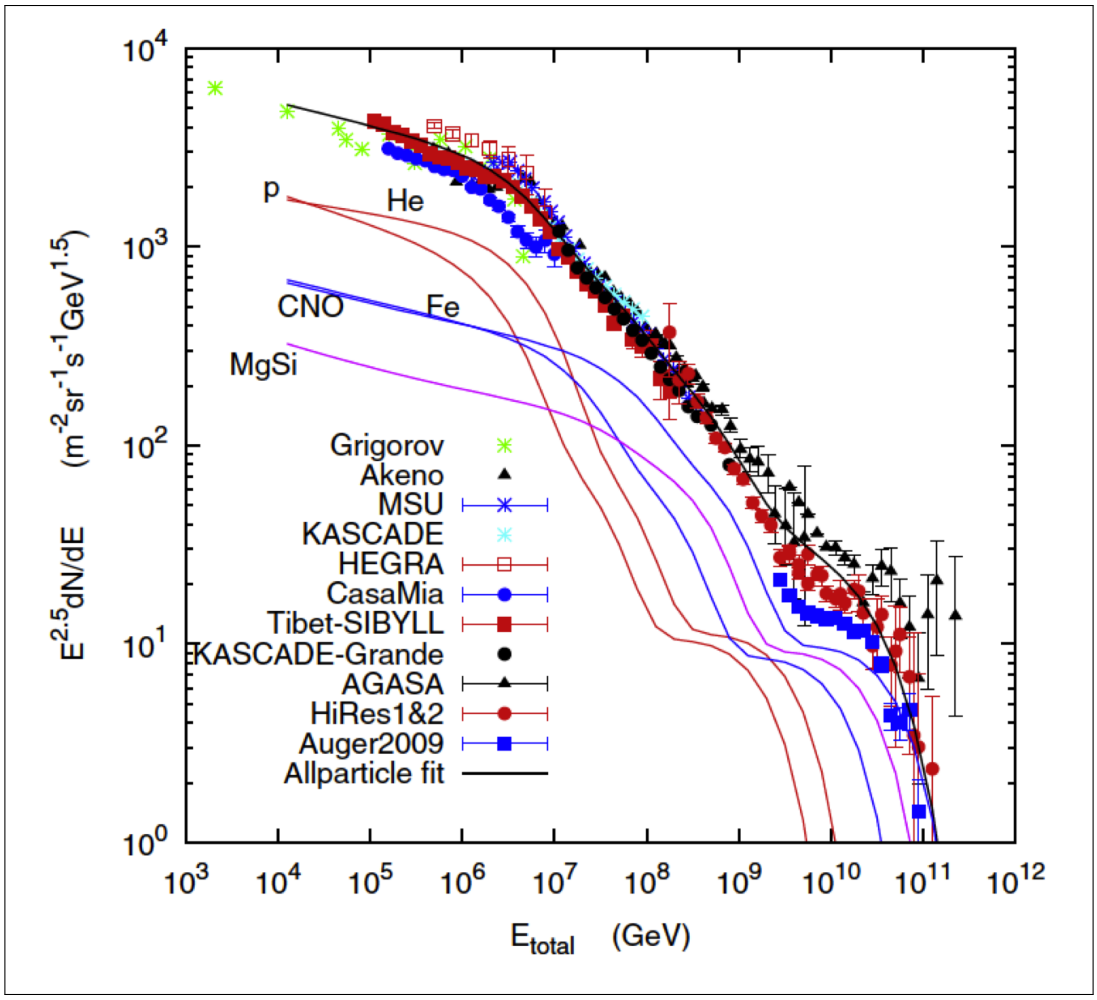

Figure 3.2: The calculation of the cosmic-ray spectrum with three populations using five mass groups, compared to data from a variety of experiments. The extra-galactic population in this calculation has a mixed composition (model H3a). From [104].

"Hörandel (modified) model." The model is an option in IceCube cosmic-ray (background) simulation but is not typically used in neutrino (signal) simulation. This subject will be discussed in Chapter 5.

3.7 Other effects on the cosmic ray flux

There are small effects on the cosmic ray flux (and thus the atmospheric neutrino flux) to consider, namely the standard atmospheric model, the seasonal changes in cosmic ray flux, and the cosmic ray anisotropy. Each will be discussed briefly.

3.7.1 Standard atmospheric model

The atmospheric density model that is typically used in all modern cosmic ray models is the 1976 U.S. Standard Atmosphere [110]. This model is also used in all IceCube simulation,

unless a more detailed model is needed, such as [111] for investigating the seasonal variation in cosmic ray rates. Although the 1976 model is a simplified and averaged version of the actual atmospheric density profile, the error is sufficiently small for the calculation of the atmospheric neutrino flux for this analysis. Temperature corrections and the effect on cross section will be discussed in the systematic studies of Chapter 9.

3.7.2 Seasonal changes

Seasonal changes in cosmic ray interaction rates have been seen in multi-year analyses from IceCube. The yearly temperature variation in the middle stratosphere (30-60 hPa) is highly correlated with the high-energy muon rate observed deep within the ice, causing a ±10% seasonal modulation in the event rate [112]. Figure 3.3 shows the variation in temperature versus the muon rate, and a direct correlation can be seen. The change in horizontal neutrino rate is only about ±5% and precedes the effect seen in down-going muons, as found by the three-year study in IceCube from 2008-2011 [113]. The kaon-dominated neutrinos are less sensitive to temperature due to the higher kaon critical energy. Since this analysis used an entire year of data, the effect would be averaged out, and other systematic effects would dominate any small change. Seasonal effects are not included in this analysis.

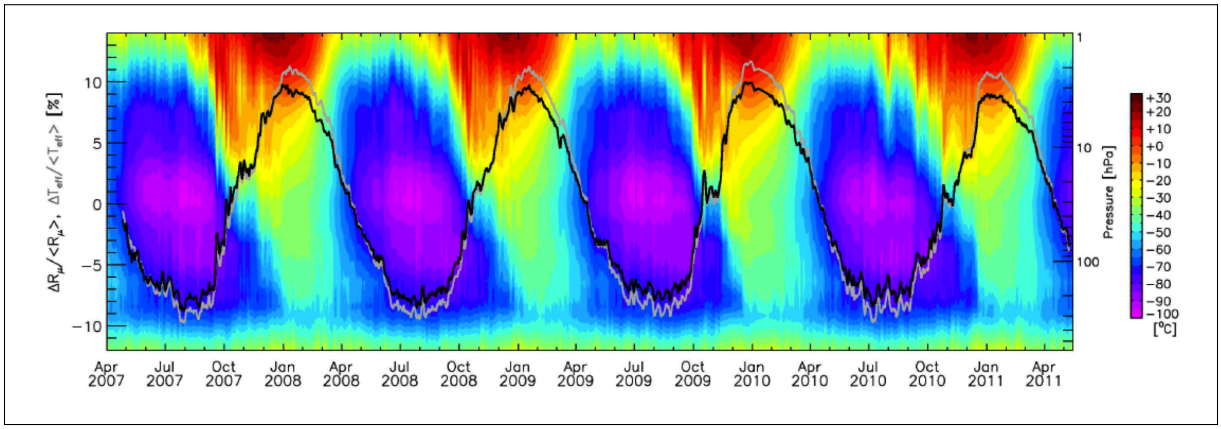

Figure 3.3: Correlation of temperature variations at the South Pole over a 4-year period and the down-going muon detection rate. Black line indicates the change in muon rate from the annual average, and the gray line indicates the change in effective temperature for the atmosphere compared to the average temperature. Background colors indicate the changes in atmospheric temperature in relation to altitude (pressure) during the same time period. From [114].

3.7.3 Cosmic ray anisotropy

Several experiments have detected a slight anisotropy in the cosmic ray arrival distributions at various energies. These include the Tibet Air Shower Array [115], Super-Kamiokande I [116], Milagro [117], and ARGO-YBJ [118]. Both IceCube and IceTop have measured an anisotropy that matched these previous results [119]. Figure 3.4 shows the combined results from these experiments. However, this anisotropy is on the order of ±0.2%. This small effect does not impact this analysis because the uncertainty on the cosmic ray flux as a whole

is ∼100 times higher than the effect of anisotropy and is already included in the analysis uncertainties. Anisotropy is not included in this analysis.

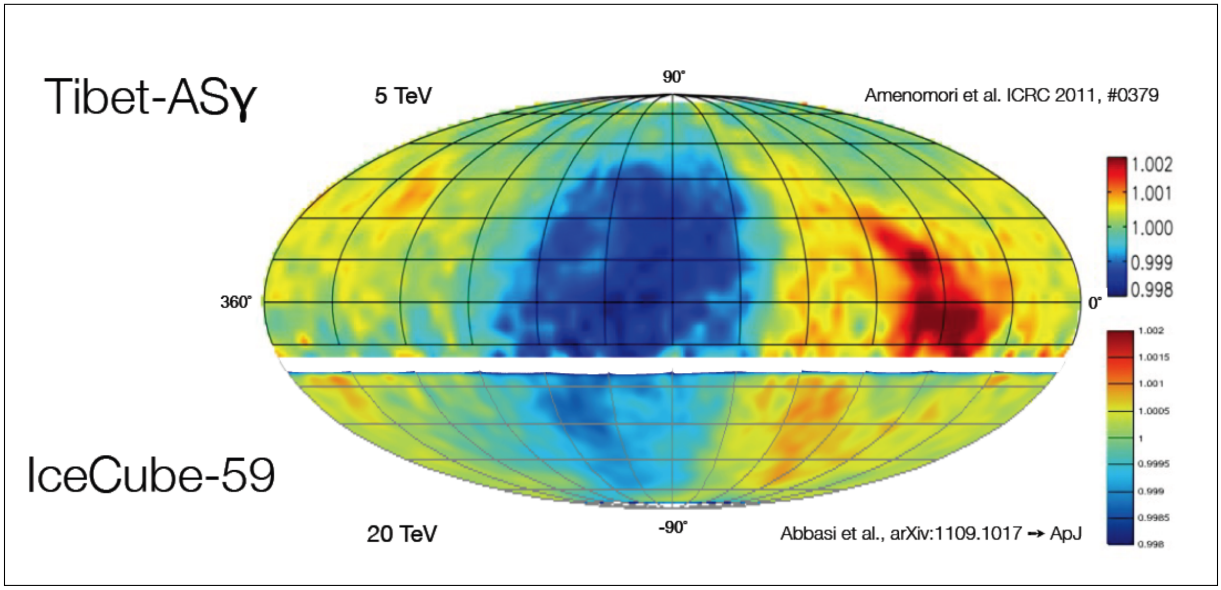

Figure 3.4: Cosmic ray anisotropy results from Tibet [115] and IceCube [119] experiments, for medium-energies. Tibet results are for cosmic ray events ∼5 TeV, while IceCube results are ∼20 TeV. Features coincide in both northern and southern hemispheres. The reason for the anisotropy is not yet known. Coordinates are equatorial. From [120].

3.8 Neutrinos from cosmic rays

Conventional neutrinos are formed from the decays of cosmic ray interaction products that do not contain bottom or charm quark components. "Prompt" neutrinos are the same as conventional neutrinos except that they are formed from interaction products that do contain bottom or charm quark components. The prompt flux has components from all three flavors of neutrinos (electron, muon, and tau), but by definition the conventional flux has only electron and muon components (no tau). The relative fluxes of each conventional component are quite different, as shown in Figure 3.5.

3.8.1 Conventional atmospheric neutrinos

The conventional neutrino flux at high energies comes mainly from the decays of kaons and charged pions that are created in the initial hadronic shower from the cosmic ray interaction. One example of an interaction chain is when a charged pion decays to a muon and a muon neutrino. Later, the muon will decay to an electron plus a muon neutrino and an electron neutrino. The high-energy neutrinos are the focus of this analysis. The equation for a typical cosmic ray interaction is as follows (where "cascade" indicates a hadronic cascade):

$$p + N \rightarrow \pi + cascade \rightarrow \mu + \nu_\mu + cascade \rightarrow e + \nu_e + \bar{\nu}_\mu + \nu_\mu + cascade \qquad (3.1)$$

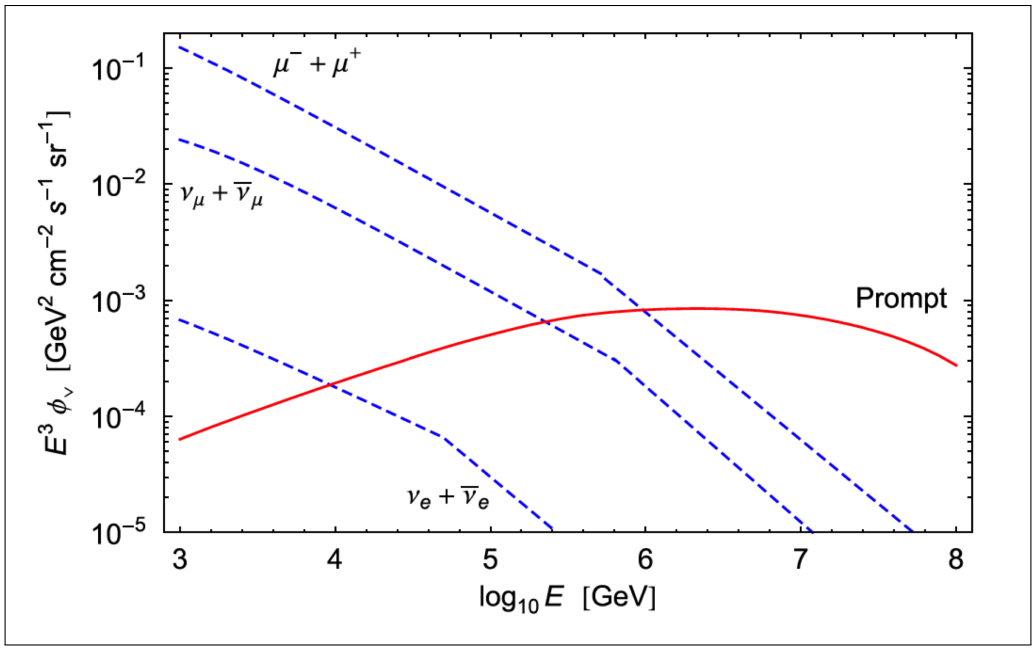

Figure 3.5: Conventional fluxes (dashed blue lines) and prompt flux (solid red line) of $\nu_\mu + \bar{\nu}_\mu$, $\nu_e + \bar{\nu}_e$, and $\mu + \bar{\mu}$, versus particle energy for the vertical direction (zenith near 0^o). The conventional fluxes are from [121]. The three prompt fluxes are approximately equal and are therefore represented by the single prompt flux. Muons that are created in the same cosmic ray interactions dominate the particle counts at most energies. The effect of the cosmic ray knee is seen near $\log_{10}(E_\nu/\text{GeV})$ of 6.0. By definition, the conventional flux does not contain a tau component. From [122].

The Frejus experiment was the first to measure this neutrino flux from cosmic rays in the energy range of 250 MeV$< E_\nu <$ 10 TeV [123].

At higher energies ($>$ 100 GeV), kaons become more important than pions. Figure 3.6 shows the transition from pion-dominated to kaon-dominated fluxes. If the kaons are formed at a shallow angle in the atmosphere, such that they have more atmosphere to traverse before arriving at the surface, then they will have more time to decay before hitting the surface. Decaying kaons will create high-energy neutrinos while interacting kaons do not, and thus the relative number of neutrinos arriving at the detector will be larger when looking towards the horizon [122]. Because the hadrons are likely to interact with other air molecules before they decay, the subsequent neutrino flux has a different energy spectrum and zenith angle distribution than the incoming cosmic rays. The energy spectrum is steeper (approximately $E^{-3.7}$ versus the cosmic ray $E^{-2.7}$), and the flux is enhanced near the horizon [90]. The equations that are relevant to this analysis will be covered later in this chapter.

The dominant particle in the interaction chain is the muon, since it is the outcome of many branches of decays. At sea level, muons comprise more than 50% of the cosmic radiation that reaches the surface. The muon neutrino comprises the next highest proportion of interaction products. Conventional muons and muon neutrinos dominate the spectrum when compared to prompt neutrinos, as shown in Figure 3.5. Although the tau component is $\sim$0 at creation, the conventional neutrinos are expected to oscillate into tau neutrinos and therefore create a conventional tau neutrino flux. However, at the very high energies of this analysis, the

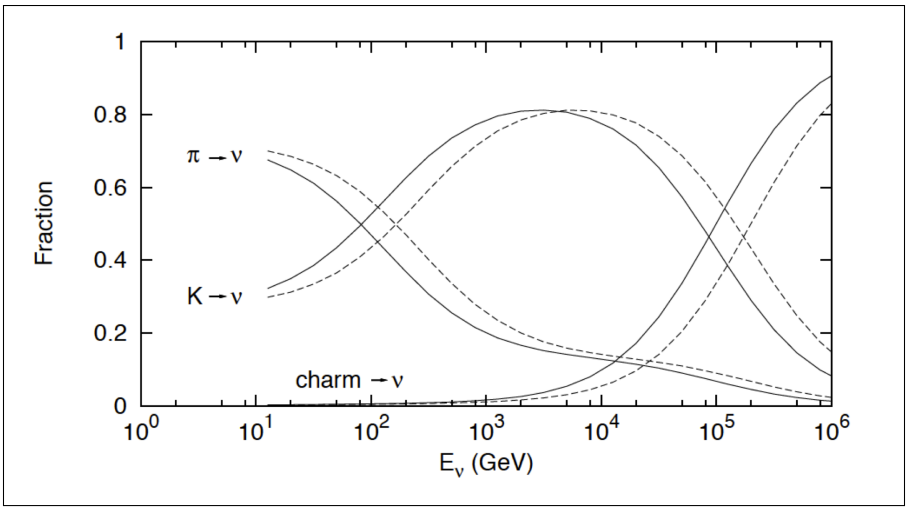

Figure 3.6: Fraction of cosmic ray interaction products that create neutrinos, as a function of neutrino energy. For this analysis, the relevant lower limit is approximately 10^3 GeV. Above this energy, kaon decay is the primary mechanism for neutrino production. Solid line represents a zenith angle of 0 degrees from vertical, and dashed line represents a zenith angle of 60 degrees from vertical. Above 10^5 GeV, particles with charm components begin to have a dominant contribution. From [124].

probability of oscillation is small (see Chapter 2), and the flux of tau neutrinos is expected to be ∼0. Thus, the conventional tau neutrino flux is considered negligible in this analysis.

3.8.1.1 Conventional neutrino flux model

The conventional neutrino flux is the largest portion of the available total neutrino flux over all energies, when compared to prompt and astrophysical, accounting for ∼98% of the flux. The conventional neutrino flux from the cosmic ray primary flux can be calculated using this equation [125]:

$$\frac{d\phi_\nu^{CR}(E_\nu,\theta^*)}{dE_\nu} = \int_{E_\nu}^{\infty} dE_N \frac{d\phi_\nu{}^{CR}}{dE_N} Y(E_\nu, E_N, \theta^*) \tag{3.2}$$

where $d\phi_\nu{}^{CR}/dE_N$ is the cosmic ray nucleon flux and $Y(E_\nu, E_N, \theta^*)$ is the neutrino yield factor, giving the number of neutrinos with energy E_ν produced by a cosmic ray nucleon of energy E_N and inclination θ^*.

Two models for the neutrino yield factor are currently used in IceCube: (1) Honda et al. 2006 model, and (2) Barr et al. model. The Honda 2006 model is often listed as the Honda 2007 model because the model was created in 2006 but published in 2007 [126]. The Barr et al. model is also referred to as the Bartol model due to the location of several of the authors at the Bartol Research Institute at the University of Delaware [127]. For this analysis, the Honda et al. 2006 model was used.

Honda et al. used multiple simulation models and fit the neutrino data from several experiments at three locations, which were Kamioka, Sudbury, and Gran Sasso. They created

neutrino flux tables for the low energy regime (below 10 GeV) at a variety of zenith angles. Then they extrapolated these fluxes to higher energies, creating tables that ranged in neutrino energy from 10 GeV to 10 TeV. The model assumed a flat $E^{-3.7}$ energy spectrum for the neutrinos, coinciding with a flat $E^{-2.7}$ spectrum for the cosmic rays. As seen in the cosmic ray discussion, however, the cosmic rays do not follow $E^{-2.7}$, and a simple power-law extrapolation to higher energies would miss the effects of the cosmic ray knee. Therefore, corrections must be made.

In 1978, Jerome Elbert created a formula that describes the muon yield from cosmic rays [128]. The Elbert formula has been modified by Gaisser, Stanev, and Lipari [129; 130] to describe the muon neutrino yield by replacing the muon parameters with neutrino parameters. In addition, the Elbert formula was modified to include propagation through rock, such as neutrinos transiting the Earth and arriving at an underground detector. These modifications produce the neutrino yield equation, $Y(E_\nu, E_N, \theta^*)$, that is needed for the total number of muon neutrinos from cosmic rays. This results in a correction to the neutrino spectrum for the cosmic ray knee. Although a newer adaptation of the Elbert formula was created [131], it was not available during this research, and this analysis used the modified Elbert formula from [130]:

$$Y(E_N, E_\nu, \cos(\theta^*)) = \frac{\epsilon_\nu^*}{E_\nu \cos(\theta^*)} \left(\frac{E_N}{AE_\nu}\right)^p \left(1 - \frac{AE_\nu}{E_N}\right)^q \tag{3.3}$$

where parameters $p \cong 0.76$, $q \cong 5.25$, and $\epsilon_\nu^* \cong 4.8$ GeV.

When all the models are combined, the Honda 2006+Gaisser H3a+Elbert model can be used to reweight simulated conventional events using a program called NeutrinoFlux. The program uses the equations to predict the number of neutrinos expected from the different sources (conventional, prompt) when given the output of a neutrino generation simulation file. The program reweights the simulated events, based upon neutrino energy (because zenith angle dependence cancels out in the sum over all energies), to give the expected neutrino rate. The new weight comes from parameterized equations comparing the uncorrected flux to the corrected flux for the desired parameter. The implementation for this analysis will be discussed in Chapter 8. Model uncertainties will be covered in the systematic studies in Chapter 9.

The combined flux of conventional neutrinos can be parametrized using Gaisser's formula [90]:

$$\phi(E_\nu, \theta, T) = \phi_N(E_\nu) \cdot \left(\frac{A_{\pi\to\nu}}{1 + B_{\pi\to\nu}\frac{E_\nu \cos\theta^*(\theta)}{E_\pi(T)}} + \frac{A_{K\to\nu}}{1 + B_{K\to\nu}\frac{E_\nu \cos\theta^*(\theta)}{E_K(T)}}\right) \tag{3.4}$$

where the flux of nucleons ϕ_N can be evaluated at the energy of each neutrino flavor individually. The angle θ^* is the local zenith angle θ of the neutrino that has been corrected for the curvature of the Earth to give the actual zenith angle at its corresponding impact point on the surface. The $\cos(\theta^*)$ term is approximated by a polynomial [132; 133]:

$$\cos\theta^* = \sqrt{\frac{\cos^2(\theta) + 0.103^2 - 0.068 \cdot \cos^{0.959}(\theta) \cdot 0.041\cos^{0.817}(\theta)}{1 + 0.103^2 - 0.068 + 0.041}} \tag{3.5}$$

The terms E_π and E_K are the critical energies for the pion and kaon, respectively, and

defined as the energies where the decay lengths and the interaction lengths are equal [90]:

$$E_{critical} = \frac{\epsilon_i}{\cos\theta^*} = \frac{m_i c^2 h_o}{\cos\theta^* c\tau_i} \tag{3.6}$$

where $m_i c^2$ is the mass of the meson in energy units, c is the speed of light, τ_i is the lifetime of the meson, h_o is the atmospheric scale height (vertical distance over which the density and pressure fall by a factor of $1/e$, usually 6.3 km) with the assumption of an isothermal atmosphere, and $\cos(\theta^*)$ is the local zenith angle, as mentioned before. The value of E_π is 115 GeV and for E_K is 850 GeV [90]. A meson with an energy above the critical energy will more likely interact than decay, producing fewer high-energy neutrinos. This changes the neutrino spectral index as energy increases because higher energy neutrinos are suppressed.

3.8.2 Prompt atmospheric neutrinos

The neutrino flux from prompt mesons should have roughly the same energy index as the cosmic rays (approximately $E^{-2.7}$) and an isotropic distribution in zenith angle. Prompt neutrinos contribute to the neutrino energy spectrum above ~1 TeV, but this flux has not yet been conclusively measured. Figure 3.5 shows how the prompt flux is a much smaller contribution compared to the conventional (non-prompt) flux except at higher energies, which makes detection of the prompt flux difficult.

Particles contributing to the prompt flux are mainly the charmed mesons, including D^0, $D^\pm$, D_s, λ_c, and their antiparticles. Their higher masses (~2 GeV) require a higher primary energy for the incident cosmic rays than is required for the production of pions and kaons. The B mesons also play a role, but their effect is small due to the very high energies required to make a bottom hadron. In most prompt production models, the charmed component is the only one considered. Although prompt neutrinos can occur in any flavor, including tau, the prediction for a flux of prompt tau neutrinos is approximately 20 times smaller than the prediction for prompt muon neutrinos [122]. Because of this, the prompt tau component is not a major part of the contribution and can be neglected in this analysis.

3.8.2.1 Prompt neutrino flux models

The calculation of the prompt neutrino flux has the same general requirements as the conventional flux: (1) a model of the incident cosmic ray flux as a function of composition, energy, and zenith angle from a cosmic ray model, and (2) the neutrino yield factor from a neutrino model. The cosmic ray model is the same for both the conventional neutrinos and the prompt neutrinos. Therefore, this analysis uses the Gaisser et al. H3a model for this requirement.

For the neutrino yield factor, there are several calculations of the prompt neutrino flux, but the theoretical predictions vary widely. The models that are used in IceCube are (1) Enberg et al., or ERS [122] (2) Martin et al. [134], and (3) Bugaev et al. [135]. Each model uses a different parameterization of the cosmic ray spectrum but includes the broken power law at the knee (changing from γ = -2.7 to γ = -3.0 at ~4 PeV).

The calculation by Martin et al. uses perturbative QCD with three different assumptions for the extrapolation of the parton distribution functions to very small x (listed as GBW,

KMS and MRST) [134], but the assumptions are not important to this analysis other than the fact that the GBW (Golec-Biernat Wüsthoff) [136] assumption is also used by ERS. Bugaev et al. provides an alternative approach to the pQCD models with a calculation of prompt atmospheric fluxes using the recombination quark-parton model (RQPM). This approach assumes charmed mesons are produced in diffractive inelastic scattering of nucleons, but this calculation is about five orders of magnitude larger than the other models and is ruled out by experiment. The shapes of the curves for all models are very similar, with mainly a normalization difference.

The ERS model takes parton saturation effects into account via the dipole model, which has a parametric form guided by QCD and constrained by data. The model focuses on the production and decay of charmed hadrons, such as the D meson and Λ baryon. There are many semi-leptonic decay channels (such as from $D^{\pm}, D^{0}, D_{s}^{\pm}$, etc.), but the most common channels have a branching ratio of 17.2% with muonic contributions [137]:

$$D^{+} \rightarrow \bar{K}^{0} + \mu^{+} + \nu_{\mu} \tag{3.7}$$

$$D^{-} \rightarrow K^{0} + \mu^{-} + \bar{\nu}_{\mu} \tag{3.8}$$

The combination of the ERS prompt model with the Gaisser et al. H3a cosmic ray model can be parameterized using the same form as Equation 3.4 but with an additional term for charm. The critical energy for D mesons is on the order of 10^{7} to 10^{8} GeV, compared to the energy for kaons, which is 10^{3} GeV [121]. There is little suppression at the energies of this analysis, which is why the prompt flux energy spectrum will generally follow the cosmic ray spectrum.

The predicted flux of prompt neutrinos is lower than the flux of conventional neutrinos below a few hundred TeV, but, above this energy range, the prompt neutrinos begin to dominate the conventional spectrum. However, the astrophysical neutrinos dominate the prompt flux in this higher energy range, making detection of the prompt flux difficult. To date, the best limit for the prompt flux is 1.06 x ERS at 90% confidence level [138], using a likelihood fit that combines six years of data from IceCube.

An updated version of ERS called BERSS (for Bhattacharya, Enberg, Reno, Sarcevic, and Stasto) [139] was published during this analysis. One advantage is that the BERSS model incorporates the H3a modification directly. However, the BERSS prediction has the same shape as ERS below ~1 PeV but with a lower normalization. Because the prompt flux is a free parameter in this analysis, the use of ERS is not in contradiction with the newer model. More importantly, previous experimental results that also used ERS for comparison permit the use of these experimental values as constraints on the fit parameters for this analysis, which are discussed in Chapter 9.

3.9 Astrophysical neutrinos

In addition to the flux of cosmic rays, there exists a flux of high-energy neutrinos that travel through the universe relatively unscathed. These neutrinos originate in different types of processes that are not yet known or understood. The electromagnetic acceleration mechanisms for charged particles cannot explain the ultra-high-energy neutral particles, including

the neutrinos, that arrive at Earth's atmosphere from the universe. The mechanism for their acceleration is only speculative since no high-energy neutrino point sources have yet been identified [140; 141].

Two known sources of these neutrinos are the Sun and Supernova 1987A (SN1987A). The neutrinos from the Sun (specifically from nuclear fusion and called "solar neutrinos") were detected in several experiments such as the one at Sudbury Mine [9] in the 5-10 MeV range. The neutrinos from SN1987A, a supernova that exploded in the Large Magellanic Cloud in 1987 [142] were created from nucleosynthesis and had energies in the 8-40 MeV range. These supernova neutrinos were detected by three independent experiments: Kamiokande II in the Mozumi mine in Japan [143], the Irvine-Michigan-Brookhaven (IMB) experiment in the Morton Salt mine [144], and the Baksan underground experiment in Russia [145], although the Baksan neutrinos arrived a few hours later. These neutrino energies are well below the lower end of this analysis' energy range.

The same acceleration mechanisms (AGN and GRB) for cosmic rays are proposed for astrophysical neutrinos. For AGN, there are two theoretical areas for the production of neutrinos, each with different mechanisms. In the first area, the production occurs in the central active region of the AGN, which contains protons and photons. Photonuclear interactions would be the dominant process because the density of photons is much higher than protons. The resulting gamma rays are absorbed, and the protons are trapped by the plasma magnetically. Only high-energy neutrinos would escape the central region [146]. In the second area, the neutrinos and gamma rays are produced in the AGN jets. Again, the dominant process would be photonuclear interactions, but here all products (charged particles, gamma rays, and neutrinos) would leave the region [85].

For GRBs, the mechanism involved is photonuclear interactions between accelerated protons and high-energy photons inside the GRB fireball. An initial IceCube analysis [147] did not detect neutrinos associated with the locations of GRBs as predicted by [148] and set a 90% confidence upper limit that was 0.82 times the prediction. A follow-on IceCube analysis [141] improved the 90% upper limit to 0.27 times the prediction. A more recent IceCube search for a prompt neutrino signature in coincidence with over 500 known GRBs during the period from April 2008 to May 2012 found that GRBs contribute at most 1% of the total diffuse flux at 90% confidence and improved the previous sensitivity by a factor of 2 [149].

These astrophysical neutrinos must be accounted for, even though the acceleration mechanisms are still a mystery. They are rare when compared to the total number of atmospheric neutrinos. For example, at 1 TeV, there are ∼1000 atmospheric neutrinos for each astrophysical neutrino, but the astrophysical flux becomes important in this analysis when the conventional flux drops off at high energy.

3.9.1 Astrophysical neutrino flux models

Theoretical models such as the benchmark paper by Waxman and Bahcall [150] used an E^{-2} spectrum over the whole sky for initial comparisons to theoretical predictions. Newer studies have shown that this spectral assumption is likely too simplistic. It is also possible that the proposed unbroken power law of E^{-2} is actually two or more power laws in combination. Or, perhaps there are different sources in the galactic plane, versus the rest of the

universe. The discovery of an astrophysical neutrino flux is a very recent occurrence, and analyses in the near future should be able to answer these questions.

Astrophysical neutrinos should be produced in the ratio $\nu_e : \nu_\mu : \nu_\tau$ of 1:2:0 [151; 152]. Due to the very long travel distances (kiloparsecs or more), the astrophysical neutrinos that arrive at the Earth are expected to oscillate to equalize the ratio to 1:1:1. This assumption was used in this analysis.

In its simplest form, the astrophysical flux Φ_ν is modeled as a single power law with two main parameters, ϕ and γ:

$$\Phi_\nu = \phi \cdot \left(\frac{E_\nu}{100\ TeV} \right)^{-\gamma} \tag{3.9}$$

in units 10^{-18} GeV^{-1} cm^{-2} sr^{-1} s^{-1}. When a measurement of the astrophysical flux is published, the two parameters are given assuming these conventional units. The neutrino energy of 100 TeV is the pivot point for different γ values, while ϕ normalizes the curve. This analysis examined the effect of various astrophysical flux results as constraints on the nuisance parameters, which will be discussed in Chapter 9.

Chapter 4

IceCube Detector

4.1 Historical background

The earliest known papers that discuss the idea of a large-scale neutrino detector were written by Markov, Fakirov, and Schwartz between 1958 and 1960 [153; 154; 155]. In addition, the idea of studying high-energy neutrinos from cosmic rays was proposed by Markov and Zheleznykh in that same time frame [156]. To achieve adequate statistics, they proposed the construction of a 1000 m^2 detector from 1 to 5 meters in depth in an underground lake or the deep ocean to detect the Cherenkov radiation produced by charged particles.

The Deep Underwater Muon and Neutrino Detection (DUMAND) project was started in 1976 [59] to put a Cherenkov detector in the ocean off the coast of Hawaii, five kilometers beneath the surface. The detector would have included thousands of strings of sensors occupying a cubic kilometer of the ocean, including both optical sensors to detect the Cherenkov light and also hydrophonic sensors to detect the acoustic signals from fast-moving protons. Although technical problems caused the cancelation of the project, DUMAND provided many proof-of-concept designs that paved the way for future detectors.

The idea to build a large array of photomultiplier tubes in the Antarctic ice to detect high-energy particles began in the late 1980's, when Francis Halzen, the principal investigator of IceCube, spoke with Edward Zeller about a Russian experiment at Vostok Station near the South Pole that was using radio detection of neutrino interaction products [157]. Instead of radio detection, Halzen wondered if the DUMAND optical detection concept would work for ice [158]. A group of scientists in California and Wisconsin explored the idea of putting DUMAND-type sensors in the deep glacial ice, with a suggestion from Zeller that they use the ice in Antarctica and technical advice from DUMAND scientists. The group tested a small number of photomultiplier tubes in the Greenland ice as a proof of concept [158]. From there, AMANDA was born [159]. Short for Antarctic Muon And Neutrino Detector Array, AMANDA was composed of 677 optical modules on 19 cables and was built near the Amundsen-Scott South Pole Station. AMANDA (and its fully constructed configuration AMANDA II) was in operation from 1992 to 2009 [160]. The project provided the proof of concept for the follow-on project called IceCube [161]. Since neutrinos have extremely small cross sections, a large volume detector was required for adequate statistics. It was determined that a cubic-kilometer-scale detector would be needed to study these neutrinos.

AMANDA II instrumented about 0.015 cubic kilometers of ice when fully constructed, but IceCube fulfilled the cubic kilometer goal [162].

Water-based detectors also developed in the same time frame, inspired by DUMAND, and continued to pioneer new technologies. They are typically smaller detectors but have the advantage of better track reconstruction than Cherenkov detectors, particularly for electron neutrinos, and better energy reconstructions from improved knowledge of the detector medium (in most cases). The Irvine-Michigan-Brookhaven (IMB) detector was a nucleon decay experiment and neutrino observatory located in the Morton Salt Mine from 1982-1991. It was one of the experiments to detect the neutrinos from SN1987A [144; 163]. Also, Kamiokande in the Mozumi mine in Japan [143] was a Cherenkov detector that started operation in 1983 and was used to study neutrinos from different sources including the Sun, supernovae (including the detection of neutrinos from SN1987A), and the atmosphere. Super-Kamiokande is the next-generation Cherenkov detector operating in the mine today [164].

In later years, larger efforts by a Russian and German collaboration in Lake Baikal, Siberia, took advantage of the deep, clear lake. The Baikal Deep Underwater Neutrino Telescope (BDUNT) was built in stages, eventually providing an instrumented mass of 10 megatons (or approximately 100 cubic meters) for extremely high-energy cascades [165]. The ANTARES detector (Astronomy with a Neutrino Telescope and Abyss environmental RESearch), located at a depth of 2400 meters near the shore of Toulon, France, consists of 12 strings, each equipped with 75 optical sensors mounted in 25 triplets [166]. Like AMANDA for IceCube, ANTARES was the proof of concept for KM3NeT, which is a planned kilometer-scale detector in the Mediterranean Sea, comparable to IceCube's volume in the South Pole ice [167].

4.2 IceCube Detector

IceCube was installed in stages from February 2005 to December 2010, during the austral summers of the southern hemisphere (roughly November to February). In the 2004-2005 season, the first hole was drilled, and the first cable (called a "string") with 60 Digital Optical Modules (DOMs) was installed in the deep ice from 1450 to 2450 meters below the surface at the South Pole. This configuration was named IC-1 for the 1-string configuration. Subsequent seasons of deployment created configurations named IC-9 (2006), IC-22 (2007), IC-40 (2008), IC-59 (2009), IC-79 (2010), and IC-86 (2011 to present). This analysis used the IC-79 data and simulation for the analysis.

IceCube consists of three main parts, as shown in Figure 4.1: the main in-ice array, the smaller densely instrumented central array (DeepCore), and the surface array (IceTop). The in-ice components are comprised of 5160 DOMs on a total of 86 strings with 60 DOMs each (numbered 1 at the top and 60 at the bottom of each string). Holes were drilled into the ice using a combination of a firn drill for the top layer of compacted snow, and then a hot-water drill to continue down into the glacial ice to a depth of 2450 meters below the surface ($\sim$370 meters above the underlying bedrock). Of the 86 strings of DOMs, 78 strings are deployed with 17-meter spacing vertically, and roughly 125 meters horizontally in a hexagonal grid. The other 8 strings are used in DeepCore with smaller spacing. After string installation, the water in each hole eventually refreezes. The cables from all strings are connected to the

IceCube Laboratory, or counting house, in the center of the grid where the data is recorded. The in-ice array is comprised of a cubic kilometer of instrumented volume, or approximately one gigaton of glacial ice [168].

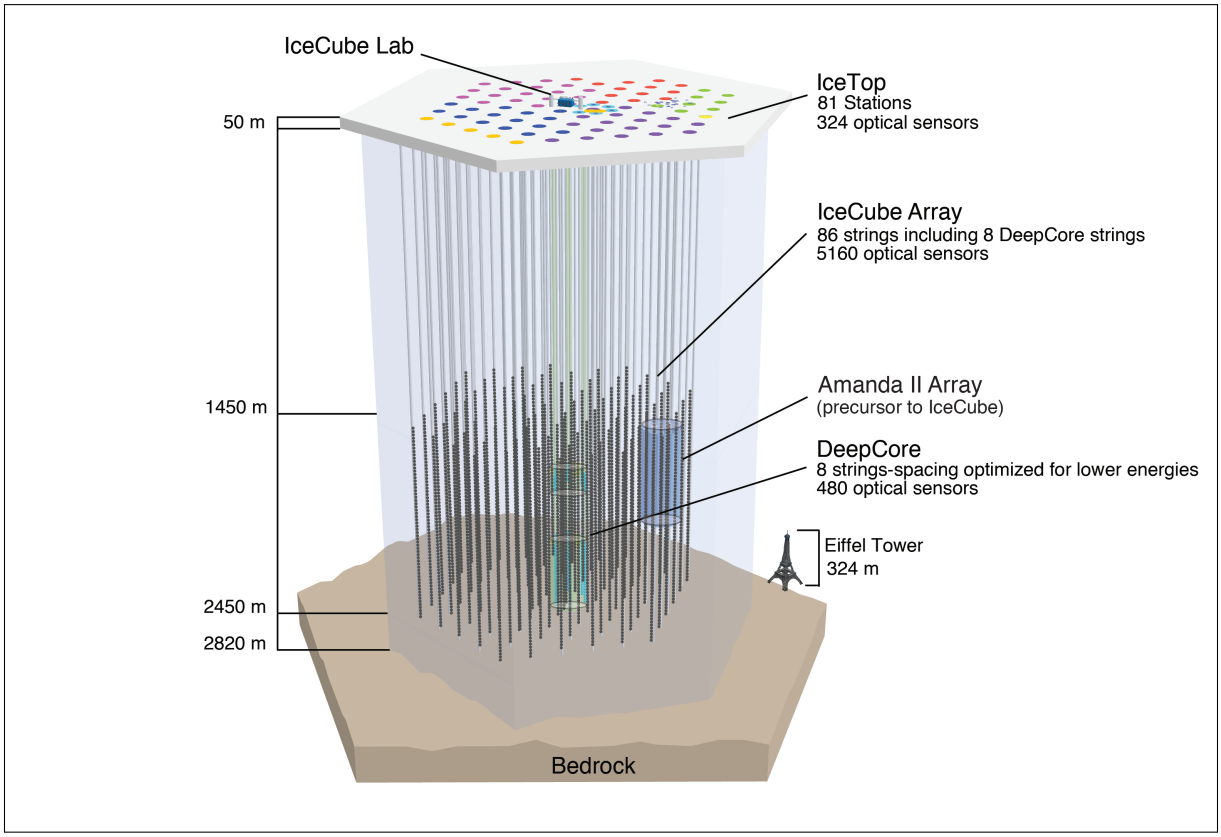

Figure 4.1: Depiction of the IceCube Detector. The main features include the support cables, or strings, represented by the gray lines, and the individual sensors called DOMs, represented by the black dots between 1450 and 2450 meters below the surface. The IceCube Lab is where all the signals from the strings are recorded. DeepCore is a more densely-instrumented array for lower-energy studies. The AMANDA II array is the precursor to IceCube and is no longer in operation. IceTop is the surface array of ice tanks with DOMs to detect cosmic ray showers. Colors at the surface represent the sequence of installation of the strings from 2005-2010 during the austral summers. From [169].

The DeepCore central subarray is a subset of the main array that includes 8 strings. Two of the strings have the standard quantum-efficiency photo-multiplier tubes (PMTs), which are the same as in the main array, while 6 strings have special higher-quantum-efficiency PMTs. The extra strings were deployed more compactly, reducing the horizontal separation to 70 meters and the vertical DOM spacing to 7 meters. In addition, the DOMs were deployed with emphasis towards the bottom of the detector where the ice is especially clear [170]. The combination of higher-efficiency PMTs with the reduced string spacing and deeper ice lowers the energy threshold of DeepCore to $\sim$10 GeV. Although not a primary part of this analysis, data from the DeepCore array are used in the reconstruction algorithms that will be discussed in Chapter 6.

The IceTop array consists of 81 surface stations near each of the IceCube strings. Each IceTop station consists of 2 ice tanks with 2 DOMs in each tank. IceTop is used mainly for calibration and as a veto of the cosmic ray background for in-ice studies. It is also used for cosmic ray air shower analyses in the higher energy range [171].

The IceCube Detector records data 24 hours a day, 7 days a week, 365 days a year, with an average up-time over 99.8%. Approximately 1 terabyte (TB) of data is recorded every day. Online filtering at the Pole reduces the data quantity to around 100 Gigabytes (GB) per day, which is transmitted daily to the North via satellite. This is the data that IceCube scientists use for their analyses. Approximately 200 million cosmic ray events are seen daily, but only 1 event in 10^6 is a neutrino. Even with online filtering, a sophisticated data selection method is required to find the signal within the background.

4.3 Digital Optical Module

The DOM is the fundamental detection unit of the IceCube Detector. The DOM construction project was an international effort by teams of engineers and scientists. Each DOM is an autonomous data acquisition system, composed of a glass pressure sphere that houses a PMT in the bottom half and supporting electronics, including the Main Board and the Flasher Board, in the top half. Figure 4.2 shows a diagram of the DOM.

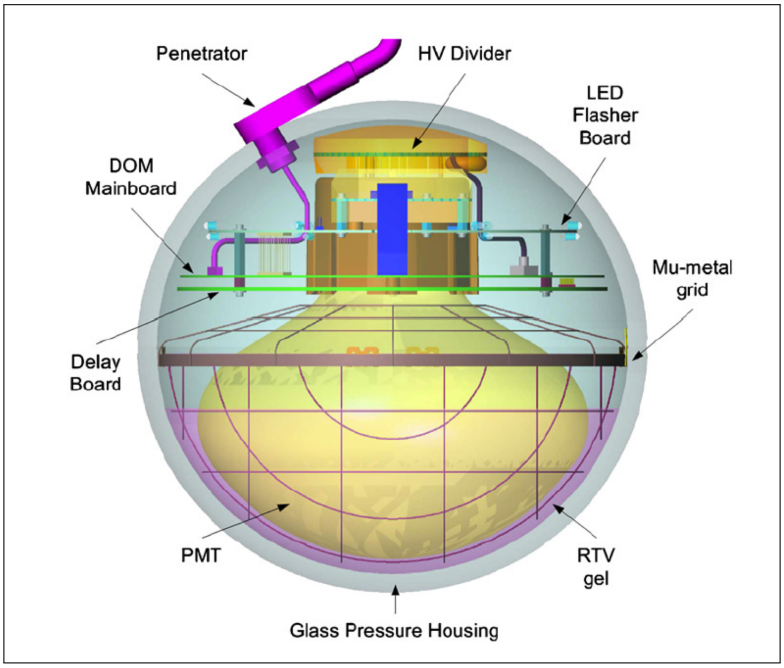

Figure 4.2: The Digital Optical Module (DOM) in IceCube. The bottom half of the pressure sphere holds the Hamamatsu PMT and magnetic shield cage. The top half contains the electronics to record and transfer the data from the DOM to the surface. From [172].

4.3.1 Glass pressure sphere

The exterior shell of each DOM is a 13-inch (33-centimeter) deep-ocean Benthos sphere. Made of $\frac{1}{2}$-inch thick, low-potassium glass to reduce radioactivity, the sphere is purged with dry nitrogen gas and evacuated to 0.5 atmospheres. This is done to keep the two sphere halves pressed firmly together while being handled before descending as far as 2.5 kilometers into the glacier. The sphere is rated to a depth of 6700 meters of water (pressures up to 70 MPa) and can withstand the extreme pressure of the deep glacial ice, protecting the equipment and hardware inside [173]. The glass is transparent to photons with a wavelength greater than 330 nm, and thus Cherenkov photons with smaller wavelengths are not detected.

4.3.2 Photomultiplier tube

The primary IceCube PMT is a 25.4-cm diameter Hamamatsu Photonics R7081-02, which is installed in all of the non-DeepCore DOMs. The PMT has a sensitive cathode area of 500 cm^2 in the range of wavelengths from 300 to 550 nm with a peak quantum efficiency of 25% [174]. For the 6 special DeepCore strings, a higher quantum efficiency version called R7081MOD was used to increase the quantum efficiency by 40% at photon wavelengths ∼400 nm [170]. This results in a lowered energy threshold for low-energy studies.

In all DOMs, the PMT is mounted in the downward-facing direction to emphasize the detection of photons from up-going particles. The PMT fills the bottom half of the glass sphere, with optically-transparent silicone coupling gel forming the interface between the PMT and the glass. Within the gel is a mu-metal grid that shields the PMT from the Earth's magnetic field. The glass and gel together set the short wavelength cutoff for the DOM at 350 nm, even though the PMT itself is capable of shorter wavelengths [174]. At a nominal gain of 10^7, the PMT response is linear within 10% up to currents of 50 mA (31 photoelectrons/ns), but saturates completely at 150 mA (93 photoelectrons/ns) [174]. The PMT trigger has a configurable minimum value, which is set to 0.25 times the nominal height of a single photoelectron pulse. The PMT information is sent to the Main Board of the data acquisition system.

4.3.3 Data acquisition system

The data acquisition system is controlled by a Field Programmable Gate Array (FPGA) located on the DOM Main Board. The FPGA interfaces with the digitizers, acquires the data, compresses the signals, and controls communications with the surface. The Main Board is located just above the PMT and amplifies, records, and digitizes the PMT signals when the trigger conditions are met. The Main Board divides the PMT signal into three paths. The first path is for the PMT trigger, the second path is the PMT signal, and the third path is sent to a converter that was designed to handle longer signals with a lower sampling speed [172].

4.3.3.1 DOM trigger condition

The DOMs can be set to operate in one of several modes to reduce the false triggers by noise. Typically, noise affects only one DOM at a time from sources such as the decay of a

radioactive potassium atom in the Benthos sphere encasing the DOM. Therefore, IceCube applies a "local coincidence" (LC) requirement before the signal from the DOM is recorded. This helps to suppress uncorrelated noise.

The first type of LC is the hard local coincidence (HLC) mode. This condition is met when one of the nearest neighbors to the DOM (on the same string) also records a signal, or when a next-to-nearest-neighbor DOM records a signal. For example, DOM 45 detects a signal. The nearest neighbors would be DOM 44 and DOM 46. Next-to-nearest-neighbors would be DOM 43 and DOM 47. If any of them detects a signal within 1 ms of the signal in DOM 45, then the HLC condition is met [168]. Local coincidence between adjacent DOMs is built into the wiring, but the next-to-nearest neighbor LC signal has to be passed through the Main Boards of the adjacent DOMs. The HLC condition reduces the trigger rate from ∼600 Hz to less than 1 Hz. If the HLC condition is not met, the waveform is stored as a soft local coincidence (SLC) hit [168]. When the HLC condition is met, the full waveform is read out, while the SLC condition merits only a shorter waveform readout.

4.3.3.2 ATWDs

The second signal path from the PMT is routed to two Analog Transient Waveform Digitizers (ATWDs). The ATWD is a waveform digitizer with four analog inputs. It stores the PMT signal using 3.3 ns binning and 128 analog samples for each input channel, for a maximum time of 422 ns. Three of the ATWD inputs are used to record the PMT signal at three different amplification gains (low, medium, and high). This ensures that the entire dynamic range of the PMT is covered, and both low-energy and high-energy events are adequately recorded. The fourth input is used for calibration and monitoring.

The ATWD is normally dormant and waits for a trigger signal to digitize the data and pass it on. If the DOM trigger condition is met, the FPGA sends a signal to the ATWD for capture, digitization, and readout to the FPGA. Because the digitization and readout time is ∼29 ms per gain, the two ATWDs alternate in taking data to reduce dead-time. If the HLC coincidence is not met, the ATWD is reset and awaits the next signal from the PMT, in turn [172].

4.3.3.3 fADC

The third path of PMT signals is routed to the fast Analog-to-Digital Converter (fADC). Because some signal events last longer than the ATWD can handle, the fADC samples the input with a coarser binning of 25 ns with 256 bins corresponding to a maximum of 6.4 μs. Because of the coarser binning, the samples are shaped. The fADC starts recording at the same time as the ATWD [172].

4.3.4 Flasher Board

The Flasher Board is located in the top half of the DOM above the Main Board. Although one low-power LED is installed on each Main Board for local PMT calibration, a separate Flasher Board is also installed. Each Flasher Board contains 12 gallium nitride LEDs pointed radially outward, 6 of which point horizontally while the other 6 point upwards at an angle of

48 degrees, with fully controllable intensity and sequencing. They produce bright ultraviolet optical pulses with a peak wavelength in the range 400-420 nm. In addition, later DOMs are fitted with flashers at four other peak wavelengths of emitted light (340, 370, 450, and 505 nm). Their main purpose is to investigate the optical properties of the glacial ice [168]. Ice modeling will be discussed later in this chapter.

4.3.5 DOM cables

The 4.6-cm diameter cable was manufactured by Ericsson Network Technologies and modified with DOM connectors by SEACON. The cable serves as both the power/data conduit and the support structure for the string. Four wires are combined to form a "twisted quad." Each pair of DOMs is connected to half of a twisted quad within the cable. The cable contains 20 quads, of which 15 are used for DOMs and the remainder for other devices deployed on the string. The total tensile strength of the cable is 55 kN [175].

4.4 IceCube Laboratory

The IceCube Laboratory (ICL) is the counting house for the detector. The building is located near the center of the hexagonal grid of strings. All 86 cables are brought into the building through silo-like structures at the ends. Each string is assigned its own computer called a DOM hub that communicates with all the DOM Main Boards for that string. The signals from the DOMs are synchronized to within a few nanoseconds of each other by comparing the DOM times to the Global Positioning System (GPS) time at the surface. All DOM hubs are connected to a central computer system that monitors the detector for the event trigger condition.

The event trigger condition is the requirement that a minimum of 8 DOMs experience an HLC condition within 5 ms, known as a simple multiplicity trigger or SMT8. If the trigger condition is met, then the readout window is ± 10 ms around the initial trigger time stamp. When triggered, the signals from all DOMs are formed into an event and stored in the IceCube Laboratory.

Data is stored using the Data Movement and Archival Subsystem (DMAS), which is a suite of Java-based software that controls the transfer of data from the South Pole to the Northern Hemisphere data warehouse, as well as the tape archiving of data. Every event is written to magnetic tape at the South Pole, and these full tapes are returned to the North at the beginning of every austral summer via aircraft for storage. The primary data storage application is called the South Pole Archival and Data Exchange (SPADE). The data is sent to the Northern Hemisphere via one of three transfer methods: high-volume bulk transfer over Tracking and Data Relay Satellite System (TDRSS), low-volume transfer by "secure copy," or transfer as an email attachment. The TDRSS method is the primary method of data transfer [176].

4.5 Optical properties of South Pole ice

The glacial ice at the South Pole was created in layers during the past 165,000 years and has a thickness between 2810 and 2857 m and varying across the kilometer footprint of the detector. The thickness of 2810 m comes from radar studies in the 1960's [177] and is the generally accepted value in the immediate vicinity of the South Pole. For this reason, IceCube simulation uses a value of 2810 m. Other studies indicate that 2820 is likely closer to the average thickness for the detector, since parts of the detector are located as much as 1.5 kilometers away from the South Pole [178]. In addition, a 2013 glaciology study indicates that this depth may be as much as 2857 m [179], and further study is needed. Fortunately, these small changes in the simulated ice depth do not change the neutrino rates appreciably.

In an ideal world, core samples would be taken from all areas of the detector ice to determine its composition. However, this is not feasible for a cubic kilometer. Instead, ice models had to be produced as the detector was built and data was recorded.

4.5.1 Absorption and scattering

The photons which are produced by particle interactions must propagate through the ice to reach the DOMs, and the photons are subject to scattering and absorption along the way. The absorption length and the scattering length of the ice are used to describe the ice properties and are defined as a function of depth and photon frequency. These parameters are affected by the ice qualities, such as the concentration of impurities (dust, bubbles, etc.).

The absorption length, λ_a, is the distance in which the survival probability of the photons drops by a factor of e. When the concentration of impurities in the medium increases, the absorption length decreases, indicating that the photons will be more affected by their travel in the medium. Absorption coefficient is simply the inverse of the absorption length, or $1/\lambda_a$ [178]. In general, a large absorption length, or small absorption coefficient, is desirable.

The scattering length, λ_s, is the average length that a photon will travel before being scattered by the mean scattering angle $\langle \cos\theta \rangle$, which is specific to each medium. The value of $\langle \cos\theta \rangle$ for the South Pole ice is estimated to be $\sim$0.94 [180], giving a value for λ_s of $\sim$1-2 m. When the scattering length decreases, the photons arrive later at the DOMs. This shifts the peak of the timing distribution to later times and also flattens the distribution. The scattering coefficient is the inverse of the scattering length, or $1/\lambda_s$. However, the parameter that is used more often is the effective scattering length, λ_e, which is defined as [178]:

$$\lambda_e = \frac{\lambda_s}{1 - \langle \cos\theta \rangle} \tag{4.1}$$

The effective scattering coefficient is therefore $1/\lambda_e$ [178]. In general, a large scattering length, or a low scattering coefficient, is desirable.

For the South Pole ice, at depths shallower than 1400 m, air bubbles are trapped in the ice and greatly increase photon scattering [178]. As pressure increases with depth, air bubbles are compressed, and eventually a phase transition from the gas phase to the solid air-hydrate clathrate phase occurs [181]. Fortunately, the refractive index of air-hydrate clathrates are almost identical to normal ice, and therefore photons pass through with almost no scattering [182].

The glacial ice is not uniform, and the biggest concern is the variable dust concentration at depth. Figure 4.3 shows the effect of the dust on the absorption and scattering coefficients. There are several minor dust layers, but there is one prominent peak in the absorption and scattering lengths coinciding with the highest concentration of dust at 2050 ±100 m, near the middle of the detector volume. These features were discovered using flasher data and other in-situ light sources from both AMANDA and IceCube [178; 183]. Ice model variations are included in the systematic error analysis in Chapter 9.

The glacial ice at the South Pole has short effective scattering lengths of ∼25 m but long absorption lengths of ∼100 m. In contrast, the water-based neutrino detectors, such as ANTARES in the Mediterranean, have long effective scattering lengths of ∼150 m but short absorption lengths of ∼60 m [184]. At the deepest ice depths in the clearest ice, the effective scattering length is 45-90 m, and the absorption length is 150-260 m [183]. Figure 4.3 shows the absorption and effective scattering coefficients for IceCube ice versus depth.

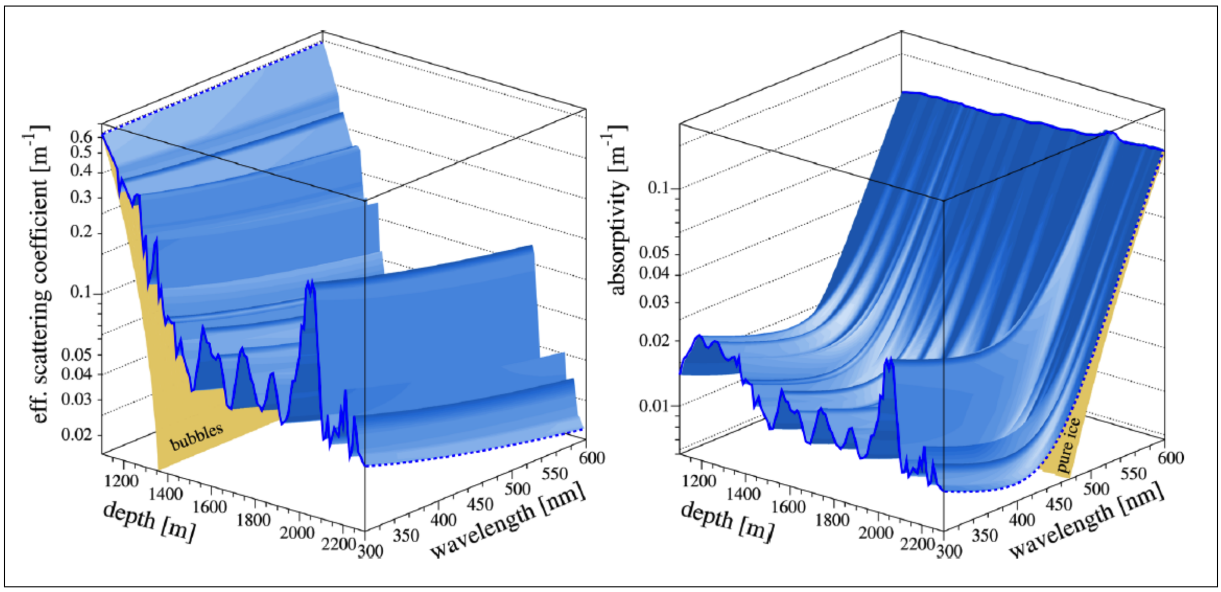

Figure 4.3: (left) Effective scattering coefficient, versus depth in the South Pole ice, versus wavelength of light. The effect of the main dust layer at ∼2050 meters depth can be easily seen. The effect of the ice bubbles is apparent above 1400 meters depth. The scattering is dependent upon the wavelength. (right) Absorptivity (or absorption coefficient), versus depth, versus wavelength of light. The main dust layer is again easily seen. From [178].

4.5.2 Mie scattering theory

The general case for photon scattering off small particles was first discussed in detail by Gustav Mie [185]. A "particle" is any closed region with a refractive index that differs from the refractive index of its surroundings. For simplicity, Mie scattering assumes spherical particles where the average distance between particles is large compared to the wavelength. In addition, the wavelength of photons is comparable to the particle size, and scattering is peaked in the forward direction.

In 1997, Price and Bergstrom [186] described this phenomenon for light scattering on microscopic particles in the deep ice, such as sub-millimeter-sized air bubbles and micron-sized dust grains that are typical in IceCube. In addition, Bohren and Huffman [187] used Mie theory to make detailed calculations to estimate the effects of scattering off randomly-distributed micron-sized particles in dusty ice [178]. Both of these concepts are currently used in IceCube ice models to represent the changes in light propagation with distance and depth, and a Mie-based ice model was used in this analysis.

4.6 IceCube ice models

"Ice model" is a description of the optical properties of the bulk ice in terms of the wavelength and depth dependencies of scattering and absorption. The original IceCube ice model was a modified form of an AMANDA model named Millennium, which was created from flasher and other light source data in AMANDA [178]. The model used single-photon arrival distributions for emitter-receiver pairs in the same horizontal layer using multiple wavelengths of low-intensity light. The Millennium model was modified by extrapolating below 2050 m (which was AMANDA's maximum depth) in 10 m increments to IceCube depths using the dust profiles from ice cores taken from East Dronning Maud Land, Antarctica (EDML) [183]. The new model was called the AHA (Additional Heterogenous Absorption) ice model.

However, IceCube flasher studies in 2008 indicated that the ice was clearer below the main dust layer than initially anticipated [180]. New flasher studies were performed in IceCube using single layers and observed numbers of photons. The result was a new model called the South Pole ICE, or SPICE, model.

4.6.1 Six-parameter ice model

SPICE uses a "six-parameter ice model" to represent the variation in the ice properties with depth. The model is centered at a wavelength of 400 nm, which is near the peak of the PMT's quantum efficiency. The model first characterizes the ice using the absorption coefficient a and the effective scattering coefficient $b_e = b{\cdot}(1{-}\langle\cos\theta\rangle)$, where θ is the deflection angle at each scatter. Additionally, the ice is parameterized in terms of the temperature of the ice, δT. Then the six main parameters, denoted by α, κ, A, B, D, and E, are defined as follows:

$$b_e(\lambda) = b_e(400nm) \cdot \left(\frac{\lambda}{400nm}\right)^{-\alpha} \tag{4.2}$$

$$a(\lambda) = a^*(400nm) \cdot \lambda^{-\kappa} + Ae^{\frac{-B}{\lambda}} \cdot (1 + 0.01\delta T) \tag{4.3}$$

$$a^*(400nm) = D \cdot A(400nm) + E \tag{4.4}$$

The parameter α accounts for the wavelength dependence of the scattering coefficient using Mie theory. The parameter A describes the absorption due to an Urbach tail [188], which is a steep exponential decrease in the absorption coefficient for wavelengths slightly longer than the electronic band-gap energy of ice. The parameter $A(400nm)$ is the specific value

at 400 nm. The parameter B describes the absorption due to the ice itself, not counting any impurities. The parameter κ accounts for the wavelength dependence of the absorption due to the dust. Parameters D and E account for the absorption due to dust and are the dominant factors that define the absorption versus depth in the wavelength range of the PMTs.

Continued improvements in the SPICE model were forthcoming with additional high-intensity flasher studies. A new approach implemented a direct fit of the flasher results to the Mie scattering functions, including a global maximum likelihood procedure for all flasher data on a single string to cover all IceCube depths simultaneously. The fit compared all photon arrival time distributions and photon counts to simulated distributions, but only at a single wavelength of 405 nm [180]. Data from all emitter-receiver pairs of DOMs (located in the same or different ice layers, amounting to 38,700 pairs) contributed to the fit of 200 ice parameters (comprised of scattering and absorption coefficients in 10 m layers at detector depths of 1450-2450 m). The resulting model of optical ice properties was called SPICE-Mie, which is the ice model used in this analysis. Figure 4.4 compares the absorption and scattering lengths for the older AHA model to the newer SPICE-Mie model.

4.6.2 Ice anisotropy

The flasher studies showed that the ice has a more complex structure consisting of non-horizontal ice layers. This layering anisotropy could not be modeled properly using the previous AHA or SPICE models. Figure 4.5 depicts the non-horizontal layering within the IceCube detector volume.

In addition to the dust layers, the flasher studies found evidence that the glacial ice exhibits a slightly different photon propagation behavior along the axis of the glacier's movement [189]. The reason is not yet understood, but possibilities include the orientations of the dust particles or the preferential alignment of the ice crystals due to glacial movement. This directional anisotropy was not incorporated into the SPICE-Mie model but was included in later models that were not available for IC-79 and this analysis.

4.6.3 Photon Propagation Code

A new program was needed to propagate individual photons in simulation, instead of relying upon binned statistical probabilities of photon distributions as was previously done. The new program is called Photon Propagation Code, or PPC [190], and was written by Dmitry Chirkin. The advent of graphics-processing-unit (GPU)-based simulation allowed this more time-consuming method to succeed. The program propagates each photon in the ice using a selected set of ice parameters, $b_e(405\text{ nm})$ and $a(405\text{ nm})$, until the photon hits a DOM or gets absorbed by the medium [180].

When used to create simulation, the SPICE-Mie model can be used with traditional Photonics tables (described below), or it can be used with PPC on GPU computers to directly propagate the photons of the event. Hence, the terminology SPICE-Mie-PPC indicates that the PPC propagator was used to generate the simulation.

The agreement between the simulated and reconstructed ice properties (both absorption and scattering) is $\sim$5-7%, with the latter number typically used in ice model systematic

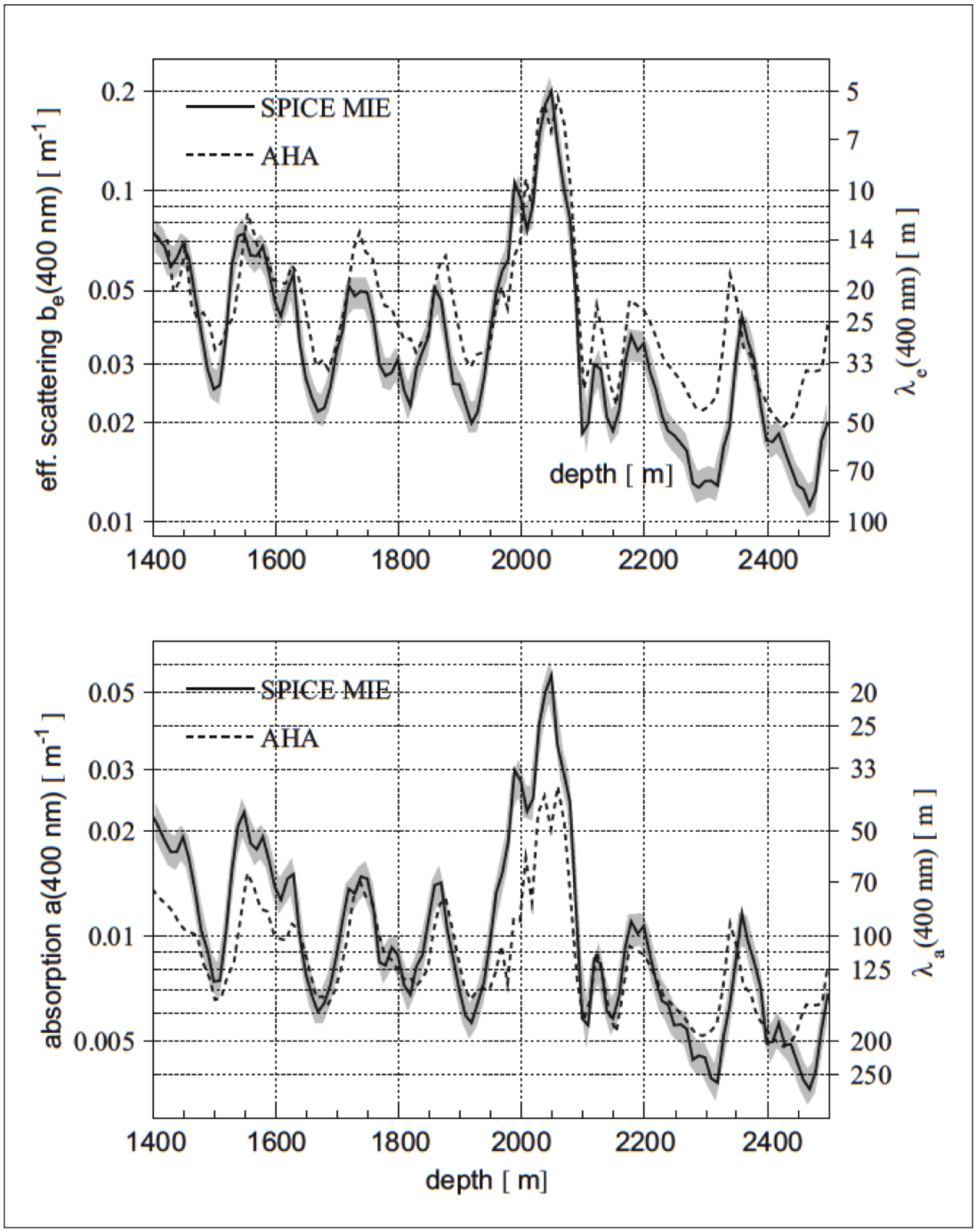

Figure 4.4: Effective scattering length (top) and absorption length (bottom) at wavelengths of 400 nm versus depth in IceCube. Peaks mark depths with increased dust concentrations, whereas valleys represent clearer ice. The dust peak at 2050 m is very prominent. The clearest ice is near the bottom of the detector volume, around 2460 m. The two IceCube ice models, AHA (older) and SPICE-Mie (newer), are compared to the data. The gray band indicates uncertainties in the models. From [183].

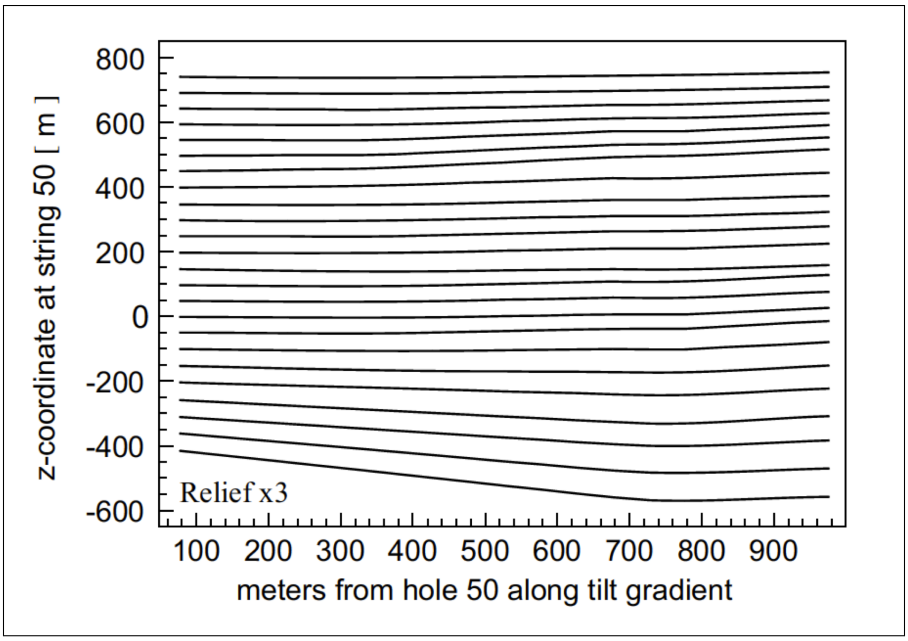

Figure 4.5: Depiction of non-horizontal layers of ice, from flasher data. Relief is magnified by a factor of 3 for clarity. From [183].

studies (Chapter 9). The official ice model for IC-79, which is used in this analysis, is the SPICE-Mie model with PPC photon propagation in simulation. It shows excellent agreement between simulation and data and is the baseline model for all reconstructions and other tools in this analysis.

4.6.4 Photonics tables

A single muon at IceCube energies creates well over a million photons. Simulating and tracking this large number of photons is computationally intensive. With the Photonics program [191], the photon flux and time distributions could be tabulated for any propagation volume and user-defined range of light source and detector properties. For IceCube, the horizontal ice layers could be modeled, but other ice characteristics, such as layer tilt, could not. Once a Photonics table set was generated, the light yields and time distributions could be accessed without the need for real-time photon propagation during event simulation or reconstruction. Photonics provided the probability density functions for arrival times of independent photons and the expected number of detected photons. From any starting location, time, and direction, the probability of a photon arriving at any other location and time could be determined using the tables. However, sometimes the transition from one bin in the tables to the next created large differences in photon behavior, resulting in "binning effects" that impacted the accuracy of the propagation especially over longer distances. With the advent of PPC-based propagation, Photonics tables became disfavored in IceCube simulation, although the tables are still used in the early stages of data processing.

4.6.5 Hole ice

The "hole ice" is a column of ice approximately 30 cm in radius immediately surrounding the IceCube DOMs that was melted and then refroze after installation. Hole ice is therefore distinguished from bulk ice, which is the pristine glacial ice into which the holes are drilled. The hole ice is described by taking into account an increased amount of scattering via a modification to the effective angular sensitivity curve of the receiving DOM [183]. Figure 4.6 shows the angular sensitivity of the DOM within the hole ice, compared to the nominal ice, from flasher studies. The angular sensitivity is the fraction of photons that are detected at a given angle with respect to the PMT axis. Photons that arrive straight into the PMT from below have cosine = 1.0, and they are the most affected. Photons that arrive from the sides of the PMT have cosine = 0.0 and are much less affected.

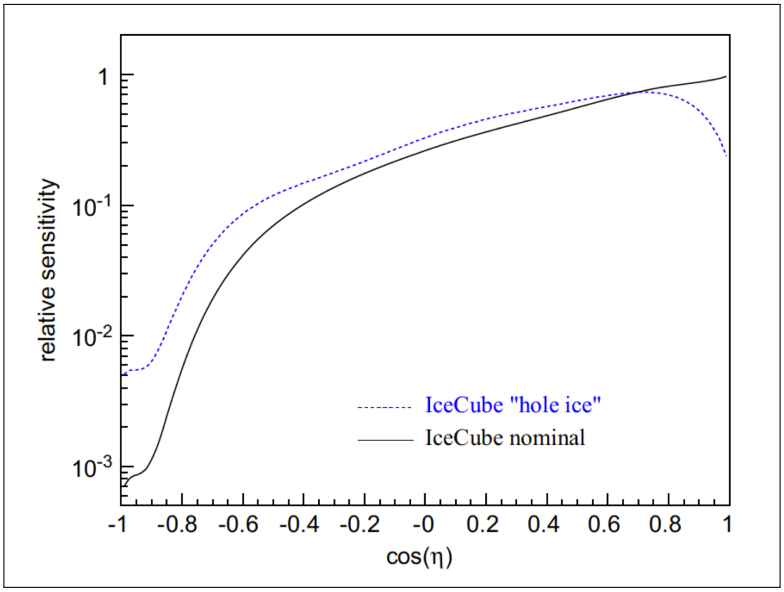

Figure 4.6: Comparison of the angular sensitivity of hole ice to nominal ice in IceCube. Cosine of 1.0 represents photons coming straight into the PMT from below, which are the most affected. From [183].

However, an additional internal IceCube study [192] using IC-22 data looked for deviations in hit times in DOMs which were believed to have larger diameters of hole ice around them due to drilling problems. Because hole ice is thought to have many more bubbles than the unperturbed Antarctic ice, the hole ice might cause extra scattering of light as photons travel to the DOM. If so, then DOMs with very wide hole ice would have later hit times due to the extra scattering. When plotting the hit times of the DOMs with wider hole ice than the others, there was no discernible difference. In other words, the hole ice did not have much impact on the transmission of photons.

By combining all these findings, the current model of the hole ice uses an effective scattering length of 50 cm due to the expected higher concentration of air bubbles [191]. These studies indicate that hole ice should not have a major impact on this analysis, but hole ice is included in the systematics studies in Chapter 9.

4.7 Particle detection and signatures

Although the CC interaction is identical for all three neutrino flavors, the signature of the outgoing charged lepton looks quite different. There are two basic event signatures in IceCube: tracks and cascades. The difference allows this analysis to select ν_μ events instead of ν_e or ν_τ events.

4.7.1 Muons

The muon signal will look like a track traversing the detector from any direction but always in a straight line. Even at the lowest muon energy of this analysis (1 TeV) and using the highest magnetic field on the surface of the earth (0.65 gauss), the change in track angle over a distance of 1.5 km (the largest diagonal dimension of IceCube) is ∼0.002 degrees. This is much smaller than the track reconstruction error of IceCube, which is ∼0.5 degree.

Because the dominant processes of energy loss for the muons in this analysis are bremsstrahlung, pair production, and photonuclear interactions, the energy loss of the muon will be sporadic but with an underlying nearly continuous energy loss. Therefore, the typical signature is a track with varying energy loss. Figure 4.7 shows examples of a classic muon track signature for two different muon energies.

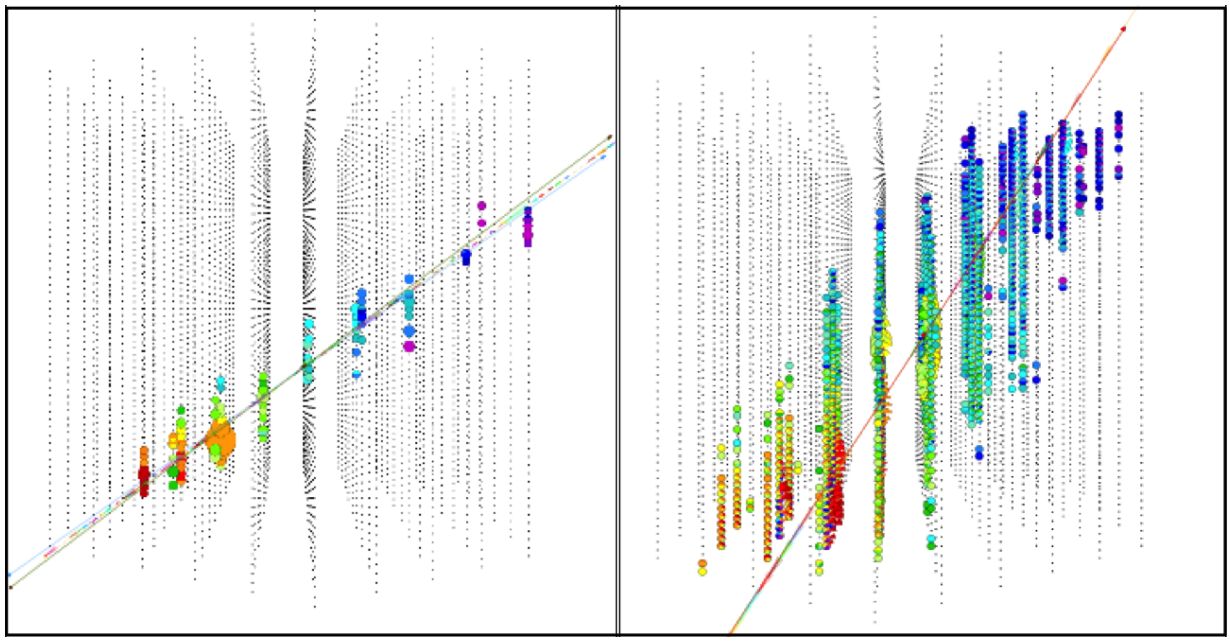

Figure 4.7: Muon signatures in IceCube, for two different energies. On the left, the muon has an energy of 6 TeV, and on the right 6000 TeV. The black dots represent the DOMs in the ice. Red DOMs indicate the ones that received the earliest photons, progressing through the rainbow to purple, which indicate the latest DOMs to receive photons. Using the timing and geometry information, the trajectory of the particle can be determined (diagonal lines). In addition, the relative sizes of the DOMs indicate the number of photons that were received, which is used to determine particle energy.

4.7.2 Electrons

Contrary to ν_μ outcomes, the ν_e interaction ends almost as soon as it begins. Because the end product of the CC interaction is an electron, that electron interacts with the surrounding matter within ~10 meters [193]. Figure 4.8 shows a typical signature of an electron cascade, which is a spherical deposit of energy whose size correlates to the energy of the electron neutrino. The spherical signature allows it to be eliminated as background for this analysis.

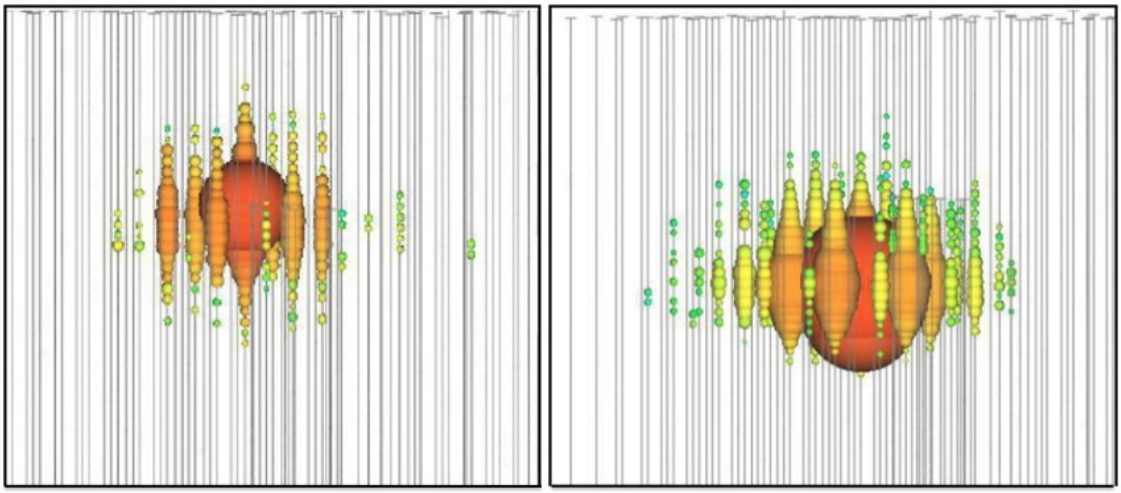

Figure 4.8: Typical signatures of a high-energy cascade from a ν_e CC interaction. The overall size of the cascade correlates to the energy of the neutrino that caused it. The left event is 110 TeV, and the right event is 1100 TeV. The large DOM in the middle of the cascade indicates the earliest hit, which is large because it was very close to the interaction vertex. From [194].

4.7.3 Taus

Charged-current ν_τ interactions above 1 PeV can yield taus that travel a detectable distance before decaying. This results in a hadronic cascade followed by a track of direct electromagnetic losses from the τ itself, in turn followed by a cascade (electron) or track (muon) from the τ decay [195]. This is called a "double-bang" signature. Taus of lower energies will decay in shorter distances, and the two cascades will be indistinguishable from each other, appearing the same as the single cascade from a ν_e. Because of this, an event selection that eliminates electron cascades would also eliminate tau cascades. Figure 4.9 shows an example of a high-energy ν_τ interaction and subsequent τ decay to an electron.

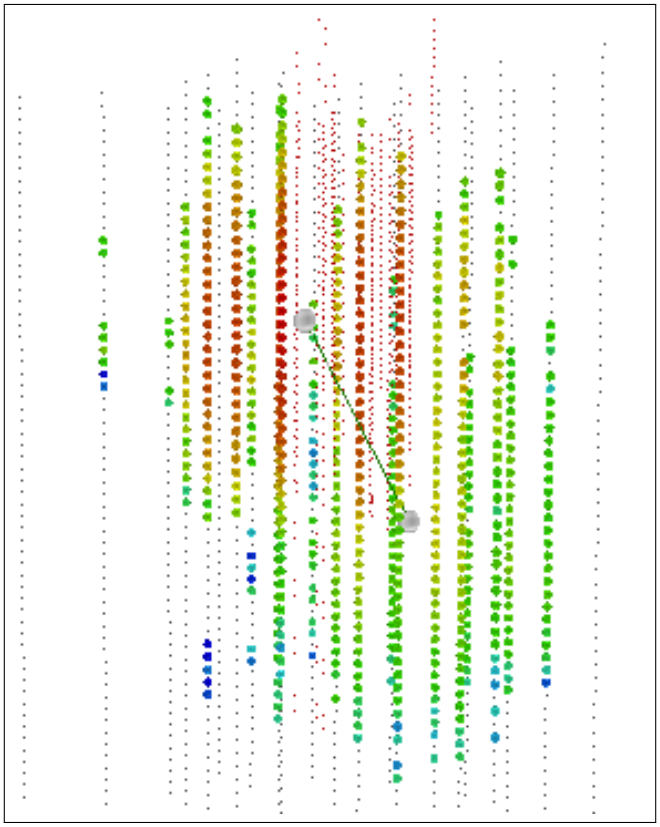

Figure 4.9: Simulated signature of a high-energy ν_τ event. The ball of light to the upper left is from the initial $\nu_\tau N$ CC interaction that forms the τ. The ball of light to the lower right is from the decay of the τ. This "double bang" signature is possible for very energetic but rare ν_τ (E $>$ 1 PeV) where the two balls of light can be discerned. Most ν_τ events would look like ν_e events.

Chapter 5

Simulation

5.1 Simulation overview

The simulation process is shown in Figure 5.1 and begins with a primary particle generator, followed by the propagation of the secondary particles to the detector volume, and finishes with the detector's response. IceCube simulation for neutrinos is called Neutrino Generator, or NuGen, which represents the signal in this analysis. The simulation for cosmic ray showers is called CORSIKA, which represents the background in this analysis. The propagation of muons is performed by Muon Monte Carlo (MMC). The propagation of all photons created in the various stages of the interactions is accomplished by Photon Propagation Code (PPC). Then the detector response is simulated in the last several steps. The simulated events are recorded using the identical file format as actual data events, with each simulation set assigned a number, such as 10904, based upon when the simulation was run. From this point forward, the same reconstruction software is used for both data and simulation. Chapter 6 will cover the initial data processing. User-defined options for the entire simulation chain will be discussed within the NuGen and CORSIKA sections.

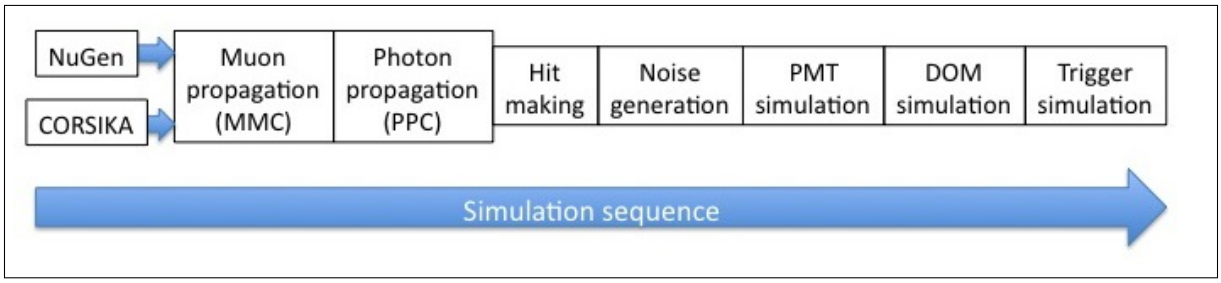

Figure 5.1: Simulation chain for muons in IceCube. Each step is discussed in the text.

5.2 Neutrino Generator

Simulated neutrino and subsequent muon trajectories were created using a program called Neutrino Generator (NuGen), which uses All Neutrino Interaction Simulation (ANIS) [196]. ANIS is a Monte Carlo event generator which creates neutrinos, propagates them through the

Earth, and simulates a neutrino interaction within a specified volume around the detector. The NuGen program includes several effects, including CC and NC interactions inside the Earth, based upon a user-designated neutrino cross section model, the density profile from a user-designated Earth model, and a model of the glacial ice. The program does not include neutrino oscillations, which are completely negligible at the high energies of this analysis. This analysis used NuGen version 02-06-03.

The neutrinos are propagated on trajectories toward the IceCube detector. The simulation steps through the Earth and calculates probabilities of interactions at each step. The neutrinos reach the detection volume where they are forced to interact with the rock or ice, as appropriate. Secondary particles are generated and stored. The actual probability of interaction is then calculated and stored as a weight factor. The program has many user-designated parameters, depending upon analysis needs.

Because NuGen is the first step in the simulation chain, the desired options for all subsequent steps in the chain are required as inputs. These options are listed below, along with the settings for this analysis in [brackets]. Additional settings were used for the systematics studies, which will be discussed in Chapter 9.

Flavor of neutrino: simulation can be created for any neutrino flavor. [muon neutrino, in the ratio of $\frac{1}{2}\nu_\mu$ and $\frac{1}{2}\bar{\nu}_\mu$]

Number of events: statistics for the analysis [10 million events]

Neutrino cross section model: choice of CTEQ5, CSS, or CSMS (see Chapter 2) [CSMS]

Initial energy spectrum of the neutrinos at the surface: frequently used energy spectra are $E^{-2.0}$ and $E^{-1.5}$ [$E^{-1.5}$]

Neutrino energy range: to match the needs of the analysis [10 GeV to 10 PeV (or $\log_{10}(E_\nu/\text{GeV})$ from 2 to 7)]

Zenith angle range: the range of zenith angles to be simulated, with the most common choices as 0 to 180^o (full range) and 90 to 180^o (up-going only) [80 to 180^o]

Zenith angle weighting: higher weighting means more events are thrown at the higher zenith angles to increase statistics there, with the most common setting at 1.0 (no weighting) [1.5, with 50% more events at the higher zenith angles]

Earth model: variations on Earth models are available (such as flat-core-density), but the most common choice is PREM [PREM]

Detector configuration: any of the established string configurations (IC-59, IC-79, IC-86, etc.) [IC-79]

DOM efficiency: photon detection efficiency can be varied in the DOMs for systematics studies, with the nominal setting at 110% for IC-79 [110%]

Ice model: several different choices available in IceCube, with the most common as SPICE-Mie (IC-59 and later) and SPICE-Lea (IC-86 and later) [SPICE-Mie]

Absorption and scattering: can be varied in a specific ice model for systematics studies, with the most common settings at +10% absorption, +10% scattering, and -7%/-7% absorption/scattering. This mode is useful when additional ice models are not available, such as in IC-79 [no change]

Muon propagation method: currently a choice between MMC and Proposal, with the most common as MMC (explained later in this chapter) [MMC]

Photon propagation method: currently a choice between Photonics and PPC, with the most common as PPC (discussed in Chapter 4) [PPC]

Simulation mode: can be selected as FULL, FINAL ONLY, or IN EARTH. FULL setting is the normal simulation mode, with full event propagation through the Earth. There are 2 submodes in FULL: NO WEIGHT and NCGR WEIGHTED. With NO WEIGHT, if an event has a CC interaction well before the detector, the event is considered absorbed before it reaches the detector, and the event is not recorded. With the NCGR WEIGHTED setting, the simulation forbids CC interactions inside the Earth. Instead, the simulation forces a NC interaction or Glashow resonance (GR, for $\bar{\nu}_e$) if a CC interaction is predicted, but the event is reweighted accordingly to compensate for this preference. Thus, all events that are thrown are recorded in the final output file. FINAL ONLY setting only simulates the detector response for interactions and does not account for any effects of the Earth transit. In the IN EARTH setting, no interaction weight is applied, and the detector is not simulated. The output represents simple counts of events that survived the journey through the Earth. This mode is used to create InEarth weights (described below) for evaluating the effects of different neutrino cross section multiples or Earth models. Stated another way, the equivalent of FULL mode is IN EARTH + FINAL ONLY. [FINAL ONLY (10904) and FULL/NCGR WEIGHTED (11493)]

The specific IceCube simulation sets in this analysis are 10904 and 11493. Each one uses identical settings for NuGen, except for the simulation mode. Set 10904 assumed no Earth effects (FINAL ONLY), and 11493 simulated real-life data events from start to finish, including Earth effects minus in-transit CC interactions (FULL/NCGR WEIGHTED). The purpose of 11493 was to cross-check the behavior of combining 10904 with InEarth weights to represent FULL simulation. This study showed that FINAL ONLY + IN EARTH was equivalent to FULL.

5.2.1 InEarth

For this analysis, we needed to know the effect of varying the cross section on the probability of an event surviving its journey through the Earth. Ideally, we would have run many different cross sections through our full simulation production process to use all its capabili-

ties, avoiding the need for additional programs to change the cross section. In order to have enough statistics to reduce error bars at high energies, we would have needed approximately 2 million events per simulation run. This would have taken approximately 3 weeks per run. With 35 runs needed for varying the cross sections for this analysis, this would have been expensive in terms of computing time.

An alternative was proposed to run the NuGen simulation in a partial mode. Instead of assuming a single cross section for each of 35 simulation sets, one very large dataset without Earth effects (FINAL ONLY) was created, and then a separate program that only looked at the Earth's effects (NC and CC interactions) with varying cross sections was run. This new program was designed by Kotoyo Hoshina at the University of Wisconsin-Madison and was called InEarth. She used the existing NuGen code to separate out the Earth's effects. With this program, it was possible to change the neutrino cross sections (by changing the theoretical model or the cross section multiple) and/or the Earth model (such as variations on PREM) without rerunning the simulation set.

Using this program, the energy spectrum of events upon detector arrival was compared with the initial spectrum at the surface. This ratio could be used as a correction factor to the weight of each event in the large simulation set that was run in FINAL ONLY mode. The correction would account for the changes in arrival and interaction probabilities due to the changes in neutrino cross section.

The method for finding these InEarth weights is as follows. The user chooses the initial spectrum at the Earth's surface. In order to have enough statistics for the high-energy and high-zenith-angle events, an E^{-1} energy spectrum was chosen with an emphasis on higher zenith angles (zenith-weight-factor = 1.5). These events were sent through the NuGen process from the surface to the detector. This was done for each specific cross section multiple, from 0.2x to 5.0x SM. Each event recorded all NC interactions and CC interactions that occurred along its path through the Earth.

Once all of the events were run, another program examined the output. Two histograms were made in three dimensions, using zenith angle, initial neutrino energy at the surface, and final neutrino energy at the detector. The first histogram showed the distribution of true zenith angle and true surface energy for the E^{-1} spectrum (the "input"). The second histogram showed the final energy for events as they arrived at the detector after transiting the Earth (the "output"). At low energies, this final energy is usually unchanged. At higher energies, however, there is a higher probability of an energy reduction due to a NC interaction along its path. Binning was small enough to ensure a smooth distribution. Since most of the cross section effect is seen in the zenith angle distribution, InEarth used zenith angle (degrees), while the analysis binning for the final result used cos(zenith angle), to minimize binning effects, which will be discussed in Chapter 8. The binning size used was 5^o in zenith angle and 0.167 in $\log_{10}(E_\nu/\mathrm{GeV})$ or 6 bins per decade for both the initial and final neutrino energies.

Then the two histograms were combined by taking output events divided by input events. This provided a histogram of "correction weights" for each bin. Bins at low energy and low zenith angle had weights near 1.0 (no correction) because the interaction probability for these neutrinos is very small, and the overall event weight would be unchanged. Bins at high energy and/or high zenith angle had much lower weights because of the higher probability that the neutrino experienced a NC or CC interaction. Also, it was possible for the input

neutrino to start in one energy bin but end up in a lower energy bin in the output histogram due to experiencing a NC interaction along the way.

Figure 5.2 shows the input spectrum and output spectrum for cross section multiples of 1.0x SM and 3.0x SM. The effects of the Earth on the spectrum are apparent as the events begin to disappear at the higher energies. These plots assumed an E^{-1} spectrum to emphasize the effects.

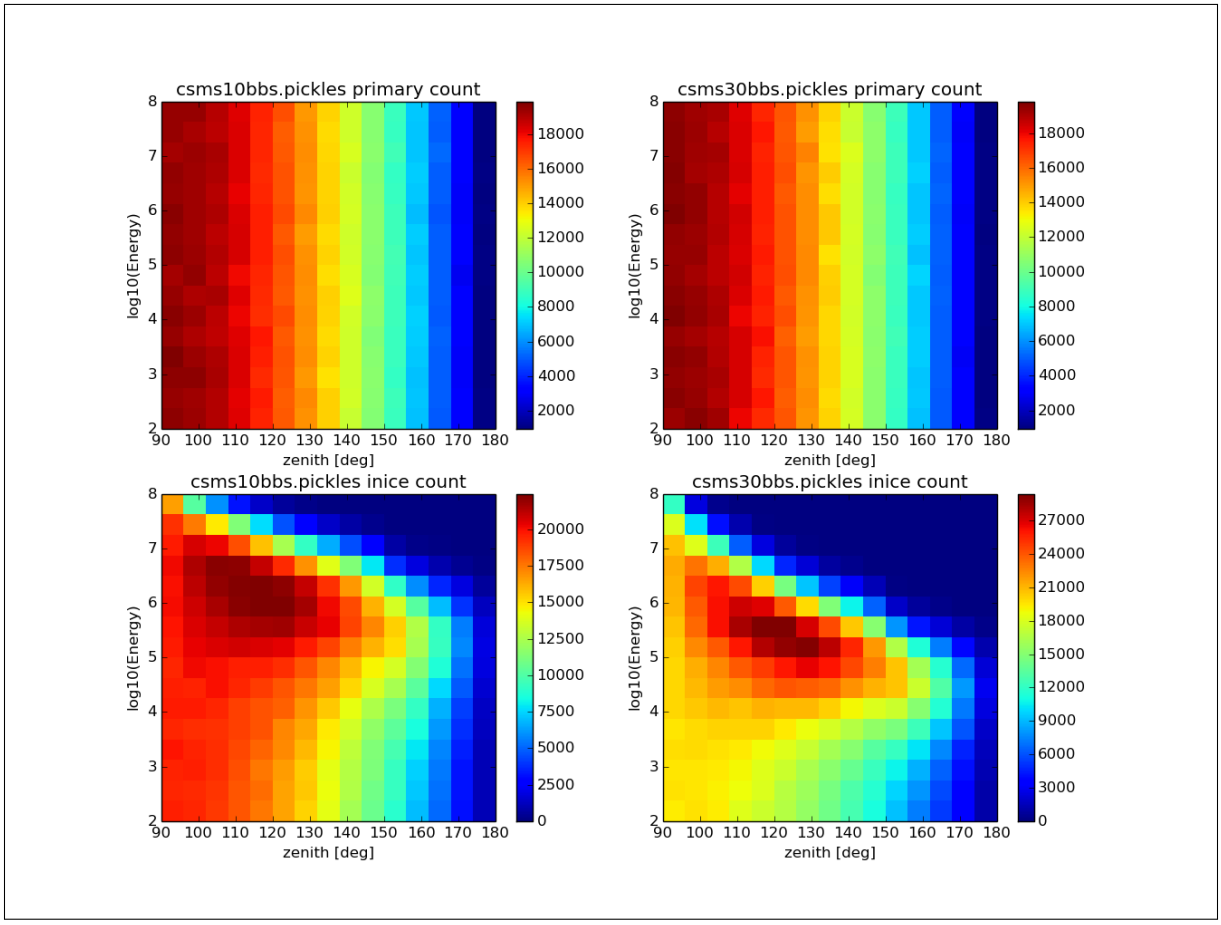

Figure 5.2: Comparison of the E^{-1} input spectrum to the output spectrum for the InEarth program for 2 million events, in energy versus zenith angle with zenith weighting of 1.0. Colors indicate number of events per bin (z-axis). On the left are the input (top) and output (bottom) for a cross section multiple of 1.0x SM. On the right are the input (top) and output (bottom) for a cross section multiple of 3.0x SM. The ratio of each output bin to the corresponding input bin gives the correction factor for that bin due to cross section effects during Earth transit for that specific spectrum.

As mentioned in Chapter 3, the surface spectrum for the neutrinos generally follows an $E^{-3.7}$ spectrum, not $E^{-1.0}$. Because of this, the event weights must be corrected before the output events are generated. Otherwise, an event that experiences a NC interaction and changes to a lower energy bin in an E^{-1} spectrum would have too much weight, when compared to a lower-energy event that had no interaction and remained in that lower-energy bin. Therefore, the plots were repeated with the corrected $E^{-3.7}$ spectrum, and the ratios

were recalculated. These correction factors were then applied when the cross section multiple was varied in this analysis. See Figure 5.3 for a comparison.

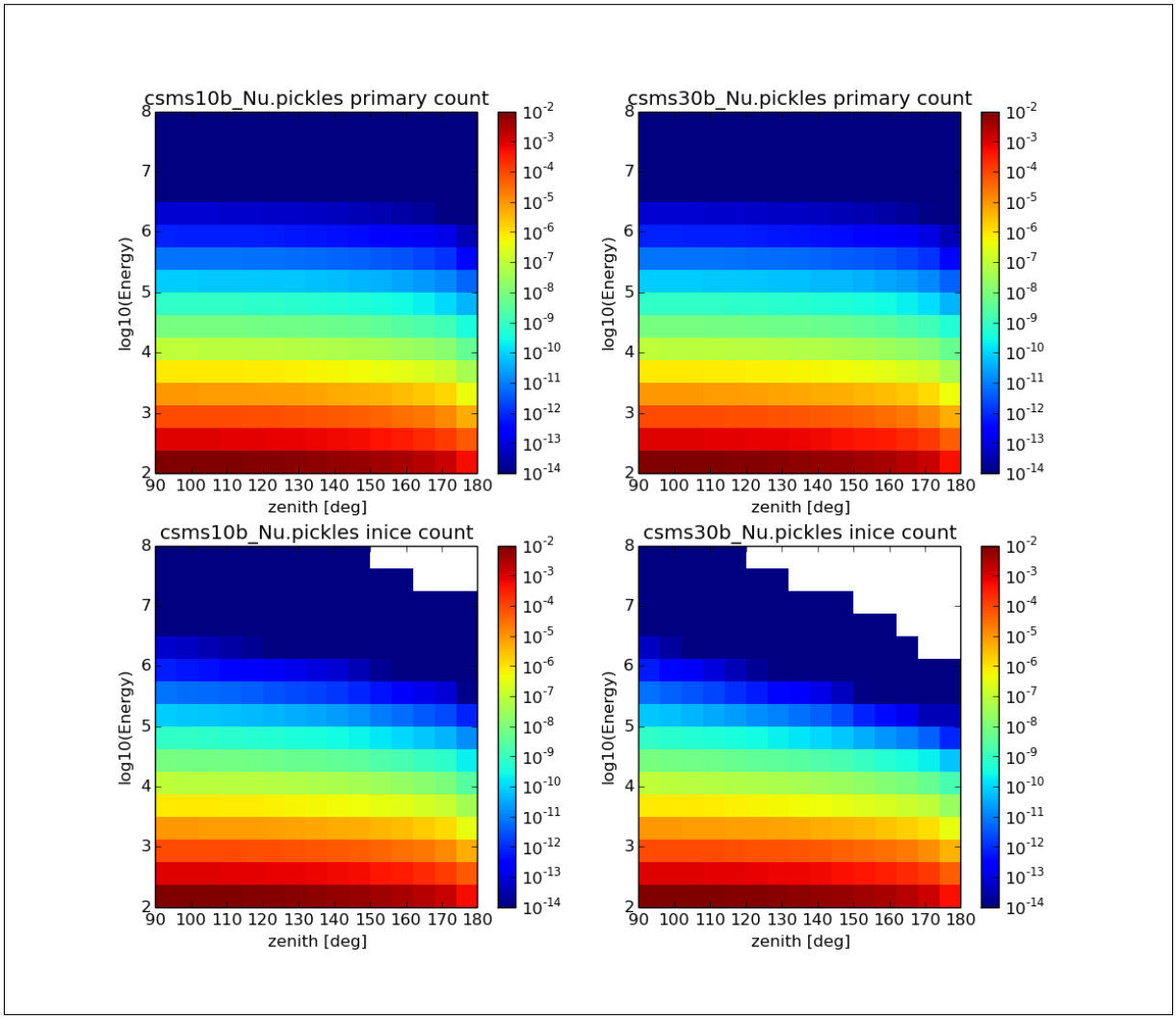

Figure 5.3: Comparison of the input spectrum to the output spectrum for the InEarth program for 2 million events, this time for $E^{-3.7}$ input spectrum (to match the incident conventional neutrino spectrum) and zenith weighting of 1.5. Colors indicate number of events per bin (z-axis). On the left are the input (top) and output (bottom) for a cross section multiple of 1.0x SM. On the right are the input (top) and output (bottom) for a cross section multiple of 3.0x SM. The ratio of each output bin to the corresponding input bin gives the correction factor for that bin due to cross section effects during Earth transit. The Earth's absorption is apparent in the upper right corners of the bottom plots, where the flux of neutrinos disappears for high energy and high zenith angle.

Because the prompt flux generally follows the cosmic ray spectrum, the weights for prompt were calculated from an $E^{-2.7}$ flux. In addition, the weights for the astrophysical flux were calculated from an $E^{-2.3}$ flux. The differences between the weights for the different energy spectra were quite small, only ∼5%. This resulted in only a 1% change in the XS result when running the fitter with individual weights. For the final result, only the $E^{-3.7}$ weights were used for adjusting all three fluxes.

Once the InEarth correction factors were calculated, each event was assigned 25 different weights, one for each cross section multiple between 0.2x and 5.0x SM. These weights were then used by the fitting program (discussed in Chapter 8) to find the best fit to the data.

5.3 CORSIKA simulation

In order to separate the signal (up-going muons from neutrinos) from the background (down-going muons from cosmic rays), a suitable background simulator was needed to test the event selection methods. The standard simulation package for cosmic ray-induced air showers in IceCube is called CORSIKA. Short for COsmic Ray SImulations for KAscade, the program was originally developed by the KASCADE experiment in Germany [101]. CORSIKA has been used by many collaborations and has experienced many refinements over the years. It is a detailed Monte Carlo program to study the evolution of extensive air showers in the atmosphere that are initiated by high-energy primary particles. The particle energy range extends up to the highest energy observed thus far ($E > 10^{20}$ eV) [197].

The program simulates the interaction of cosmic-ray particles with the molecules of the Earth's atmosphere. Then it propagates all subsequent air shower particles through the atmosphere, including simulation of all the relevant physics processes. CORSIKA is useful for studying a variety of cosmic-ray compositions and energy spectra and can provide corrected atmospheric density profiles for the seasons. For underground detectors, only the muons and neutrinos that are formed in the air showers will reach the detectors. Although CORSIKA can simulate both muons and neutrinos for IceCube, CORSIKA is typically used to simulate the muons, while NuGen is used for the neutrinos because NuGen is more efficient than CORSIKA.

CORSIKA is usually run with an $E^{-\gamma}$ spectrum, which is then corrected to whatever spectrum is needed for the analysis. The program is highly modular, and these modules are interchangeable. This analysis used the air shower simulation based on the SIBYLL 2.1 hadronic model [198]. SIBYLL 2.1 is used in most IceCube analyses because it is one of the faster modules.

The muon contribution from prompt decays is not included in SYBILL 2.1, but the fraction of the prompt contribution in the overall muon background is very small, much smaller than the effect on neutrinos. For the purposes of background simulation, however, it is sufficient to test event selection methods.

IceCube uses version 7.4 of CORSIKA in most of its analyses. Just as with NuGen, CORSIKA has many user-defined parameters, which are listed below, along with the settings used in this analysis in [brackets] for the entire simulation chain.

Cosmic ray model: 5-component (Gaisser model) [5-component]

Cosmic ray spectrum weighting: Simple power law (typically E^{-2}) or poly-gonato (Hörandel) (see Chapter 3) [both E^{-2} and Hörandel were used, explained below]

Hadron model: SYBILL 2.1, QGSJET, QGSJET2, DPMJET, EPOS, others [SYBILL 2.1]

Number of files: statistics for the analysis [30,000 files]

Primary cosmic ray energy range: to match the needs of the analysis [multiple settings, explained below]

Zenith angle range: the range of zenith angles to be simulated, with the most common as 0 to 89.99^o (down-going) [multiple settings, explained below]

Detector configuration: any of the established string configurations (IC-59, IC-79, IC-86, etc.) [IC-79]

DOM efficiency: photon detection efficiency can be varied in the DOMs for systematics studies, with the nominal setting as 110% for IC-79 [110%]

Ice model: many different choices available in IceCube, with the most common as SPICE-Mie (IC-59 and later) and SPICE-Lea (IC-86 and later) [SPICE-Mie]

Absorption and scattering: can be varied in a specific ice model for systematics studies, with the most common as +10% absorption, +10% scattering, and -7%/-7% absorption/scattering [no change]

Muon propagation method: currently a choice between MMC and Proposal, with the most common as MMC (explained later in this chapter) [MMC]

Photon propagation method: currently a choice between Photonics and PPC, with the most common as PPC (discussed in Chapter 4) [Photonics]

Simulation mode: most common choices are In-Ice (no IceTop response, muons in ice only) or Diplopia (multiple particles per event), with subsettings of CORSIKA-on-CORSIKA (coincident down-going air showers) or Neutrinos with CORSIKA (muon events from neutrinos with coincident CORSIKA air showers) [multiple settings, explained below]

This analysis used two different CORSIKA simulation sets to test the veto power of the event selection criteria (discussed in Chapter 7). One problem with reconstructing real data is that ∼10% of the up-going signal events are predicted to have a coincident down-going muon from an air shower. In these events, two unrelated muons transit the detector in the same time window. The detector triggers on the first muon but records all photons received from all muons. The 10% number comes from the average number of muons from showers versus the expected number from neutrinos and the length of time that the detector is recording. In addition, ∼10% of the 10%, or 1%, should have a third coincident event. Because the reconstruction algorithms assume a single muon in the time window, the resulting reconstructed track can be completely and randomly inaccurate.

Therefore, two simulation sets were needed to reproduce the reconstruction problems that would be encountered with the data. Specifically, this analysis used IceCube simulation set 6850 (which became 6937 with offline processing), which included neutrino-induced muon

events with coincident CORSIKA showers (Diplopia setting, NuGen with CORSIKA, zenith angle 0 to 89.99^o), and set 7204 (7260 with offline processing), which included coincident CORSIKA-on-CORSIKA events (Diplopia setting, CORSIKA-on-CORSIKA, zenith angle 0 to 89.99^o). Settings for 6850 included an E^{-2} spectrum, SPICE-MIE Photonics, zenith angle from 1 to 180^o, and neutrino energy range in $\log_{10}(E_\nu/\text{GeV})$ from 1 to 9. Settings for 7204 included the spectrum weighted to the Hörandel poly-gonato (modified) model, SPICE-MIE Photonics, zenith angle range from 0 to 89.99^o, and cosmic ray primary energy from 600 GeV to 10^{11} GeV (or $\log_{10}(E_\nu/\text{GeV})$ from 2.8 to 11).

5.4 Muon propagation

Both the NuGen and CORSIKA programs create muons that must be propagated through the rock and ice. This muon propagation is simulated with the program called Muon Monte Carlo, or MMC [86]. A muon may experience hundreds of interactions while it transits IceCube, and precise simulation of each interaction is important. Written in the Java language, MMC was designed to minimize the error by evaluating multiple integrals for the interaction cross sections along the track in centimeter segments with 10^{-6} accuracy.

Each energy loss mechanism (ionization, bremsstrahlung, pair production, and photonuclear interactions) has a corresponding cross section formula in MMC with expected accuracy to within 1% for muon energies below 10 TeV, although theoretical uncertainties in the photonuclear cross section above 100 TeV are higher [86]. All of the energy loss mechanisms are assumed to have a continuous component and a stochastic component, although the dividing line is superficially created. If the program did not use this dividing line, called E_{cut}, the number of energy loss events would diverge. The continuous component is found by integrating the energy loss from 0 to E_{cut}, and the stochastic component is found by calculating the probability of a large energy loss greater than E_{cut}. A "continuous randomization" process is used to estimate the stochastic effects. Both the muon and secondary particles are propagated using this program. The resulting photons are stored for the next step in the simulation chain [86].

5.5 Photon propagation

The photons that have been stored up to this point must be propagated through the detector volume to determine if they would trigger the PMT in a DOM. Every photon is tracked through the detector medium until it is absorbed by the medium or it intersects with an optical module. The photons are propagated using either the Photon Propagation Code (PPC) or Photonics. These were discussed in Chapter 4. This analysis used the PPC option for photon propagation in NuGen and Photonics in CORSIKA.

5.6 Hit making

Once the photons have been propagated through the detector and their paths determined, the program called Hit Maker then determines whether each photon's path encountered a

DOM along the way, using the established geometry of DOMs within IceCube. The hit is then recorded in the event's "hit series" for use in later steps of the simulation chain. This is also the step where the prepulses, late pulses, and afterpulses are generated, either with Hit Maker or with other modules, and then fed to the PMT Simulator for processing.

5.6.1 Prepulses, late pulses, and afterpulses

Each photon that strikes the photocathode of the PMT creates photoelectrons (PEs). These PEs are then amplified in the dynodes to create a current that is detected by the hardware. However, not all photons interact with the PMT in the expected way. If the photon comes in at a certain angle to the PMT, it will bypass the photocathode and directly hit the first dynode. The result is that the time of flight and the amplification of the charge are reduced. This creates "prepulses" with an abnormally small amplitude occurring early in the event [174]. The simulated amplitude is 1/15 of a standard pulse, with a timing 30 ns early, and accounting for ∼0.7% of all PEs.

Another possibility occurs when a PE trajectory is elastically scattered backwards off the first dynode towards the photocathode, where it turns around and then eventually arrives back at the first dynode to initiate the pulse [199]. These are called "late pulses", which have the expected amplitude but are delayed in time. The simulated delay is 25 to 160 ns, accounting for ∼3.5% of the pulses [174].

Lastly, a PE may interact with a residual gas atom inside the PMT, which ionizes the atom. The original PE is not substantially affected by the interaction, and thus it is amplified normally. The positively charged ion drifts slowly toward the photocathode (its kinetic energy is low due to its larger mass). When the ion strikes the photocathode, many electrons are ejected. These electrons accelerate to the dynodes, causing a larger pulse at a much later time. This is called an "afterpulse." The simulated probability for a PE to create an afterpulse is ∼5.9%, with a time delay ranging from 250 ns to 10,000 ns [174].

These three effects will become important during the simulation, reconstruction processing, and event selection phases in the coming chapters.

5.7 Noise generation

After the photons have been recorded, a program called Noise Generator is called to simulate the noise that is encountered in actual data. This program simulates the random noise that is encountered at all times within the detector. The noise consists of dark noise (thermally-generated electrons), correlated noise (from fluorescence and decays of isotopes in the glass), and sub-threshold muons. The correlated noise is not simulated, but the other sources are. The program accounts for the differences in quantum efficiencies of the normal DOMs and the high quantum efficiency DOMs within DeepCore [174]. The noise hits are recorded in the hit series for later processing stages.

5.8 PMT simulation

In the previous steps, the photon hits and noise were recorded in the hit series. With the PMT Simulator, the response of the PMT to each hit is determined. These are recorded in a "response map", which is then later used to create the waveform that combines all individual photon signals into a continuous response.

5.9 DOM simulation

Once the PMT response is determined, the DOM's hardware response is simulated with a program called DOM Simulator. The timing intervals of the detector's built-in delays, event windows, etc., are used to determine how the DOM would have recorded the event, including the digitization sequence.

5.10 Trigger simulation

This simulator takes all the signals from the DOMs into account before determining if the trigger conditions for data recording were met. The same trigger conditions are required for the simulation as for data coming from the ice.

5.11 Final output

Once the simulation chain is completed, the final output file is written in the same format as the data files. The next step is the reconstruction software and filtering, which is discussed in Chapter 6.

Chapter 6

Data Processing

6.1 Processing introduction

Many steps are required to convert the IceCube PMT signals into a dataset of neutrino events, including both online processing and offline processing. Online processing refers to software that is run at the South Pole in order to perform a rough cut on the overwhelming amount of data that comes from the detector to determine if the event qualifies for transmission to the North. Once the data arrives in the North, offline processing can occur to perform more detailed reconstruction programs. Mass processing of all IC-79 simulation and experimental data was conducted with official software known as std-processing 11-02-00.

If the event meets the overall triggering criteria (Level 0) (discussed in Chapter 4), the first stage of data filtering is performed at the South Pole (Level 1, or online filtering), using basic reconstructions to reduce the overall event rate before the data is transmitted. In the North, the next stage is Level 2, or the start of offline filtering. This stage involves several computer algorithms for basic track and energy reconstructions. The processing for all events has been standardized up to this point and is not specialized for any particular type of physics. However, each event is classified according to whether it meets specific filter requirements. Examples include the Muon Filter, the Point-Source Filter, the Low-Energy Filter, and so on. This chapter will discuss Level 0 through Level 2 processing, including the relevant modules that were specifically used in this analysis. Chapter 7 will cover the remaining levels of processing leading to final event selection, starting with the data from the Level 2-Muon Filter.

6.2 Level 0: Triggers and online processing

The IceCube trigger conditions, including SMT8 (described in Chapter 4), are designed to reduce the trigger rate due to low-level noise and improve the chances of keeping physics events. If triggered, the response of the entire IceCube array (in-ice, IceTop, and DeepCore) is recorded. Then, the Processing and Filtering system runs some simple but fast reconstruction programs to determine if the event qualifies for one of the analysis filters and subsequent recording in the appropriate physics stream. The main programs and algorithms, followed by the output variables used by this analysis, will be discussed.

6.2.1 Feature extractor

The response of the PMT in the DOMs is initially recorded as a waveform, but IceCube reconstruction software requires a list of PEs and their timing. The task of the feature extractor program is to analyze calibrated digital waveforms in the DOMs for the number and arrival times of photons at the PMTs. Feature extraction calibrates the waveforms to known PMT response patterns using a set of algorithms. Then, the waveforms from all overlapping digitizer outputs are unfolded together in terms of basis functions designed from the average response of the combined photomultiplier-amplifier system to an ideally amplified single PE. This provides the best statistical approximation of the times at which incoming photons arrived at the DOM. The algorithms extract the times for single PEs (SPEs) to create a frame object of these times called "RecoHits." In addition, the algorithms extract a series of waveform pulses called "RecoPulses." A RecoPulse is recorded with a leading edge time, a total charge, and a width. PEs that arrive at nearly the same time are assigned to a single RecoPulse [193].

The feature extractor can be run with multiple settings to create a variety of pulse series that are available to the reconstruction software. At processing level 0, the specific feature extractor output used in this analysis was called TWCMuonPulseSeriesReco. The TWC designation stands for time window cleaning, and this action is performed primarily to correct event times where coincident events occur in the same time window. The feature extraction method is important because the choice of pulse series can slightly alter the results of a reconstruction [200].

6.2.2 LineFit

The LineFit program is a basic track reconstruction that uses the simple assumption that the detected light is emitted by a plane wave moving linearly with constant velocity through the detector. The program performs a least squares linear regression on the times of observed pulses, usually restricted to only the first observed PE in each DOM. This rough approximation to the zenith angle is mainly used to determine whether the particle was up-going or down-going. More rigorous (and time-consuming) track reconstructions are performed in later stages, and most of them use LineFit as the seed to find the best-fit track.

6.2.3 SPEFit

SPEFit is short for single-photoelectron fit and is a track reconstruction program that uses a likelihood maximization instead of least-squares. The SPEFit program uses the earliest detected PEs in the DOMs, just as LineFit does, but SPEFit corrects the timing to include uncertainty. In LineFit, the program uses only the time of the first PE, despite the fact that the DOM's distance from the actual muon track will cause a spread in the PE timing distribution due to scattering. SPEFit uses a Pandel Function to model the timing distributions more accurately. Due to uncertainties in the DOM timing calibration and timing output of the feature extractor, the timing distribution may be too early when compared to the speed of light timing that the program expects, which causes the Pandel Function to break down. Accounting for the timing uncertainty in the model can be achieved by convolv-

ing the Pandel Function with an additional Gaussian term for the timing uncertainties [201]. Then, SPEFit performs a likelihood analysis based upon a given seed track (usually LineFit) to determine the most likely track to fit the corrected timing PDFs. The fit can be run with one or multiple iterations, and thus SPEFit4 would indicate four iterations, where each step uses the output of the previous step as the seed and in principle would improve the reconstruction at each step. If the final SPEFit likelihood (SPEFit LLH) value is large, then the event is likely well-described by the fit. SPEFit is typically used as an intermediate track fit on the way to more rigorous track reconstructions in later levels.

6.2.4 NCh

The number of DOMs that are launched in an event is called NCh, or the number of channels. NCh can be used as a simple energy proxy, with more DOMs launching for higher-energy events. However, NCh does not take into account the dust layers and hence the lower numbers of DOM launches when the track traverses these layers. It also does not take into account if the event clips the edge of the detector.

6.2.5 Qtot

This variable is calculated by integrating the total charge of the PEs from both HLC and SLC triggered DOMs. Like NCh, it can be used as a simple energy proxy but with the same limitations due to dust layers and edge-clipping events.

6.2.6 Time residual window

Some event variables are designated by the time residual window used to count the hits received by the DOMs. For example, NDirA is NDir (described below) with a time residual window of [-15 ns, +15 ns]. B has a time window of [-15 ns, +25 ns]. C has a time window of [-15 ns, +75 ns]. D has a time window of [-15 ns, +150 ns]. E has a time window of [-15 ns, +250 ns]. For this analysis, a time window of [-15 ns, +200 ns] was used, unless otherwise noted.

6.2.7 NDir

The event variable NDir is the number of direct hits in the event, where a direct hit is defined to have a specific range of time residuals in the DOM (time-residual window), measured from the time of first hit (which is defined as time residual = 0 ns). An event with low NDir means that the photons from the event were not very direct, possibly from a low-energy event or an event track that only clipped the edge of IceCube.

6.2.8 LDir

The event variable LDir is the length of the projection along the reconstructed track of all direct hits NDir in the event. In other words, when the perpendicular location of each DOM along the reconstructed track is plotted, LDir is the distance along the track between

the furthest two points. This variable is calculated by projecting the direct hits (there are NDir of them in the event) along the reconstructed track direction and taking the distance between the earliest and the latest of these hits. An event with low LDir means that the projected track was not very long, possibly from a low-energy event, an event track that only clipped the edge of IceCube, or a cascade.

6.2.9 SDir

The smoothness, called SDir, looks at the direct hits NDir that are projected on to the reconstructed track and calculates how smoothly spaced the projected hits are. A smoothness SDir of 0 has projected direct hits that are evenly spaced, while a value closer to +1 or -1 has the projected direct hits clumped on either end of the track.

6.3 Level 1: Online filters

The data for this analysis came from the IceCube Muon Filter [202], which was designed to select events that were likely to be muon tracks. Because of the large percentage of down-going tracks and the need to reduce the data load for later processing, the Muon Filter was defined in terms of two angular regions, the up-going region and the down-going region.

First, a general cut was performed. If the event's LineFit zenith angle was less than 70^o, an additional cut kept events with NCh $\geq$ 10. Then, the SPEFit was performed on the remaining events, using the LineFit zenith angle as the seed.

For the up-going region (defined as SPEFit zenith angles $> 78.5^o$), a cut in the quality of the track was performed to reduce the number of misreconstructed tracks. This quality parameter was defined as (-SPEFit LLH)/(NCh - 2), and a cut was applied for values ≤ 8.1.

For the down-going region (defined as SPEFit zenith angles $\leq 78.5^o$), two possibilities existed for event cuts. Both cuts used Qtot and SPEFit zenith angle. For zenith angles $\leq 60^o$, events were kept if $\log_{10}$(Qtot) $\geq$ (0.6 $\cdot$ (cos(SPEFit.zenith) - 0.5) + 2.5). For zenith angles $> 60^o$, events were kept if $\log_{10}$(Qtot) $\geq$ (3.9 $\cdot$ (cos(SPEFit.zenith) - 0.5) + 2.5). The result of these cuts is that only the higher-energy down-going events would be kept. Later, more detailed reconstructions would be performed to see if any of those events had been misreconstructed and were actually up-going signal events.

Once the cuts were completed in this level, the events that met the Muon Filter were identified in the data stream that was transmitted to the North. With the events safely transferred and stored, the Level 2 processing could begin.

6.4 Level 2: Offline processing

The offline processing for this analysis was the Level 2-Muon processing. The steps are described in detail in the following sections.

6.4.1 NewFeatureExtractor

At the start of this processing, a more complete feature extraction of the waveforms called NewFeatureExtractor (NFE) was performed using more complex algorithms. NFE employs multiple algorithms for the same event, choosing an appropriate algorithm according to the waveform's complexity, while the simpler feature extractor in Level 0 only used one waveform algorithm per event [200]. The specific feature extractor outputs used in this analysis were called TWSRTOfflinePulses and TWNFEMergedPulsesHLC. TW is a alternate abbreviation for time window cleaning (TWC). SRT stands for SeededRTCleaning, which is described below. NFE also had the option to include or exclude DeepCore DOMs, for specific reconstruction needs. The pulse series name would have a suffix of _NoDC if DeepCore was excluded and _DC if DeepCore was included. The reconstructions in this analysis used both of the DeepCore options.

6.4.2 SeededRTCleaning

SeededRTCleaning is a program that allows SLC hits to be included in the pulse series, if they meet certain radius (R) and time (T) conditions. First, the module starts with the locations and times of the HLC hits. Then, the module looks at any SLC hits that meet the RT conditions as selected by the user. In the case of this analysis, the settings were less than 150 m radius and within 1 ms of the HLC hit. The module then compares the hit time of each SLC hit to a hypothesis that the light from the HLC DOM traveled at the speed of light to reach the SLC DOM. If the SLC DOM's time and radius meet the criteria, then the SLC hit is kept in the SLC pulse series. The overall goal of this module is to reduce noise in the SLC pulse series that is used later in reconstructions [203].

6.4.3 Track reconstructions

Using the new hit series and pulse series from this processing level, LineFit was reaccomplished, followed by SPEFit. After this, the additional track reconstruction algorithms were run using these outputs as seeds. These included SPEFit32, the Bayesian reconstruction, Split Bayesian, and MPEFit.

6.4.3.1 Bayesian reconstruction

The Bayesian reconstruction uses SPEFit32 as the seed. In this reconstruction, a down-going event that was mis-reconstructed by SPEFit might be reconstructed correctly if the seed is assumed to be down-going and if the fit direction is weighted according to the known distribution of cosmic ray directions using a Bayesian statistical technique. Figure 6.1 shows the Bayesian prior, which is based upon the amount of matter that an event would have to traverse to arrive at the detector. Thus, a down-going event with zenith angle of 0^o would have a Bayesian prior near 1, while all up-going events would have an extremely small Bayesian prior. If an event is reconstructed accurately, then both reconstructions (SPEFit32 and Bayesian) will have the same parameters, and the only difference will be the change in the likelihood due to the prior.

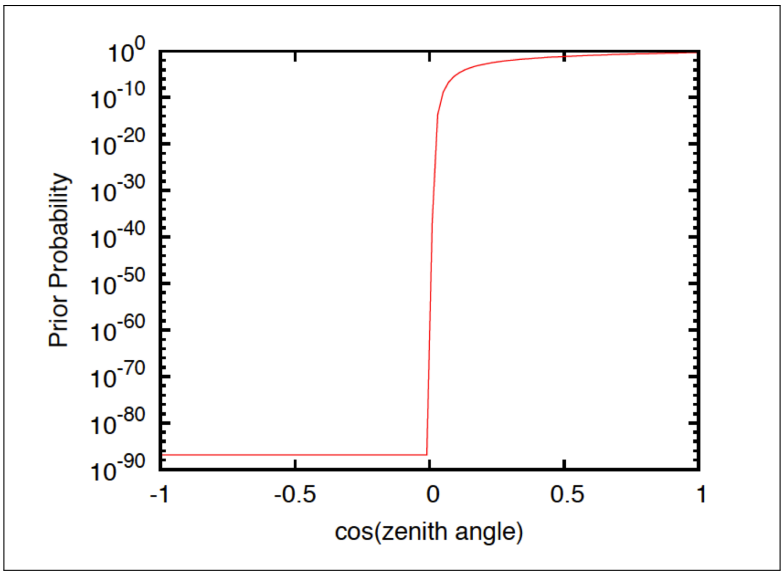

Figure 6.1: Bayesian prior used to weight the directions to the cosmic ray spectrum. Up-going directions are heavily penalized while down-going directions are less penalized as they approach the vertical direction. From [204].

6.4.3.2 Split Bayesian

The Split Bayesian reconstruction was run with the assumption that each event was a two-muon combination and therefore split the event while retaining the Bayesian weight for the fit direction. Each muon hypothesis was then reconstructed using SPEFit16. This reconstruction sought to improve the accuracy of the output track by separating potentially coincident events.

6.4.3.3 MPEFit

The MPEFit is the multiple-photoelectron (MPE) version of SPEFit, using SPEFit32 as the seed. MPEFit was run on the HLC pulse series alone and also the HLC/SLC pulse series. MPEFit was the preferred track reconstruction for this analysis, although other track fits were also used at various points in the event selection process, which will be discussed in Chapter 7.

6.4.4 Track quality parameters

Since the MPEFit is a maximum likelihood calculation, some additional track quality information can be extracted from the likelihood calculation. One parameter is the Paraboloid Sigma, and the other is the reduced log likelihood, or RLogL.

6.4.4.1 Paraboloid Sigma

Paraboloid Sigma is a parameter for estimating the uncertainty in the likelihood function used in track reconstructions. This can be used to determine the error in the reconstruction

of the zenith angle and the azimuth angle. The module is called I3ParaboloidFitter, and the region of the likelihood space around a given track reconstruction for a particular confidence level (usually 68%) can be approximated with a paraboloid. The elliptical cross-section of the paraboloid is then determined, and the lengths of the axes for the ellipse are averaged to create a reconstruction quality parameter called the Paraboloid Sigma. A large Paraboloid Sigma would indicate a large uncertainty in the track reconstruction and thus low quality.

6.4.4.2 Reduced log likelihood

The reduced log likelihood, or RLogL, is a parameter that allows the comparison of track reconstructions across events. The term "reduced" means that the logarithm of the likelihood has been normalized by dividing it by the number of degrees of freedom in the fit. The degrees of freedom are calculated by taking the number of data points used in the fit (usually NCh) and subtracting the number of fit parameters (5 for tracks). The RLogL can be used as a quality measure of the fit.

6.4.5 Photorec energy reconstruction

The last step in Level 2-Muon processing is the Photorec energy reconstruction. Photorec uses the MPEFit track to calculate the energy of the muon using Photonics tables. The program first adds up all the PE detected in the event. Then, using the MPEFit track, the program calculates how many PE would have been seen by the DOMs along that track for a constant energy loss of 1 GeV/m, equating to a muon energy of $\sim$1 TeV. It does this by accessing the Photonics tables for the preferred ice model and adding up the PE that should arrive at the DOMs. By dividing the actual PE by the expected PE for a known energy loss, the multiplicative factor is found. Because the energy loss is approximately linear with energy, the multiplicative factor represents the energy of the muon in TeV. This method provides a rough-estimate of the muon energy, but the method is susceptible to errors from large stochastic energy losses, which will skew the result towards higher energies [191].

Chapter 7

Event Selection

7.1 Introduction

This analysis began the event selection process with events from the Level 2-Muon Filter from standardized IceCube processing, as described in Chapter 6. The reason to start here instead of with the available Level 3-Muon sample was to use additional reconstruction software tools that were developed in the years after the original Level 3 processing in order to improve event selection. Thus, the newer programs were applied in a modified version of the Level 3 processing, and the subsequent event selection methods are described in this chapter.

Because IceCube records an enormous amount of data daily, a sophisticated data selection method was required to find a pure sample of up-going neutrinos for this analysis. Data selection was performed according to simple guidelines: (1) cosmic ray air shower contamination must be minimized, and (2) events with higher observable energies should be preserved. The event selection for this analysis was developed by Christopher Weaver at the University of Wisconsin-Madison in the IceCube collaboration for his analysis [204] with results published in [205].

7.2 Overall data rates

The overall results of the data selection process are shown in Table 7.1. They include the Level 2-Muon Filter and the subsequent levels of event selection in this analysis, which are discussed in the next sections. Background events from cosmic ray air showers were reduced such that they comprised only $\sim$0.1% of the final data.

7.3 Level 3: Pre-cuts

The first step in the event selection process involved the pre-cuts, called Level 3. The variables that were used in the pre-cuts were as follows (see Chapter 6 for specifics): (1) zenith angle of MPEFit; (2) Qtot (excluding DeepCore strings); and (3) the "charge-weighted distance." The charge-weighted distance is a new parameter that is calculated by summing

Table 7.1: Comparison of data rates after each of the event selection levels. Conventional neutrinos were reduced to 32,761 events in the final sample, and approximately 24% of the astrophysical and prompt neutrinos were retained (assuming an E^{-2} astrophysical index and ERS prompt expectations), with only 0.1% background contamination. Percents are in relationship to the detector trigger level [204].

Cut level	Air shower background		Conventional ν		Astro+ prompt	Data
	Rate (Hz)	Number of events	Rate (Hz)	Number of events	Percent remaining	Rate (Hz)
Level 2-Muon Filter	32.6	$1.86\text{x}10^{9}$	$1.17\text{x}10^{-2}$	666,672	93.2%	32.6
Level 3-Precuts (7.3)	10.6	$6.04\text{x}10^{8}$	$9.13\text{x}10^{-3}$	520,061	89.7%	10.6
TrackFit zenith (7.8.1)	3.88	$2.21\text{x}10^{8}$	$8.08\text{x}10^{-3}$	460,403	68.8%	3.9
Track quality (7.8.2)	$4.59\text{x}10^{-4}$	26,130	$1.36\text{x}10^{-3}$	77,248	31.3%	$4.6\text{x}10^{-4}$
LLH comparison (7.8.3)	$1.66\text{x}10^{-4}$	9,463	$1.12\text{x}10^{-3}$	63,797	28.6%	$1.7\text{x}10^{-4}$
NCh directional (7.8.4)	$2.01\text{x}10^{-6}$	115	$5.75\text{x}10^{-4}$	32,784	23.8%	$5.8\text{x}10^{-4}$
SplitFits+NDirC (7.8.5)	$5.56\text{x}10^{-7}$	32	$5.75\text{x}10^{-4}$	32,761	23.8%	$5.8\text{x}10^{-4}$

up each DOM's perpendicular distance from the track, multiplied by the charge detected in the DOM, and then divided by the total charge detected. This term should be small for well-reconstructed tracks, since most of the charge is located close to the true track. The charge-weighted distance used the pulses named TWSRTOfflinePulses_NoDC and the track reconstruction named MPEFit_SLC.

The first Level 3 pre-cut was similar to that used in the Level 2-Muon Filter, but using the higher-quality MPEFit track instead of the rougher LineFit track. Events were kept if cos(zenith) $>$ 0.2 (78.5^{o}) and if $\log_{10}(\text{Qtot}) \geq 0.6 \cdot (\cos(\text{zenith}) - 0.5) + 2.5$. For the second pre-cut, events were kept for cos(zenith) $<$ 0 (up-going) if the charge-weighted distance was less than 200 meters (well-reconstructed) or the total charge was greater than 100 PE (higher-energy). If cos(zenith) was between 0.0 and 0.2, no cuts were performed in this step.

These conservative cuts were intended to remove only the lowest energy events, which were not applicable to this analysis. The first cut reduced the background rate but did not significantly impact the signal rate because eventually only the events with cos(zenith) $<$ 0.0 would be used in the analysis. The events with more horizontal zenith angles were kept in these earlier levels because it was possible that a signal event was misreconstructed with a track above the horizon, and reconstructions in subsequent levels might correct this.

The output of the Level 2-Muon Filter was expected to include up-going (signal) conventional neutrinos at a passing rate of 1.17 x 10^{-2} Hz (93%) and down-going (background) air showers at a rate of 32.6 Hz, estimated from simulation studies. After the Level 3 pre-cuts, the overall data rate was reduced to 10.6 Hz while keeping 520,000 conventional neutrinos (which still included lower-energy neutrinos) and 90% of the astrophysical and prompt neutrinos.

7.4 Level 4a: Event splitter

The next assumption was that many of the remaining background events were coincident events. Because of the high rate of down-going muons created in the cosmic ray showers, there is a sizable probability that the track of a down-going muon will coincide with a rare up-going muon track from a neutrino, and both tracks will be recorded at the same time in the same event. Track reconstruction algorithms that are used on these coincident events usually perform poorly. Therefore, events which passed the pre-cuts were sent through an event-splitting program called TopologicalSplitter. The splitter performs poorly when analyzing events with random noise in the pulses. Therefore, the pulse cleaner called SeededRTCleaning was used on the pulse series before running the splitter (see Chapter 6).

TopologicalSplitter is designed to separate coincident tracks. The program recognizes the spatial or temporal separation of the DOM hits and can split the event into two or more distinct events, as needed. A small optimization study was performed using simulation that contained neutrino-induced events with coincident cosmic ray showers (CORSIKA set 6937), coincident CORSIKA-on-CORSIKA events (CORSIKA set 7260), and single muons from neutrino interactions (NuGen set 6726, E^{-2} spectrum). For each event, the actual number of particles in the event was compared with the number of sub-events produced by the splitter. In a perfect world, these numbers would be the same. The settings were chosen to give the highest percentage of correct splittings for particles in the energy range of this analysis.

Additionally, sometimes the TopologicalSplitter algorithm placed a group of afterpulses (late hits in the DOMs, see Chapter 5) into their own subgroup in the split output. This was not a serious problem overall, especially since afterpulses are relatively rare, but future cuts were planned on the number of PEs and number of DOMs that were hit in the event. A simple algorithm was created to identify sub-events that consisted mainly of afterpulses. Therefore, if at least 75% of the pulses overlapped between the afterpulse sub-event and the main event, the afterpulse sub-event was ignored, and the main event was kept. Another characteristic of an afterpulse sub-event is that it should have pulses at a later average time than the main event. A simple condition required that the mean pulse time of any sub-event should be at least 3 ms later than the mean pulse time of the main event. Finally, an afterpulse tends to have a higher output charge, typically about 5-10% as much charge as the main pulses. The end result of applying this set of criteria was conservative, since an afterpulse sub-event was always flagged as an afterpulse, and the rate of incorrectly flagging sub-events as afterpulses was less than $\sim$1%.

7.5 Level 4b: Best track

After applying the splitter, the events were reprocessed through the reconstruction algorithms because the original reconstructions were performed on the full sets of pulses that had been split. If an event did not experience any splitting, the original reconstructions were used in this step. The track reconstructions were performed in sequence, using the previous track result as the seed for the next reconstruction. This list included LineFit, SPEFit, SPEFit4, and finally MPEFit.

After this reprocessing, the "best" successful track fit was selected for each event. First choice was MPEFit_TT, where TT designates the track reconstruction using the split pulses. If not, then the next choice was SPEFit4_TT. If not, then the next choice was SPEFit_TT. Finally, if all previous fits did not succeed, the last choice was LineFit_TT. This best fit was then labeled "TrackFit" in the data frame, for later use in calculations and cuts.

7.6 Level 4c: Intermediate cuts part 1

After splitting and reprocessing, more cuts were applied to further reduce the data rate. An analysis of the effect of these cuts was performed to ensure that no events were removed which were not also removed by the more strict cuts of the next level. These cuts continued to clean out events with energies that were too low for this analysis. Events were kept if they met all of the following conditions:

At least one likelihood track fit succeeded (TrackFit = MPEFit, SPEFit4, or SPEFit, but not LineFit)

TrackFit cos(zenith) < 0.2 (horizontal or up-going)

NChan ≥ 15 (a minimum number of DOMs were hit, excluding DeepCore)

NDir > 6 (a minimum number of direct hits within the time window, including DeepCore)

LDir ≥ 200 meters (projected length along track between first and last hit DOM, including DeepCore)

abs(SDir) < 0.6 (event hits not clumped at either end of the track, including DeepCore)

7.7 Level 4d: High-quality track processing

Next, the more intensive track reconstructions were performed. The reconstructions in this step used the best track stored in TrackFit and the pulses from TTPulses (which were split by the TopologicalSplitter). These new parameters were used as cut variables in the next level: I3IterativeFitter, I3ParaboloidFitter, and I3ResponseMapSplitter. I3IterativeFitter is a directional reconstruction with a Bayesian prior that assumes that events should be distributed like background cosmic rays in zenith angle. The I3ParaboloidFitter uses a profile likelihood estimate of the reconstruction error of the final MPEFit to create the Paraboloid Sigma. I3ResponseMapSplitter treats the event as if it contained a pair of muons, in case the TopologicalSplitter algorithm had failed for that event, using both the time splitter mode and geometric (space) splitter mode.

7.8 Level 4e: Intermediate cuts part 2

Once the Level 4d track processing was completed, another set of cuts was performed before processing the data through the time-intensive energy reconstructions in the next level. The cuts up to this point were relatively loose to retain as much of the signal as possible. Analysis of the remaining simulation events showed that there was still a significant number of background muons in the sample. These cuts were designed to decrease the background before the energy reconstructions. The cuts (without DeepCore DOMs) are as follows (each cut is discussed below):

TrackFit cos(zenith) < 0.1

TrackFit RLogL $<$ -42.97 $\cdot$ (corrected Paraboloid Sigma) + 8.6

TrackFit RLogL $<$ -5 $\cdot$ (corrected Paraboloid Sigma) + 7.625

Comparison of the log likelihood values for two different track fits

NCh ≥ 30 for up-going events

NCh $\geq 30 \cdot \exp(17.0 \cdot \cos(\text{zenith}))$ for down-going events

Comparison of NDir for the reconstructions on the geometric-split pulses from SplitFits

Comparison of NDir for the reconstructions on the time-split pulses from SplitFits

7.8.1 TrackFit cos(zenith)

The inclusion of events with TrackFit cos(zenith) > 0.0 (above the horizon) originated from the initial analysis by Weaver (who used events above the horizon in his analysis). Keeping these events allowed for comparisons of other cut parameters that helped in removing background events in the up-going sample. The overall background rate improved to 3.88 Hz while keeping 460,000 conventional neutrinos and 69% of the astrophysical and prompt neutrinos.

7.8.2 Corrected Paraboloid Sigma and RLogL

Paraboloid Sigma and RLogL (see Chapter 6) are measures of track reconstruction quality. In theory, Paraboloid Sigma is a good description of the statistical angular uncertainty of the track reconstruction. In reality, the actual reconstruction error does not agree with the computed Paraboloid Sigma because the likelihood function is not completely accurate. The parameter does have a strong correlation with the actual error, but a correction was required to achieve agreement with the actual error. This led to the "corrected Paraboloid Sigma," which was created during this level of processing. A correction function was determined by

manually comparing the ratio of the mean Paraboloid Sigma to the mean true error. The correction that was used in this analysis is shown in Figure 7.1. The corrected Paraboloid Sigma had a more consistent interpretation for events of all energies, which made it easier to use as a data selection parameter.

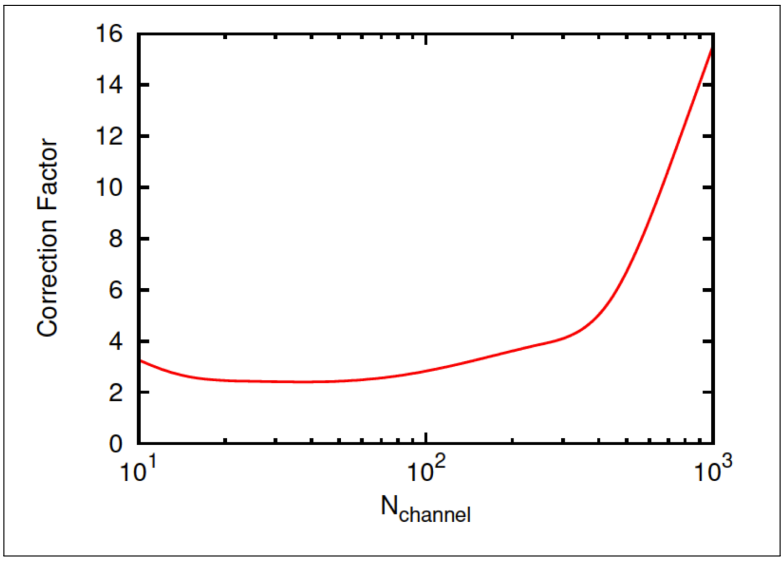

Figure 7.1: The correction function that was applied to Paraboloid Sigma to create the corrected Paraboloid Sigma parameter used in later event selection stages. From [204].

For most of the events, MPEFit was chosen as the best fit in TrackFit, which meant that RLogL was calculated mainly on MPEFit. On the other hand, Paraboloid Sigma (and corrected Paraboloid Sigma) was always computed using the MPEFit likelihood. Plotting these parameters in two dimensions provided a more powerful cut parameter than one-dimensional cuts. An optimization study was performed to find the best cut parameters to maximize the ratio of signal to background. As shown in Figure 7.2, the values of Paraboloid Sigma and RLogL for simulated background (cosmic ray) events are larger (worse) than for signal (neutrino) events. By cutting on small values of both variables, the majority of the surviving background events were eliminated. The overall background rate improved to 4.6 x 10^{-4} Hz while keeping 77,000 conventional neutrinos and 31% of the astrophysical and prompt neutrinos.

7.8.3 Log likelihood comparison

The two tracks that were used in the log likelihood comparison were SPEFit4_TT and TrackFitBayesian. The latter was created in the most recent level of track reconstructions using I3IterativeFitter with a Bayesian prior that approximately matched the known distribution of cosmic ray arrival directions.

The likelihood values of the two fits were compared. For a true up-going event, if the up-going reconstruction (for example, SPEFit4_TT) had a substantially better likelihood than the down-going fit (TrackFitBayesian), it was assumed that the up-going fit was more correct. For true down-going events, the situation was modified because of the prior. For

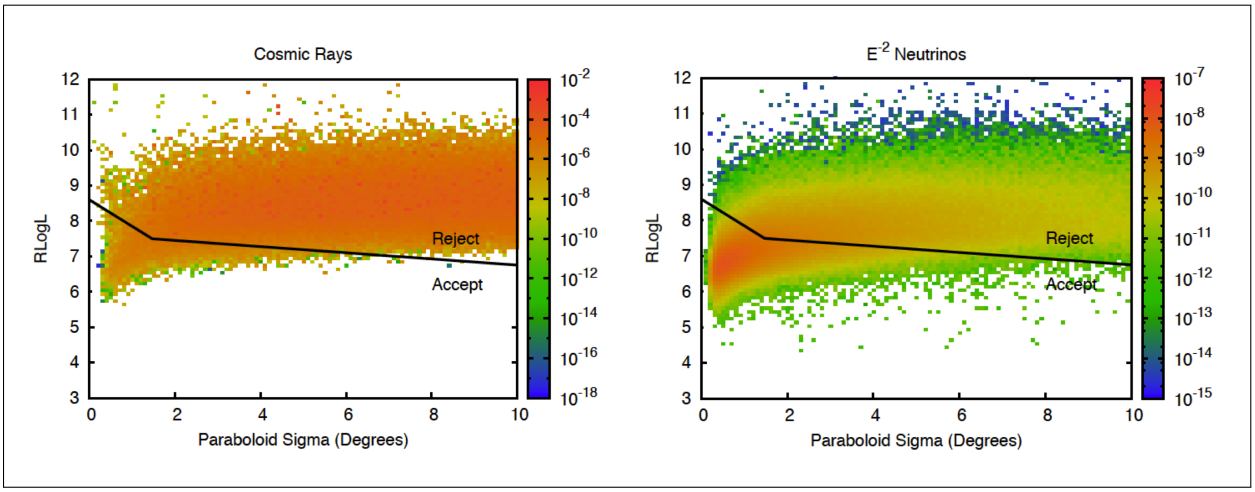

Figure 7.2: (left) Distribution of cosmic ray (background) events for RLogL vs corrected Paraboloid Sigma values. Black line designates the cuts performed. (right) Distribution of neutrino (signal) events for RLogL vs corrected Paraboloid Sigma values. Black line designates the cuts performed. From [204].

a well-reconstructed event, the two fits would have roughly the same direction but different likelihood values because of the Bayesian prior. Therefore, a down-going event was considered to be well reconstructed if the difference between the fit likelihood values was nearly equal to the value of the prior for that particular reconstructed zenith angle. For up-going events, the difference between the log likelihood values must be at least 33 to make the final cut. The overall background rate improved to 1.7 x 10^{-4} Hz while keeping 64,000 conventional neutrinos and 29% of the astrophysical and prompt neutrinos.

7.8.4 NCh

Many air shower events still remained in the sample at this point. Before proceeding with another splitting and track reconstruction level, the cut on NCh listed above was used for up-going and down-going events. The cut eliminated virtually all of the air showers but attempted to preserve the more horizontal events for comparisons in later cuts. The overall background rate improved to 2.0 x 10^{-6} Hz while keeping 33,000 conventional neutrinos and 23.8% of the astrophysical and prompt neutrinos.

7.8.5 SplitFits and NDirC

Very few simulated air shower events remained in the sample at this point. However, some of the remaining events were actually misreconstructed coincident muon bundles that had survived the splitter and all attempts to eliminate the poor track fits. For the next step, a very old IceCube technique named SplitFits was used, and then the number of direct hits (NDir) were counted within the time interval [-15 ns, +75 ns] from the track, creating the variable NDirC.

Each event was split into two halves using two different techniques. The first technique

involved dividing the observed pulses at the median time (Time Split), and the second technique involved dividing the pulses geometrically (Geo Split), using a plane through the center of gravity of the pulses and perpendicular to the MPEFit track. Then the reconstruction algorithms were run on the resulting sub-events. The Time Split mode assumes that one muon passed through the detector before the second entered. The Geo Split assumes that two coincident muons were separated by distance, and thus splitting the combined MPEFit track in half might separate the two sets of pulses to permit separate reconstructions. The algorithms are relatively simple and have been replaced by more sophisticated algorithms in IceCube, but this splitting algorithm is relatively fast.

Each sub-event was then reconstructed using LineFit and the iterated SPEFitX, for X=1, 4, 16, and 32 (MPEFit was not run because of computational time). A new NDirC value was calculated for each sub-event and reconstruction. The sum of the NDir values for the halves would be significantly larger than the NDirC value of the whole event if the event was misreconstructed from two or more tracks. A well-reconstructed single track would also show an increase in the new NDirC value because of the new time windows, but rarely did the sum go above a factor of two larger. If the sum of the new NDirC values was greater than twice the original NDirC, the event most likely consisted of two separate tracks. This final cut on the ratio of $\sum$(new NDirCs)/(original NDirC) > 2 eliminated a large portion of the remaining air shower background events. The overall background rate improved to 5.56 x 10^{-7} Hz while keeping 32,761 conventional neutrinos and 23.8% of the astrophysical and prompt neutrinos.

7.9 Level 4f: Energy reconstructions

Once the event samples were cleaned of most of the background events, the more intensive energy reconstructions were performed. These included updated versions of MuEx and TruncatedEnergy, both of which were not available during the standard Level 3-Muon processing of IC-79. Both reconstructions were run in order to cross-check fit results from two different energy reconstruction methods. No further cuts were performed in this level.

7.9.1 MuEx

The likelihood-based energy estimator MuEx uses an analytic approximation for the observed light distributions and includes specific details of the ice model such as ice layering. The expected number of detected photons is estimated by photon distribution functions of muon energy assuming a roughly linear relationship. The technique lessens the effects of stochastic energy losses but does not account for them completely. The energy from MuEx is roughly equivalent to muon energy near 1 TeV, but the algorithm does not perform as well at other energies because the linear relationship does not take into account DOM saturation (high energy) or ionization-dominant losses (low energy) [206; 193]. Figure 7.3 compares MuEx output to true muon energy for the simulated events used in this analysis. Most of the event distribution is off axis, making the method less than ideal as a muon energy reconstructor for this analysis, although the method was used in other IC-79 analyses [204]. This analysis needed a method whose output more closely represented the true muon energy.

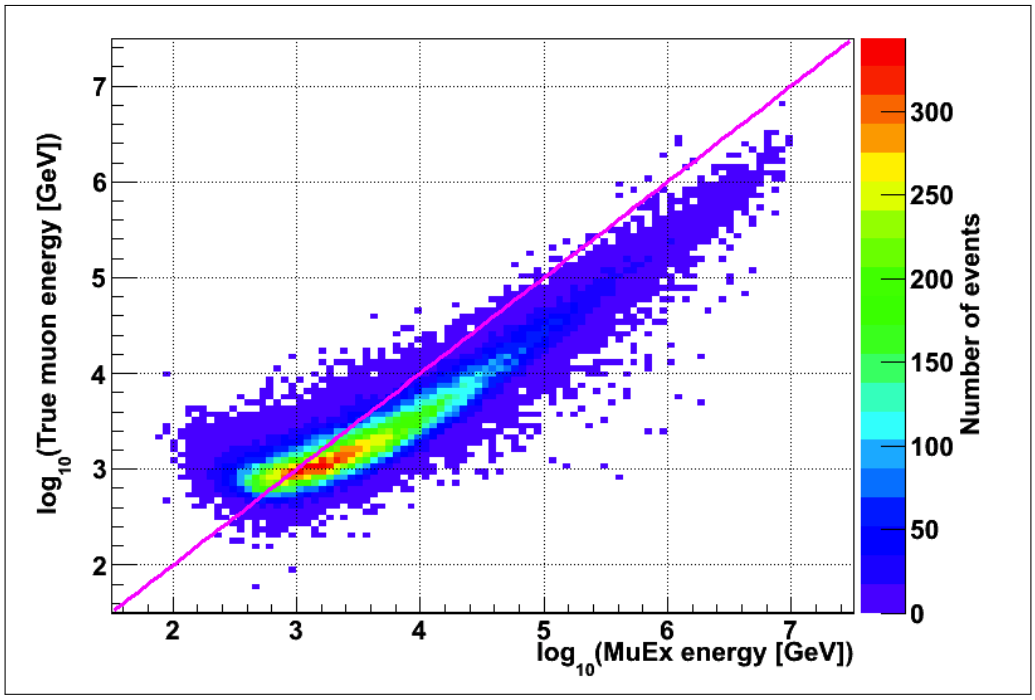

Figure 7.3: Comparison of reconstructed muon energy from MuEx versus true muon energy from simulation. The magenta line is 1:1 correspondence, indicating agreement between reconstructed energy and true energy. The reconstructed muon energy is overestimated at the lower energies and underestimated at higher energies.

7.9.2 TruncatedEnergy

As was mentioned in Chapter 6, the Photorec $\langle dE/dx \rangle$ reconstruction method has a rather large uncertainty in the energy calculation at the higher energies of this analysis. The large uncertainty was the motivation behind finding a new muon energy reconstruction method. For $E_\mu > 1$ TeV, muons lose most of their energy stochastically, and a small number of high-energy interactions will not only skew the mean but also enlarge the spread in $\langle dE/dx \rangle$ values. In order to proceed with this analysis, an improved method for calculating the muon energy was needed.

A new method based upon the truncated mean was developed and systematically applied to the energy measurement of high-energy muons. The program was named TruncatedEnergy, and a full description of the method is located in the journal article in Appendix A [207]. The idea was also proposed by K. Mitsui in 1992 in regards to the then-upcoming DUMAND experiment, extrapolating data from Mutron [208].

Instead of calculating the muon $\langle dE/dx \rangle$ over the entire observed muon path length as in Photorec, the path is divided into independent segments, or bins. A $\langle dE/dx \rangle$ value is calculated separately for each bin. Then, the bins with the highest $\langle dE/dx \rangle$ values are discarded before calculating a new $\langle dE/dx \rangle$ for the event, thus producing a truncated mean. The binning can be performed by distance in the detector (called the BINS method) or by

using each DOM as its own bin (the DOMS method). Thus TruncatedEnergy-DOMS would be the DOMs method of binning, and this method for chosen for this analysis because it had the best reconstruction uncertainty throughout the energy range.

This energy method is successful because the truncated mean minimizes the effects of the large stochastic losses which would otherwise skew the mean and enlarge the spread. Figure 7.4 shows a 10 TeV muon event passing horizontally through IceCube and the characteristic stochastic energy losses along the track. The truncated method resulted in a 25% improvement in the muon energy resolution. The performance of TruncatedEnergy will be discussed later in this chapter.

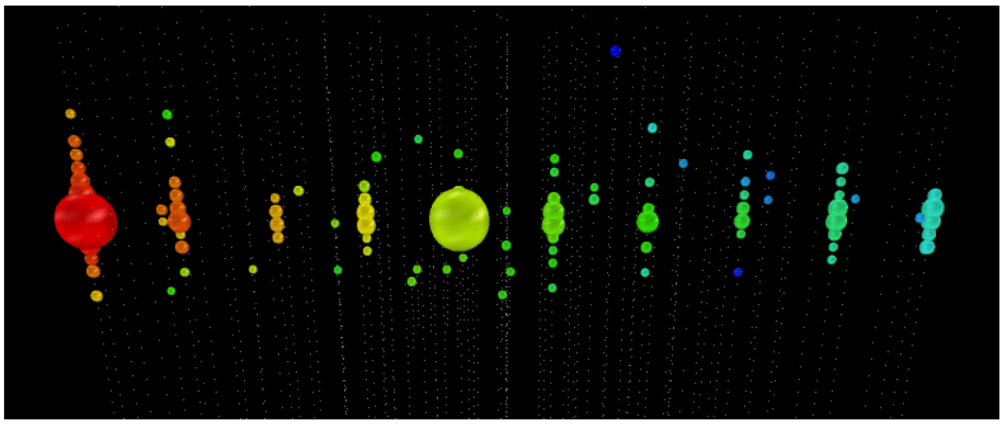

Figure 7.4: Simulated muon event at 10 TeV, demonstrating the stochastic nature of the energy losses along the track. Dots represent individual DOMs, and sizes of DOMs represent the number of photons received. Red indicates earlier hits, while blue represents later hits. The muon track is horizontal from left to right across the strings of IceCube. Large losses occurred in the vicinity of the first and fifth strings in this event.

7.10 Effective areas

At this point, the effective areas for the muon neutrino were examined, comparing the distributions to previous IceCube data years to ensure the data selection methods were in relative agreement. Figure 7.5 shows the effective areas.

7.11 Level 5: Final analysis cuts

The simulation and data sets contained lower-energy events and horizontal events after the final cuts at the end of Level 4. For this analysis, the final event cuts were performed, keeping the events with TruncatedEnergy-DOMS muon energy > 1 TeV and TrackFit zenith $> 90^o$. This provided the higher-energy sample of up-going events needed for the cross-section determination. From here, the events were prepared for the fitter, which is the subject of Chapter 8.

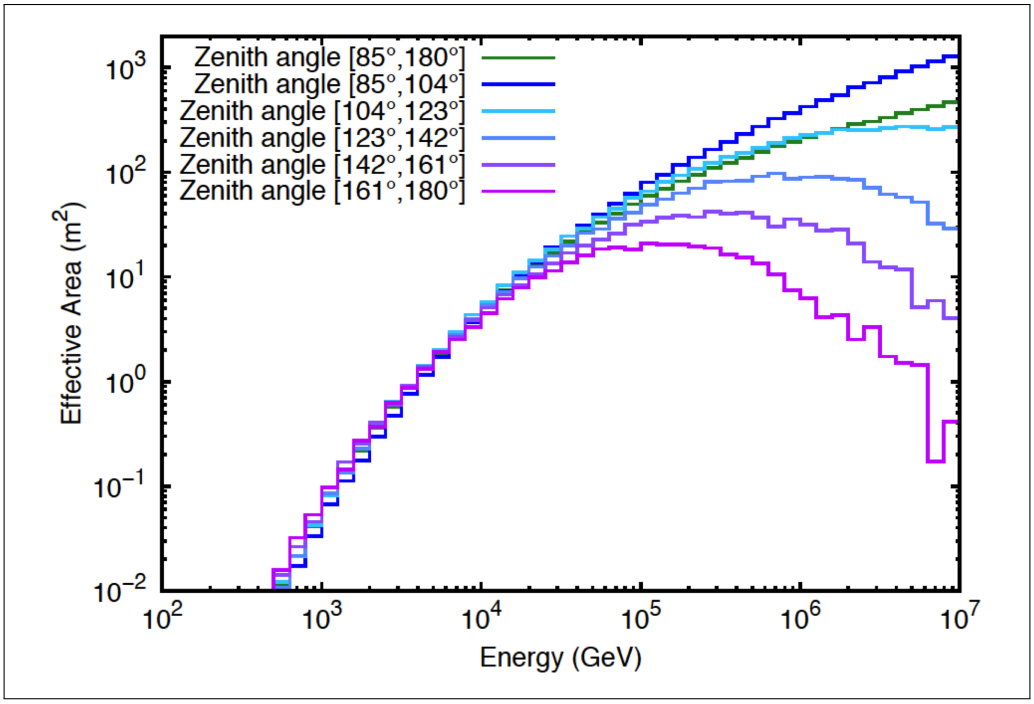

Figure 7.5: Neutrino effective area comparing energy for several zenith angle ranges. Effective area decreases for increasing zenith angle at high energy. From [204].

7.12 Comparison of data to simulation

An initial comparison of data to simulation was made to cross-check the output of the event selection process, as shown in Figure 7.6. The total number of data events with TruncatedEnergy-DOMS $>$ 1 TeV and TrackFit-zenith $>$ 90 degrees was 10,784 events. The total number of simulated events predicted with nominal fluxes and a XS value of 1.0x SM was 10,119 events. Of this number, approximately 96 events (0.9%) were expected from astrophysical neutrinos (assuming an E^{-2} flux), and 72 events (0.7%) were expected from prompt neutrinos (assuming ERS). Although this analysis used a two-dimensional fit for the final result, the initial one-dimensional energy distribution was in good agreement with the data, while the zenith angle distribution was not. A normalization constant could be used to allow simulation to agree with data, and the one-dimensional distributions would be in better agreement with the data. The assumption was that the simulation was accurate and the normalization would be accounted for with the fitter parameters. Although the data and simulation were not initially consistent, when systematic uncertainties were taken into account, the agreement improved to well within errors.

7.13 Track angular resolution

With the final dataset in hand, track reconstruction accuracy was checked, using simulation. The results for the angular resolution are shown in Figure 7.7. The plot shows the difference between the true and reconstructed tracks, versus reconstructed muon energy. For

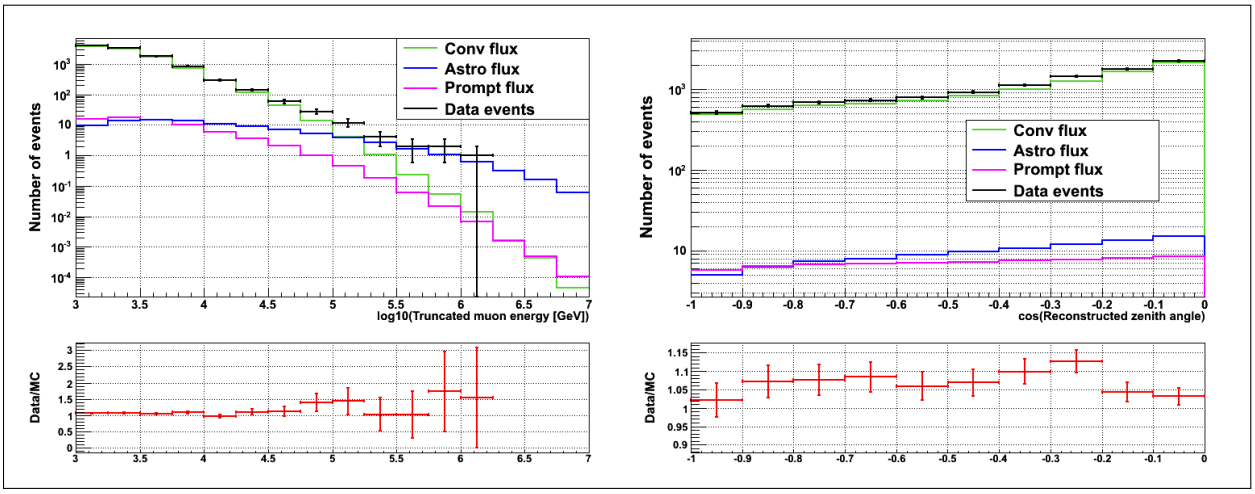

Figure 7.6: Initial comparison of data to simulation for $\log_{10}$(TruncatedEnergy muon energy) (left) and cos(TrackFit zenith) (right), assuming nominal values for all fluxes (conventional, prompt, astrophysical) and a XS value of 1.0x SM. Although this analysis used a two-dimensional fit, the initial one-dimensional energy distribution was in good agreement with the data, while the zenith angle distribution was not.

this analysis, the angular resolution was better than 0.55^o at all energies. This is important not only for the actual direction of the muon for the analysis, but also for the energy reconstruction algorithms, which perform less accurately if given a poor track reconstruction.

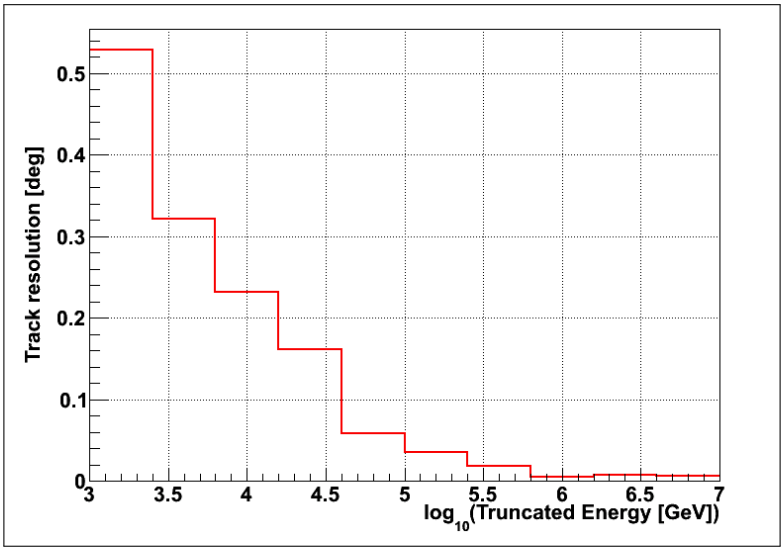

Figure 7.7: Track resolution for simulation events in final sample. The reconstructed zenith angle was accurate to within 0.55^o for the energy range of this analysis.

7.14 Muon energy resolution

Energy resolution is difficult overall because of the stochastic nature of muon energy losses at the high energies of this analysis. This leads to a large spread in the distribution of energy losses, even for muons with exactly the same true energy. Figure 7.8 shows the distribution of reconstructed muon energy values from TruncatedEnergy-DOMS as a function of true muon energies (at the point of entry to the detector). Figure 7.3 shows the same distribution for the MuEx algorithm. The vertical spread of the energy distribution at a particular muon energy stems from the statistical variation in stochastic losses from muons with the same true energy.

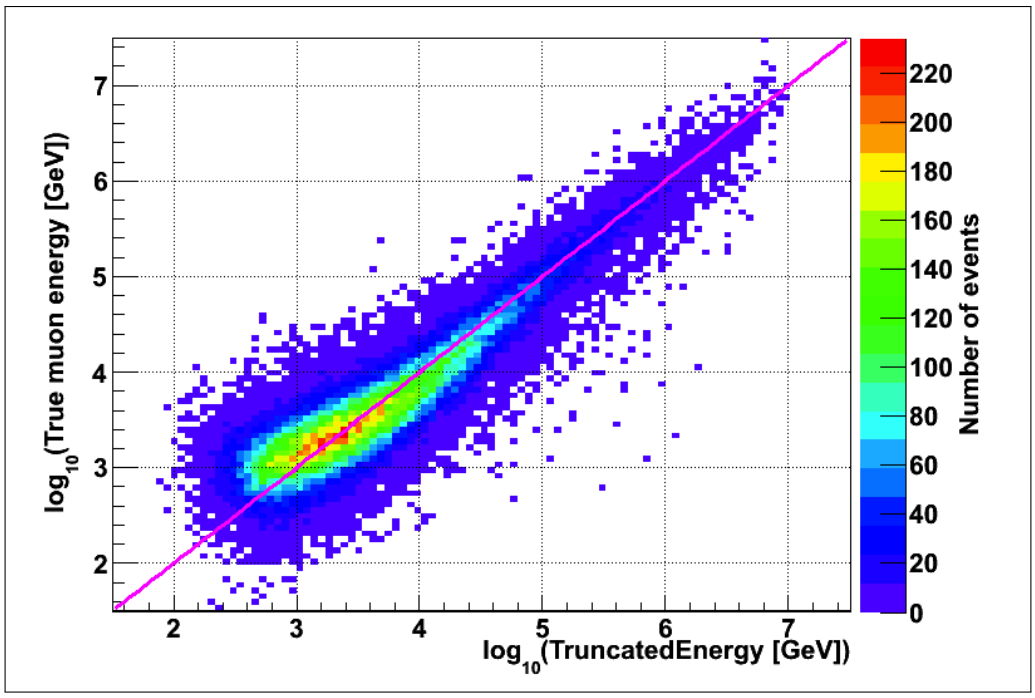

Figure 7.8: Comparison of reconstructed muon energy from TruncatedEnergy versus true muon energy from simulation. The magenta line is 1:1 correspondence, indicating agreement between reconstructed energy and true energy. The energy resolution (width of the distribution) for higher energies is smaller than for lower energies.

The actual energy resolution is dependent upon the energy spectrum of the incident neutrinos. Figure 7.9 shows the expected energy resolution for muons with energies between 1 TeV and 1 EeV for an E^{-1} spectrum, using the TruncatedEnergy program. The width of the distribution, which compares the reconstructed energy to the true energy of the muon, determines the energy resolution. Gaussian statistics were used to find the 1σ range for the energy resolution. For an E^{-1} spectrum, this error is 0.22 in $\log_{10}(\text{true } E_\mu)$. This equates to an energy resolution, for a muon of 10 TeV, between 6.0 TeV and 16.6 TeV. Energy resolutions are smaller for higher energies because the TruncatedEnergy algorithms remove most of the stochastic losses when calculating the muon energy.

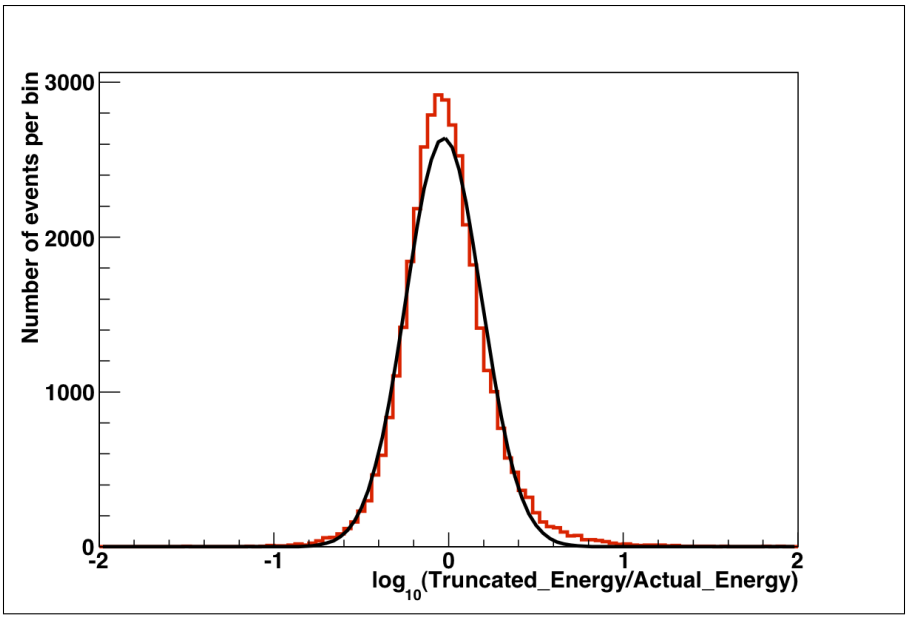

Figure 7.9: Muon energy resolution for the DOMs method of TruncatedEnergy, for simulated muon energies between 1 TeV and 1 EeV and an energy spectrum of E^{-1}. The energy resolution for 1σ using a Gaussian distribution (black line) is 0.22 in $\log_{10}(E_\mu)$.

7.15 Highest energy events

The three highest energy events in the final data sample are shown in Figures 7.10, 7.11, and 7.12. The highest muon energy event was 1.02 PeV at 90.2^o zenith angle, followed by 645 TeV at 101.1^o, and 631 TeV at 106.3^o.

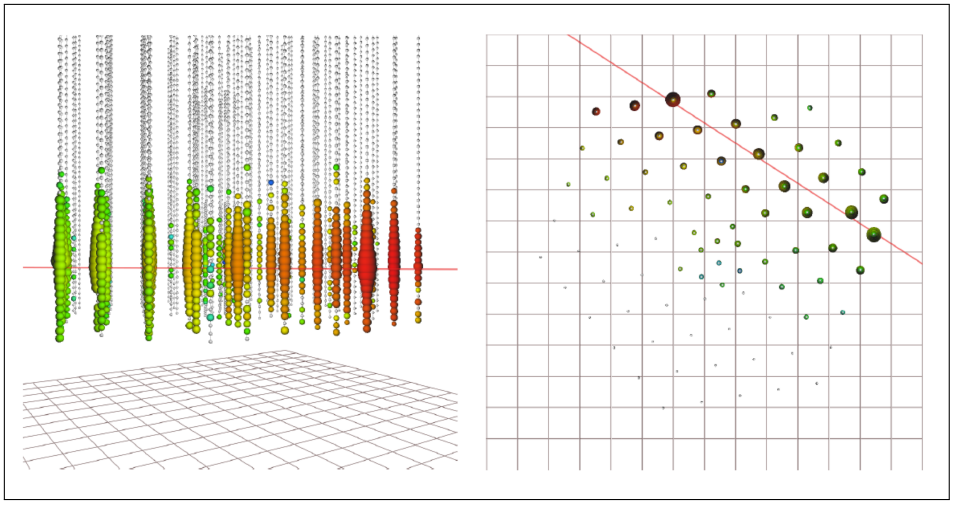

Figure 7.10: The event with the highest TruncatedEnergy muon energy in the final data sample, with energy of 1.02 PeV and a zenith angle of 90.2^o. On the left is the side view, and on the right is the top view, with the red line depicting the reconstructed track. From [204].

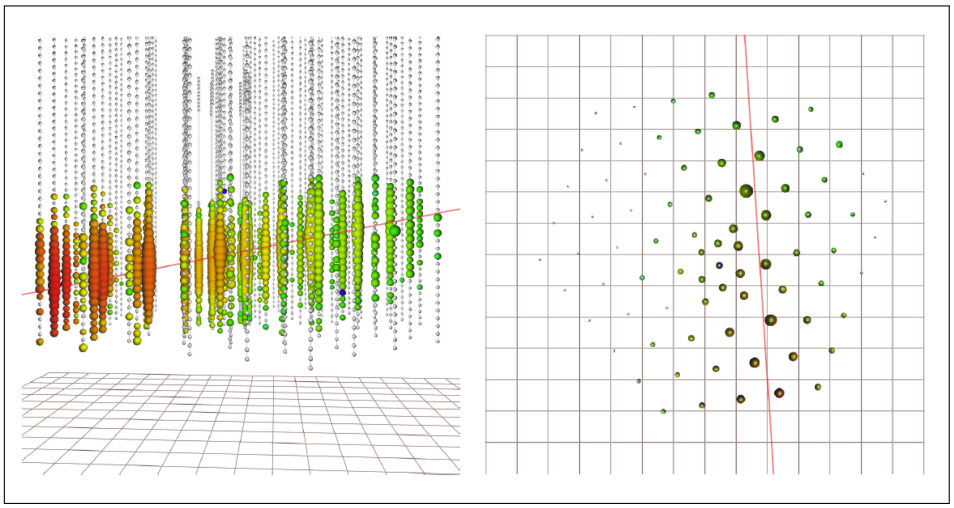

Figure 7.11: The event with the second highest TruncatedEnergy muon energy in the final data sample, with energy of 645 TeV and a zenith angle of 101.1^o. On the left is the side view, and on the right is the top view, with the red line depicting the reconstructed track. From [204].

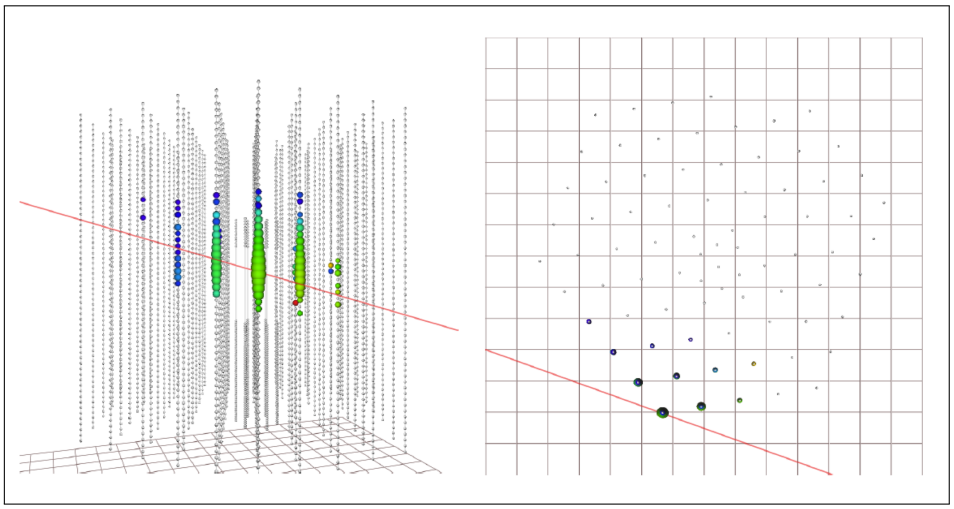

Figure 7.12: The event with the third highest TruncatedEnergy muon energy in the final data sample, with energy of 631 TeV and a zenith angle of 106.3^o. On the left is the side view, and on the right is the top view, with the red line depicting the reconstructed track. From [204].

Chapter 8

Analysis Procedures

8.1 Introduction

After processing all simulation through the event selection algorithms of Chapter 7, the next step was to apply those algorithms to the data. Collaboration approval of the analysis method was required before proceeding. This was accomplished using a small subset of the full dataset. Then full access to the data was granted, and data processing could begin. Once this was accomplished, the data and simulation could be compared in the log-likelihood fitter to determine the best-fit cross-section value. This chapter will discuss all the steps leading to that value.

8.2 IceCube data

The IceCube data is recorded in "runs", which are approximately 8 hours in length and identified by 6 digits, using the numbers 0 through 9. For example, the first run in the IC-79 dataset was designated 115975, recorded on 31 May 2010.

The last digit of the run number determines whether the run is dedicated to the burn sample, which is roughly 10% of the year's total data. Typically, all runs ending in 0 are used for the burn sample. For IC-79, the burn sample amounted to 33.5 days of livetime.

For the full IC-79 dataset, data was recorded from 31 May 2010 through 13 May 2011. Run numbers included 115975 through 118174. A total of 340.92 days of livetime were represented in these runs, but due to calibration runs and intermittent problems with the detector, a total of 319.65 days were usable. Of this usable amount, 315.76 days remained after additional processing. This is the final livetime of data that was used in this analysis.

8.3 Log-likelihood fitter

The fit method for the final data in this analysis was a log-likelihood (LLH) fitter using the program created by Gary Binder at the Lawrence-Berkeley National Laboratory and the University of California-Berkeley. The fitter is a Python program that uses the MINUIT and MIGRAD functions from pyminuit [209] to calculate the LLH best fit to the neutrino

cross-section multiple and the remaining fit parameters (considered as nuisance parameters). The remainder of this chapter will cover the various parts of the program. Most of the theoretical concepts used in the fitter program come from Chapter 37 of the Particle Data Group [210], but a summary of the relevant concepts is provided here.

8.3.1 Likelihood method

The goal was to find the best agreement between the model predictions and the experimental data. This required the use of a likelihood method where model parameters would be varied to determine the best-fit values. The amount of agreement would be determined by a "test statistic." Calculation of the test statistic depended upon whether the data was described as fixed or variable. In either case, the number of events n_{tot} would be described as:

$$n_{tot} = \sum_i n_i \tag{8.1}$$

where n_i is the number of events in the i-th bin. In the case of this analysis, the events were considered independent and Poisson-distributed. Then the data distribution could be described as a product of Poisson probabilities:

$$f_p(n;\theta) = \prod_{n=1}^{N} \frac{\mu_i^{n_i}}{n_i!} e^{-\mu_i} \tag{8.2}$$

where the values μ_i are the expected number of events per bin as a function of θ, with θ representing the set of fit parameters, and N the number of bins. Based upon this distribution, a likelihood $L(\theta)$ would then be maximized. For Poisson-distributed data, an alternative method is to minimize this quantity:

$$-2\ln\lambda(\theta) = 2\sum_i^N \left[\mu_i(\theta) - n_i + n_i \ln\frac{n_i}{\mu_i(\theta)}\right] \tag{8.3}$$

where the ln term is set to 0 for data bins with $n_i = 0$. This quantity is called the $-2LLH$. The value is minimized to give the best-fit result, creating a "least log likelihood" fit [210]. In simpler terms, the $-2LLH$ can be written as:

$$-2LLH = -2\sum_i^N \left[(Simulation - Data) + \left(Data \cdot \ln\left(\frac{Data}{Simulation}\right)\right)\right] \tag{8.4}$$

where "Simulation" includes the contributions from conventional, prompt, and astrophysical neutrinos (which will be covered in detail in later sections). The $-2LLH$ is the test statistic for this analysis. The calculation of $-2LLH$ is a complex multi-step process involving many adjustments to the number of simulated events while the fitter is changing the fit parameters. This will be the subject of the remainder of this chapter.

8.3.2 MINUIT and MIGRAD

MINUIT finds the minimum value of a multi-parameter user-defined function and analyzes the shape of the function around the minimum. One principal application is to compute best-fit parameter values and uncertainties, including correlations between the parameters [211]. Because of these capabilities, MINUIT is frequently used in high-energy physics applications.

MINUIT offers the user a choice of several minimization algorithms. In general, the MIGRAD algorithm is the best choice for the minimizer for nearly all functions and is also the choice for this analysis. It is a variable-metric method with inexact line search, a stable metric updating scheme, and checks for positive-definiteness. Its main weakness is that it depends heavily upon knowledge of the first derivatives, and it fails if the derivatives are inaccurate [211].

MIGRAD produces an error matrix, also called the covariance matrix. Errors based on the error matrix take account of all the parameter correlations but not non-linearities if they exist. This matrix is the inverse of the matrix of second derivatives of the user-designated function with respect to its free parameters. In the case of this analysis, the function was the calculation of the $-2LLH$ value when comparing the number of events per bin while varying the fitter parameters, which will be discussed in later sections. Once the error matrix is calculated, the fit parameter errors are the square roots of the diagonal elements of the error matrix. In addition, the off-diagonal elements can be accessed to determine the correlation matrix for the parameters [211].

8.3.3 Preparing files for the fitter

For the final processing step, the required information from the simulation events and data events were copied into text files for loading into the fitter. For data, only two primary event parameters were needed: TrackFit zenith angle and TruncatedEnergy-DOMS muon energy. For simulation, other event parameters were also needed in order to calculate the proper weighting for each event, and these included true neutrino energy, true zenith angle, and particle type (ν or $\bar{\nu}$). The list of additional weights (discussed below) included OneWeight, NeutrinoFlux, astrophysical flux, and InEarth weights. The final event weight would be formulated in the fitter as the product of OneWeight, NeutrinoFlux (for conventional and prompt) or the astrophysical flux weight, and the InEarth weight for a given cross-section value.

8.3.3.1 OneWeight

A total of 2.5 million simulated events in the final sample were available to represent ~10,000 data events. Each simulated event was weighted to its true probability of occurrence using the simulation-generated OneWeight. When NuGen simulation is run in FULL mode, OneWeight incorporates all effects and represents the probability of each event occurring in nature. Because it was necessary to separate out the Earth effects, OneWeight for this analysis only included the probability due to the initial energy spectrum and zenith weighting. The energy spectrum represented the injection spectrum beginning at the detector and not at the surface. The zenith weighting forced the simulation to throw more

events in the higher zenith bins to increase statistics in these important bins. OneWeight was adjusted for each of these variables.

8.3.3.2 NeutrinoFlux

The NeutrinoFlux program uses the neutrino flux concepts covered in Chapter 3. The conventional flux module that was used for this analysis was called ConventionalNeutrinoFluxWithKnee, using the flux file called "honda2006-gaisserH3a-elbert-v2-numu." The prompt flux module that was used was called PromptNeutrinoFluxWithKnee, using the prompt flux file called "sarcevic-std-gaisserH3a-elbert-numu."

8.3.3.3 Astrophysical flux

A baseline astrophysical flux weight was calculated for each event. This was done by multiplying the OneWeight by the factor $10^{-18}(\frac{E_\nu}{100\ TeV})^{-2.0}$. This represents the baseline $E^{-2.0}$ flux.

8.3.3.4 InEarth weights

The weights for different neutrino cross sections for each simulated event were stored in the text file, for cross-section values from 0.2x SM to 5.0x SM, in 0.2x increments. These weights were generated by the InEarth program and represented the changes in event weights for the different neutrino cross sections under evaluation. Weights steadily decreased with increasing cross-section multiple. For a neutrino with energy ∼5 TeV, the cross-section weight is ∼1.0 for a cross-section multiple of 1.0x SM near the horizon. At 5.0x SM, the cross-section weight is ∼0.7, indicating the lower survival rate and higher absorption probability for the neutrino in the Earth.

8.3.4 Spline fits

The fitter reads in each simulated event and its weights, and then the fitter creates a one-dimensional spline to the XS weights for each event. The user chooses the method to bridge the gaps between cross-section points, using either a linear or quadratic relationship. For this analysis, the linear relationship was chosen since the quadratic relationship did not change the result appreciably but extended computation time considerably. The one-dimensional splines would then be used to predict the number of events in two dimensions using zenith angle and muon energy bins. The fitter would then create a surface in two-dimensional space for each XS value, which would be compared to the binned data.

Figure 8.1 shows the XS weights for a representative sample of events while varying the neutrino energy with a constant zenith angle and also for varying the zenith angle with a constant neutrino energy. The trend of decreasing weights as XS multiple increases is apparent.

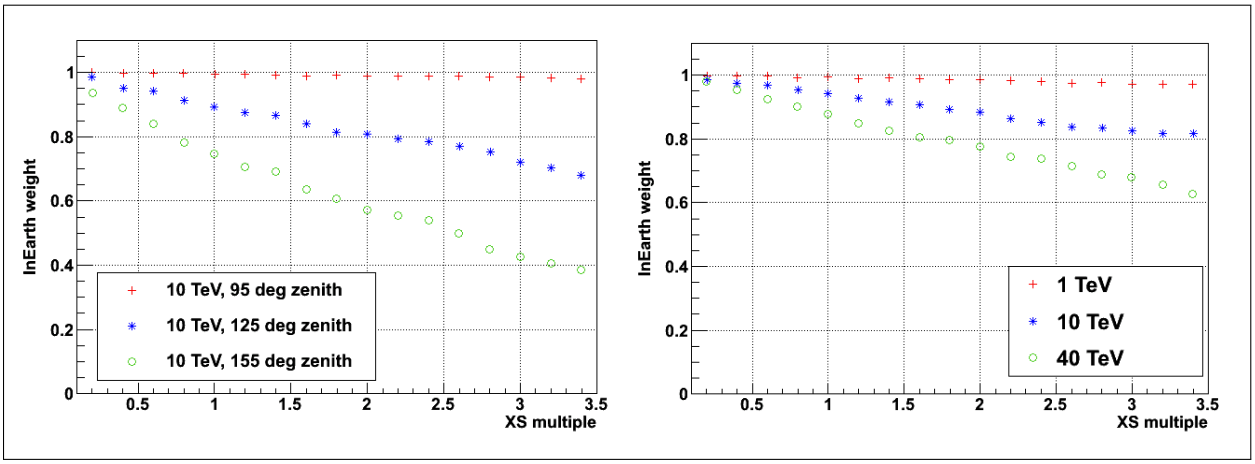

Figure 8.1: InEarth weights versus cross-section multiple, XS, for a representative sample of events. The general trend of decreasing weights as XS multiple increases is shown, along with the relationships for a change in zenith or energy. The weight indicates survival probability. (left) The change in weights for a change in zenith angle, at a constant neutrino energy of 10 TeV. (right) The change in weights for a change in neutrino energy, at a constant zenith angle of 110^o.

8.3.5 Fitter variables, parameters, and equations

There are many internal variables, fitter parameters, and equations required for this analysis. The overall method involves reading in the "internal fitter variables" from the simulation text files. The splines are created from the cross-section weights for each event. An initial two-dimensional histogram in muon energy and zenith angle is created, using the default values of the "primary fit parameters" provided by the user. This simulation histogram is compared to the two-dimensional histogram of the data events. The $-2LLH$ value is computed by comparing bin contents from these two histograms, using Equation 8.3. Then the fitter changes the primary fit parameters in small increments and recalculates individual event weights using the equations listed in the "fit model." The modified event contributions are then summed into a new simulation histogram. This histogram is then compared to the data histogram to compute a new $-2LLH$ value. The process repeats until the lowest value of $-2LLH$ is found, and the program outputs the best corresponding values for the XS and the nuistance parameters.

Although several systematic parameters could be incorporated directly into the fitter as nuisance parameters, not all systematics could be parameterized. Instead, they are evaluated separately in the systematics analysis of Chapter 9.

8.3.5.1 Internal fitter variables

First is a discussion of the variables that are used internally by the fitter. Once the simulation text files are loaded into the fitter, these internal variables do not change:

prop-weight-fcn(XS): This is the spline function of propagation weights created by MINUIT MIGRAD. The fitter uses the event weights for the cross-section multiples from

the simulation text file to create a spline for each event to represent the effect of cross section changes in two dimensions of muon energy and zenith angle. The parameter XS is the overall goal of the analysis, to find the best-fit cross-section multiple of the SM.

conv-weight: This variable represents each event's initial conventional weight in the simulation text file, but it only includes the NeutrinoFlux and OneWeight event weights and not the weights due to the cross-section multiple.

prompt-weight: This variable represents each event's initial prompt weight in the simulation text file, but it only includes the NeutrinoFlux and OneWeight event weight and not the weights due to the cross-section multiple.

astro-weight: This variable represents each event's initial astrophysical weight in the simulation text file. It includes the astrophysical event expectation assuming an $E^{-2.0}$ energy spectrum plus the OneWeight portion of the event weight but not the weights due to the cross-section multiple. This variable represented the ϕ portion of the astrophysical flux.

nu-energy: This variable stores the true neutrino energy from simulation.

nu-zenith: This variable stores the true neutrino zenith angle from simulation.

ptype: This variable stores the parent particle type, with 68 for ν_μ and 69 for $\bar{\nu}_\mu$, from simulation.

8.3.5.2 Primary fitter parameters

Listed below are the primary fitter parameters that are optimized to provide the best $-2LLH$ value for the fit. These are the output parameters after the fit is complete. Other than XS, all other fitter parameters are nuisance parameters.

XS: Neutrino cross section, the goal of the analysis (in multiples of the SM expectation, with nominal value of 1.0x SM).

phi-conv: XS·Conventional neutrino flux coefficient (nominal value of 1.0x Honda2006+Gaisser H3a+Elbert).

phi-prompt: XS·Prompt neutrino flux coefficient (nominal value of 1.0x ERS).

phi-astro: XS·Astrophysical neutrino flux coefficient (nominal value of 1.0).

astro-index: Astrophysical neutrino energy index, or γ (nominal value of -2.0). The initial astro-weight in the simulation text file was calculated using this index.

cr-index: Cosmic ray energy index (nominal value of -2.65). This parameter is directly tied to the conventional flux and prompt flux energy indices. All changes in the fitter are considered as deltas from a baseline value of -2.65, although this value is an arbitrary choice used only for calculating the differentials in the fitter. If the fitter gives the best fit index as -2.66, then this represents a delta of -0.01 from the baseline. When the fitter changes the cosmic ray index, the conv-weight and the prompt-weight are adjusted.

nu-scaling: Percentage of ν compared to $(\nu + \bar{\nu})$ parameter (nominal value 1.0). This parameter represents the percent change in the number of ν (versus $\bar{\nu}$) when compared to the total number of neutrinos. NeutrinoFlux was used to calculate the expected number of ν and $\bar{\nu}$ for a nominal conventional flux from theoretical expectations (which is on average 70% ν and 30% $\bar{\nu}$ over the entire analysis' energy and zenith range). This parameter is allowed to vary from 100% ν (or nu-scaling = 1.4388) to 100% $\bar{\nu}$ (or nu-scaling = 0.0). An alternative parameterization (the ratio of the flux of ν to the flux of $\bar{\nu}$) was investigated and found to be too sensitive to small adjustments in the fitter, which is discussed in Chapter 9. Figures 8.2 and 8.3 show the changes to the conventional flux distributions for the extreme cases of 100% ν and 100% $\bar{\nu}$ for the parameterization used in this analysis. The changes are larger in the energy distribution than in the zenith distribution.

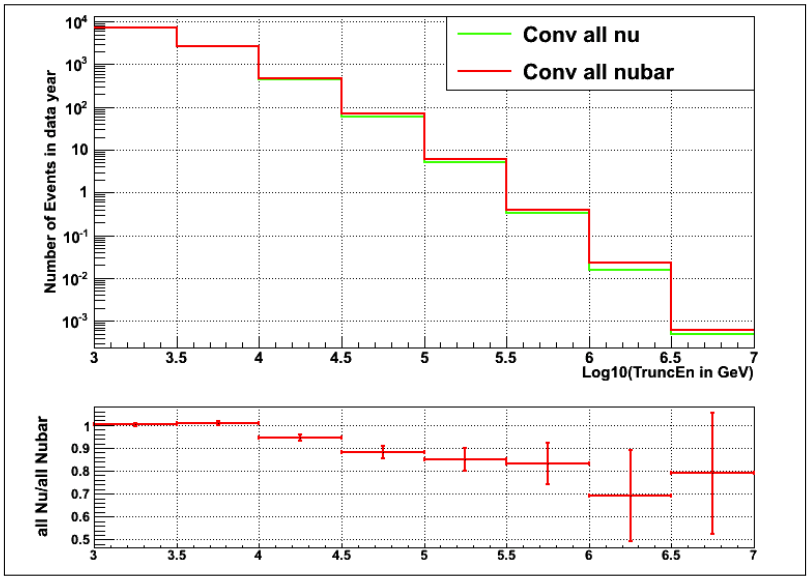

Figure 8.2: Comparison in $\log_{10}$(TruncatedEnergy) of changing the nu-scaling parameter from 100% ν (green line) to 100% $\bar{\nu}$ (red line) for XS = 1.0x. The ratio change is shown in the lower part of the figure, which demonstrates that there are fewer total events predicted at high energies if there are more ν than theory predicts. Large error bars are due to low statistics. The effect on the distribution could be as much as 30%.

DE: DOM efficiency (DE) parameter representing the change as compared to baseline (nominal value of 0.0). If the DOM is more (or less) efficient at detecting photons than modeled, the reconstructed energy will change, especially for low energy muons because their detection depends upon surpassing thresholds of photon counts in the DOMs. A low-energy

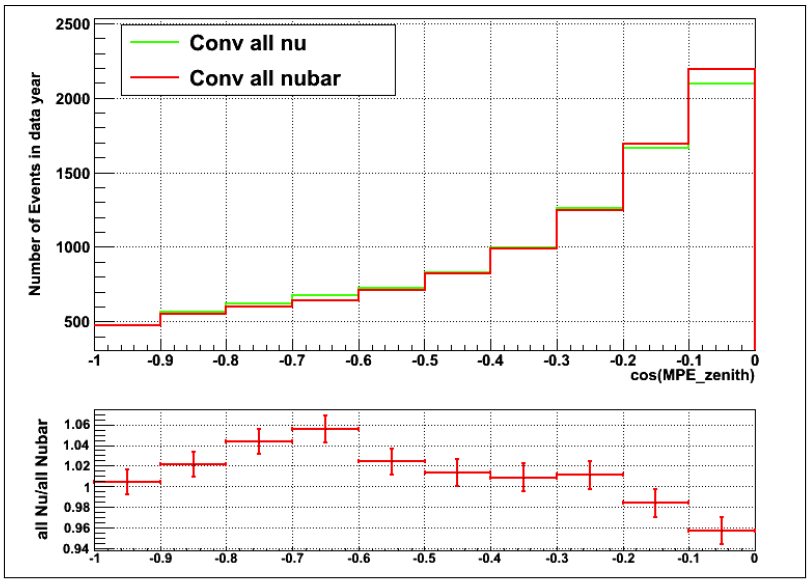

Figure 8.3: Comparison in cos(zenith) of changing the nu-scaling parameter from 100% ν (green line) to 100% $\bar{\nu}$ (red line) for XS = 1.0x. The ratio change is shown in the lower part of the figure. The effects of nu-scaling are more complex in zenith angle than in energy. If there are more ν than theory predicts, there are fewer events at the horizon and more at the median zenith angles because ν has a higher cross section than $\bar{\nu}$, which mostly affects the large number of events at lower energies. However, the maximum effect on the distribution is only ∼6%.

event might be recorded if the DE is 10% higher than expected, but it might not be recorded if the DE is 10% lower than expected.

The effects of DE on the shapes of the two-dimensional energy-zenith curves were initially plotted from 5 different simulation sets that were run specifically to check DE systematic errors. The simulation with the highest DE (set 10873 with 118.8% DE) and lowest DE (set 10902, 100% DE), plus the nominal DE (set 10904 with 110% DE), were used to create equations to represent the effects of changing the DE. The intermediate DE simulation sets (set 11224 with 115% DE and set 11206 with 105% DE) were cross-checked to ensure the equations represented the intermediate behavior.

When plotted, the effect of changing DE was mainly as a scaling factor, as shown in the ratios in the bottom of Figure 8.4. There is no substantial shape change in the curves with changing DE. However, the scaling is different for each energy index, requiring different factors for the conventional, astrophysical, and prompt components of the flux. These linear equations are incorporated into the fitter to generate correction factors on each flux, named DE-conv, DE-astro, and DE-prompt:

$$\text{DE-conv} = 1.0 + (0.023) \cdot \text{DE}$$
$$\text{DE-astro} = 1.0 + (0.012) \cdot \text{DE}$$
$$\text{DE-prompt} = 1.0 + (0.013) \cdot \text{DE}$$

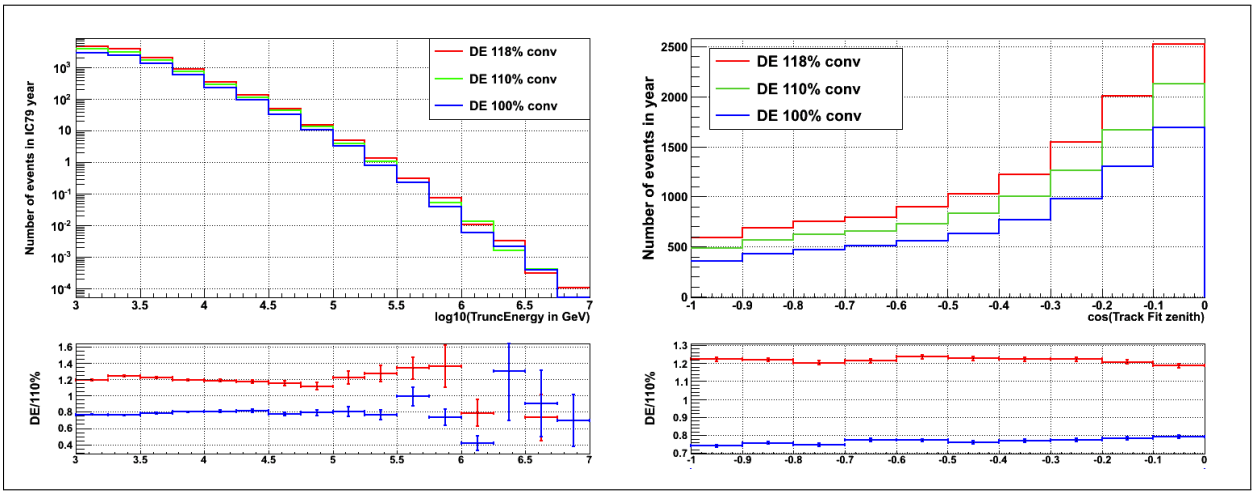

Figure 8.4: Effect of DOM efficiency (DE) on event energy distribution (left) and cos(zenith) (right), for the conventional flux for three DE settings. The ratio of DE to the 110% nominal DE is shown in the bottom section of each plot. The effect is a scaling factor on the number of events, which is incorporated into the fitter using three linear equations, one for each flux.

K-scaling: Multiplicative factor on the kaon portion of the pion + kaon contribution to the conventional neutrino flux (nominal value 1.0). The number of neutrinos from pion decays and from kaon decays is calculated using Equation 3.4. First, the local zenith angle at the neutrino's point of impact on the surface is calculated from the IceCube zenith angle, using Equation 3.5. Then the unchanged flux equation is solved. This represents the baseline number of events predicted for the specific zenith angle and neutrino energy. Then the K-scaling parameter is multiplied on the kaon contribution, thus increasing or decreasing the number of kaon-generated neutrinos, but the total number of events is not rescaled afterwards.

8.3.6 Fit model

All the preceding variables and parameters are combined into the following equations, which are used by the fitter to create a new simulation histogram and minimize the $-2LLH$ value. Where a summation is used, the sum is over all events in the simulation set. As the events are summed, they are placed into the corresponding energy-zenith bins for comparison to the data. When the fitter changes a primary fit parameter, these fit variables are recalculated. Changes in XS and energy indices result in changes to the overall number of events, but the fitter is trying to find a shape change in the two-dimensional curve, not a scaling change, and therefore the number of events are renormalized.

ntot: This parameter represents the total expected number of $\mu + \bar{\mu}$ (from ν and $\bar{\nu}$) from the conventional atmospheric flux for all energies and zenith angles by summing all the conv-weight values for individual events. This is the baseline value before changes by the fitter to the cr-index parameter and is used to rescale the number of conventional events

in the fitter on an event-by-event basis. The effect of the XS is included here to ensure that each event is rescaled due to the changes to both the cr-index and the XS value.

$$\text{ntot} = \sum(\text{conv-weight} \cdot \text{prop-weight-fcn(XS)})$$

nptot: This parameter represents the total expected number of $\mu + \bar{\mu}$ (from ν and $\bar{\nu}$) from the prompt flux for all energies and zenith angles by summing all the prompt-weight values for individual events. This is the baseline value before changes by the fitter to the cr-index parameter and is used to rescale the number of prompt events in the fitter on an event-by-event basis. The effect of the XS is included here to ensure that each event is rescaled due to the changes to both the cr-index and the XS value.

$$\text{nptot} = \sum(\text{prompt-weight} \cdot \text{prop-weight-fcn(XS)})$$

mod-conv-weight: This parameter stores the modified conventional weight for the event when the fitter parameters change. First, the cr-index is changed from the baseline value of -2.65. For reference, if the neutrino energy is 3 TeV, a change in the cr-index of ± 0.01 gives a change in the conv-weight of about $\pm 8\%$:

$$\text{mod-conv-weight} = \text{conv-weight} \cdot \text{nu-energy}^{(2.65-\text{cr-index})}$$

The modified conventional weight for each event requires adjustment from a change in the total number of events when the fit procedure changes the conventional index and cross-section multiple during its evaluation. This adjustment is required in order to conserve the number of events that were predicted from simulation, since the shape change is important and not necessarily the overall scaling factor in the fitter. This means that there is no "pivot point" as in the astrophysical flux curve that pivots around $E_\nu = 100$ TeV. After multiplying the conventional flux by the new energy index, the event weights are rescaled so as to conserve the total number of events as expected from NeutrinoFlux (Honda2006+GaisserH3a+Elbert). For example, a change in XS from 1.0x SM by +0.2x SM reduces the conv-weight by 6% (when other parameters are held fixed). For increasing XS values, the weight decreases due to decreasing survival probability:

$$\text{mod-conv-weight} \mathrel{*}= \text{ntot} \;/\; \sum(\text{mod-conv-weight} \cdot \text{prop-weight-fcn(XS)})$$

countnu: This parameter calculates the total number of conventional ν events after changes in the energy index during the fit procedure. The effect of the XS is included here to ensure that each event is rescaled due to the changes to both the cr-index and the XS value, but separately for ν and $\bar{\nu}$:

$$\text{countnu} = \sum(\text{mod-conv-weight} \cdot \text{prop-weight-fcn(XS)} \cdot (\text{ptype}==68.))$$

countnubar: This parameter calculates the total number of conventional $\bar{\nu}$ events after changes in the energy index during the fit procedure. The effect of the XS is included here to ensure that each event is rescaled due to the changes to both the cr-index and the XS value, but separately for ν and $\bar{\nu}$:

$$\text{countnubar} = \sum(\text{mod-conv-weight} \cdot \text{prop-weight-fcn(XS)} \cdot (\text{ptype}==69.))$$

Next, the conventional weight needs adjustment for the change in the ratio of ν and $\bar{\nu}$ events during the fit procedure. If the nu-scaling parameter increases (more ν), then the number of $\bar{\nu}$ must be reduced to conserve the total number of events. For example, if there are 100 total events ($\nu+\bar{\nu}$), then originally there are 70 ν and 30 $\bar{\nu}$ from theoretical expectations. If the nu-scaling changes from 1.0 (baseline) to 1.1, then the number of ν becomes 77. Since there are 100 total events, then there must be 100 - 77 = 23 $\bar{\nu}$ events now. This equation changes the conventional weight for each event according to whether the event is ν (ptype 68) or $\bar{\nu}$ (ptype 69) to reflect this conservation of events. If the event is ν, then its modified conventional weight is adjusted by the nu-scaling factor, as shown in the first part of the equation below. If the event is $\bar{\nu}$, then its modified conventional weight is adjusted by the second part of the equation.

$$\begin{aligned}\text{mod-conv-weight} \mathrel{*}= {} & (\text{ptype}==68.) \cdot \text{nu-scaling} + \\ & (\text{ptype}==69.) \cdot (\text{ntot - countnu} \cdot \text{nu-scaling}) \,/\, \text{countnubar}\end{aligned}$$

Lastly, the mod-conv-weight is changed by the DE-conv factor as the DOM efficiency changes in the fitter, plus the K-scaling factor as the number of neutrinos from kaons is changed in the fitter:

$$\text{mod-conv-weight} \mathrel{*}= \text{DE-conv} \cdot \text{K-scaling}$$

mod-prompt-weight: This parameter stores the modified prompt weight for each event when the fitter changes the energy index (cr-index) from the baseline value of -2.65:

$$\text{mod-prompt-weight} = \text{prompt-weight} \cdot \text{nu-energy}^{(2.65-\text{cr-index})}$$

Similar to the conventional flux, this next equation renormalizes the prompt weight for a change in the number of events that occurs from the change in energy index during the fit procedure. This is required in order to conserve the number of events that are predicted from simulation.

$$\text{mod-prompt-weight} \mathrel{*}= \text{nptot} \,/\, \sum(\text{mod-prompt-weight} \cdot \text{prop-weight-fcn(XS)})$$

In addition, the mod-prompt-weight is modified by the DE-prompt factor as the DOM efficiency changes in the fitter, but the K-scaling is not included because the mechanism for creating prompt neutrinos is different from the pion-kaon mechanism:

$$\text{mod-prompt-weight} \mathrel{*}= \text{DE-prompt}$$

mod-astro-weight: This parameter stores the modified astrophysical weight for the event when the fitter changes the astrophysical energy index (astro-index) from the baseline value of -2.0. Because the astrophysical index is normalized at an energy of 100 TeV (by convention), there is no adjustment to the number of events for this index change except in the normalization factor that is automatically calculated by the fitter.

$$\text{mod-astro-weight} = \text{astro-weight} \cdot (\text{nu-energy}/100\ \text{TeV})^{(2.0-\text{astro-index})}$$

In addition, the mod-astro-weight is modified by the DE-astro factor as the DOM efficiency changes in the fitter, but the K-scaling is not included because astrophysical neutrinos are not created in the pion-kaon mechanism:

$$\text{mod-astro-weight} \mathrel{*}= \text{DE-astro}$$

All of these parameters are then combined into the total cross-section equation that leads to the best-fit values for all of the fit parameters. The fitter determines the best values for phi-conv, phi-prompt, and phi-astro, using the weights provided. This is the "Simulation" equation that was mentioned in the discussion of Equation 8.4. The binned numbers of events that come from this equation are then compared to the binned data events to determine the best fit:

$$\begin{aligned}&[(\text{phi-conv} \cdot \text{mod-conv-weight} + \\ &\text{phi-prompt} \cdot \text{mod-prompt-weight} + \\ &\text{phi-astro} \cdot \text{mod-astro-weight})] \cdot \text{prop-weight-fcn(XS)}\end{aligned}$$

One feature needs to be emphasized. The XS parameter is not specifically included in this equation as a separate multiplicative factor because each fit parameter (phi-conv, phi-prompt, and phi-astro) already includes the XS parameter. In short, phi-conv is actually XS·conventional normalization, and likewise for the other parameters. This is necessary if previous experimental results are to be used as constraints on the fitter parameters. For example, previous conventional flux results assumed a neutrino cross section of 1.0x SM when measuring a flux of 1x theoretical expectations. If the cross section is actually 2x SM, then the actual conventional flux is ∼0.5x theoretical expectation because a cross section that is 2x bigger will cause ∼2x the number of interactions in the detector. Multiplying 2x cross section with 0.5x flux gives 1x the number of events, thus agreeing with observed numbers. In essence, the number of events must be conserved because a specific number of particles is measured at the surface, and both the cross section and the flux play a role in that number.

8.3.7 Calculating the log likelihood value

The MINUIT MIGRAD module was called in the fitter to calculate the $-2LLH$ value and all parameter values. The differences between the simulation expectation and the actual data were minimized until a best-fit value for the cross-section multiple was found. Figure 8.5 shows a test plot of $-2LLH$ values versus XS for a fixed set of test assumptions. The values for 1, 2, and 3 σ uncertainty are also shown.

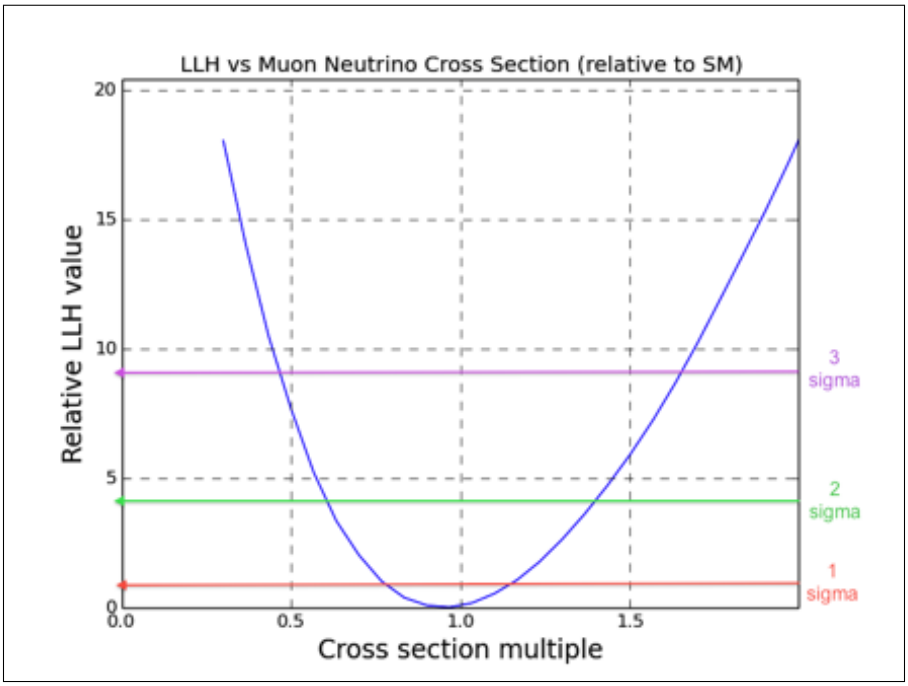

Figure 8.5: Relative "profile" log likelihood ($-2LLH$) values for the cross-section multiple XS from 0.3x SM to 2.0x SM. A change in $-2LLH$ value of 1.0 represented 1σ (orange line), while a change of 4.0 represented 2σ (green line), and a change of 9.0 represented 3σ (magenta line). This test plot was used to examine the fitter's functions and did not use actual data. Lowest value of $-2LLH$ occurred at 0.98x SM, with 1σ errors giving the range 0.78x to 1.17x SM.

Chapter 9

Results

9.1 Overview

This chapter discusses the choice of binning and ranges for the fitter, then the first fit result without using constraints from previous experiments. The term "priors" will be used here to represent previous experimental results that serve as constraints on the nuisance parameters for this analysis. The available experimental results to use as priors for each of the nuisance parameters from Chapter 8 are discussed. Using the selected priors, the best fit results are given, along with the statistical errors and systematic uncertainties.

9.2 Binning and ranges

Since the fit is performed in two dimensions using muon energy and cos(zenith), an evaluation is required for the range of muon energies, the range of zenith angles, the number of energy bins, and the number of zenith bins. Unless otherwise specified, muon energy units will be GeV, such that 1 TeV would have a $\log_{10}(E_\mu/\text{GeV})$ of 3.0. For brevity, the GeV will be omitted and understood.

Theory predicts minimal absorption of neutrinos below an energy of 1 TeV for cross-section values near SM predictions. A lower limit of $\log_{10}(E_\mu)$ of 3.0 was chosen. The determination of the higher end of the energy range depended mainly upon the available data. The data sample contained events up to 6.1 in $\log_{10}(E_\mu)$. A lack of events is also important information for the fitter, and the upper muon energy range was chosen at 7.0. Therefore, the energy range for this analysis was (3.0, 7.0) in $\log_{10}(E_\mu)$.

For the zenith range, Earth effects occur only for zenith angles of 90 to 180 degrees. Using bins in cosine of the zenith angle removes some of the effects of the solid angle in the binning. Therefore, the zenith range for this analysis is cos(zenith) from (-1.0, 0.0).

With a muon energy resolution of 0.20-0.25 in $\log_{10}(E_\mu)$, the energy binning should be no smaller than the resolution. Therefore, the chosen energy bin width is 0.25 in $\log_{10}(E_\mu)$.

Binning in zenith angle is not restricted by track resolution, since all events are reconstructed within 1 degree. For this analysis, the choice of 10 cos(zenith) bins is used because this provides a smooth distribution of simulation events and an adequate distribution of the data events.

To summarize, binning was set at 16 energy bins for $\log_{10}$(TruncatedEnergy-DOMS muon energy) from 3.0 to 7.0, and 10 bins in cos(TrackFit zenith) from -1.0 to 0.0. Table 9.1 shows the final distribution of data events using this binning method. In addition, Figures 9.1 and 9.2 compare the surface neutrino spectrum to the spectrum arriving at the detector, indicating the expected absorption of neutrinos for a SM cross-section assumption.

Table 9.1: The number of data events that survived the final cuts, binned in $\log_{10}(E_\mu/\text{GeV})$ from TruncatedEnergy, and cos(zenith) from TrackFit. The events with $\log_{10}(E_\mu)$ greater than 5.0 are relatively rare, and the sources are predicted to be the astrophysical and prompt neutrino fluxes. The absence of events at high energy and high zenith angle is caused by Earth absorption of neutrinos.

$\log_{10}$ (energy range)	cos(zenith)									
	-1.0 to -0.9	-0.9 to -0.8	-0.8 to -0.7	-0.7 to -0.6	-0.6 to -0.5	-0.5 to -0.4	-0.4 to -0.3	-0.3 to -0.2	-0.2 to -0.1	-0.1 to 0.0
3.00-3.25	224	246	282	307	306	336	435	545	648	791
3.25-3.50	149	208	232	219	267	281	358	458	567	699
3.50-3.75	86	85	111	118	113	171	195	245	288	424
3.75-4.00	35	52	32	56	54	68	92	132	149	172
4.00-4.25	11	2	2	18	26	25	29	32	53	64
4.25-4.50	1	6	6	5	11	19	9	22	21	42
4.50-4.75	1		2	2	4	6	3	6	21	14
4.75-5.00		2		2	3	2	1	3	7	8
5.00-5.25				1		2		2	3	4
5.25-5.50			1			1	1			1
5.50-5.75								1		1
5.75-6.00								1	1	
6.00-6.25										1
6.25-6.50										
6.50-6.75										
6.75-7.00										

9.3 Initial fit of the data

The data was initially fit without using any priors. Table 9.2 lists the nuisance parameters and their limits. Using this set of limits, the fitter was run without priors on the nuisance parameters, with the results shown in Table 9.3. This fit indicates that the XS multiple of the SM cross section was 3.11x the theoretical value. However, upon closer examination, large changes in some of the parameters, specifically phi-astro, astro-index, and phi-prompt, resulted in only small changes in $-2LLH$ when evaluated singly. This is mainly due to a lack of statistics above $\log_{10}(E_\mu)$ of 5.0. The large deviations in these nuisance parameters forced the other nuisance parameters to take fit values that impacted the cross-section result.

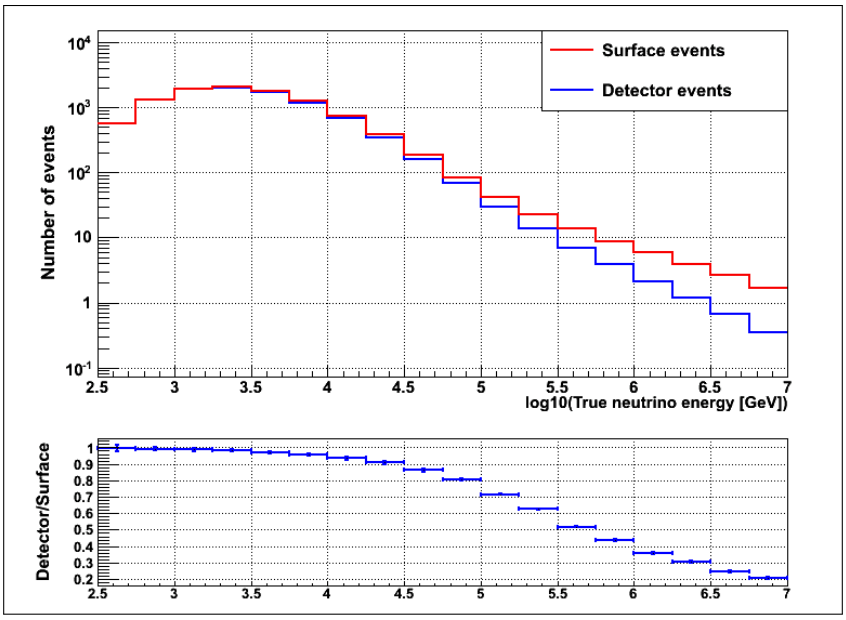

Figure 9.1: Changes in energy distribution from neutrino absorption in the Earth. The initial energy distribution at the surface (red) becomes the energy distribution at the detector (blue). Numbers are from simulation and include final event cuts. A cross-section multiple (XS) of 1.0x SM was assumed for these plots, along with the theoretical expectations for the conventional, prompt, and astrophysical fluxes. A ratio below 1.0 indicates absorption.

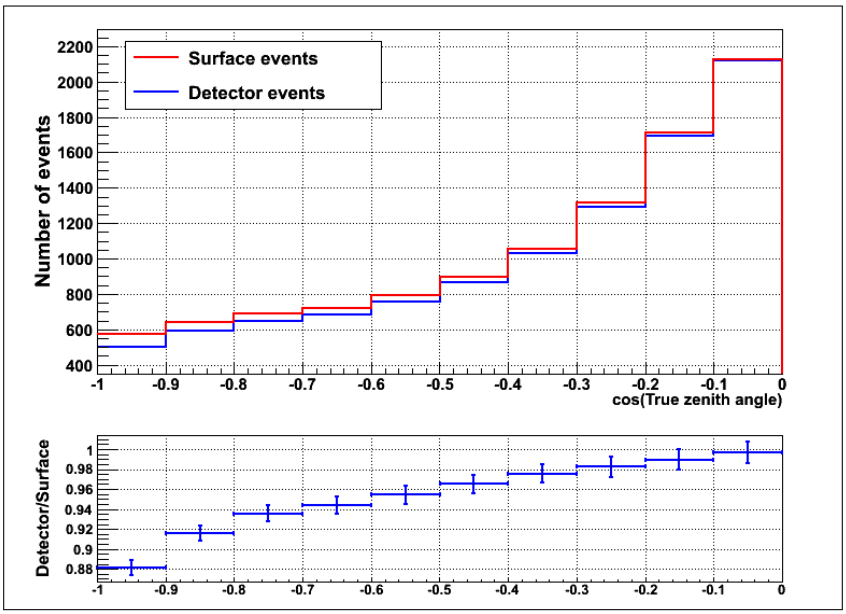

Figure 9.2: Changes in zenith angle distribution from neutrino absorption in the Earth. The initial zenith distribution at the surface (red) becomes the zenith distribution at the detector (blue). Numbers are from simulation and include final event cuts. A cross-section multiple (XS) of 1.0x SM was assumed for these plots, along with the theoretical expectations for the conventional, prompt, and astrophysical fluxes. A ratio below 1.0 indicates absorption.

Because of this insensitivity, many of the nuisance parameter values are in conflict with recent experimental results. For example, a prompt flux 18.7 times ERS expectations is not feasible because a recent six-year IceCube diffuse flux analysis already excludes more than 1.06x ERS with 90% confidence [138]. Therefore, previous experimental results are used as priors on the nuisance parameters to ensure the final values are in agreement with these results.

Table 9.2: Parameters and limits for initial fit without priors.

Parameter name	Nominal value	Initial fitter limits
XS	1.0x	0.2x to 5.0x SM
phi-conv	1.0	0.5x to 2.0x Honda 2006+Gaisser H3a+Elbert
phi-prompt	1.0	0x to 20.0x ERS
phi-astro	1.0	0 to 20.0
astro-index	-2.0	-0.1 to -3.9
cr-index	0	-0.25 to +0.15
nu-scaling	1.0	0.0 (100% $\bar{\nu}$) to 1.43882 (100% ν)
DE	0.0	-20% to +20%
K-scaling	1.0	0.5x to 2.0x kaon portion of Gaisser formula

Table 9.3: Initial fit result (without priors). Many nuisance parameter values were in conflict with previous experimental results.

Parameter name	Nominal value	Fit results	Variable identification
XS	1.0x	3.11x	x SM (CSMS calculation)
phi-conv	1.0	0.76	x Honda 2006+Gaisser H3a+Elbert
phi-prompt	1.0	18.7	x ERS calculation
phi-astro	1.0	5.45	ϕ term
astro-index	-2.0	-1.97	γ term
cr-index	0	-0.08	change from nominal energy index
nu-scaling	1.0	0.65	x NeutrinoFlux ν contribution
DE	0.0	-11%	change from 110% nominal
K-scaling	1.0	1.9x	x kaon portion of Gaisser formula
-2LLH	-	118.1	

9.4 Previous experimental results for priors

Several experimental results were available for this analysis to use as priors on the nuisance parameters, to ensure the results of this analysis are in agreement with known results. These previous results are categorized by fitter parameter (phi-conv, cr-index, phi-astro, astro-index, phi-prompt, nu-scaling, DE, and K-scaling) and are discussed in the following sections. Once chosen, the priors are applied to the fitter parameters using a Gaussian distribution about the mean with the constraint representing one standard deviation. Table 9.5 later in this chapter summarizes all the priors used.

9.4.1 Conventional flux coefficient and cosmic ray index priors

Because the conventional atmospheric neutrinos are produced in cosmic ray air showers, their energy distribution depends upon the initial energy distribution of the cosmic ray particles. Although many experiments have measured the cosmic ray energy spectrum and normalization, there are still differences between the various experimental results.

The variations in the cosmic ray flux and subsequent neutrino production are managed in this analysis in two ways. First, the energy index is varied within the small difference between experimental results. Parameterizations of the cosmic ray energy spectrum depend upon the source populations and composition (see Chapter 3). When comparing the most favored methods of parameterization (mainly Gaisser H3a and Hörandel-modified), the spectral index varied up to ± 0.05 for energies below the cosmic ray knee. Therefore, the cr-index parameter was assigned a prior with mean -2.65 and standard deviation ± 0.05 in this analysis. As was discussed in Chapter 8, the weights of the conventional and prompt fluxes were multiplied by a factor $(E_\nu)^{-\Delta\gamma}$, where E_ν is the true neutrino energy from simulation, and $\Delta\gamma$ is the change in the cosmic ray spectral index (cr-index) from theoretical expectations.

When examining the theoretical expectations, the uncertainty in the conventional neutrino flux normalization arises from uncertainties in the production cross sections for pions and kaons, the hadronic interaction cross sections, and the atmospheric density profile. The main contribution comes from the meson production cross sections. According to Honda et al. [126], the conservatively estimated uncertainties on the total neutrino flux, averaged over all zenith angles, are ∼20-25% at 1 TeV. The peak of the energy distribution of events in this data sample is near 1 TeV, and approximately 70% of all events in the final data sample are in the two lowest energy bins (below 3.2 TeV).

The effect of different choices for the prior on the fit results were examined, from 0% (no prior) to 30%, while the DOM efficiency and Kaon scaling factors were held fixed (since the three parameters affect the result in similar ways). There was almost no difference in the XS result (± 0.01x SM), the phi-conv value (± 0.01x expectation), or the $-2LLH$ value (± 0.5). Therefore, for the final fit, a conventional flux prior (phi-conv) of 1.0x ± 0.25x and a cosmic ray index prior (cr-index) of -2.65 ± 0.05 is assumed.

9.4.2 Astrophysical flux coefficient and energy index priors

There are a large number of recent astrophysical flux results that are available to use as priors for the phi-astro and astro-index fit parameters. In all cases, two assumptions are made in the analyses. The first is that there are equal numbers of ν and $\bar{\nu}$ arriving at the Earth. The second is that the neutrino flavor ratio is 1:1:1 at the Earth due to neutrino oscillations on the long journeys through the universe. Two analyses in IceCube [212; 213] examined the flavor ratio and determined that the particles detected in IceCube are consistent with a 1:1:1 ratio and the assumptions.

Most analyses are starting-event analyses, such as the high-energy starting event (HESE) analysis. The neutrino interactions occurred within the detector volume, with no evidence of a muon track before the large cascade in the detector. Most of these events were electron neutrinos. Other analyses looked for muon neutrino events, which resulted in a track signature in the detector. Still others combined the flavors into one analysis.

Before discussing each analysis, a reminder is that the important astrophysical parameters are ϕ, which is the astrophysical flux coefficient at 100 TeV, and γ, which is the spectral index of the flux. The units for a flux with ϕ = 1.0 and γ = -2.0 are 1.0 x $(E_\nu/100\ \text{TeV})^{-2.0} \cdot 10^{-18}$ GeV^{-1} cm^{-2} sr^{-1} s^{-1}. The coefficient and energy index are the values that differ in each analysis, and the results are listed with their 1σ uncertainties in Table 9.4.

The first analysis with an astrophysical flux measurement that was evaluated was the HESE-4 analysis in IceCube [214]. This is a follow-up analysis to HESE-3 [215] using four years of data. The second analysis was the starting-track analysis by Jakob van Santen and the IceCube collaboration [216]. The third analysis was the starting track analysis by Gary Binder and the IceCube Collaboration [212]. The fourth analysis was the high-energy astrophysical analysis by Christopher Weaver and the IceCube Collaboration [205]. In this analysis, the muon neutrino flux result was in statistical agreement with the electron neutrino flux from the van Santen analysis, which further supported the assumption of a 1:1:1 flavor ratio for astrophysical neutrinos at the Earth. However, the method of event selection for this analysis is nearly identical to that used by Weaver for his astrophysical analysis. Therefore, this astrophysical flux was not used for the prior, although it is included in the systematics evaluation later in this chapter.

The fifth analysis was the two-year Cascade analysis by the IceCube Collaboration [217]. The sixth analysis was the Global Fit analysis by Lars Mohrmann and the IceCube Collaboration [218]. The analysis combined the results from several previous IceCube astrophysical flux analyses (starting events, up-going and down-going muon tracks, etc.) from 2008-2013 and compared the distributions of energy, zenith angle, and particle type to various models and assumptions. The seventh analysis was the Multi-Year analysis by Leif Raedel and Sebastian Schoenen with the IceCube collaboration [138]. This analysis compared up-going muon neutrinos from six years of data from 2009-2014. Using high-purity samples of well-reconstructed up-going muon neutrinos, they used a forward-folding likelihood fit in two dimensions (energy and zenith).

The selection of the most suitable astrophysical flux prior involved several considerations. First, there was no choice but to use an IceCube measurement instead of an independent measurement because no other results were available. This should not pose a problem, however, since the analyses were performed for different neutrino flavors, directions, event selection techniques, and years of data, where the detector size changed. In the end, the choice of prior did not affect the analysis results, which is discussed later in this chapter.

Next, the available analyses were evaluated by particle type, particle direction, number of years of data, and energy ranges of the results. This narrowed the choices to Global Fit and Multi-Year, since both experiments combined six years of data in a weighted fit. The most important factor was whether the analysis included the data from this analysis and in what proportion. Both analyses used the data from this analysis as a small subset of their data. The proportion was larger in Multi-Year than in Global Fit because Multi-Year only looked for muon neutrinos while Global Fit looked for all flavors. Therefore, the astrophysical flux result that was chosen as the prior for this analysis was Global Fit. The analysis involved the comprehensive compilation of all previous results using all types of particle signatures from all directions in the widest energy range and with the lowest percentage overlap with this analysis' data sample. All astrophysical flux results were eventually included in the systematic studies later in this chapter.

Table 9.4: Summary of astrophysical flux results that were evaluated as priors for this analysis. Astrophysical flux values are listed as ϕ ($\pm\phi$ error) x $E^{-\gamma\pm\gamma\ error}$, which represents a flux expressed fully as (for example HESE-4) 2.2 ($\pm$0.7) x $(E_\nu/100\ \text{TeV})^{-2.58\pm0.25} \cdot 10^{-18} GeV^{-1} cm^{-2} sr^{-1} s^{-1}$. Energy ranges are different because of the different analysis methods. There is currently some tension between results for cascades and for tracks. $\star$ NOTE: valid energy range was not available; analysis energy range is listed for comparison

Result name	Best fit E^{-2}	Best fit flux	Energy range
HESE-4 (prelim) [214]	0.84 ($\pm$0.3)	2.2 ($\pm$0.7) x $E^{-2.58\pm0.25}$	60 TeV - 3 PeV $\star$
van Santen [216]	1.22 ($\pm$0.5)	2.06 $(^{+0.35}_{-0.26})$ x $E^{-2.46\pm0.12}$	25 TeV - 1.4 PeV
Binder [212]	0.6 $(^{+0.3}_{-0.2})$	2.3 ($\pm$0.4) x $E^{-2.6\pm0.15}$	35 TeV - 1.9 PeV
Weaver [205]	0.99 $(^{+0.39}_{-0.34})$	1.7 $(^{+0.6}_{-0.8})$ x $E^{-2.2\pm0.2}$	330 TeV - 1.4 PeV
Cascades [217]	-	2.3 ($\pm$0.7) x $E^{-2.67\pm0.13}$	10 TeV - 1 PeV $\star$
Global Fit (all) [218]	1.73 $(^{+0.63}_{-0.50})$	2.23 $(^{+0.40}_{-0.37})$ x $E^{-2.50\pm0.09}$	25 TeV - 2.8 PeV
Global Fit (north) [218]	-	0.7 $(^{+1.0}_{-0.5})$ x $E^{-2.0+0.3-0.4}$	25 TeV - 2.8 PeV
Global Fit (south) [218]	-	2.3 ($\pm$0.5) x $E^{-2.56\pm0.12}$	25 TeV - 2.8 PeV
Multi-Year (prelim) [138]	0.46 $(^{+0.24}_{-0.19})$	0.82 $(^{+0.30}_{-0.26})$ x $E^{-2.08\pm0.13}$	170 TeV - 3.8 PeV

9.4.3 Prompt flux coefficient and energy index priors

No experiment to-date has made a significant discovery of a prompt atmospheric neutrino flux, but a prompt flux from cosmic rays is expected. Over the years, several limits have been placed on the multiple of the ERS theoretical prompt flux. In every case, the assumption is that the change in prompt energy index follows the change in cosmic ray spectral index. This analysis made the same assumption about the change in index.

Most analyses with an astrophysical flux measurement found the best-fit prompt flux to be 0. If the uncertainty was +1.0x ERS, then the allowable range of the prompt flux in the fitter would be 0 $\pm$ 1.0 with a Gaussian distribution. However, a negative flux is not physical, and thus a hard lower limit of 0 had to be included. For the fitter in this analysis, a Gaussian distribution of 0$\pm$1.0 with a hard limit at 0 was easily incorporated. The best prompt flux limit to-date is from the Multi-Year analysis at 1.06 x ERS expectation at 90% confidence [138]. The prompt flux limit (0.0 $\pm$ 1.06) is used for the prior in this analysis.

In the end, the fit was not sensitive to changes in the prompt flux limit, so the exact choice of prompt prior was not critical to the final result of this analysis. However, the effect of the prompt prior on the XS values is evaluated in the combined astrophysical/prompt flux systematics section of this chapter.

9.4.4 Nu-scaling prior

Theoretical predictions for the ratio of ν to $\bar{\nu}$ in the conventional flux are based upon cosmic ray composition models and are subject to uncertainties. Previously published works do not provide much guidance since there are no measurements of the ratio in the high-energy range. There are three main papers to review: Agrawal et al. [219], Honda et al. [126], and Gaisser [220]. The Agrawal and Honda papers provide some guidance on the uncertainty in the ratio but do not extend into the energy range of this analysis.

In the Gaisser paper, the μ to $\bar{\mu}$ ratio results of OPERA [221] are converted to atmospheric ν and $\bar{\nu}$ and their ratio extrapolated to higher energies. Since the equation representing the flux of muons in the atmosphere is similar to the flux of muon neutrinos, the measured spectrum of atmospheric muons can be used to tune the hadronic production model for neutrino flux calculations to determine the ratio of ν to $\bar{\nu}$. This ratio is shown in Figure 9.3. The ν to $\bar{\nu}$ ratio at the highest energy in the figure is ~2.4 ($\pm$ 0.1) for 100 TeV.

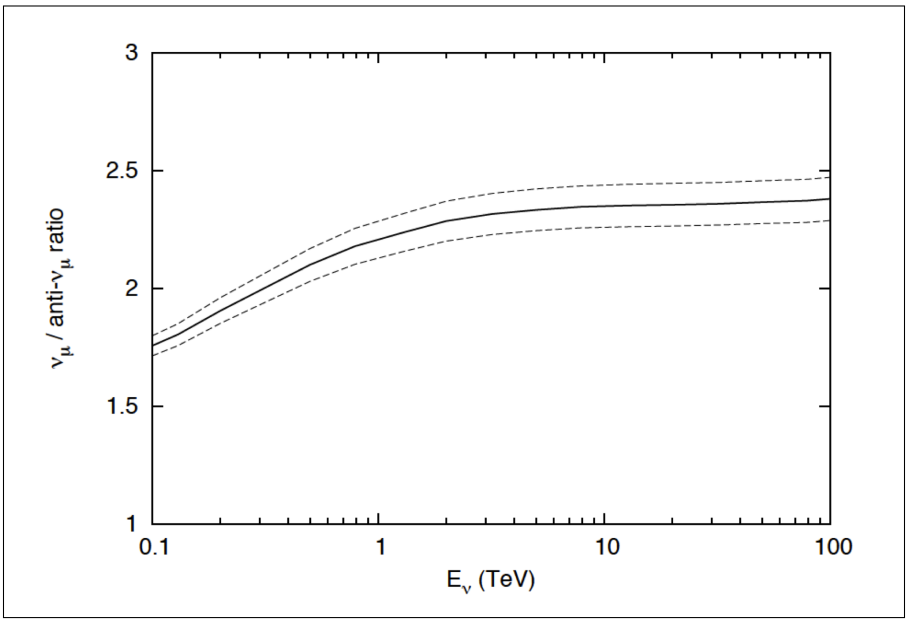

Figure 9.3: Ratio of ν to $\bar{\nu}$, inferred from the results of OPERA [221]. The ratio for the highest energy of 100 TeV is 2.4 ($\pm$ 0.1), for use as a prior on the nu-scaling parameter. From [220].

Because this analysis uses a nu-scaling parameter, instead of the ratio of ν to $\bar{\nu}$, the percent ratio uncertainty from the Gaisser paper needs to be converted into the appropriate uncertainty on the nu-scaling parameter. An equation that relates the two variables is $G = 0.7n/(1-0.7n)$, where G is the ratio from Gaisser's paper, 0.7 is the baseline fractional expectation of ν from NeutrinoFlux, and n is the nu-scaling parameter. Differentiating both sides and setting n equal to 1.0, the change in the nu-scaling parameter is ~0.13 times the change in the Gaisser ratio. Thus, a change of 0.1 in the Gaisser ratio becomes ~0.01 for the nu-scaling parameter, or only $\pm$1%.

Because of the extrapolation and unknown uncertainties at higher energies, a more conservative range for the nu-scaling parameter of $\pm$10% (1.0 $\pm$ 0.10) is used in this analysis. In the end, the fit was not sensitive to changes in the nu-scaling parameter, and so the choice of prior was not critical to the final result of this analysis.

9.4.5 DOM efficiency prior

The DOM efficiency in IceCube has been studied in several different ways. One early study [222] examined the systematic uncertainty of the absolute calibration of the DOMs. This was done using four different wavelengths of light from LEDs in the laboratory and comparing responses. The result was a $\pm$7.8% variation between DOMs in the study. For

the fully-constructed detector, this variation should have minimal impact on the overall DOM efficiency factor due to averaging of the influence from more than 5,000 DOMs.

Another study used a sample of minimum-ionizing muons (MIMs) from cosmic-ray showers [193] in the detector. These muons are well-suited for energy scale calibrations (which directly relate to DOM efficiency) because they are abundant, they have a known constant light emission, and they leave well-defined tracks in the detector. Using a sample of MIMs from the deep clear ice, the events were binned based upon the observed charge versus the track-to-DOM distance. Figure 9.4 shows the results of that analysis, along with expectations for DOM efficiencies ±10% from nominal. Although the curves in the plot start to deviate ∼100 meters, the energy reconstruction algorithms in this analysis only use DOMs up to 60 meters from track. The muon energy would be the most impacted by a change in DOM efficiency. Overall, the findings were an average charge excess $< 5\%$ in data compared to simulation with up to 9% deviations at some distances, indicating that the uncertainty in DOM efficiency might be as much as 10%.

A later study [223] examined MIMs to see if the modeled DOM efficiency in simulation correctly matched the efficiency from data. This study found that the DOM efficiency would be more correctly modeled if the nominal 100% efficiency were changed to 110%±3%. This change was adopted in the IC-79 data year and is the reason why the nominal efficiency is referred to as 110% in this analysis.

Combining the results and information from all these studies, one might assume an initial uncertainty of ±3-5%. For this analysis, a conservative uncertainty of ±10% for the DE parameter is used.

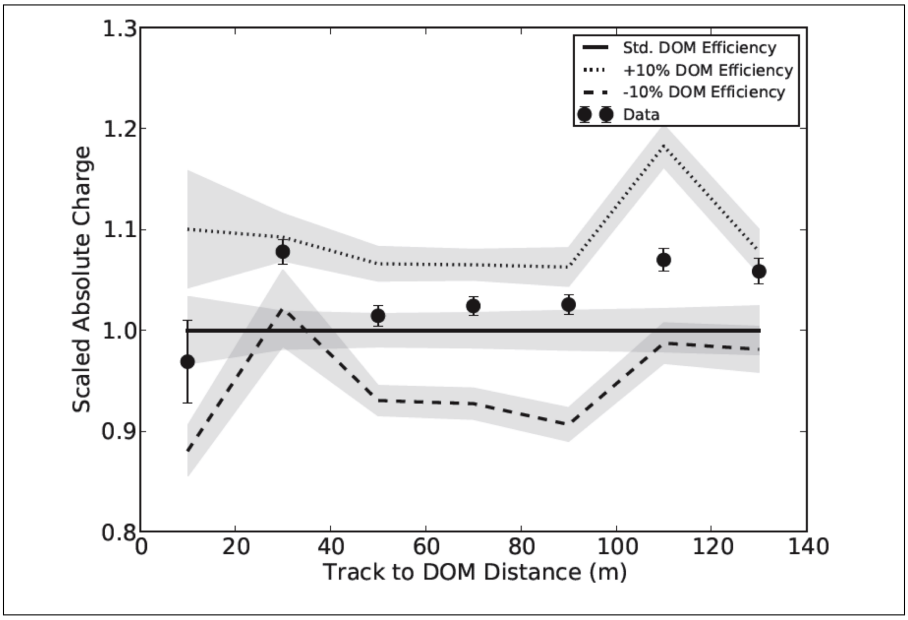

Figure 9.4: Average charge versus track-to-DOM distance, normalized to the charge expected from simulation and compared to data. Simulations with different DOM efficiencies are shown for comparison. The observed charge is slightly higher than nominal values but below the charge expected for a DOM efficiency increased by 10% (upper band). Error bars reflect statistical uncertainties, but systematic uncertainties are not included. From [193].

9.4.6 Kaon scaling prior

Changes in the ratio of kaons to pions in the initial cosmic ray interaction create a slight shift in the energy and zenith angle distributions. A larger kaon fraction will shift the flux to higher energies and decrease the flux at the horizon. The Honda et al. 2006 model for the conventional neutrino flux compares the flux of horizontal neutrinos to vertical neutrinos. Their flux uncertainty is 3% and comes mainly from the kaon-pion ratio [126]. Converting this to the kaon scaling factor that was used in this analysis, the uncertainty becomes 10%. The prior used in this analysis for K-scaling is therefore 1.0 ± 0.1.

9.5 Final cross-section results with priors

Once the appropriate priors from the previous experimental results were determined, a final fit result was obtained by applying the priors using a Gaussian distribution and running the MINUIT MIGRAD fitting program. Figure 9.5 shows the ΔLLH values versus the XS value, along with the values of some of the nuisance parameters. The overall fit results are given in Table 9.5, with a summary of the selected priors.

The final XS value is 1.30 (+0.21 -0.19 statistical) times the SM expectation from the CSMS cross-section calculation for the total muon neutrino to nucleon cross section, including both CC and NC interactions for both ν and $\bar{\nu}$. Note that the initial assumption is that the CC and NC cross sections scale together, and that ν and $\bar{\nu}$ cross sections are scaled by the same factor equally.

The statistical uncertainty for the XS value is calculated by fixing all of the nuisance parameters to their best-fit values. Then the change in the XS value for a change in $-2LLH$ of ±1.0 is determined. In addition, the uncertainties on the nuisance parameters are determined by allowing all parameter values to float, then calling the function "optimize.brentq", which uses the classic Brent method to find the bounds on the likelihood function where that function is flat within the bounds [224]. This method provides the 1σ limit for the parameter under investigation.

The XS systematic uncertainty (due to the fit parameters) is determined by first finding the 1σ change in the $-2LLH$ value with all fit parameters floating, which would be the combined uncertainty due to both the systematic and statistical uncertainties. From this uncertainty of (+0.32 -0.27), the statistical uncertainty of (+0.21 -0.19) is subtracted in quadrature. The remaining uncertainty is then the systematic uncertainty due to the fit parameters, which is (+0.24 -0.19).

The normalization factor on the conventional flux is 0.92 (+0.07 -0.06), which is close to the nominal 1.0 and well within the 1σ Gaussian prior. The normalization on the prompt flux is 0.50 (+0.99 -0.50) times ERS predictions, but the flux is not measured with significance here. The astrophysical flux coefficient of 2.62 is 1σ higher than the Global Fit prior. The astrophysical energy index is also 1σ higher than Global Fit, at -2.42. The cosmic ray energy index change is +0.007 (±0.019) from nominal, in good agreement with model expectations. The nu-scaling parameter is only 1% different from expectations, which agrees with the uncertainty expectation from the Gaisser paper. The DE factor is 4.9% higher, but with a large uncertainty of (+8.5% -7.6%). The K-scaling factor is 1.05 (±0.09), a 5% increase

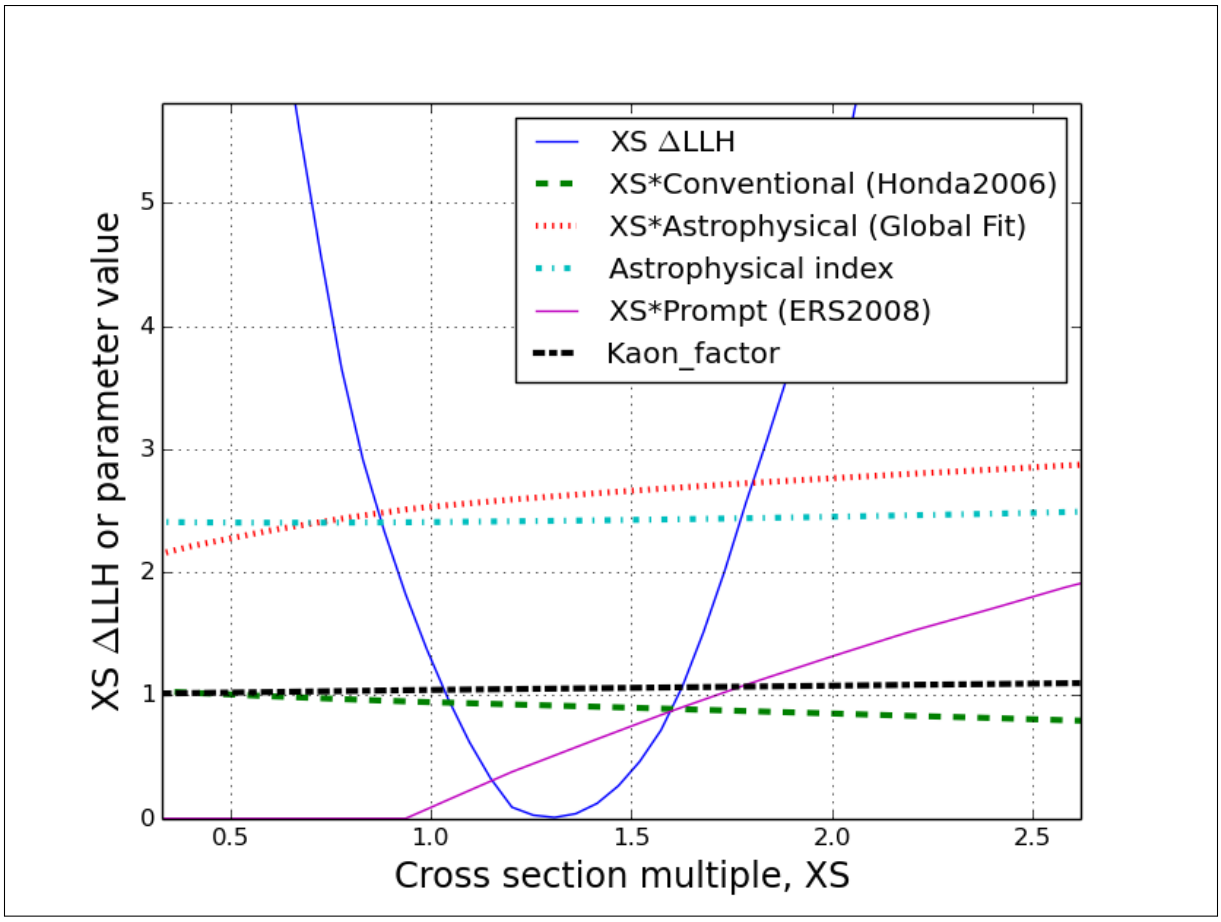

Figure 9.5: Fitter ΔLLH values versus cross-section multiple, XS (blue line). The best fit XS value was 1.30 (+0.21 -0.19 stat). Some nuisance parameters are also shown, in response to changes in XS value. The negative energy index was changed to a positive value to be visible on this plot.

Table 9.5: Final fit results with uncertainties and priors. Previous experimental results which were used as priors assumed a Gaussian distribution of the uncertainties.

Parameter	Prior value	Fit value (uncertainty)	Variable identification
XS	-	1.30x $^{(+0.21\ -0.19\ \text{stat})}_{(+0.24\ -0.19\ \text{syst})}$	x SM (CSMS calculation)
phi-conv	1.0 ±0.25	0.92 (+0.07 -0.06)	x Honda2006+GaisserH3a+Elbert
phi-prompt	0 +1.06	0.50 (+0.99 -0.50)	x ERS calculation
phi-astro	2.23 ±0.4	2.62 (+0.38 -0.37)	ϕ term
astro-index	-2.50 ±0.09	-2.42 (±0.09)	γ term
cr-index	± 0.05	+0.007 (±0.019)	change from nominal energy index
nu-scaling	1.0 ±0.1	1.01 (±0.01)	x NeutrinoFlux ν contribution
DE	0 ± 10%	+4.9% (+8.5% -7.6%)	change from 110% nominal
K-scaling	1.0 ±0.1	1.05 (±0.09)	x kaon portion of Gaisser formula
$-2LLH$	-	139.8	

in the number of kaons compared to predictions. The $-2LLH$ value is 139.8, which is ∼21 points higher than the fit without priors, higher than anticipated. The possible causes of this difference are examined later in this chapter.

Figures 9.6 and 9.7 show the agreement between the fluxes for the best-fit XS of 1.3x SM and the data, in one dimension for TruncatedEnergy muon energy and for reconstructed zenith angle. The best fit curves agree with the data within the statistical error bars in most bins.

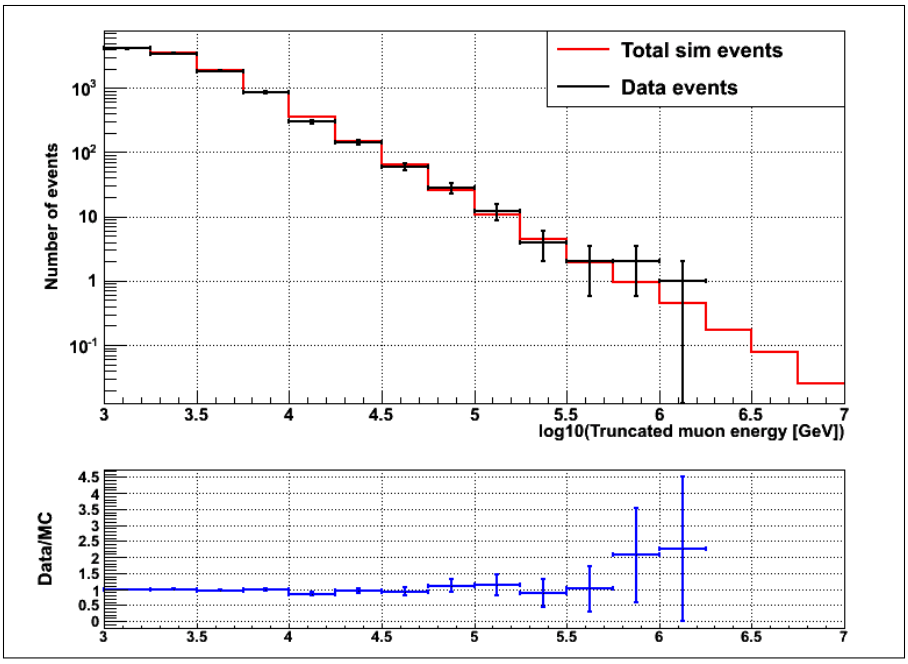

Figure 9.6: Muon flux versus TruncatedEnergy muon energy for the best fit XS of 1.3x SM. The best fit curve agrees with the data within the statistical error bars in most bins.

9.6 Correlation matrices

The fit was cross-checked by examining the correlation matrices of the fit parameters and comparing the results with priors and without priors. Tables 9.6 and 9.7 show the matrices. Without priors, there are correlations (> 0.50) and anti-correlations ($<$ -0.50) between the fit parameters, which demonstrates how the data constrains the values of the fit parameters.

The highest correlation occurs between phi-astro and astro-index. This is understandable because of the conservation of the number of events when comparing simulation to data. If the astrophysical index becomes more negative, the astrophysical coefficient increases to compensate for the loss of events due to the steeper energy curve. The higher correlations indicate that it is difficult to determine which parameter in the correlation should be higher and in what amount. The correlations are reduced with priors because the Gaussian application of the priors creates a penalty to the $-2LLH$ value if the nuisance parameter varies too far from its value with the prior. The priors constrain the nuisance parameters to the point of breaking the degeneracy and providing a better fit result. Since the fitter is minimizing

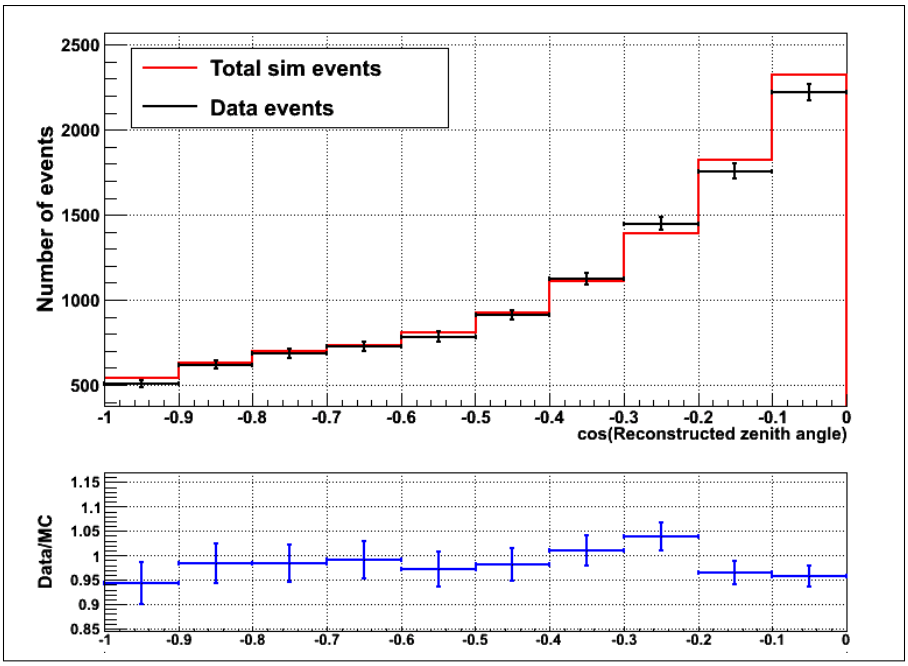

Figure 9.7: Muon flux versus cosine of reconstructed zenith angle for the best fit XS of 1.3x SM. The best fit curve agrees with the data within the statistical error bars in most bins.

Table 9.6: Correlation matrix for the fitter parameters, without priors. Boldface numbers (on only one side of the diagonal) show correlations larger than ± 0.5.

	XS	phi-conv	phi-prompt	phi-astro	cr-index	astro-index	DE	K-scaling	nu-scaling
XS	1.	**-0.51**	-0.01	**0.78**	**0.56**	**0.67**	**0.51**	-0.05	0.01
phi-conv	-0.51	1.	0.06	-0.39	-0.39	-0.21	**-0.99**	0.04	-0.15
phi-prompt	-0.01	0.06	1.	-0.02	-0.01	-0.01	-0.06	0.03	0.00
phi-astro	0.78	-0.39	-0.02	1.	**0.77**	**0.91**	0.34	-0.04	-0.08
cr-index	0.56	-0.39	-0.01	0.77	1.	**0.65**	0.35	-0.04	-0.24
astro-index	0.67	-0.21	-0.01	0.91	0.65	1.	0.16	-0.05	-0.08
DE	0.51	-0.99	-0.06	0.34	0.35	0.16	1.	-0.04	0.16
K-scaling	-0.05	0.04	0.03	-0.04	-0.04	-0.05	-0.04	1.	0.00
nu-scaling	0.01	-0.15	0.00	-0.08	-0.24	-0.08	0.16	0.00	1.

$-2LLH$, constraining some nuisance parameters with strict priors might force other nuisance parameters to a region of the likelihood space where they now become more correlated with other parameters.

In addition, the conventional flux and DOM efficiency anti-correlation remained essentially the same after the priors were included, but the prompt flux correlation with XS increased. This was due to the relatively strict priors on the other parameters, keeping them within experimental bounds while the phi-prompt parameter had more room to maneuver within its constraints, giving the appearance of a higher correlation.

Table 9.7: Correlation matrix for the fitter parameters, with priors. Boldface numbers (on only one side of the diagonal) show correlations larger than ± 0.5, which have been significantly reduced in number by the use of priors.

	XS	phi-conv	phi-prompt	phi-astro	cr-index	astro-index	DE	K-scaling	nu-scaling
XS	1.	-0.19	0.43	0.22	-0.09	0.14	0.18	0.12	0.05
phi-conv	-0.19	1.	-0.03	-0.01	-0.14	-0.02	**-0.92**	-0.28	0.00
phi-prompt	0.43	-0.03	1.	-0.05	0.19	0.05	0.01	-0.00	0.01
phi-astro	0.22	-0.01	-0.05	1.	0.15	0.03	-0.00	0.02	0.01
cr-index	-0.09	-0.14	0.19	0.15	1.	-0.00	-0.10	0.07	-0.10
astro-index	0.14	-0.02	0.05	0.03	-0.00	1.	0.02	-0.03	-0.02
DE	0.18	-0.92	0.01	-0.00	-0.10	0.02	1.	-0.11	0.01
K-scaling	0.12	-0.28	-0.00	0.02	0.07	-0.03	-0.11	1.	-0.04
nu-scaling	0.05	0.00	0.01	0.01	-0.10	-0.02	0.01	-0.04	1.

9.7 Comparison of LLH values, with and without priors

When comparing the $-2LLH$ values for the fit with and without priors, a difference of ∼21 seemed large (118.1 without priors compared to 139.8 with priors). A difference of 2.3 for a 2-dimensional fit represents a 1σ deviation, and a difference of 21 is over 4σ. The reason for this difference was investigated. The first possibility was that the low statistics for the higher energy events might have caused some difficulties with the fit. The data sample had very few events with $\log_{10}(E_\mu)$ above 5.0. In total, there were only 21 events above 5.0 in the final data sample, out of 10,784, as shown in Table 9.1. As the $\log_{10}(E_\mu)$ increased above 5.0, the conventional flux was expected to drop, and the astrophysical and prompt fluxes would become dominant.

First was an examination of the differences in fit results and $-2LLH$ values when changing the upper limit of the energy range of the fit. Keeping the same binning (4 bins per energy decade and 10 cos(zenith) bins), the energy range was reduced by half decades and the fitter run again. The XS result did not change appreciably and remained within the 1σ statistical uncertainty of the final result. The difference in $-2LLH$ became smaller as the upper limit of the energy range was lowered. This agreed with the initial assumption that the large difference in $-2LLH$ values (between the fit with priors and the fit without priors) was due to the data events at higher energies versus the astrophysical and prompt flux predictions. When removing this part of the energy range from the fit, the $-2LLH$ values were more in agreement, as expected.

An additional study was performed at the lower energy of the analysis fitter range. In this study, events were eliminated at the lower energies and the fit reaccomplished. The $-2LLH$ values decreased when the value of $\log_{10}(E_\mu)$ at the low end of the range was changed from 3.0 to 3.25 and then 3.5. However, in all cases (both changing the upper fitter range limit and the lower fitter range limit), the best fit XS value was well within 1σ of the best fit value without changes. The conclusion of these studies was that low statistics in the data were responsible for the changes in $-2LLH$ values, with 10,784 events divided amongst 160 bins.

It was anticipated that this same change in the $-2LLH$ value would not occur when using more than one year of data.

9.8 Systematic uncertainties

Generally, for the systematics studies in this analysis, parameters were used that were as uncorrelated as possible, although some parameters could contain combined uncertainties on more than one sub-parameter. The list of systematic studies performed included the ice model plus hole ice, Earth composition model, atmospheric temperature model, and astrophysical flux + prompt flux results.

9.8.1 Ice model systematics

The ice model in IceCube has a large number of highly-correlated parameters that would be difficult to treat individually. There is no obvious parameterization of the effects of a changing ice model, other than to use another ice model. IceCube simulation for IC-79 used the SPICE-Mie ice model (see Chapter 4). Older models were labeled as outdated and were not used for systematic studies, and newer models were not available until IC-86.

Thus, in IceCube IC-79, the only available method for determining systematic uncertainties in the ice model was to change the absorption and scattering effectiveness and run separate simulation sets. This new simulation was created with ∼1 million events (about 1/10 of the main simulation file) and then processed through the full event selection method. The output text files were then run individually through the fitter, and the results were compared to the final cross-section result. The largest differences in the fit results would determine the uncertainty for that parameter.

The ice model variations used in this analysis included the following: scattering length +10% (simulation set 11067); absorption length +10% (set 11028); and both scattering and absorption length -7.1% (set 11100). The results of this systematic uncertainty analysis are shown in Table 9.8. The differences between the nominal XS value and the extremes of the ice model results are +0.30 and -0.38.

Table 9.8: Cross section results for ice model variance (absorption and scattering). The highest and lowest values were used to calculate the systematic uncertainty due to the ice model.

Parameter	Best fit (+10% abs)	Best fit (+10% scat)	Best fit (nominal)	Best fit (-7%/-7%)
XS	1.16x	0.92x	1.30x	1.60x

Because a variance in absorption has been shown to be similar to a simple shift in the muon energy reconstructions, these numbers were checked using a 10% shift in the energy of each simulated event. This was applied in a direct way by simply shifting all muon energies in the same direction, which equated to 0.04 in $\log_{10}(E_\mu)$. When running the fitter with the energies shifted in this way, the results were generated and are shown in Table 9.9. The difference between the best fit and the energy scale variance is +0.31 and -0.28, which is in general agreement with the results from the ice model variance. Therefore, the ice model

systematic uncertainty is estimated to be +0.30x -0.38x SM, which is the largest systematic uncertainty in this analysis.

Table 9.9: Cross section results for a muon energy shift, with 10% equating to a shift of 0.04 in $\log_{10}(E_\mu)$. The results were similar to the ice model systematic evaluation.

Parameter	Best fit (-10% energy)	Best fit (0% energy)	Best fit (+10% energy)
Cross section multiple XS	1.61x	1.30x	1.02x

9.8.2 Hole ice systematics

As mentioned in Chapter 4, hole ice increases the local scattering of photons near the DOMs, most likely due to residual air bubbles after deployment. Standard IceCube simulation already includes a model for hole ice. However, the proper tables could not be located for IC-79. Instead, IC-86 simulation and data were used for this systematic analysis. New simulation (set 12057 for nominal hole ice, and set 12059 for no hole ice) were created and processed through the event selection method for IC-86 [204], along with the IC-86 data. The difference between the XS value for nominal hole ice and no hole ice was +0.04x. Therefore, the hole ice systematic uncertainty is estimated to be +0.04x -0.0x SM.

9.8.3 Earth model systematics

The Earth model PREM has remained basically unchanged since it was published in 1981. Although the model has been very stable, there is always the possibility that the model has errors. For this reason, simulation was run assuming a XS = 1.0x SM but varying PREM in both the core density and the core radius. The variation in the core properties would have the biggest possible impact on the cross-section measurement. The decision to use a generous ±10% variation in both the density and radius in simulation would adequately cover these parameters. However, the available variations in simulation started at ±20%. If the effect was linear, this would allow interpolation. Figure 9.8 shows the comparison for PREM core density changes. The effect is indeed linear, and an interpolation of the effect was made to 10%, essentially taking $\frac{1}{2}$ of the variation at 20%. The systematic uncertainty for PREM core density ±10% is ±0.04x and for PREM core radius is ±0.01x SM. The study demonstrated that a relatively large change in PREM would produce a very small change in the cross-section measurement.

9.8.4 Atmospheric temperature model systematics

In Chapter 3, the use of a standard atmospheric model instead of a model with temperature variations for the seasons was discussed. The changes in density with temperature would affect the neutrino output during the year. Two methods were considered for accounting for effects of temperature variations. The first method was created by Christopher Wiebusch and his team at Rheinisch-Westfalische Technische Hochschule (RWTH) Aachen.

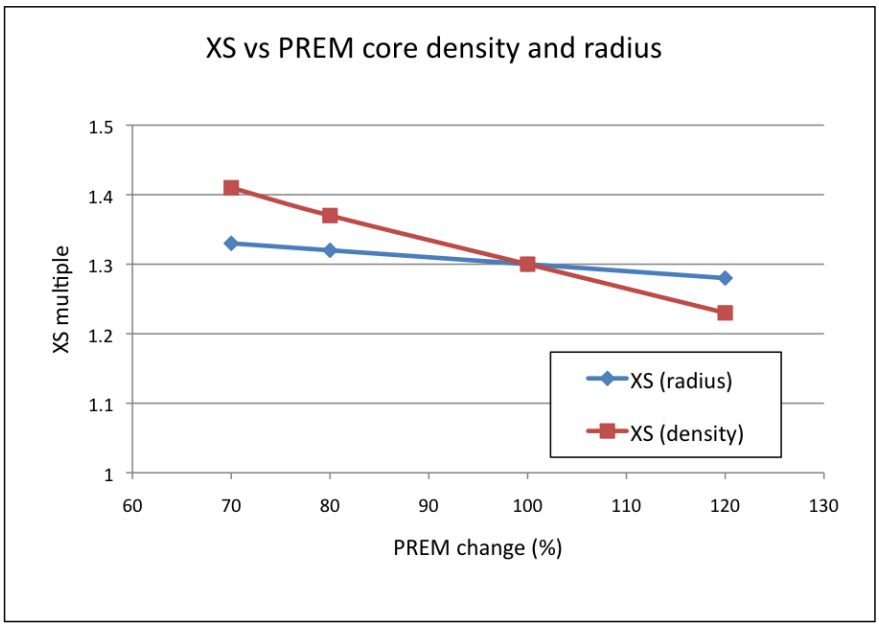

Figure 9.8: Effects of changing the PREM core density and radius on the XS value. The effect is linear for the small changes of interest, allowing interpolation to lower variations.

In the Aachen method [225], a simple correction is applied to the original predictions from NeutrinoFlux due to the actual temperature variations of the atmosphere based on actual satellite measurements.

The second method was created by Gary Binder at Lawrence Berkeley National Laboratory [226]. The Binder method used the modified Gaisser formula (Equation 3.4) for the neutrino flux but corrected the column depth directly for density changes due to temperature effects. The U.S. Standard Atmospheric seasonal model was used from the National Aeronautics and Space Administration website [227]. The Binder method was chosen for this analysis because of the method's simplicity and ease of incorporation into existing software.

At low neutrino energy < 1 TeV, the temperature effect is minimal. At higher energies, however, the corrected column height in the critical energy equation for each decaying meson becomes more important. A reweighting factor $R(E_\nu, \theta)$ for each meson's contribution is calculated using Equation 3.4. The reweighting factor is equal to the sum of all expected contributions using the temperature-corrected critical energy (E_i^{eff}), divided by the sum of the contributions using the standard critical energy (E_i), for $i = \pi$ and K:

$$R(E_\nu, \theta) = \frac{\sum_i \frac{A_{i\nu}}{1+B_{i\nu}E_\nu/E_i^{eff}(\theta)}}{\sum_i \frac{A_{i\nu}}{1+B_{i\nu}E_\nu/E_i(\theta)}} \tag{9.1}$$

After incorporating the correction factor into the event weights in simulation, the fitter was run again with the new weights. The flux rates changed by ~2-5%, depending upon the zenith angle. Cross section results from this fit were -0.04x with the temperature correction applied, compared to the overall fit result without temperature corrections. Therefore, the uncertainty from atmospheric temperature effects is estimated to be +0.0x -0.04x SM.

9.8.5 Astrophysical flux and prompt flux systematics

Although the prompt flux and astrophysical flux systematics have already been incorporated into the cross-section measurement via the nuisance parameters, an additional systematic study was performed to incorporate the variability in the result due to the choice of prior combination for astrophysical and prompt fluxes.

Earlier in this chapter, the astrophysical flux results that were evaluated for the role of the prior for the final result of this analysis were discussed. If an astrophysical flux measurement listed more than one result (such as northern sky only, southern sky only, whole sky, etc.), each result was used as a separate set of priors. The corresponding cross-section results using each set of priors in the fitter are listed in Table 9.10. The astrophysical flux result was implemented as two continuous parameters (astrophysical coefficient and astrophysical index) within the given error bars which are represented by a Gaussian curve. The prior for the prompt flux was 0 + 1.06 x ERS from the Multi-Year analysis.

Table 9.10: Astrophysical flux and prompt flux systematics study. Summary of XS results using various astrophysical flux analysis results as priors, including the prompt flux prior of 0 + 1.06 x ERS from Multi-Year. NOTE: Astrophysical flux values are listed as ϕ ($\pm\phi$ error) x $E^{-\gamma}$ ($\pm\gamma$ error), which represents a flux expressed fully as (for example HESE-4) 2.2 ($\pm$0.7) x $(E_\nu/100\ \text{TeV})^{-2.58}$ ($\pm$0.25) $\cdot\ 10^{-18}\ \text{GeV}^{-1} cm^{-2} sr^{-1} s^{-1}$.

Result name	Astro flux	XS fit	$-2LLH$
HESE-4 (prelim) [214]	2.2 ($\pm$0.7) x $E^{-2.58}$ ($\pm$0.25)	1.32x	135.9
van Santen [216]	2.06 $(^{+0.35}_{-0.26})$ x $E^{-2.46}$ ($\pm$0.12)	1.21x	139.4
Binder [212]	2.3 ($\pm$0.4) x $E^{-2.6}$ ($\pm$0.15)	1.29x	140.0
Weaver [205]	1.7 $(^{+0.6}_{-0.8})$ x $E^{-2.2}$ ($\pm$0.2)	1.22x	134.0
Cascades [217]	2.3 ($\pm$0.7) x $E^{-2.67}$ ($\pm$0.13)	1.47x	140.4
Global Fit (all) [218]	2.23 $(^{+0.40}_{-0.37})$ x $E^{-2.50}$ ($\pm$0.09)	1.30x	139.8
Global Fit (north) [218]	0.7 $(^{+1.0}_{-0.5})$ x $E^{-2.0}$ $(^{+0.3}_{-0.4})$	1.23x	133.6
Global Fit (south) [218]	2.3 ($\pm$0.5) x $E^{-2.56}$ ($\pm$0.12)	1.35x	139.5
Multi-Year (prelim) [138]	0.82 $(^{+0.30}_{-0.26})$ x $E^{-2.08}$ ($\pm$0.13)	1.10x	140.3

All of the results from this study agreed within statistical uncertainties with the final XS value of 1.30x. Using the results in Table 9.10, the standard deviation of the XS values was determined, which was $\pm$0.10x. This value is used as the systematic uncertainty for the choice of astrophysical and prompt priors. The conclusion from this study is that the choice of the astrophysical and prompt flux priors does not have an appreciable effect on the XS result, but the error is included in the systematic uncertainties.

9.9 Final result with uncertainties

A summary of all the systematic uncertainties discussed in this chapter is shown in Table 9.11. The total uncertainty from the individual systematic uncertainties added in quadrature is shown at the bottom of the table. The final cross-section multiple with its statistical and systematic uncertainties is shown in Table 9.12.

Table 9.11: Summary of systematic uncertainties for this analysis. The largest source of uncertainty is the ice model, and all other systematics are small in comparison, except for the uncertainty from the fit parameters calculated earlier.

Uncertainty source	Systematic error (+)	Systematic error (-)
Ice model	+0.30x	-0.38x
Hole ice	+0.04x	-0.00x
Earth core density	+0.04x	-0.04x
Earth core radius	+0.01x	-0.01x
Atmos. temp. model	+0.00x	-0.04x
Astrophysical+prompt prior	+0.10x	-0.10x
Fit parameter uncertainty	+0.24x	-0.19x
TOTAL	+0.40x	-0.44x

Table 9.12: Final cross-section result with statistical and systematic uncertainties. The cross-section multiple is 1.30x SM expectation from the CSMS model.

	Best fit value	Statistical error	Systematic error
Cross section multiple XS	1.30x SM	+0.21 -0.19	+0.40 -0.44

The XS result of this analysis is expressed as a multiple of the expectation from the CSMS model. The model also has built-in uncertainties from the formalism that derived the cross-section values [21]. The worst case uncertainty occurs at the lowest neutrino energy of 1 TeV for $\bar{\nu}$ N CC interactions. This uncertainty is +9.4% -5.2%. However, the uncertainties for this analysis are on order of 30%, which are much larger than the worst-case model errors.

The overall conclusion is that this measurement of 1.30 for the multiple of the theoretical expectation of the total muon neutrino-to-nucleon cross section is in agreement with the expectation of 1.0x SM.

9.10 Energy range of result

For the energy range in which this cross-section result is considered valid, three different methods were evaluated, which are called "surface versus detector" method, weighted LLH method, and Delta LLH method. Both the number of events detected and the fraction of neutrinos that are absorbed are important in the calculation. Each method is described below.

9.10.1 Surface versus detector method

The surface versus detector method involves the absorption of neutrinos, when comparing the surface flux to the detector flux from simulation. This method would showcase the Earth's effects from NC and CC interactions while taking into account the number of available particles per energy bin. Figure 9.9 shows the number of neutrinos interacting after arriving at the detector, from simulation. These plots are for the events that survived the final

data cuts, with a nominal XS = 1.0x SM, and the theoretical expectations for conventional, astrophysical, and prompt fluxes. For context, the fraction of neutrino events that survives the transit through the Earth is shown in Figure 9.1. The energy range that corresponds to the central 90% of available events in the detector is $\log_{10}(E_\nu)$ from 3.06 to 5.55, shown with the arrows in the figure. This energy range equates to 1.1 TeV to 350 TeV, with the mean at 10.0 TeV. This method does not take into account the contribution of individual events to the $-2LLH$ value.

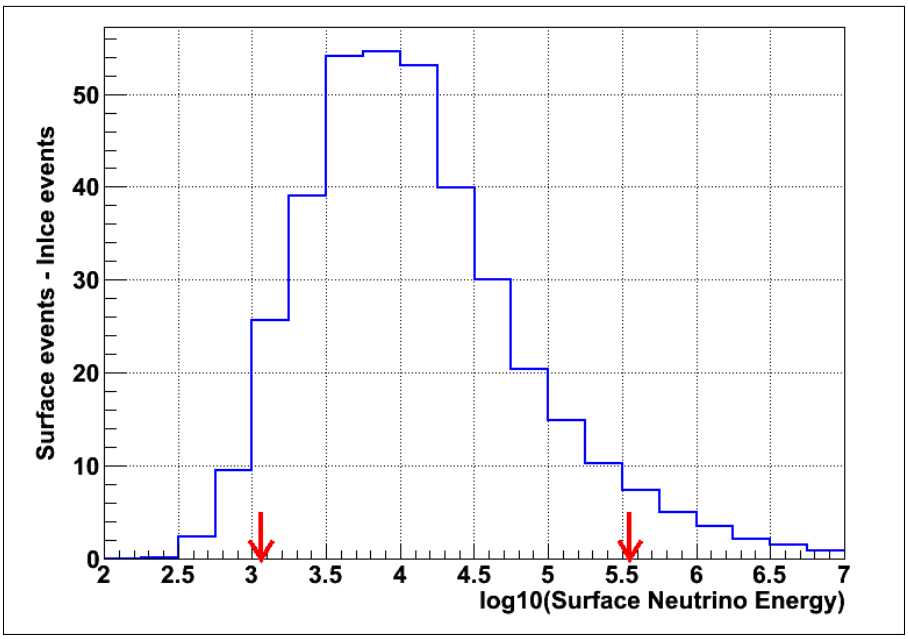

Figure 9.9: Difference between the number of total neutrinos (conventional + astrophysical + prompt) available at the Earth's surface versus the number reaching the detector and interacting. The central 90% energy range is noted with the arrows, which is $log_{10}(\mathrm{E}_\nu)$ from 3.06 to 5.55, or 1.1 to 350 TeV, with the mean at 10 TeV.

9.10.2 Weighted LLH method

The weighted LLH method was used in the Multi-Year astrophysical flux analysis [228] where each event's contribution to the $-2LLH$ value was weighted to the total $-2LLH$ value for the bin in which the event was found. Although the astrophysical flux analysis is somewhat different than this cross-section analysis (they used a forward-folding likelihood fit to the astrophysical flux in two dimensions), the energy range method can be adapted. The method is applied as follows. First, the best-fit $-2LLH$ values for each energy-zenith bin are recorded. Then, the number of events in each bin for both simulation and data are recorded. Using Equation 8.3 for the $-2LLH$ value, a weighted LLH value for each bin is calculated. Events that land in a bin are assigned the Δ LLH value for that bin. Then, each event is assigned a new LLH weight = Δ LLH $\cdot$ event weight / (sum of all event weights in that bin). A plot is made for true neutrino energy versus weighted Δ LLH value. The method is repeated for the case where there is no Earth absorption (Earth invisible), using

best-fit numbers for that scenario and the recalculation of all the parameters. Figure 9.10 shows the results of both options. The energy range from the best-fit with absorption is 3.00 to 5.93 in $\log_{10}(E_\nu)$, which equates to 1.0 TeV to 850 TeV and an average neutrino energy of 12.6 TeV (or 4.1 in $\log_{10}$). For the best-fit without absorption, the energy range is 3.07 to 6.25 in $\log_{10}(E_\nu)$, which equates to 1.2 TeV to 1.8 PeV, and an average neutrino energy of 20 TeV.

Overall, the method is well-suited for analyses with fewer numbers of events, such as astrophysical flux analyses, to determine the importance of each event in the LLH value towards to goal of a discovery. For this analysis, bins with higher numbers of events would dominate the energy range method, which is why this range extends to such a low energy where very little absorption is expected.

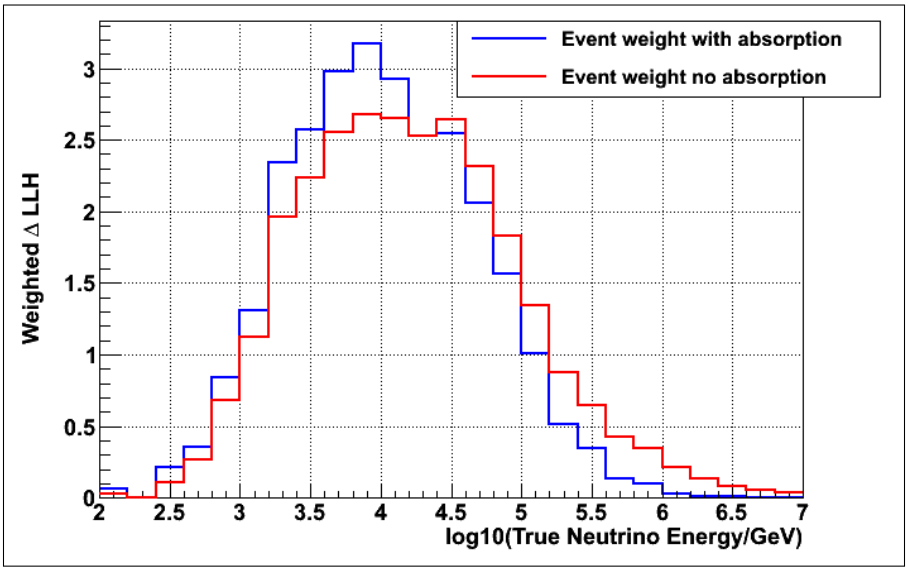

Figure 9.10: Weighted LLH energy range method, where each event is weighted according to its contribution to the overall $-2LLH$ value of the fit. Blue line shows the contributions of events using an "absorption" best fit, and red line shows the contributions using a "no absorption" (or Earth invisible) best fit. No significant difference was noted between the two methods, but both methods overestimate the lower energy range where very little neutrino absorption is expected.

9.10.3 Delta LLH method

In the Delta LLH method, the concept is to "remove events" from simulation at the ends of the energy range and refit the data, repeating this until the overall $-2LLH$ value increases by 1.0 for a 1σ change. This same energy range method was used by the Global Fit astrophysical flux result [218]. For this analysis, instead of removing the events, the requirement is to make the Earth invisible for those events. To do this, the InEarth weight was changed to 1.0, indicating no probability of absorption, for all events above or below the neutrino energy under investigation.

This method is accomplished separately on the low-energy range and the high-energy range. The results of this method are shown in Figure 9.11. The $-2LLH$ values at the

low-energy range actually slightly improved (became lower) as events were removed. This was due to some low-energy events that were below the threshold of the analysis but had been reconstructed with higher energies and thus made the final cut. Removing them from the sample would improve the fit. The energy range for this method for $\log_{10}(E_\nu)$ was 3.80 to 5.99, equating to 6.3 TeV to 980 TeV, with a median energy of 25 TeV. This value made sense because the pole-to-pole distance through the Earth's core is one absorption length for a neutrino energy of 40 TeV [27].

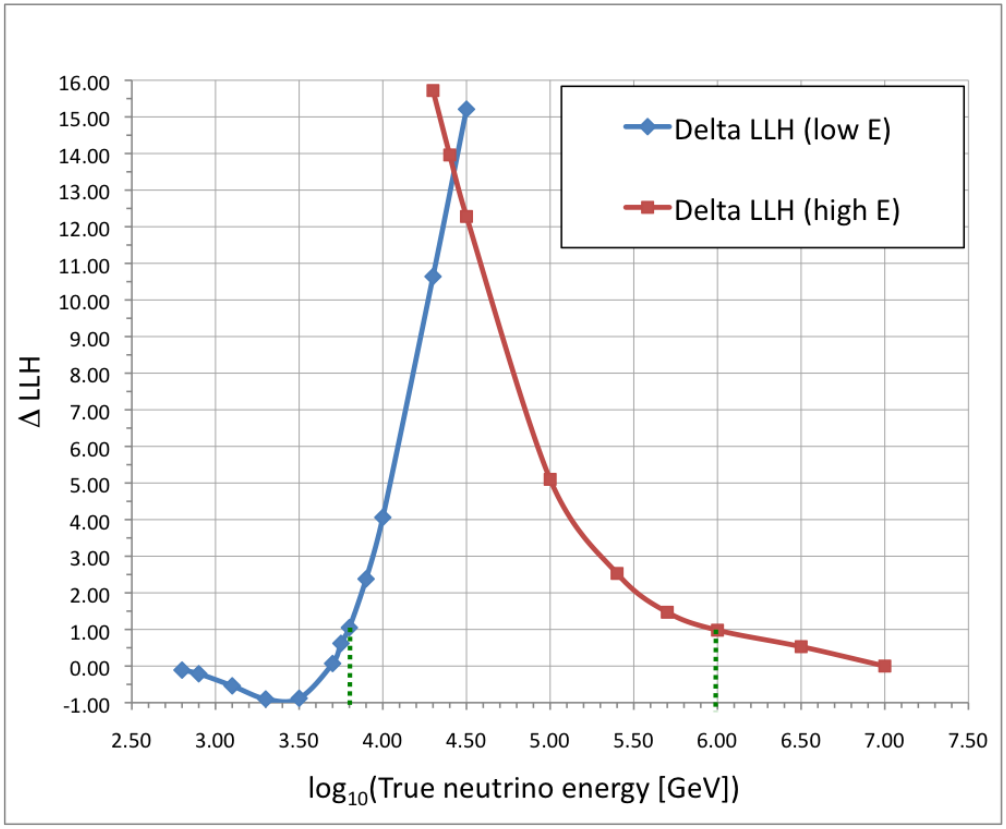

Figure 9.11: Results of the Delta LLH energy range method. Each point on the plot represents the energy where all InEarth weights were set to 1.0 (no absorption). Blue line indicates the low-energy evaluation of the Delta LLH, and red line the high-energy evaluation. The low-energy curve actually improves slightly (lower $-2LLH$ value) when removing events due to some low-energy events that were misreconstructed with higher energies, thus improving the fit when those events were removed. A Delta LLH value of 1.0 at each end equated to an energy range of 6.3 to 980 TeV, as indicated by the green lines.

Comparing the methods just described, it was determined that the most applicable energy range method for this analysis would be the Delta LLH method. The method directly tests the absorption versus no absorption hypothesis to determine the energy range. In addition, this method seems the least affected by systematics, especially at low energies with high statistics but where minimal absorption occurs. Therefore, the valid energy range for this result is determined to be 6.3 to 980 TeV, with a median energy of 25 TeV.

Chapter 10

Conclusions and Outlook

10.1 Overview of results

This analysis measured, for the first time, the total neutrino-to-nucleon cross section at multi-TeV energies, using the IceCube Neutrino Detector, by measuring the absorption of neutrinos by the Earth. The results are in agreement with the neutrino-nucleon cross-section from the Standard Model for a combination of conventional, astrophysical, and prompt neutrino sources, for the energy range from 6.3 to 980 TeV. The measurement was made with the detector in its IC-79 configuration, the year before it was fully completed. The reference cross-section calculation was CSMS 2011, the first to reach into the IceCube energy range without extrapolation. The event selection process was adopted from the Weaver analysis [204]. The simulation used NuGen and CORSIKA with the ice model SPICE-Mie-PPC. The fit was performed using a log-likelihood fitter in two dimensions which included muon energy and zenith angle. Experimental priors were used to constrain the fit parameters, and systematic uncertainties were calculated individually for cases that could not be parameterized. The final cross-section result was 1.30x SM expectations with statistical uncertainties of (+0.21 -0.19) and systematic uncertainties of (+0.40 -0.44). Figure 10.1 compares the previous accelerator results as summarized in Chapter 49 of the Particle Data Group [39] with this result. Because this cross-section measurement is for the combination of $\nu + \bar{\nu}$, the result is represented as a combination of cross sections, weighted to their average appearance in the atmospheric neutrino spectrum. The analysis finds little support for some proposed theories that predict a higher cross section as a sign of new physics. In addition, each of the analysis elements described above are possible areas for improvement in any follow-on analysis.

10.2 Possible improvements for a future analysis

There are several possible areas for improvement in a follow-on analysis, but the main area involves using a different detector. Future large detectors should be able to measure the cross section at a full range of energies. The detectors can be classified as optical or radio. In the optical category, the IceCube collaboration has proposed improvements to the detector, including GEN2 [229]. The plan is to install additional sensors using a larger

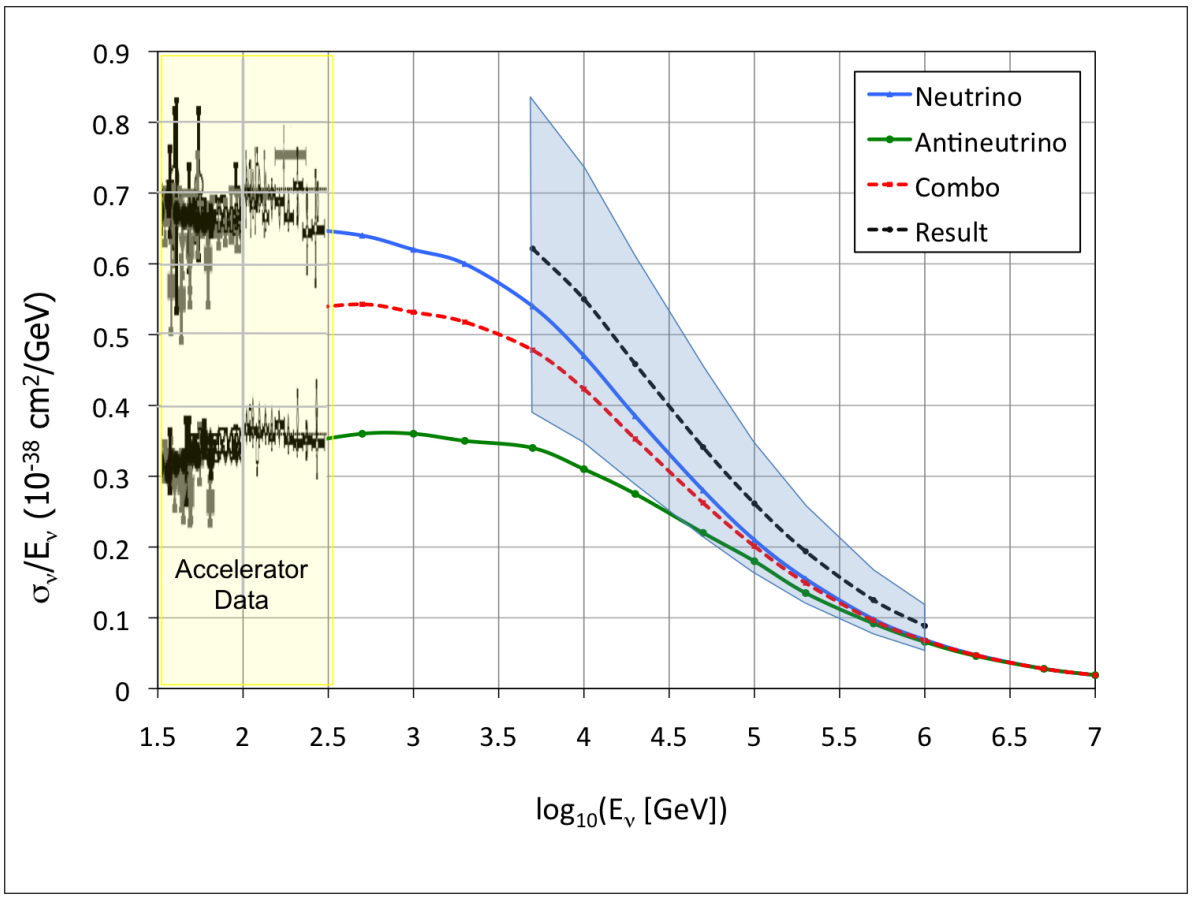

Figure 10.1: Previous accelerator results (shaded in yellow, from [39]), compared to the result from this analysis for the combined $(\nu_\mu + \bar{\nu}_\mu)N$ CC cross section. Accelerator data comes from Figure 2.7 and compressed to fit a $\log_{10}$ scale. Blue line represents the SM expectation for $\nu_\mu N$ CC cross section using CSMS. Green line represents the SM expectation for $\bar{\nu}_\mu N$ CC cross section. Dotted red line represents the flux weighted average of the two cross sections. Dotted black line represents the result of 1.3x expectation for the energy range 6.3 to 980 TeV, plus the uncertainty (blue shaded region) which includes both statistical and systematic errors added in quadrature. The result is in agreement with the SM expectation.

spacing, increasing the IceCube footprint 10-fold to provide large samples of very high energy astrophysical neutrinos, in the PeV to EeV range, and increase the yield of neutrinos across all flavors at energies above 100 TeV. The effective area for GEN2 should be ∼6 times that of IceCube. The improvements would allow additional cross-section analyses to be performed in a similar energy range to this result. Other optical detectors similar to IceCube include the Cubic Kilometre Neutrino Telescope (KM3NeT) [230] in the Mediterranean, which has been operating a prototype DOM and taking data successfully for more than a year as part of the ANTARES telescope [166]. Each of these experiments could perform a cross-section measurement to complement this result.

In the radio category, detection capabilities can be expanded in the ultra-high-energy range by a proposed extended surface array called the Askaryan Radio Array (ARA) [68], as mentioned earlier. ARA will help achieve improved sensitivity to neutrinos in the 10 PeV

to 10 EeV energy range, including cosmogenic neutrinos. The array will cover ∼200 square kilometers of ice and will detect the enhanced radio-frequency radiation from the electromagnetic and hadronic showers produced by neutrino interactions in the Antarctic ice sheet. The detection is based on the Askaryan effect, proposed by Gurgen Askaryan [231; 232] The Antarctic Ross Ice Shelf Antenna Neutrino Array (ARIANNA) [69; 233] is another proposed experiment using radio detection for neutrinos in the 100 PeV to 10 EeV energy range. A limited number of events at the higher neutrino energies ($E_\nu > 10^{17}$ eV) is expected for ARA, with less than one event in three years of ARA data with the 37-station configuration. Other experiments have already been using the radio detection concept, including the Antarctic Impulse Transient Antenna (ANITA) [234; 235] and Radio Ice Cherenkov Experiment (RICE) [236], although the latter experiment is completed and the former is nearly complete.

Figures 10.2 and 10.3 show the different energies where the detectors would be sensitive to the cross section, covering a wide range of energies. Above 100 PeV, the changes in cross section become flatter at higher neutrino energies. In addition, the small fluxes of particles would require many years of data to achieve enough statistics for a cross-section measurement, and Earth absorption would restrict cross-section measurements to near the horizon. Because of the limited zenith angle available, track reconstructions would need to be very precise.

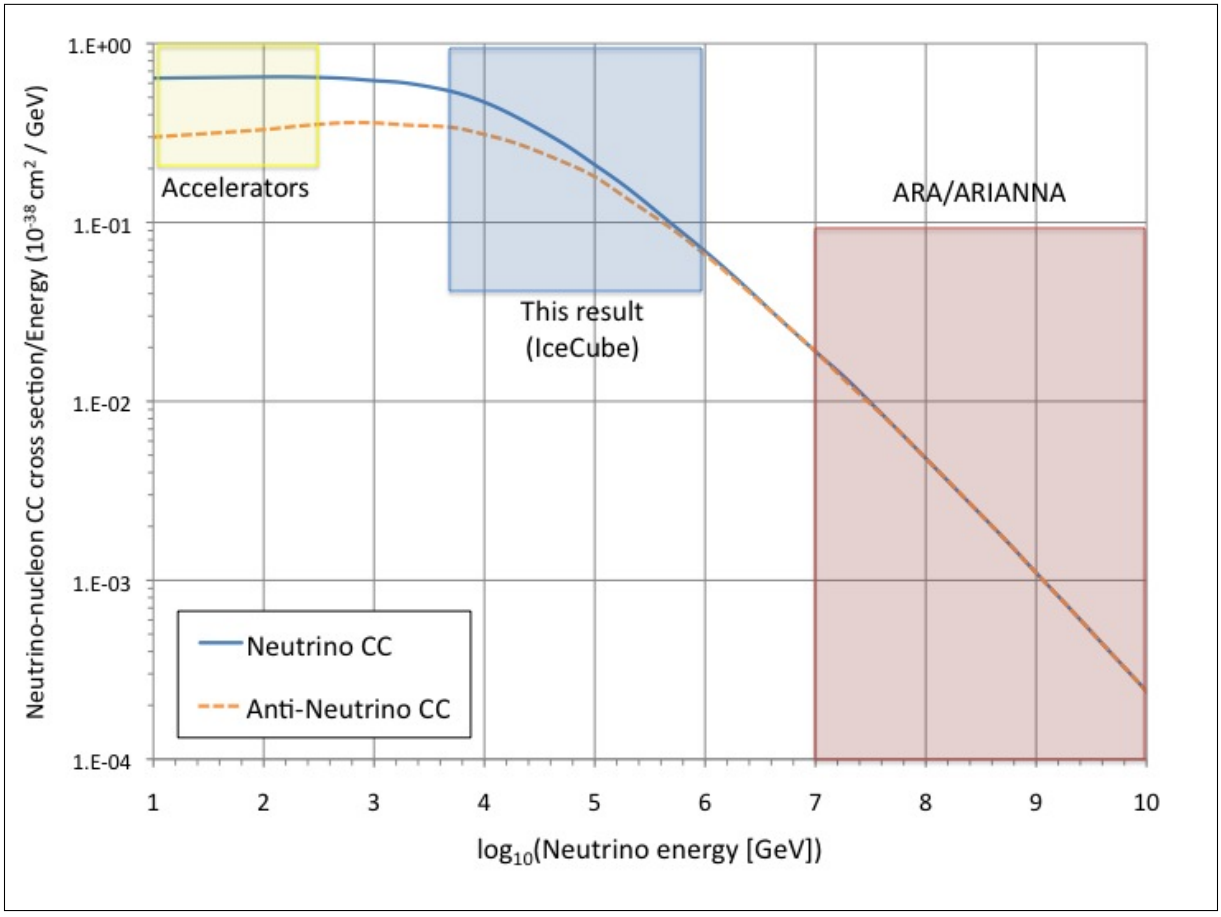

Figure 10.2: Energy ranges for cross-section measurements from the different types of experiments, including accelerators (shaded yellow), this result in IceCube (also representative of other Cherenkov detectors) (shaded gray), and ARA/ARIANNA (and other radio detectors) (shaded red). Cross section data from CSMS [21] is divided by neutrino energy.

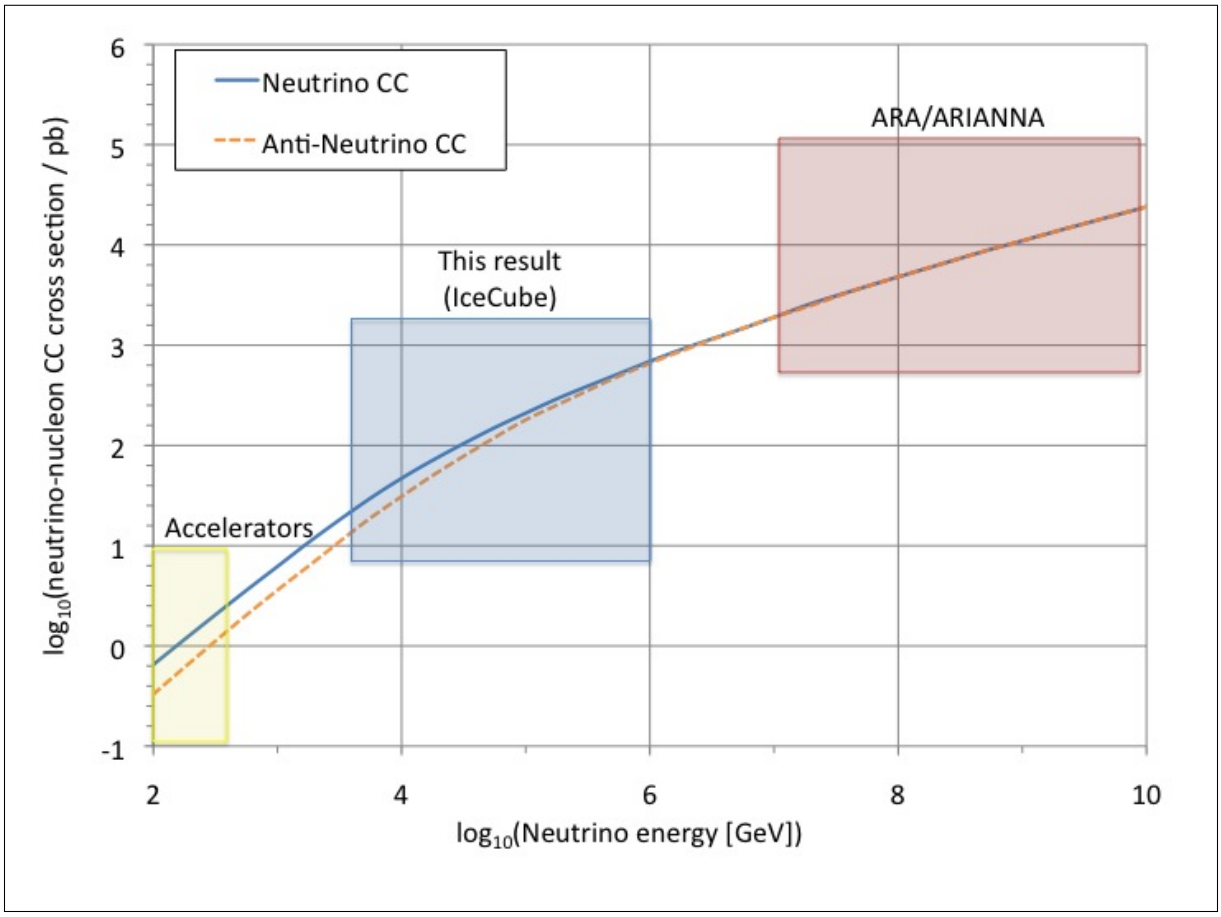

Figure 10.3: Energy ranges for cross-section measurements from the different types of experiments, including accelerators (shaded yellow), this result in IceCube (also representative of other Cherenkov detectors) (shaded gray), and ARA/ARIANNA (and other radio detectors) (shaded red). Cross section data is from CSMS [21] but not divided by neutrino energy, showing a flattening of the cross section curve.

Bibliography

[1] W. Pauli, "Dear radioactive ladies and gentlemen," *Physics Today* **31N9** (1978) 27.

[2] C. L. Cowan, F. Reines, F. B. Harrison, H. W. Kruse, and A. D. McGuire, "Detection of the free neutrino: A confirmation," *Science* **124** (1956) 103–104.

[3] M. Tzanov *et al.*, NuTeV Collaboration, "Precise measurement of neutrino and anti-neutrino differential cross sections," *Physical Review* **D74** (2006) 012008, arXiv:hep-ex/0509010 [hep-ex].

[4] G. Danby, J. M. Gaillard, K. A. Goulianos, L. M. Lederman, N. B. Mistry, M. Schwartz, and J. Steinberger, "Observation of High-Energy Neutrino Reactions and the Existence of Two Kinds of Neutrinos," *Physical Review Letters* **9** (1962) 36–44.

[5] M. L. Perl *et al.*, "Evidence for Anomalous Lepton Production in e^+ e^- Annihilation," *Physical Review Letters* **35** (1975) 1489–1492.

[6] K. Kodama *et al.*, DONUT Collaboration, "Observation of tau neutrino interactions," *Physics Letters* **B504** (2001) 218–224, arXiv:hep-ex/0012035 [hep-ex].

[7] M. Goldhaber, L. Grodzins, and A. W. Sunyar, "Helicity of Neutrinos," *Physical Review* **109** (1958) 1015–1017.

[8] B. Pontecorvo, "Neutrino Experiments and the Problem of Conservation of Leptonic Charge," *Soviet Physics Journal of Experimental and Theoretical Physics* **26** (1968) 984–988. [Zhurnal Eksperimental'noi i Teoreticheskoi Fiziki 53, 1717 (1967) (in Russian)].

[9] Q. R. Ahmad *et al.*, SNO Collaboration, "Measurement of the rate of $\nu_e + d \rightarrow p + p + e^-$ interactions produced by ^8B solar neutrinos at the Sudbury Neutrino Observatory," *Physical Review Letters* **87** (2001) 071301, arXiv:nucl-ex/0106015 [nucl-ex].

[10] B. T. Cleveland, T. Daily, R. Davis, Jr., J. R. Distel, K. Lande, C. K. Lee, P. S. Wildenhain, and J. Ullman, "Measurement of the solar electron neutrino flux with the Homestake chlorine detector," *Astrophysical Journal* **496** (1998) 505–526.

[11] M. G. Aartsen *et al.*, IceCube Collaboration, "Measurement of Atmospheric Neutrino Oscillations with IceCube," *Physical Review Letters* **111** no. 8, (2013) 081801, arXiv:1305.3909 [hep-ex].

[12] M. Apollonio *et al.*, CHOOZ Collaboration, "Search for neutrino oscillations on a long baseline at the CHOOZ nuclear power station," *European Physical Journal* **C27** (2003) 331–374, arXiv:hep-ex/0301017 [hep-ex].

[13] F. J. Hasert *et al.*, Gargamelle Neutrino Collaboration, "Observation of Neutrino

Like Interactions Without Muon Or Electron in the Gargamelle Neutrino Experiment," *Physics Letters* **B46** (1973) 138–140.
[14] S. L. Glashow, J. Iliopoulos, and L. Maiani, "Weak Interactions with Lepton-Hadron Symmetry," *Physical Review* **D2** (1970) 1285–1292.
[15] A. Salam, *Elementary Particle Theory*. Almquist and Wikselis, Stockholm, 1969.
[16] S. Weinberg, "A Model of Leptons," *Physical Review Letters* **19** (1967) 1264–1266.
[17] M. N. Rosenbluth, "High Energy Elastic Scattering of Electrons on Protons," *Physical Review* **79** (1950) 615–619.
[18] M. Thomson, "Electron-proton scattering." http://www.hep.phy.cam.ac.uk/~thomson/partIIIparticles/handouts/Handout_5_2011.pdf, 2011.
[19] J. Sakurai, *Advanced Quantum Mechanics*. Addison-Wesley, Reading, MA, 1967.
[20] R. Devenish and A. Cooper-Sarkar, *Deep inelastic scattering*. Oxford University Press, Oxford U.K., 2004.
[21] A. Cooper-Sarkar, P. Mertsch, and S. Sarkar, "The high energy neutrino cross-section in the Standard Model and its uncertainty," *Journal of High Energy Physics* **08** (2011) 042, arXiv:1106.3723 [hep-ph].
[22] J. Botts, J. G. Morfin, J. F. Owens, J.-w. Qiu, W.-K. Tung, and H. Weerts, CTEQ Collaboration, "CTEQ parton distributions and flavor dependence of sea quarks," *Physics Letters* **B304** (1993) 159–166, arXiv:hep-ph/9303255 [hep-ph].
[23] S. Kuhlmann, "CTEQ5 parton distributions and ongoing studies," *Nuclear Physics B - Proceedings Supplements* **79** (1999) 108–110.
[24] M. Wlasenko, ZEUS, H1 Collaboration, "Measurement of the Structure of the Proton at HERA," *Nuclear Physics* **A827** (2009) 276C–278C, arXiv:0902.0563 [hep-ex].
[25] A. Cooper-Sarkar, ZEUS Collaboration and H1 Collaboration, "Proton Structure from HERA to LHC," in *Proceedings, 40th International Symposium on Multiparticle Dynamics (ISMD 2010)*. 2010. arXiv:1012.1438 [hep-ph]. http://inspirehep.net/record/879722/files/arXiv:1012.1438.pdf.
[26] P. Mertsch, "Neutrino interactions at high energy," in *Neils Bohr International Academy PhD School*. 2016. https://indico.nbi.ku.dk/contributionDisplay.py?contribId=48&sessionId=3&confId=859. Neutrinos Underground and in the Heavens II.
[27] R. Gandhi, C. Quigg, M. H. Reno, and I. Sarcevic, "Ultrahigh-energy neutrino interactions," *Astroparticle Physics* **5** (1996) 81–110, arXiv:hep-ph/9512364 [hep-ph].
[28] A. Connolly, R. S. Thorne, and D. Waters, "Calculation of High Energy Neutrino-Nucleon Cross Sections and Uncertainties Using the MSTW Parton Distribution Functions and Implications for Future Experiments," *Physical Review* **D83** (2011) 113009, arXiv:1102.0691 [hep-ph].
[29] Y. L. Dokshitzer, "Calculation of the Structure Functions for Deep Inelastic Scattering and e^+ e^- Annihilation by Perturbation Theory in Quantum Chromodynamics.," *Soviet Physics Journal of Experimental and Theoretical Physics* **46** (1977) 641–653. [Zhurnal Eksperimentalnoi i Teoreticheskoi Fiziki 73, 1216 (1977) (in Russian)].
[30] V. N. Gribov and L. N. Lipatov, "Deep inelastic e p scattering in perturbation theory," *Soviet Physics Journal of Experimental and Theoretical Physics* **15** (1972)

438–450. [Yadernaya Fizika 15, 781 (1972) (in Russian)].
[31] G. Altarelli and G. Parisi, "Asymptotic Freedom in Parton Language," *Nuclear Physics* **B126** (1977) 298–318.
[32] J. A. Formaggio and G. P. Zeller, "From eV to EeV: Neutrino Cross Sections Across Energy Scales," *Reviews of Modern Physics* **84** (2012) 1307, arXiv:1305.7513 [hep-ex].
[33] A. Cooper-Sarkar and S. Sarkar, "Predictions for high energy neutrino cross-sections from the ZEUS global PDF fits," *Journal of High Energy Physics* **01** (2008) 075, arXiv:0710.5303 [hep-ph].
[34] F. D. Aaron *et al.*, ZEUS, H1 Collaboration, "Combined Measurement and QCD Analysis of the Inclusive e+ p Scattering Cross Sections at HERA," *Journal of High Energy Physics* **01** (2010) 109, arXiv:0911.0884 [hep-ex].
[35] H.-L. Lai, M. Guzzi, J. Huston, Z. Li, P. M. Nadolsky, J. Pumplin, and C. P. Yuan, "New parton distributions for collider physics," *Physical Review* **D82** (2010) 074024, arXiv:1007.2241 [hep-ph].
[36] A. D. Martin, W. J. Stirling, R. S. Thorne, and G. Watt, "Heavy-quark mass dependence in global PDF analyses and 3- and 4-flavour parton distributions," *European Physical Journal* **C70** (2010) 51–72, arXiv:1007.2624 [hep-ph].
[37] S. Sarkar and P. Mertsch, "Energy ranges for CSMS calculations." Personal communication, 2016.
[38] "Abundance of the chemical elements." https://en.wikipedia.org/wiki/Abundance_of_the_chemical_elements. Accessed: 2016-06-21.
[39] K.A. Olive and others, Particle Data Group (PDG) Collaboration, "Chapter 49: Neutrino cross section measurements," *Chinese Physics* **C38** (2014) 090001.
[40] C. Anderson *et al.*, ArgoNeuT Collaboration, "First Measurements of Inclusive Muon Neutrino Charged Current Differential Cross Sections on Argon," *Physical Review Letters* **108** (2012) 161802, arXiv:1111.0103 [hep-ex].
[41] K. Abe *et al.*, T2K Collaboration, "Measurement of the inclusive ν_μ charged current cross section on carbon in the near detector of the T2K experiment," *Physical Review* **D87** no. 9, (2013) 092003, arXiv:1302.4908 [hep-ex].
[42] A. Kayis-Topaksu *et al.*, CHORUS Collaboration, "Leading order analysis of neutrino induced dimuon events in the CHORUS experiment," *Nuclear Physics* **B798** (2008) 1–16, arXiv:0804.1869 [hep-ex].
[43] O. Samoylov *et al.*, NOMAD Collaboration, "A Precision Measurement of Charm Dimuon Production in Neutrino Interactions from the NOMAD Experiment," *Nuclear Physics* **B876** (2013) 339–375, arXiv:1308.4750 [hep-ex].
[44] D. Mason *et al.*, NuTeV Collaboration, "Measurement of the Nucleon Strange-Antistrange Asymmetry at Next-to-Leading Order in QCD from NuTeV Dimuon Data," *Physics Review Letters* **99** (2007) 192001.
[45] L. A. Anchordoqui, J. L. Feng, and H. Goldberg, "Particle physics on ice: Constraints on neutrino interactions far above the weak scale," *Physical Review Letters* **96** (2006) 021101, arXiv:hep-ph/0504228 [hep-ph].
[46] R. Gandhi, C. Quigg, M. H. Reno, and I. Sarcevic, "Neutrino interactions at ultrahigh-energies," *Physical Review* **D58** (1998) 093009, arXiv:hep-ph/9807264

[hep-ph].
[47] H. L. Lai, J. Huston, S. Kuhlmann, F. Olness, J. Owens, D. Soper, W. K. Tung, and H. Weerts, "Improved parton distributions from global analysis of recent deep inelastic scattering and inclusive jet data," *Physical Review* **D55** (Feb, 1997) 1280–1296. http://link.aps.org/doi/10.1103/PhysRevD.55.1280.
[48] K. Greisen, "End to the cosmic ray spectrum?," *Physical Review Letters* **16** (1966) 748–750.
[49] G. T. Zatsepin and V. A. Kuzmin, "Upper limit of the spectrum of cosmic rays," *Journal of Experimental and Theoretical Physics Letters* **4** (1966) 78–80. [Zhurnal Eksperimentalnoi i Teoreticheskoi Fiziki-Pisma 4, 114 (1966) (in Russian)].
[50] Fenfang Wu, *Using ANITA-I to Constrain Ultra High Energy Neutrino-Nucleon Cross Section*. PhD thesis, University of California-Irvine, 2009.
[51] P. Miocinovic, "Results of ANITA-lite prototype antenna array." Neutrino 2004, Paris.
[52] L. Volkova and G. Zatsepin, "Passage of neutrinos through the Earth." Bulletin of the Russian Academy of Sciences: Physics, Volume 38, p. 151, 1974. [Izvestiya Akademii Nauk SSSR, Seriya Fizicheskaya; v. 38(5), pp. 1060-1063 (1974) (in Russian)].
[53] Tommy Ohlsson and Walter Winter, "Reconstruction of the Earth's matter density profile using a single neutrino baseline," *Physics Letters B* **512** no. 3-4, (2001) 357 – 364. http://www.sciencedirect.com/science/article/pii/S0370269301007316.
[54] C. Rott, A. Taketa, and D. Bose, "Spectrometry of the Earth using Neutrino Oscillations," *Scientific Reports* **5** no. 15225, (2015) 1–10, arXiv:1502.04930 [physics.geo-ph].
[55] A. De Rujula and S.L. Glashow and R.R. Wilson and G. Charpak, "Neutrino exploration of the Earth," *Physics Reports* **99** no. 6, (1983) 341 – 396. http://www.sciencedirect.com/science/article/pii/0370157383901084.
[56] M. M. Reynoso and O. A. Sampayo, "On neutrino absorption tomography of the earth," *Astroparticle Physics* **21** (2004) 315–324, arXiv:hep-ph/0401102 [hep-ph].
[57] T. L. Wilson, "Neutrino tomography: Tevatron mapping versus the neutrino sky," *Nature* **309** (1984) 38–42.
[58] A. M. Dziewonski and D. L. Anderson, "Preliminary reference earth model," *Physics of the Earth and Planetary Interiors* **25** (1981) 297–356.
[59] J. Babson *et al.*, DUMAND Collaboration, "Cosmic Ray Muons in the Deep Ocean," *Physical Review* **D42** (1990) 3613–3620.
[60] H. J. Crawford, R. Jeanloz, and B. Romanowicz, DUMAND Collaboration, "Mapping the Earth's Interior with Astrophysical Neutrinos," 1995. http://adsabs.harvard.edu/full/1995ICRC....1..804D. (24th International Cosmic Ray Conference, Aug-Sep 1995, Rome, Italy).
[61] P. Jain, J. P. Ralston, and G. M. Frichter, "Neutrino absorption tomography of the earth's interior using isotropic ultrahigh-energy flux," *Astroparticle Physics* **12** (1999) 193–198, arXiv:hep-ph/9902206 [hep-ph].
[62] M. C. Gonzalez-Garcia, F. Halzen, M. Maltoni, and H. K. M. Tanaka, "Radiography of earth's core and mantle with atmospheric neutrinos," *Physical Review Letters* **100** (2008) 061802, arXiv:0711.0745 [hep-ph].
[63] G. Miele and O. Pisanti, "Neutrino radiography," *Nuclear Physics B - Proceedings*

Supplements **217** (2011) 149–151.
[64] K. Hoshina and H. Tanaka, "Neutrino radiography of the Earth with the IceCube Neutrino Observatory," *AGU Fall Meeting Abstracts* (2012) 1–22. http://adsabs.harvard.edu/abs/2012AGUFM.P23D..03H. Provided by the SAO/NASA Astrophysics Data System.
[65] D. Hooper, "Measuring high-energy neutrino nucleon cross-sections with future neutrino telescopes," *Physical Review* **D65** (2002) 097303, arXiv:hep-ph/0203239 [hep-ph].
[66] W. Winter, "Neutrino Tomography – Learning About The Earth's Interior Using The Propagation Of Neutrinos," *Earth, Moon, and Planets* **99** no. 1, (2006) 285–307. http://dx.doi.org/10.1007/s11038-006-9101-y.
[67] E. Borriello, A. Cuoco, G. Mangano, G. Miele, S. Pastor, O. Pisanti, and P. D. Serpico, "Disentangling neutrino-nucleon cross section and high energy neutrino flux with a km^3 neutrino telescope," *Physical Review* **D77** (2008) 045019, arXiv:0711.0152 [astro-ph].
[68] P. Allison *et al.*, ARA Collaboration, "Performance of two Askaryan Radio Array stations and first results in the search for ultrahigh energy neutrinos," *Physical Review D* **93** (2016) 082003. http://link.aps.org/doi/10.1103/PhysRevD.93.082003.
[69] S. W. Barwick *et al.*, "Design and Performance of the ARIANNA Hexagonal Radio Array Systems," arXiv:1410.7369 [astro-ph.IM].
[70] S. R. Klein and A. Connolly, "Neutrino Absorption in the Earth, Neutrino Cross-Sections, and New Physics," arXiv:1304.4891 [astro-ph.HE].
[71] A. Dziewonski, *The Encyclopedia of Solid Earth Geophysics*. Van Nostrand Reinhold, New York, 1989.
[72] P. A. Cherenkov, "Visible luminescence of pure fluids induced by gamma rays," *Doklady Akademii Nauk SSSR* **2** (1934) 451–454.
[73] I. M. Frank and I. Tamm, "Coherent visible radiation of fast electrons passing through matter," *Doklady Akademii Nauk SSSR* **14** (1937) 109–114.
[74] P. A. Cherenkov, "Visible radiation produced by electrons moving in a medium with velocities exceeding that of light," *Physical Review* **52** (1937) 378–379.
[75] K. Olive *et al.*, Particle Data Group Collaboration, "Chapter 32: Passage of particles through matter," *Chinese Physics* **C38** (2014) 090001.
[76] D. E. Groom, N. V. Mokhov, and S. I. Striganov, "Muon stopping power and range tables 10-MeV to 100-TeV," *Atomic Data and Nuclear Data Tables* **78** (2001) 183–356.
[77] H. Bethe, "Zur Theorie des Durchgangs schneller Korpuskularstrahlen durch Materie," *Annalen der Physik* **5** (1930) 325–400. [Annalen Phys. 397, 325 (1930)] (translation in 'Theory of the passage of fast corpuscular rays through matter', in 'Selected works of Hans A. Bethe: with commentary', World Scientific Series in 20th Century Physics, Volume 18 (1997) pp. 77-154).
[78] P. Sigmund, *Particle Penetration and Radiation Effects*. Springer-Verlag, Berlin-Heidelberg, Germany, 2006. Springer Series in Solid State Sciences.
[79] F. Bloch, "Zur Bremsung rasch bewegter Teilchen beim Durchgang durch Materie," *Annalen der Physik* **16** (1933) 285–320.

[80] "Bremsstrahlung." https://en.wikipedia.org/wiki/Bremsstrahlung. Accessed: 2016-06-21.
[81] L. D. Landau and I. Pomeranchuk, "The limits of applicability of the theory of bremsstrahlung by electrons and of the creation of pairs at large energies," *Doklady Akademii Nauk SSSR* **92** (1953) 535. (translated in L.D. Landau, 'The Collected Papers of L. D. Landau', Oxford: Pergamon (1965) pp. 586-588).
[82] A. B. Migdal, "Bremsstrahlung and pair production in condensed media at high-energies," *Physical Review* **103** (1956) 1811–1820.
[83] S. Klein, "Suppression of Bremsstrahlung and pair production due to environmental factors," *Reviews of Modern Physics* **71** (1999) 1501–1538, arXiv:hep-ph/9802442 [hep-ph].
[84] E. V. Bugaev and Yu. V. Shlepin, "Photonuclear interaction of high-energy muons and tau leptons," *Physical Review* **D67** (2003) 034027, arXiv:hep-ph/0203096 [hep-ph].
[85] T. Stanev, *High energy cosmic rays*. Springer-Praxis, Germany, second ed., 2010.
[86] D. Chirkin and W. Rhode, "Propagating leptons through matter with Muon Monte Carlo (MMC)," arXiv:hep-ph/0407075v2 [hep-ph].
[87] C. V. Achar *et al.*, "Detection of muons produced by cosmic ray neutrinos deep underground," *Physics Letters* **18** (1965) 196–199.
[88] F. Reines, M. F. Crouch, T. L. Jenkins, W. R. Kropp, H. S. Gurr, G. R. Smith, J. P. F. Sellschop, and B. Meyer, "Evidence for high-energy cosmic ray neutrino interactions," *Physical Review Letters* **15** (1965) 429–433.
[89] V. Hess, "The cosmic-ray spectrum: from the knee to the ankle," *Physikalische Zeitschrift* **13** (1912) 1084–1091.
[90] T. K. Gaisser, *Cosmic Rays and Particle Physics*. Cambridge University Press, Cambridge U.K., 1990.
[91] J. N. Matthews and C. C. H. Jui, Fly's Eye Collaboration, "First results from the high resolution Fly's Eye experiment," *Nuclear Physics B - Proceedings Supplements* **87** (2000) 411–413.
[92] P. Sokolsky, HiRes Collaboration, "Final Results from the High Resolution Fly's Eye (HiRes) Experiment," *Nuclear Physics B - Proceedings Supplements* (2010) 444, arXiv:1010.2690 [astro-ph.HE].
[93] J. J. Beatty and S. Westerhoff, "The Highest-Energy Cosmic Rays," *Annual Review of Nuclear and Particle Science* **59** (2009) 319–345.
[94] E. Fermi, "On the Origin of the Cosmic Radiation," *Physical Review* **75** (1949) 1169–1174.
[95] A. Bell, "The non-linear self-regulation of cosmic ray acceleration at shocks," *Monthly Notices of the Royal Astronomical Society* **225** no. 3, (1987) 615–626.
[96] S. R. Kelner, F. A. Aharonian, and V. V. Bugayov, "Energy spectra of gamma-rays, electrons and neutrinos produced at proton-proton interactions in the very high energy regime," *Physical Review* **D74** (2006) 034018, arXiv:astro-ph/0606058 [astro-ph]. [Erratum: Phys. Rev. D79, 039901 (2009)].
[97] J. R. Horandel, "On the knee in the energy spectrum of cosmic rays," *Astroparticle Physics* **19** no. 2, (2003) 193 – 220. http://www.sciencedirect.com/science/article/pii/S0927650502001986.

[98] M. Boezio *et al.*, "The space experiment PAMELA," *Nuclear Physics B - Proceedings Supplements* **134** (2004) 39–46.

[99] R. Battiston, AMS-02 Collaboration, "The Anti Matter Spectrometer (AMS-02): a Particle Physics Detector In Space," *Nuclear Physics B - Proceedings Supplements* **166** (2007) 19 – 29. http://www.sciencedirect.com/science/article/pii/S0920563206009947. Proceedings of the Third International Conference on Particle and Fundamental Physics in Space.

[100] O. Adriani *et al.*, "PAMELA Results on the Cosmic-Ray Antiproton Flux from 60 MeV to 180 GeV in Kinetic Energy," *Physical Review Letters* **105** (Sep, 2010) 121101. http://link.aps.org/doi/10.1103/PhysRevLett.105.121101.

[101] W. D. Apel, KASCADE Collaboration, "Energy Spectra of Elemental Groups of Cosmic Rays: Update on the KASCADE Unfolding Analysis," *Astroparticle Physics* **31** (2009) 86–91, arXiv:0812.0322 [astro-ph].

[102] H. P. Dembinski, Pierre Auger Collaboration, "Latest results from the Pierre Auger Observatory," *Journal of Physics Conference Series* **337** (2012) 012068.

[103] T. Gaisser, F. Halzen, and T. Stanev, "Particle Physics with High Energy Neutrinos," arXiv:hep-ph/9410384v1 [hep-ph].

[104] T. K. Gaisser, "Spectrum of cosmic-ray nucleons, kaon production, and the atmospheric muon charge ratio," *Astroparticle Physics* **35** (2012) 801–806, arXiv:1111.6675 [astro-ph.HE].

[105] T. K. Gaisser, T. Stanev, and S. Tilav, "Cosmic Ray Energy Spectrum from Measurements of Air Showers," *Frontiers of Physics (Beijing)* **8** (2013) 748–758, arXiv:1303.3565 [astro-ph.HE].

[106] H. S. Ahn *et al.*, CREAM Collaboration, "Energy spectra of cosmic-ray nuclei at high energies," *Astrophysical Journal* **707** (2009) 593–603, arXiv:0911.1889 [astro-ph.HE].

[107] H. S. Ahn *et al.*, CREAM Collaboration, "Discrepant hardening observed in cosmic-ray elemental spectra," *Astrophysical Journal* **714** (2010) L89–L93, arXiv:1004.1123 [astro-ph.HE].

[108] A. M. Hillas, "Can diffusive shock acceleration in supernova remnants account for high-energy galactic cosmic rays?," *Journal of Physics* **G31** (2005) R95–R131.

[109] T. Stanev, T. K. Gaisser, and S. Tilav, "High energy cosmic rays: sources and fluxes," *Nuclear Instruments and Methods* **A742** (2014) 42–46.

[110] "U.S. Standard Atmosphere." http://nssdc.gsfc.nasa.gov/space/model/atmos/us_standard.html, 1976. U.S. Government Printing Office, Washington, D.C.

[111] J. Picone *et al.*, "NRLMSISE-00 empirical model of the atmosphere: Statistical comparisons and scientific issues," *Journal of Geophysical Research* **107** no. A12, (2002) 1468. http://nssdc.gsfc.nasa.gov/space/model/atmos/nrlmsise00.html.

[112] S. Tilav, P. Desiati, T. Kuwabara, D. Rocco, F. Rothmaier, M. Simmons, and H. Wissing, IceCube Collaboration, "Atmospheric Variations as Observed by IceCube," arXiv:1001.0776 [astro-ph.HE]. http://inspirehep.net/record/841872/files/arXiv:1001.0776.pdf.

[113] P. Desiati *et al.*, IceCube Collaboration, "Seasonal variation of atmospheric

neutrinos in IceCube," arXiv:1309.7003.
[114] P. Desiati, T. Kuwabara, T. K. Gaisser, S. Tilav, and D. Rocco, IceCube Collaboration, "Seasonal Variations of High Energy Cosmic Ray Muons Observed by the IceCube Observatory as a Probe of Kaon/Pion Ratio," arXiv:1111.2735. http://inspirehep.net/record/1346027/files/v1_0662.pdf.
[115] M. Amenomori, Tibet AS-gamma Collaboration, "Anisotropy and Corotation of Galactic Cosmic Rays," *Science* **314** (2006) 439–443, arXiv:astro-ph/0610671 [astro-ph].
[116] G. Guillian *et al.*, Super-Kamiokande Collaboration, "Observation of the anisotropy of 10-TeV primary cosmic ray nuclei flux with the Super-Kamiokande-I Detector," *Physical Review* **D75** (2007) 062003, arXiv:astro-ph/0508468 [astro-ph].
[117] A. A. Abdo *et al.*, "The Large Scale Cosmic-Ray Anisotropy as Observed with Milagro," *Astrophysical Journal* **698** (2009) 2121–2130, arXiv:0806.2293 [astro-ph].
[118] B. Bartoli *et al.*, ARGO-YBJ Collaboration, "Medium scale anisotropy in the TeV cosmic ray flux observed by ARGO-YBJ," *Physical Review* **D88** no. 8, (2013) 082001, arXiv:1309.6182 [astro-ph.HE].
[119] P. Desiati, IceCube Collaboration, "Observation of TeV-PeV cosmic ray anisotropy with IceCube, IceTop and AMANDA," *Nuclear Instruments and Methods* **A742** (2014) 199–202, arXiv:1308.0246 [astro-ph.HE].
[120] P. Desiati *et al.*, IceCube Collaboration, "Galactic cosmic ray anisotropy in IceCube." GALPROP workshop, Stanford University, 2011.
[121] T. K. Gaisser and M. Honda, "Flux of atmospheric neutrinos," *Annual Review of Nuclear and Particle Science* **52** (2002) 153–199, arXiv:hep-ph/0203272 [hep-ph].
[122] R. Enberg, M. H. Reno, and I. Sarcevic, "Prompt neutrino fluxes from atmospheric charm," *Physical Review* **D78** (2008) 043005, arXiv:0806.0418 [hep-ph].
[123] K. Daum *et al.*, Frejus Collaboration, "Determination of the atmospheric neutrino spectra with the Frejus detector," *Zeitschrift fur Physik* **C66** (1995) 417–428.
[124] P. Desiati and T. K. Gaisser, "Seasonal variation of atmospheric leptons as a probe of charm," *Physical Review Letters* **105** (2010) 121102, arXiv:1008.2211 [astro-ph.HE].
[125] C. Haack, A. Schukraft, A. Zilles, and C. Wiebusch, "Re-weighting atmospheric neutrino fluxes to account for the cosmic ray knee with NeutrinoFlux." IceCube internal report 201301002, 2013.
[126] M. Honda, T. Kajita, K. Kasahara, S. Midorikawa, and T. Sanuki, "Calculation of atmospheric neutrino flux using the interaction model calibrated with atmospheric muon data," *Physical Review* **D75** (2007) 043006, arXiv:astro-ph/0611418 [astro-ph].
[127] G. D. Barr, T. K. Gaisser, P. Lipari, S. Robbins, and T. Stanev, "A Three - dimensional calculation of atmospheric neutrinos," *Physical Review* **D70** (2004) 023006, arXiv:astro-ph/0403630 [astro-ph].
[128] *Multiple muons produced by cosmic ray interactions*, vol. 2. Scripps Institution of Oceanography, La Jolla CA, 1979. Proceedings of the DUMAND Summer Workshop, 24 July to 2 September 1978.
[129] T. K. Gaisser and T. Stanev, "Muon bundles in underground detectors," *Nuclear*

Instruments and Methods **A235** (1985) 183–192.
[130] P. Lipari, "TeV muons in hadronic showers," *Astroparticle Physics* **1** (1993) 399–416, arXiv:hep-ph/9307289 [hep-ph].
[131] T. K. Gaisser, K. Jero, A. Karle, and J. van Santen, "Generalized self-veto probability for atmospheric neutrinos," *Physical Review* **D90** no. 2, (2014) 023009, arXiv:1405.0525 [astro-ph.HE].
[132] "NeutrinoFlux." http://icecube.wisc.edu/~tmontaruli/neutrinoflux/NeutrinoFlux.html. (internal IceCube website).
[133] "NeutrinoFlux." https://code.icecube.wisc.edu/svn/projects/neutrinoflux/. (internal IceCube website).
[134] A. D. Martin, M. G. Ryskin, and A. M. Stasto, "Prompt neutrinos from atmospheric $c\bar{c}$ and $b\bar{b}$ production and the gluon at very small x," *Acta Physica Polonica* **B34** (2003) 3273–3304, arXiv:hep-ph/0302140 [hep-ph].
[135] E. V. Bugaev, V. A. Naumov, S. I. Sinegovsky, and E. S. Zaslavskaya, "Prompt Leptons in Cosmic Rays," *Il Nuovo Cimento* **C12** (1989) 41–73.
[136] K. J. Golec-Biernat and M. Wusthoff, "Saturation effects in deep inelastic scattering at low Q^2 and its implications on diffraction," *Physical Review* **D59** (1998) 014017, arXiv:hep-ph/9807513 [hep-ph].
[137] C. G. S. Costa, "The prompt lepton cookbook," *Astroparticle Physics* **16** (2001) 193–204, arXiv:hep-ph/0010306 [hep-ph].
[138] M. G. Aartsen *et al.*, IceCube Collaboration, "Observation and Characterization of a Cosmic Muon Neutrino Flux from the Northern Hemisphere using six years of IceCube data," arXiv:1607.08006 [astro-ph.HE].
[139] A. Bhattacharya, R. Enberg, M. H. Reno, I. Sarcevic, and A. Stasto, "Perturbative charm production and the prompt atmospheric neutrino flux in light of RHIC and LHC," *Journal of High Energy Physics* **06** (2015) 110, arXiv:1502.01076 [hep-ph].
[140] M. G. Aartsen *et al.*, IceCube Collaboration, "Searches for small-scale anisotropies from neutrino point sources with three years of IceCube data," *Astroparticle Physics* **66** (2015) 39–52, arXiv:1408.0634 [astro-ph.HE].
[141] R. Abbasi *et al.*, IceCube Collaboration, "An absence of neutrinos associated with cosmic-ray acceleration in γ-ray bursts," *Nature* **484** (2012) 351–353, arXiv:1204.4219 [astro-ph.HE].
[142] W. Arnett, J. Bahcall, R. Kirshner, and S. Woosley, "Supernova 1987a," *Annual Review of Astronomy and Astrophysics* **27** (1989) 629.
[143] K. Hirata *et al.*, Kamiokande-II Collaboration, "Observation of a Neutrino Burst from the Supernova SN 1987a," *Physical Review Letters* **58** (1987) 1490–1493.
[144] R. M. Bionta *et al.*, "Observation of a Neutrino Burst in Coincidence with Supernova SN 1987a in the Large Magellanic Cloud," *Physical Review Letters* **58** (1987) 1494.
[145] E. N. Alekseev, L. N. Alekseeva, I. V. Krivosheina, and V. I. Volchenko, "Detection of the Neutrino Signal From SN1987A in the LMC Using the INR Baksan Underground Scintillation Telescope," *Physics Letters* **B205** (1988) 209–214.
[146] O. Kalashev, D. Semikoz, and I. Tkachev, "Neutrinos in IceCube from AGN's," arXiv:1410.8124 [astro-ph.HE].
[147] R. Abbasi *et al.*, IceCube Collaboration Collaboration, "Limits on Neutrino

Emission from Gamma-Ray Bursts with the 40 String IceCube Detector," *Physical Review Letters* **106** (Apr, 2011) 141101. http://link.aps.org/doi/10.1103/PhysRevLett.106.141101.

[148] D. Guetta, D. Hooper, J. Alvarez-Muniz, F. Halzen, and E. Reuveni, "Neutrinos from individual gamma-ray bursts in the BATSE catalog," *Astroparticle Physics* **20** (2004) 429–455, arXiv:astro-ph/0302524 [astro-ph].

[149] M. G. Aartsen *et al.*, IceCube Collaboration, "Search for Prompt Neutrino Emission from Gamma-Ray Bursts with IceCube," *Astrophysical Journal* **805** no. 1, (2015) L5, arXiv:1412.6510 [astro-ph.HE].

[150] E. Waxman and J. N. Bahcall, "High-energy neutrinos from astrophysical sources: An upper bound," *Physical Review* **D59** (1999) 023002, arXiv:hep-ph/9807282 [hep-ph].

[151] H. Athar, C. S. Kim, and J. Lee, "The intrinsic and oscillated astrophysical neutrino flavor ratios," *Modern Physics Letters* **A21** (2006) 1049–1066, arXiv:hep-ph/0505017 [hep-ph].

[152] J. F. Beacom, N. F. Bell, D. Hooper, S. Pakvasa, and T. J. Weiler, "Measuring flavor ratios of high-energy astrophysical neutrinos," *Physical Review* **D68** (2003) 093005, arXiv:hep-ph/0307025 [hep-ph]. [Erratum: Phys. Rev. D72, 019901 (2005)].

[153] M. A. Markov, "On high energy neutrino physics," 1960. Proceedings, 10th International Conference on High Energy Physics (ICHEP 60).

[154] D. Fakirov, "On Spacial Distribution of the Neutrino Beam Generated by High Energy Nucleon Collisions," *Faculté des Sciences de Sofia* **2** (1958) 53.

[155] M. Schwartz, "Feasibility of using high-energy neutrinos to study the weak interactions," *Physical Review Letters* **4** (1960) 306–307.

[156] M. A. Markov and I. M. Zheleznykh, "On high energy neutrino physics in cosmic rays," *Nuclear Physics* **27** (1961) 385–394.

[157] C. Spiering, "Towards High-Energy Neutrino Astronomy. A Historical Review," *European Physical Journal* **H37** (2012) 515–565, arXiv:1207.4952 [astro-ph.IM].

[158] D. M. Lowder, T. Miller, P. B. Price, A. Westphal, S. W. Barwick, F. Halzen, and R. Morse, "Observation of muons using the polar ice cap as a Cherenkov detector," *Nature* **353** (1991) 331–333.

[159] E. Andres *et al.*, "The AMANDA neutrino telescope: Principle of operation and first results," *Astroparticle Physics* **13** (2000) 1–20, arXiv:astro-ph/9906203 [astro-ph].

[160] A. Karle, "Astrophysics from Antarctica," in *Proceedings IAU Symposium No. 288*, M. Burton, X. Cui, and N. Tothill, eds. Cambridge University Press, Cambridge U.K., 2012.

[161] J. Ahrens *et al.*, IceCube Collaboration, "Sensitivity of the IceCube detector to astrophysical sources of high energy muon neutrinos," *Astroparticle Physics* **20** (2004) 507–532, arXiv:astro-ph/0305196 [astro-ph].

[162] T. DeYoung, IceCube Collaboration, "Results from Seven Years of AMANDA-II," *Journal of Physics - Conference Series.* **136** (2008) 022046, arXiv:0810.4513 [astro-ph].

[163] D. Sinclair *et al.*, "IMB Detector: The first 30 days," in *Proceedings, Workshop on Science Underground*, pp. 138–142. 1982.

[164] S. Fukuda and others, "The Super-Kamiokande detector," *Nuclear Instruments and Methods* **A501** no. 2-3, (2003) 418 – 462. http://www.sciencedirect.com/science/article/pii/S016890020300425X.
[165] V. Aynutdinov *et al.*, BAIKAL Collaboration, "Search for a diffuse flux of high-energy extraterrestrial neutrinos with the NT200 neutrino telescope," *Astroparticle Physics* **25** (2006) 140–150, arXiv:astro-ph/0508675 [astro-ph].
[166] S. Adrian-Martinez *et al.*, ANTARES Collaboration, "Searches for Point-like and extended neutrino sources close to the Galactic Centre using the ANTARES neutrino Telescope," *Astrophysics Journal* **786** (2014) L5, arXiv:1402.6182 [hep-ex].
[167] E. Migneco, "Progress and latest results from Baikal, Nestor, NEMO and KM3NeT," *Journal of Physics: Conference Series* **136** (2008) 022048.
[168] A. Achterberg *et al.*, IceCube Collaboration, "First Year Performance of The IceCube Neutrino Telescope," *Astroparticle Physics* **26** (2006) 155–173, arXiv:astro-ph/0604450 [astro-ph].
[169] "IceCube Detector." https://icecube.wisc.edu/gallery/press/view/1336. Accessed: 2016-06-21.
[170] R. Abbasi *et al.*, IceCube Collaboration, "The Design and Performance of IceCube DeepCore," *Astroparticle Physics* **35** (2012) 615–624, arXiv:1109.6096 [astro-ph.IM].
[171] R. Abbasi *et al.*, IceCube Collaboration, "IceTop: The surface component of IceCube," *Nuclear Instruments and Methods* **A700** (2013) 188–220, arXiv:1207.6326 [astro-ph.IM].
[172] R. Abbasi *et al.*, IceCube Collaboration, "The IceCube Data Acquisition System: Signal Capture, Digitization, and Timestamping," *Nuclear Instruments and Methods* **A601** (2009) 294–316, arXiv:0810.4930 [physics.ins-det].
[173] T. Stezelberger, "IceCube construction." Personal communication, 2015.
[174] R. Abbasi *et al.*, IceCube Collaboration, "Calibration and Characterization of the IceCube Photomultiplier Tube," *Nuclear Instruments and Methods* **A618** (2010) 139–152, arXiv:1002.2442 [astro-ph.IM].
[175] J. Nilsson, "Surface to DOM cable," 2005. (Ericsson Product Code TEH 301 9099/0040).
[176] "Data Movement." https://icecube.wisc.edu/science/data/datamovement. Accessed: 2016-06-21.
[177] G. d. Q. Robin, "Radio-echo sounding applied to the investigation of the ice thickness and sub-ice relief of Antarctica," *Antarctic Geology and Geophysics* (1971) 675–682. (Universitetsforlaget, Oslo).
[178] M. Ackermann *et al.*, "Optical properties of deep glacial ice at the South Pole," *Journal of Geophysical Research* **111** no. D13, (2006) D13203.
[179] IceCube Collaboration, "South Pole glacial climate reconstruction from multi-borehole laser particulate stratigraphy," *Journal of Glaciology* **59** no. 218, (2013) 1117–1128.
[180] D. Chirkin, IceCube Collaboration, "Study of South Pole ice transparency with IceCube flashers," arXiv:1111.2731. Proceedings, 32nd International Cosmic Ray Conference (ICRC 2011).
[181] S. Miller, "Clathrate hydrates of air in Antarctic ice," *Science* **165** no. 3892, (1969)

489–490.
[182] T. Uchida, W. Shimada, T. Hondoh, S. Mae, and N. Barkov, "Refractive-index measurements of natural air-hydrate crystals in an Antarctic ice sheet," *Applied Optics* **34** no. 25, (1995) 5746–5749.
[183] M. G. Aartsen *et al.*, IceCube Collaboration, "Measurement of South Pole ice transparency with the IceCube LED calibration system," *Nuclear Instruments and Methods* **A711** (2013) 73–89, arXiv:1301.5361 [astro-ph.IM].
[184] J. A. Aguilar *et al.*, ANTARES Collaboration, "Transmission of light in deep sea water at the site of the ANTARES Neutrino Telescope," *Astroparticle Physics* **23** (2005) 131–155, arXiv:astro-ph/0412126 [astro-ph].
[185] G. Mie, "Beitrage zur Optik truber Medien, speziell kolloidaler Metallosungen," *Annalen der Physik* **330** no. 3, (1908) 377–445. http://dx.doi.org/10.1002/andp.19083300302.
[186] P. Price and L. Bergstrom, "Optical properties of deep ice at the South Pole: Scattering," *Applied Optics* **36** (1997) 4181–4194.
[187] C. Bohren and D. Huffman, *Absorption and scattering of light by small particles*. John Wiley and Sons, Hoboken NJ, 1983.
[188] F. Urbach, "The long-wavelength edge of photographic sensitivity and of the electronic absorption of solids," *Physical Review* **92** (1953) 1324.
[189] D. Chirkin, IceCube Collaboration, "Evidence of optical anisotropy of the South Pole ice," arXiv:1309.7010. http://www.cbpf.br/%7Eicrc2013/papers/icrc2013-0580.pdf.
[190] D. Chirkin, "Photon Propagation Code." http://icecube.wisc.edu/~dima/work/WISC/ppc, 2010. Accessed: 2016-06-21.
[191] J. Lundberg, P. Miocinovic, T. Burgess, J. Adams, S. Hundertmark, P. Desiati, K. Woschnagg, and P. Niessen, "Light tracking for glaciers and oceans: Scattering and absorption in heterogeneous media with Photonics," *Nuclear Instruments and Methods* **A581** (2007) 619–631, arXiv:astro-ph/0702108 [ASTRO-PH].
[192] L. Gerhardt, "Effects of hole ice on hit time." internal IceCube report 200904001, 2009.
[193] M. G. Aartsen *et al.*, IceCube Collaboration, "Energy Reconstruction Methods in the IceCube Neutrino Telescope," *Journal of Instrumentation* **9** (2014) P03009, arXiv:1311.4767 [physics.ins-det].
[194] M. G. Aartsen *et al.*, IceCube Collaboration, "Evidence for High-Energy Extraterrestrial Neutrinos at the IceCube Detector," *Science* **342** (2013) 1242856, arXiv:1311.5238 [astro-ph.HE].
[195] M. G. Aartsen *et al.*, IceCube Collaboration, "Search for Astrophysical Tau Neutrinos in Three Years of IceCube Data," *Physical Review* **D93** no. 2, (2016) 022001, arXiv:1509.06212 [astro-ph.HE].
[196] A. Gazizov and M. P. Kowalski, "ANIS: High energy neutrino generator for neutrino telescopes," *Computer Physics Communications* **172** (2005) 203–213, arXiv:astro-ph/0406439 [astro-ph].
[197] D. Heck, G. Schatz, T. Thouw, J. Knapp, and J. N. Capdevielle, "CORSIKA: A Monte Carlo code to simulate extensive air showers," 1998. (Forschungszentrum Karlsruhe Report 6019).

[198] E.-J. Ahn, R. Engel, T. K. Gaisser, P. Lipari, and T. Stanev, "Cosmic ray interaction event generator SIBYLL 2.1," *Physical Review* **D80** (2009) 094003, arXiv:0906.4113 [hep-ph].
[199] O. Yu. Smirnov, P. Lombardi, and G. Ranucci, "Precision measurements of timing characteristics of the ETL9351 series photomultiplier," *Instruments and Experimental Techniques* **47** (2004) 69–80, arXiv:physics/0403029 [physics]. [Pribory i Tekhnika Eksperimenta 2004, no.1, 77 (2004) (in Russian)].
[200] M. Wallraff, "Design, implementation and test of a new feature extractor for the IceCube Neutrino Observatory." https://internal.icecube.wisc.edu/reports/details.php?type=report&id=icecube%252F201003002. (internal IceCube report 201003002).
[201] N. van Eijndhoven, O. Fadiran, and G. Japaridze, "Implementation of a Gauss convoluted Pandel PDF for track reconstruction in Neutrino Telescopes," *Astroparticle Physics* **28** (2007) 456–462, arXiv:0704.1706 [astro-ph].
[202] M. Baker and J. A. Aguilar and J. Dumm and T. Montaruli, "IceCube Muon Filter for 2010 Pole Season." https://docushare.icecube.wisc.edu/dsweb/Get/Document-52529/2010_TFT_MuonFilterv1p1-1.pdf. (internal IceCube website).
[203] O. Schulz, "SeededRT Cleaning." http://code.icecube.wisc.edu/svn/projects/SeededRTCleaning. (internal IceCube website).
[204] C. Weaver, *Evidence for Astrophysical Muon Neutrinos from the Northern Sky*. PhD thesis, University of Wisconsin-Madison, 2015.
[205] M. G. Aartsen *et al.*, IceCube Collaboration, "Evidence for Astrophysical Muon Neutrinos from the Northern Sky with IceCube," *Physical Review Letters* **115** no. 8, (2015) 081102, arXiv:1507.04005 [astro-ph.HE].
[206] D. Chirkin, "MuEx." http://code.icecube.wisc.edu/svn/projects/mue/trunk. (internal IceCube website).
[207] R. Abbasi *et al.*, IceCube Collaboration, "An improved method for measuring muon energy using the truncated mean of dE/dx," *Nuclear Instruments and Methods* **A703** (2013) 190–198, arXiv:1208.3430 [physics.data-an].
[208] K. Mitsui, "Muon energy loss distribution and its applications to muon energy determination," *Physical Review* **D45** (1992) 3051–3060.
[209] "Pyminuit." https://github.com/jpivarski/pyminuit.
[210] J. Beringer *et al.*, Particle Data Group Collaboration, "Review of Particle Physics (RPP) - Statistics," *Physical Review* **D86** (2012) 010001.
[211] F. James, "MINUIT Function Minimization and Error Analysis: Reference Manual Version 94.1," 1994.
[212] M. G. Aartsen *et al.*, IceCube Collaboration, "Flavor Ratio of Astrophysical Neutrinos above 35 TeV in IceCube," *Physical Review Letters* **114** no. 17, (2015) 171102, arXiv:1502.03376 [astro-ph.HE].
[213] S. Palomares-Ruiz, A. C. Vincent, and O. Mena, "Spectral analysis of the high-energy IceCube neutrinos," *Physical Review* **D91** no. 10, (2015) 103008, arXiv:1502.02649 [astro-ph.HE].
[214] C. Kopper, W. Giang, and N. Kurahashi, IceCube Collaboration, "Observation of Astrophysical Neutrinos in Four Years of IceCube Data," arXiv:1510.05223v2. 34th

International Cosmic Ray Conference - The Hague, The Netherlands.
[215] M. G. Aartsen *et al.*, IceCube Collaboration, "Observation of High-Energy Astrophysical Neutrinos in Three Years of IceCube Data," *Physical Review Letters* **113** (2014) 101101, arXiv:1405.5303 [astro-ph.HE].
[216] M. G. Aartsen *et al.*, IceCube Collaboration, "Atmospheric and astrophysical neutrinos above 1 TeV interacting in IceCube," *Physical Review* **D91** no. 2, (2015) 022001, arXiv:1410.1749 [astro-ph.HE].
[217] H. Niederhausen, M. Lesiak-Bzdak, and A. Stoessl, IceCube Collaboration, "High energy astrophysical neutrino flux characteristics for neutrino-induced cascades using IC79 and IC86-string IceCube configurations," arXiv:hep-ph/1510.05223v2.
[218] M. G. Aartsen *et al.*, IceCube Collaboration, "A combined maximum-likelihood analysis of the high-energy astrophysical neutrino flux measured with IceCube," *Astrophysical Journal* **809** no. 1, (2015) 98, arXiv:1507.03991 [astro-ph.HE].
[219] V. Agrawal, T. K. Gaisser, P. Lipari, and T. Stanev, "Atmospheric neutrino flux above 1-GeV," *Physical Review* **D53** (1996) 1314–1323, arXiv:hep-ph/9509423 [hep-ph].
[220] T. K. Gaisser, "Atmospheric Lepton Fluxes," *European Physical Journal Web Conference* **99** (2015) 05002, arXiv:1412.6424 [astro-ph.HE].
[221] N. Agafonova *et al.*, OPERA Collaboration, "Measurement of the atmospheric muon charge ratio with the OPERA detector," *European Physical Journal* **C67** (2010) 25–37, arXiv:1003.1907 [hep-ex].
[222] M. Inaba, "The Summary of Error Estimation due to the Detector." http://www.ppl.phys.chiba-u.jp/research/IceCube/pmt/GoldenPMT/error_summary/index.html. Chiba University, Japan.
[223] J. Feintzeig, *Searches for Point-like Sources of Astrophysical Neutrinos with the IceCube Neutrino Observatory*. PhD thesis, University of Wisconsin-Madison, 2014.
[224] R. Brent, *Algorithms for Minimization Without Derivatives*. Prentice-Hall, Englewood Cliffs, NJ, 1973.
[225] C. Wiebusch, J. Auffenberg, C. Haack, D. Hellwig, L. Raedel, and S. Schoenen, "On the correction of atmospheric temperature variations in atmospheric neutrino flux simulations." (IceCube internal report 201505001-v3), 2015.
[226] G. Binder, "Reweighting neutrino flux calculations to general atmospheric models." Lawrence Berkeley National Laboratory IceCube group meeting (internal document), 2015.
[227] "U.S. Seasonal Standard Atmosphere." http://ccmc.gsfc.nasa.gov/modelweb/models/nrlmsise00.php.
[228] L. Raedel and S. Schoenen, IceCube Collaboration, "A measurement of the diffuse astrophysical muon neutrino flux using multiple years of IceCube data," *Proceedings of Science* (2015) 1079, arXiv:1510.05223.
[229] M. G. Aartsen *et al.*, IceCube Collaboration, "IceCube-Gen2 - The Next Generation Neutrino Observatory at the South Pole: Contributions to ICRC 2015," arXiv:1510.05228 [astro-ph.IM].
[230] S. Adrian-Martinez *et al.*, KM3NeT Collaboration, "Deep sea tests of a prototype of the KM3NeT digital optical module," *Euopean Physical Journal* **C74** no. 9, (2014) 3056, arXiv:1405.0839 [astro-ph.IM].

[231] G. Askaryan, "Excess Negative Charge of an Electron-Photon Shower And Its Coherent Radio Emission," *Soviet Physics - Journal of Experimental and Theoretical Physics* **14** no. 2, (1962) 441–443.

[232] G. Askaryan, "Coherent Radio Emission from Cosmic Showers in Air and in Dense Media," *Soviet Physics - Journal of Experimental and Theoretical Physics* **21** no. 3, (1965) 658.

[233] S. Barwick *et al.*, ARIANNA Collaboration, "A first search for cosmogenic neutrinos with the ARIANNA Hexagonal Radio Array," *Astroparticle Physics* **70** (2015) 12 – 26. http://www.sciencedirect.com/science/article/pii/S0927650515000638.

[234] S. W. Barwick *et al.*, ANITA Collaboration, "Constraints on cosmic neutrino fluxes from the ANITA experiment," *Physical Review Letters* **96** (2006) 171101, arXiv:astro-ph/0512265 [astro-ph].

[235] P. W. Gorham *et al.*, "Characteristics of Four Upward-pointing Cosmic-ray-like Events Observed with ANITA," *Physical Review Letters* **117** no. 7, (2016) 071101, arXiv:1603.05218 [astro-ph.HE].

[236] I. Kravchenko, S. Hussain, D. Seckel, D. Besson, E. Fensholt, J. Ralston, J. Taylor, K. Ratzlaff, and R. Young, "Updated Results from the RICE Experiment and Future Prospects for Ultra-High Energy Neutrino Detection at the South Pole," *Physical Review* **D85** (2012) 062004, arXiv:1106.1164 [astro-ph.HE].

Appendix A

Truncated Energy Journal Article

Nuclear Instruments and Methods in Physics Research A 703 (2013) 190–198

Contents lists available at SciVerse ScienceDirect

Nuclear Instruments and Methods in Physics Research A

journal homepage: www.elsevier.com/locate/nima

An improved method for measuring muon energy using the truncated mean of dE/dx

R. Abbasi [ab], Y. Abdou [w], M. Ackermann [ap], J. Adams [p], J.A. Aguilar [v], M. Ahlers [ab], D. Altmann [i], K. Andeen [ab], J. Auffenberg [ab], X. Bai [af,1], M. Baker [ab], S.W. Barwick [x], V. Baum [ac], R. Bay [g], K. Beattie [h], J.J. Beatty [r,s], S. Bechet [m], J. Becker Tjus [j], K.-H. Becker [ao], M. Bell [am], M.L. Benabderrahmane [ap], S. BenZvi [ab], J. Berdermann [ap], P. Berghaus [ap], D. Berley [q], E. Bernardini [ap], D. Bertrand [m], D.Z. Besson [z], D. Bindig [ao], M. Bissok [a], E. Blaufuss [q], J. Blumenthal [a], D.J. Boersma [a], C. Bohm [ai], D. Bose [n], S. Böser [k], O. Botner [an], L. Brayeur [n], A.M. Brown [p], R. Bruijn [y], J. Brunner [ap], S. Buitink [n], M. Carson [w], J. Casey [e], M. Casier [n], D. Chirkin [ab], B. Christy [q], F. Clevermann [t], S. Cohen [y], D.F. Cowen [am,al], A.H. Cruz Silva [ap], M. Danninger [ai], J. Daughhetee [e], J.C. Davis [r], C. De Clercq [n], F. Descamps [ab], P. Desiati [ab], G. de Vries-Uiterweerd [w], T. DeYoung [am], J.C. Díaz-Vélez [ab], J. Dreyer [j], J.P. Dumm [ab], M. Dunkman [am], R. Eagan [am], J. Eisch [ab], R.W. Ellsworth [q], O. Engdegård [an], S. Euler [a], P.A. Evenson [af], O. Fadiran [ab], A.R. Fazely [f], A. Fedynitch [j], J. Feintzeig [ab], T. Feusels [w], K. Filimonov [g], C. Finley [ai], T. Fischer-Wasels [ao], S. Flis [ai], A. Franckowiak [k], R. Franke [ap], K. Frantzen [t], T. Fuchs [t], T.K. Gaisser [f], J. Gallagher [aa], L. Gerhardt [h,g], L. Gladstone [ab], T. Glüsenkamp [ap], A. Goldschmidt [h], J.A. Goodman [q], D. Góra [ap], D. Grant [u], A. Groß [ae], S. Grullon [ab], M. Gurtner [ao], C. Ha [h,g], A. Haj Ismail [w], A. Hallgren [an], F. Halzen [ab], K. Hanson [m], D. Heereman [m], P. Heimann [a], D. Heinen [a], K. Helbing [ao], R. Hellauer [q], S. Hickford [p], G.C. Hill [b], K.D. Hoffman [q], R. Hoffmann [ao], A. Homeier [k], K. Hoshina [ab], W. Huelsnitz [q,2], P.O. Hulth [ai], K. Hultqvist [ai], S. Hussain [af], A. Ishihara [o], E. Jacobi [ap], J. Jacobsen [ab], G.S. Japaridze [d], O. Jlelati [w], A. Kappes [i], T. Karg [ap], A. Karle [ab], J. Kiryluk [aj], F. Kislat [ap], J. Kläs [ao], S.R. Klein [h,g,*], J.-H. Köhne [t], G. Kohnen [ad], H. Kolanoski [i], L. Köpke [ac], C. Kopper [ab], S. Kopper [ao], D.J. Koskinen [am], M. Kowalski [k], M. Krasberg [ab], G. Kroll [ac], J. Kunnen [n], N. Kurahashi [ab], T. Kuwabara [af], M. Labare [n], K. Laihem [a], H. Landsman [ab], M.J. Larson [ak], R. Lauer [ap], M. Lesiak-Bzdak [aj], J. Lünemann [ac], J. Madsen [ah], R. Maruyama [ab], K. Mase [o], H.S. Matis [h], F. McNally [ab], K. Meagher [q], M. Merck [ab], P. Mészáros [al,am], T. Meures [m], S. Miarecki [h,g,**], E. Middell [ap], N. Milke [t], J. Miller [n], L. Mohrmann [ap], T. Montaruli [v,3], R. Morse [ab], S.M. Movit [al], R. Nahnhauer [ap], U. Naumann [ao], S.C. Nowicki [u], D.R. Nygren [h], A. Obertacke [ao], S. Odrowski [ae], A. Olivas [q], M. Olivo [j], A. O'Murchadha [m], S. Panknin [k], L. Paul [a], J.A. Pepper [ak], C. Pérez de los Heros [an], D. Pieloth [t], N. Pirk [ap], J. Posselt [ao], P.B. Price [g], G.T. Przybylski [h], L. Rädel [a], K. Rawlins [c], P. Redl [q], E. Resconi [ae], W. Rhode [t], M. Ribordy [y], M. Richman [q], B. Riedel [ab], J.P. Rodrigues [ab], F. Rothmaier [ac], C. Rott [r], T. Ruhe [t], B. Ruzybayev [af], D. Ryckbosch [w], S.M. Saba [j], T. Salameh [am], H.-G. Sander [ac], M. Santander [ab], S. Sarkar [ag], K. Schatto [ac], M. Scheel [a], F. Scheriau [t], T. Schmidt [q], M. Schmitz [t], S. Schoenen [a], S. Schöneberg [j], L. Schönherr [a], A. Schönwald [ap], A. Schukraft [a], L. Schulte [k], O. Schulz [ae], D. Seckel [af], S.H. Seo [ai], Y. Sestayo [ae], S. Seunarine [l], M.W.E. Smith [am], M. Soiron [a], D. Soldin [ao], G.M. Spiczak [ah], C. Spiering [ap], M. Stamatikos [r,4], T. Stanev [af], A. Stasik [k], T. Stezelberger [h], R.G. Stokstad [h], A. Stößl [ap], E.A. Strahler [n], R. Ström [an], G.W. Sullivan [q], H. Taavola [an], I. Taboada [e], A. Tamburro [af], S. Ter-Antonyan [f], S. Tilav [af], P.A. Toale [ak], S. Toscano [ab], M. Usner [k], D. van der Drift [h,g], N. van Eijndhoven [n], A. Van Overloop [w], J. van Santen [ab], M. Vehring [a], M. Voge [k], C. Walck [ai], T. Waldenmaier [i], M. Wallraff [a], M. Walter [ap], R. Wasserman [am], Ch. Weaver [ab], C. Wendt [ab], S. Westerhoff [ab], N. Whitehorn [ab], K. Wiebe [ac], C.H. Wiebusch [a], D.R. Williams [ak], H. Wissing [q], M. Wolf [ai], T.R. Wood [u], K. Woschnagg [g], C. Xu [af], D.L. Xu [ak], X.W. Xu [f], J.P. Yanez [ap], G. Yodh [x], S. Yoshida [o], P. Zarzhitsky [ak], J. Ziemann [t], A. Zilles [a], M. Zoll [ai]

[a] *III. Physikalisches Institut, RWTH Aachen University, D-52056 Aachen, Germany*
[b] *School of Chemistry & Physics, University of Adelaide, Adelaide SA, 5005 Australia*

0168-9002/$ - see front matter
http://dx.doi.org/10.1016/j.nima.2012.11.081

[c] Department of Physics and Astronomy, University of Alaska Anchorage, 3211 Providence Dr., Anchorage, AK 99508, USA
[d] CTSPS, Clark-Atlanta University, Atlanta, GA 30314, USA
[e] School of Physics and Center for Relativistic Astrophysics, Georgia Institute of Technology, Atlanta, GA 30332, USA
[f] Department of Physics, Southern University, Baton Rouge, LA 70813, USA
[g] Department of Physics, University of California, Berkeley, CA 94720, USA
[h] Lawrence Berkeley National Laboratory, Berkeley, CA 94720, USA
[i] Institut für Physik, Humboldt-Universität zu Berlin, D-12489 Berlin, Germany
[j] Fakultät für Physik & Astronomie, Ruhr-Universität Bochum, D-44780 Bochum, Germany
[k] Physikalisches Institut, Universität Bonn, Nussallee 12, D-53115 Bonn, Germany
[l] Department of Physics, University of the West Indies, Cave Hill Campus, Bridgetown BB11000, Barbados
[m] Université Libre de Bruxelles, Science Faculty CP230, B-1050 Brussels, Belgium
[n] Vrije Universiteit Brussel, Dienst ELEM, B-1050 Brussels, Belgium
[o] Department of Physics, Chiba University, Chiba 263-8522, Japan
[p] Department of Physics and Astronomy, University of Canterbury, Private Bag 4800, Christchurch, New Zealand
[q] Department of Physics, University of Maryland, College Park, MD 20742, USA
[r] Department of Physics and Center for Cosmology and Astro-Particle Physics, Ohio State University, Columbus, OH 43210, USA
[s] Department of Astronomy, Ohio State University, Columbus, OH 43210, USA
[t] Department of Physics, TU Dortmund University, D-44221 Dortmund, Germany
[u] Department of Physics, University of Alberta, Edmonton, Alberta, Canada T6G 2G7
[v] Département de physique nucléaire et corpusculaire, Université de Genève, CH-1211 Genève, Switzerland
[w] Department of Physics and Astronomy, University of Gent, B-9000 Gent, Belgium
[x] Department of Physics and Astronomy, University of California, Irvine, CA 92697, USA
[y] Laboratory for High Energy Physics, École Polytechnique Fédérale, CH-1015 Lausanne, Switzerland
[z] Department of Physics and Astronomy, University of Kansas, Lawrence, KS 66045, USA
[aa] Department of Astronomy, University of Wisconsin, Madison, WI 53706, USA
[ab] Department of Physics and Wisconsin IceCube Particle Astrophysics Center, University of Wisconsin, Madison, WI 53706, USA
[ac] Institute of Physics, University of Mainz, Staudinger Weg 7, D-55099 Mainz, Germany
[ad] Université de Mons, 7000 Mons, Belgium
[ae] T.U. Munich, D-85748 Garching, Germany
[af] Bartol Research Institute and Department of Physics and Astronomy, University of Delaware, Newark, DE 19716, USA
[ag] Department of Physics, University of Oxford, 1 Keble Road, Oxford OX1 3NP, UK
[ah] Department of Physics, University of Wisconsin, River Falls, WI 54022, USA
[ai] Oskar Klein Centre and Department of Physics, Stockholm University, SE-10691 Stockholm, Sweden
[aj] Department of Physics and Astronomy, Stony Brook University, Stony Brook, NY 11794-3800, USA
[ak] Department of Physics and Astronomy, University of Alabama, Tuscaloosa, AL 35487, USA
[al] Department of Astronomy and Astrophysics, Pennsylvania State University, University Park, PA 16802, USA
[am] Department of Physics, Pennsylvania State University, University Park, PA 16802, USA
[an] Department of Physics and Astronomy, Uppsala University, Box 516, S-75120 Uppsala, Sweden
[ao] Department of Physics, University of Wuppertal, D-42119 Wuppertal, Germany
[ap] DESY, D-15735 Zeuthen, Germany

ARTICLE INFO

Article history:
Received 23 August 2012
Received in revised form
29 October 2012
Accepted 4 November 2012
Available online 23 November 2012

Keywords:
Muon energy
dE/dx
Neutrino energy
Truncated mean
Cherenkov
IceCube detector

ABSTRACT

The measurement of muon energy is critical for many analyses in large Cherenkov detectors, particularly those that involve separating extraterrestrial neutrinos from the atmospheric neutrino background. Muon energy has traditionally been determined by measuring the specific energy loss (dE/dx) along the muon's path and relating the dE/dx to the muon energy. Because high-energy muons ($E_\mu > 1$ TeV) lose energy randomly, the spread in dE/dx values is quite large, leading to a typical energy resolution of 0.29 in $\log_{10}(E_\mu)$ for a muon observed over a 1 km path length in the IceCube detector. In this paper, we present an improved method that uses a truncated mean and other techniques to determine the muon energy. The muon track is divided into separate segments with individual dE/dx values. The elimination of segments with the highest dE/dx results in an overall dE/dx that is more closely correlated to the muon energy. This method results in an energy resolution of 0.22 in $\log_{10}(E_\mu)$, which gives a 26% improvement. This technique is applicable to any large water or ice detector and potentially to large scintillator or liquid argon detectors.

1. Introduction

Large ice or water Cherenkov detectors may observe up to 100,000 ν_μ per year [1]. These events are used for a wide variety of analyses, including searches for point sources of neutrinos [2–4], diffuse extraterrestrial neutrinos [4–6], standard and non-standard neutrino oscillations [7], and measurements of the total neutrino-nucleon cross-section via neutrino absorption in the Earth.

These analyses rely upon the measurement of the neutrino energy, which is determined from the energy of the muon that is created in the neutrino interaction. Above ~ 1 TeV, the muon energy is usually determined by measuring the specific energy loss, dE/dx, of the muon as it travels through the detector. The Cherenkov photons from the muon and also those derived from the charged particles produced by stochastic (random) muon

* Corresponding author at: Lawrence Berkeley National Laboratory, 1 Cyclotron Rd, Mail Stop 50R5008, Berkeley, CA 94720, USA. Tel.: +1 510 486 5470; fax: +1 510 486 6738.
** Corresponding author at: Lawrence Berkeley National Laboratory, 1 Cyclotron Rd, Mail Stop 50R5008, Berkeley, CA 94720, USA. Tel.: +1 510 486 7620; fax +1 510 486 6738.
E-mail addresses: srklein@lbl.gov (S.R. Klein), miarecki@berkeley.edu (S. Miarecki).

[1] Physics Department, South Dakota School of Mines and Technology, Rapid City, SD 57701, USA.
[2] Los Alamos National Laboratory, Los Alamos, NM 87545, USA.
[3] also Sezione INFN, Dipartimento di Fisica, I-70126 Bari, Italy.
[4] NASA Goddard Space Flight Center, Greenbelt, MD 20771, USA.

interactions are then detected. This approach is disadvantageous because, for $E_\mu > 1$ TeV, muons lose most of their energy stochastically, and a small number of high-energy interactions will not only skew the mean but also enlarge the spread in dE/dx values.

In this paper, we present an improved method for calculating the muon energy loss, which leads to significant improvement in the energy resolution. Instead of averaging the muon dE/dx over the entire observed muon path length, we divide the path into independent segments, or bins. The dE/dx is calculated separately for each bin. Then, the bins with the highest dE/dx values are discarded before calculating a new average dE/dx, thus producing a truncated mean. This method is successful because the truncated mean minimizes the effects of the large stochastic events which would otherwise skew the mean and enlarge the spread.

This is the first time that the truncated mean has been systematically applied to the energy measurement of high-energy muons. The truncated mean method has previously been calculated for muons [8], although that analysis did not use it to determine the muon energy. The method was also explored at a basic level for the DUMAND project [9]. The method has parallels to the one that was used to identify pions, kaons, and protons in wire chambers from their specific energy loss dE/dx in the gas. By discarding the highest 30% or 40% of the dE/dx measurements from the wires, the energy resolution was greatly improved [10,11]. As with wire chamber dE/dx measurements, the muon energy resolution is improved by discarding the most energetic stochastic losses. This method should be applicable to any large water or ice Cherenkov detector, such as IceCube [1], ANTARES [12], or the proposed KM3NeT [13], MEMPHYS [14], or Hyper-Kamiokande (Hyper-K) [15]. This approach may also be useful for proposed scintillator or liquid argon detectors, such as the Low Energy Neutrino Astronomy detector (LENA) [16] or the Long-Baseline Neutrino Experiment (LBNE) [17].

2. Muon energy loss

Muons lose energy via ionization and by stochastic processes such as bremsstrahlung, pair production, and photonuclear interactions [18–21]. Muons also emit Cherenkov radiation, but this is a very small fraction of the total energy loss. Ionization loss is roughly independent of muon energy and essentially constant per unit length, while the dE/dx due to stochastic processes rises linearly with the energy. Thus, the total average energy loss of the muon is [22]

$$\frac{dE_\mu}{dx} = A + BE_\mu \tag{1}$$

where $A \approx 0.0024$ GeV $(\mathrm{g/cm^2})^{-1}$ accounts for the energy loss due to ionization, and $B \approx 0.000032$ $(\mathrm{g/cm^2})^{-1}$ is due to the stochastic energy loss [20]. Ionization effects are dominant for muons below ~ 500 GeV, at which point the sum of bremsstrahlung, pair production, and photonuclear effects is larger than ionization. As muon energy increases to ~ 10 TeV, ionization effects account for only $\sim 9\%$ of the total muon energy loss, with a much reduced contribution as muon energy increases [20].

Two main methods are used to measure E_μ. For lower-energy muons, the energy is proportional to the path length. This approach works if the muon is contained within the detector, and the starting and stopping points can be determined. For example, a 300 GeV muon has a most probable path length of ~ 1 km in ice. The most probable path length is ~ 2 km for a 1 TeV muon, and the length rises only logarithmically with E_μ, reaching 20 km for a 1 PeV muon [20].

At energies above a few hundred GeV, one measures the dE/dx and infers E_μ from that value, either by using Eq. (1) as an approximation or by calculating the correlation using Monte Carlo simulation. The total energy loss in the entire detector is summed, either using calorimetric measurements of dE/dx (such as by the Frejus collaboration) [23] or by observing the light produced by the stochastic interactions of the muon and charged particles [24].

Muon energy loss is a complex sequence of events where the stochastic processes create many secondary particles that are also subject to further interactions that can result in additional charged particles. The charged particles produce Cherenkov light with a flux that is proportional to the particle energy.

The IceCube Neutrino Detector is highly suited for a study involving muon energy loss. This analysis used IceCube in its 2010 configuration, when the detector consisted of 79 vertical strings (with roughly 125 m horizontal spacing in a triangular grid), with 60 optical modules per string (with 17 m vertical spacing) between 1450 and 2450 m below the surface of the ice sheet at the South Pole. This included DeepCore, which is a denser subarray of strings near the detector center with more-sensitive optical modules placed preferentially on the bottom 400 m of each string [25]. Each optical module holds a 25 cm photomultiplier tube (PMT), plus associated electronics for data acquisition, control, and calibration [1].

Simulated muon trajectories were determined using a program called neutrino-generator (NUGEN) which is based upon the All Neutrino Interaction Simulation (ANIS) [26]. NUGEN simulation includes several effects, including the ice/rock boundary below the detector, Earth-neutrino absorption using the density profile from the Preliminary Reference Earth Model (PREM) [27], neutral current regeneration, etc., but it does not include neutrino oscillations. The program starts with an isotropic distribution of neutrinos on the Earth's surface, following, in this case, a E_ν^{-1} spectrum between 10 GeV and 1 EeV. These neutrino events can be reweighted to simulate softer spectra. NUGEN then propagates the neutrinos to the South Pole, accounting for neutrino absorption in the Earth. Finally, NUGEN simulates the neutrino interactions. The resulting muons are propagated through the ice using the Muon Monte Carlo (MMC) code [20], which includes detailed models for muon energy loss and the Landau–Pomeranchuk–Migdal effect [28].

From the energy deposition determined by MMC, a program called Photonics determines the number and timing distribution of expected photoelectrons for a given optical module [29]. Photonics also accounts for the detector geometry of the optical modules. Finally, a set of detector simulation programs model the response of the PMT, electronics, and triggers [30]. Then the simulated data are analyzed using standard IceCube reconstruction programs. Muon tracks are typically reconstructed with an angular resolution of $< 1^\circ$ [31] and a positional accuracy (in the plane perpendicular to the track) of a few meters.

Detailed simulation verification studies at a low-level [32] and high-level [24] have been published. The systematic uncertainty in simulation is largely due to the understanding of the optical properties of the ice, with smaller contributions from the angular acceptance and saturation effects of the optical sensors. An analysis using in situ light sources [33] discusses the ice properties in detail, with a new paper from IceCube forthcoming. In addition, simulations were completed using three different ice models that resulted in a shifting of the mean but no degradation in the energy resolution, with an overall maximum variation of 13% in the energy reconstruction.

2.1. Conventional dE/dx

Before discussing the truncated mean dE/dx in detail, we will discuss the more conventional approach. First, the number of photoelectrons observed by all the optical modules is summed. Then, the expected number of photoelectrons for a fixed energy

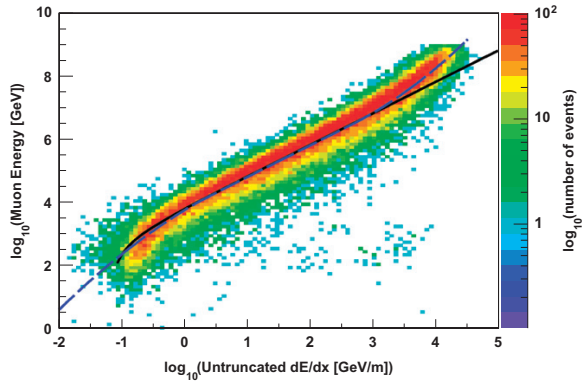

Fig. 1. Simulated E_μ vs. conventional (untruncated) dE/dx at the center of the detector. The dE/dx value is calculated from the ratio of the observed energy deposition to the expected deposition for a minimum ionizing muon with the same trajectory. The solid line uses Eq. (1) for the "linear" fit. The dashed line uses the 3-equation fit described by Eq. (2) and (3).

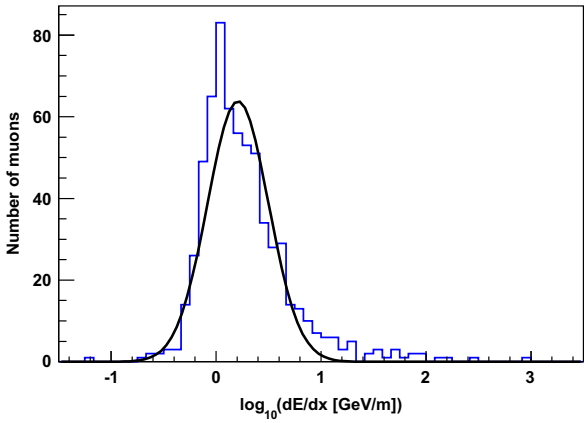

Fig. 2. Conventional (untruncated) muon dE/dx, for muons with simulated energies ~ 10 TeV ($\log_{10}(E_\mu) = 4.0 \pm 0.05$). The black line is a Gaussian fit, with $\sigma = 0.29 \pm 0.01$, and RMS=0.44. The excess of events to the right of the Gaussian curve are muons with large stochastic losses.

loss of 1 GeV/m with the same trajectory is calculated. Since the photoelectron yield is expected to be directly proportional to the muon energy loss rate, the calculated dE/dx value is equal to the ratio of the observed number of photoelectrons to the expected number for the 1 GeV/m track, multiplied by 1 GeV/m. This linear relationship is a proper dE/dx approximation for muon energies above ~ 1 TeV. Because the method uses the distance between each sensor and the muon track, it automatically accounts for varying track geometries, sensor densities, and optical properties of the detector medium, since those effects are included in both the observed and expected numbers of photoelectrons.

Fig. 1 shows a scatter plot of simulated muon energy versus calculated dE/dx. Because the entire track is used, the simulated muon energy value comes from the track's closest approach to the center of the detector (instead of at the entrance to or exit from the detector volume). The dE/dx values have a large spread. Some of the spread is due to the limited sampling by the sensors and consequently the uncertain measurement of the energy loss. However, most of the spread is from the event-by-event variation in stochastic energy losses.

The spread in dE/dx values for a given true energy is quite large for the conventional (untruncated) method. Fig. 2 shows a typical example of the spread for a narrow energy slice, with this one at ~ 10 TeV. The excess of events to the right of the Gaussian curve is a direct result of the large stochastic losses.

The desired output of the method is the energy for each muon. This is done using a fit to the curve in Fig. 1 to calculate E_μ from the dE/dx value, and then we can compare the calculated energy to the simulated energy.

It is apparent that the "linear" fit curve from Eq. (1) does not follow the data precisely, particularly at higher energies. The main experimental effect is saturation in the PMT at very high light intensities [34]. During the reconstruction of both actual and simulated data, no correction is applied for PMT saturation. This produces the upturn in the curve at higher energies for $dE/dx \gtrsim 10^3$ GeV/m. For $dE/dx \lesssim 1$ GeV/m, there is also a small down-turn in the curve, making it S-shaped. This occurs because the muon range at lower energy is less than the size of the detector, while the truncated method assumes that the track is infinite.

We examined a variety of simple fit equations to improve our ability to characterize the muon energy resolution. The optimal fit had three separate sections: a second-order logarithmic ($\log_{10}$) polynomial fitted to the lower energy curve (for $dE/dx \lesssim 1.5$ GeV/m) and another second-order logarithmic polynomial to the higher energy curve ($dE/dx \gtrsim 500$ GeV/m)

$$\log(E_\mu) = A' + B' \log\left(\frac{dE}{dx}\right) + C' \log^2\left(\frac{dE}{dx}\right) \quad (2)$$

where E_μ is the energy of the muon (in GeV) at the track's closest approach to the center of the detector, dE/dx is the calculated value (in GeV/m), and A', B', and C' are dimensionless constants from the best fits to the curves. For the mid-range, we used the logarithmic version of the linear dE/dx equation (Eq. (1))

$$\log(E_\mu) = \log\left(\frac{1}{B''}\left[\frac{dE}{dx} - A''\right]\right) \quad (3)$$

where E_μ is the energy of the muon (in GeV), dE/dx is the calculated value (in GeV/m), and A'' and B'' are dimensionless constants from the best fit to the curve. Because of PMT saturation and other detector effects, the constants in Eq. (3) must be adjusted for a proper fit. The new fit curve is shown in Fig. 1 as a dashed line. We used this 3-equation fit throughout this analysis, instead of the linear fit.

The energy residual E_{res} is nominally defined as $E_{reco} - E_{sim}$, where E_{reco} and E_{sim} are the reconstructed and actual simulated energies, respectively, at the track's closest approach to the center of the detector. Since this analysis covered a wide range of energies, the energy residual was redefined as $E_{res} = \log_{10}(E_{reco}) - \log_{10}(E_{sim})$. Fig. 3 shows the results of this energy comparison, using the 3-equation fit. The distribution is skewed, with a long tail of events containing large stochastic energy deposition, indicating that the energies for these events are badly overestimated. About 5.4% of the muon energies are overestimated by more than a factor of 5.

If the distribution of energies is fit to a Gaussian, the energy resolution σ is 0.29 in $\log_{10}(E_\mu)$, or roughly a factor of 2.0 in energy. The statistical error is less than 1% for this resolution and all other resolutions presented in this paper (unless otherwise noted). However, the peak of the curve is offset from 0 by -0.08, and the curve is skewed. The shift towards lower muon energies occurs because the fit curve in Fig. 1 does not line up with the highest concentration of events. This occurs because the fit curve is pulled towards higher dE/dx values for a given muon energy due to the stochastic losses. For a specific dE/dx value, the calculated energy using the fit equations for the bulk of the events will be too low. This pushes the peak of the distribution of energy residuals toward the negative. Fortunately, in a full analysis, this bias would cancel out if the method were used identically for both data and simulation, and the spread would be the most relevant issue.

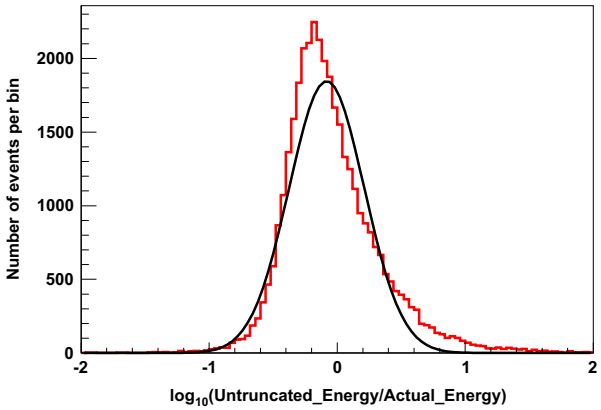

Fig. 3. Conventional (untruncated) muon energy resolution, using the 3-equation fit curve from Fig. 1, for muons with simulated energies between 1 TeV and 1 EeV. The black line is a Gaussian fit, with the peak offset by -0.08 in $\log_{10}(E_\mu)$, $\sigma = 0.29$, and with an RMS of 0.37. The excess of events to the right of the Gaussian curve is a direct result of the large stochastic losses.

In this analysis, we used both the Gaussian σ and the RMS to characterize the improvements in the spread in calculated dE/dx and E_μ. In most cases, the RMS was significantly larger than σ because the RMS is more sensitive to the high-energy tails in the distributions.

2.2. Truncated mean dE/dx

The truncated mean method divides the track into bins which are bordered by planes perpendicular to the track, and the sensor data are binned accordingly by their location. The dE/dx value is determined as before by finding the ratio of the observed photoelectrons to the expected photoelectrons, but a separate ratio is determined for each bin instead of the event as a whole. Then a fraction of the bins (using the optimization discussed below) with the highest ratios are discarded, and the truncated dE/dx is calculated by summing the remaining observed photoelectrons and expected photoelectrons and creating a new ratio.

Many factors influence the choice of bin size, with the objective to create bins as independent from each other as possible. Large Cherenkov detectors use sparse sampling with sizeable distances between sensors, and each sensor observes light over a limited track segment. The length of the segment depends on the optical properties of the medium, with different properties for sea water, ice, and liquid scintillators that vary with the wavelength of light.

In water, absorption effects are much stronger than scattering. Thus the most appropriate measure of optical properties would be the absorption length, which peaks at wavelengths ~ 470 nm. The absorption length is ~ 22 m in lake water [35] and ~ 60 m in seawater [36].

In deep glacial ice, however, scattering effects are stronger than absorption, and the appropriate measure is the light propagation length, which peaks ~ 400 nm. This length depends on both the effective scattering length λ_{es} and the absorption length λ_a in the medium, using the relation

$$\lambda_{prop} = \sqrt{\frac{\lambda_{es}\lambda_a}{3}}. \quad (4)$$

In IceCube, for example, the average absorption coefficient is $\sim 0.008\ \mathrm{m}^{-1}$, or an absorption length of 125 m, while the average effective scattering coefficient is $\sim 0.040\ \mathrm{m}^{-1}$, or an effective scattering length of 25 m [33]. The average propagation length is thus ~ 32 m, which increases to ~ 45 m for the very clear ice in the bottom of the detector.

For liquid scintillator detectors, the absorption length is the appropriate measure of optical properties, which is typically 10–20 m [16].

The detector geometry may also impose constraints on the truncated mean's binning method. In ANTARES, for example, the string spacing is 70 m, which is more than the reported absorption length. In Hyper-K, with its large photocathode coverage, the water properties may be the determining factor for the optimal bin length. Hyper-K's 250-m tank length is far longer than the light attenuation length, and the detector geometry will naturally allow for track segmentation.

Most of the vertical strings of optical modules in IceCube are deployed on a 125-m grid, making the detector roughly hexagonal in shape. For near-horizontal tracks, this string separation sets the minimum sampling distance, and hence a minimum bin length. In this study, since the IceCube array is not perfectly regular and to avoid having 0 or 2 strings in a bin for horizontal tracks, a 120-m bin length was used, spreading the energy more evenly across the bins. Due to the size of the detector, events could have up to 15 bins. For comparison, the average distance between the occurrence of any stochastic event, where the muon loses more than 1% of its energy, is ~ 250 m at 1 TeV, using the MMC program for ice [20]. This distance is much larger than the bin size.

Fig. 4 shows a scatter plot of simulated E_μ versus truncated dE/dx for the same events as in Fig. 1, but now using the truncated dE/dx with 40% of the highest bins discarded, and including the optimizations discussed in Section 3. For this analysis, a minimum of three bins was required for the event to qualify, since a 40% truncation would result in 0 bins omitted for a 2-bin event. The distribution is much narrower than the conventional untruncated dE/dx method but retains the same S-shape, for the same reasons.

The spread in dE/dx values is much narrower for the truncated method than for the conventional method. A comparison of the distributions of dE/dx values for the same narrow energy range as in Fig. 2 is shown in Fig. 5. For the truncated method, the Gaussian σ is 0.18, compared to the untruncated value of 0.29, which constitutes a significant improvement, and the skewness is much reduced.

Fig. 6 shows the corresponding energy resolution using the 3-equation fit from Fig. 4 to calculate the energy. Compared to Fig. 3, the high-energy tail is much smaller in the truncated plot, with only 1.3% of the events reconstructed with more than five times their actual energy. The Gaussian resolution has improved to 0.22 in $\log_{10}(E_\mu)$, which is a factor of 1.6 as compared to 2.0 for the conventional untruncated method (with the 3-equation fit).

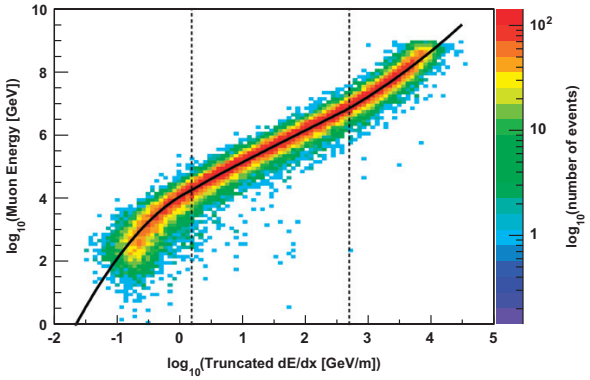

Fig. 4. Simulated E_μ vs. truncated dE/dx at the center of the detector, for the optimized 40% truncation. The distribution is much narrower than in Fig. 1. The vertical dashed lines identify the ranges for the three fit equations (represented by the solid black line).

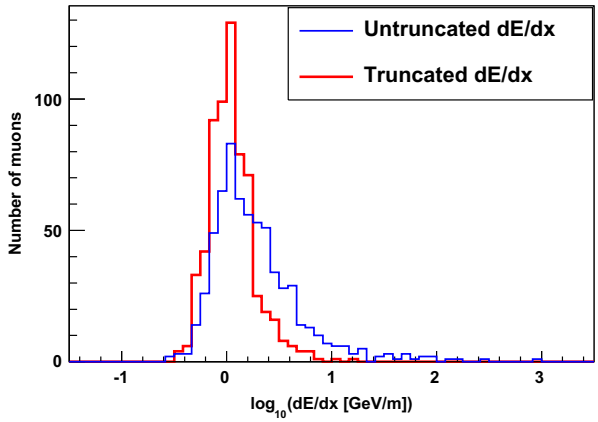

Fig. 5. Truncated muon dE/dx vs. conventional (untruncated) muon dE/dx, for simulated energies ~ 10 TeV ($\log_{10}(E_\mu) = 4.0 \pm 0.05$). For the truncated method, the Gaussian $\sigma = 0.18 \pm 0.01$, and RMS=0.22, compared to the untruncated method values of $\sigma = 0.29$ and RMS=0.44. The effect of the large stochastic events has been greatly diminished, thus reducing the spread.

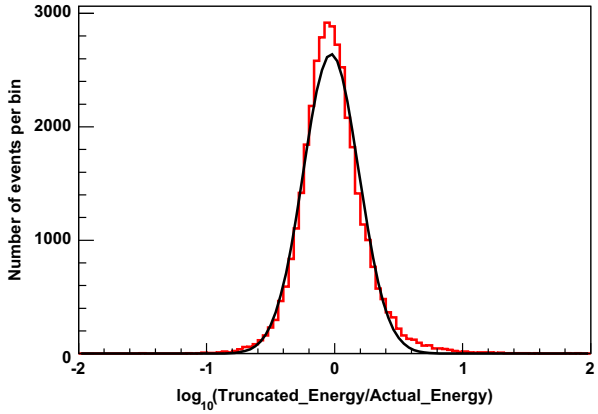

Fig. 6. Truncated muon energy resolution, using the fit curve from Fig. 4, for muons with simulated energies between 1 TeV and 1 EeV. The number of entries to the right of the Gaussian curve (black line) is much smaller with the truncated method, as compared to Fig. 3. The energy resolution improved to $\sigma = 0.22$ in $\log_{10}(E_\mu)$ (a factor of 1.6 in energy), with the mean of the Gaussian curve slightly offset by -0.03, and an RMS value of 0.25.

3. Algorithm optimization and performance

We studied several variations of the algorithm to optimize performance. The parameters included the fraction of bins discarded in the truncated mean (Section 3.1) and limits on the distance between the sensor and the reconstructed track (Section 3.2). We also evaluated the inclusion or exclusion of the unhit sensors in the calculation (Section 3.3), and we explored a variation in the truncated method that treated each sensor as its own bin (the "DOMs method") (Section 3.4). Lastly, we looked at the median versus the mean for both the binning and DOMs methods (Section 3.5).

3.1. Truncation percentage

The optimal truncation was determined by evaluating truncation percentages between 0 and 80% of the bins. If the percentage of cut bins resulted in a non-integer value, the fraction was rounded down (for example, 40% of four bins would result in one bin cut). Fig. 7 shows the resulting energy resolutions for different

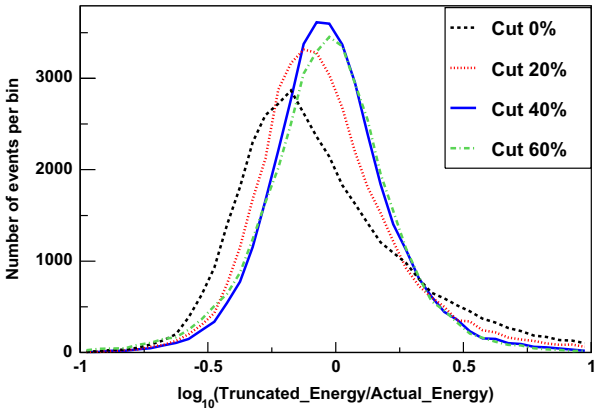

Fig. 7. Energy resolution for truncation percentages ranging from 0% to 60%, for $E_\mu > 1$ TeV. The optimal truncation percentage was 40%. Gaussian σ were 0.27, 0.23, 0.22, and 0.23 for 0, 20, 40, and 60%, respectively. The optimization techniques described in Sections 3.2 and 3.3 have already been applied.

truncating percentages (up to 60% shown). In this analysis, 40% was the optimal cut.

3.2. Distance of optical modules from track

Energy measurement by dE/dx relies on an accurate measurement of the distance between the tracks and the optical modules. However, the reconstructed track positions (transverse to the direction of motion) can be off by several meters. Also, data from optical modules that are very far from the track are less useful because of the increased chance that the sensor hits are noise.

To avoid these issues, we evaluated the performance of the method when requiring a minimum and maximum distance between the track and the sensors. The resolutions for various distances are shown in Table 1 for horizontal muons with simulated energy > 10 TeV. The optimal energy resolution used optical modules that were located between 10 and 80 m from the track. In an optically noisy environment, such as seawater, a smaller maximum distance likely would be optimal.

3.3. Optical modules without observed photoelectrons

In IceCube, most energy reconstruction methods (such as the truncated mean method) use a Gaussian error model, which is valid at high energy but not at low energy where the number of detected photons is bounded at the low end by zero but is not bounded above. For optical modules that detect many photons, this is mostly irrelevant because Poisson errors become symmetrical. Therefore, the inclusion of many low-amplitude sensors, such as those that did not observe any photons (the "unhit" sensors), could bias the likelihood calculation.

In addition, isolated hits (optical modules without hits in their nearest or next-to-nearest neighbors) are likely to be noise. For these reasons, these energy-loss calculations only used the data from optical modules where the nearest or next-to-nearest neighbors were hit within ± 1 μs [37], otherwise known as coincident-hit modules.

In calculating the number of expected photoelectrons, there is no distinction between hit and unhit optical modules, and Photonics will return non-zero amplitudes for all optical modules. To reduce the effect of this mismatch, we studied the effect of counting the expected photoelectrons from only the optical modules with coincident hits, rather than using all the optical modules.

Table 1
Energy resolution σ in $\log_{10}(E_\mu)$ for varying truncated percentage cuts and cylinder distances (in meters) from track, for muons with simulated energy >10 TeV. The optimal resolution occurred with 40% truncation and a cylinder of 10–80 m. When the lower-energy muons are included ($E_\mu > 1$ TeV), the energy resolution is slightly degraded ($\sigma = 0.22$).

	Cylinder distance (meters)						
Cuts (%)	None	0–100	10–100	0–80	10–80	0–60	10–60
0	0.362	0.345	0.331	0.342	0.328	0.329	0.308
10	0.324	0.316	0.282	0.307	0.291	0.319	0.298
20	0.276	0.273	0.222	0.244	0.216	0.242	0.221
30	0.255	0.231	0.211	0.228	0.206	0.229	0.204
40	0.248	0.227	0.210	0.229	**0.198**	0.225	0.204
50	0.250	0.234	0.215	0.229	0.200	0.227	0.202

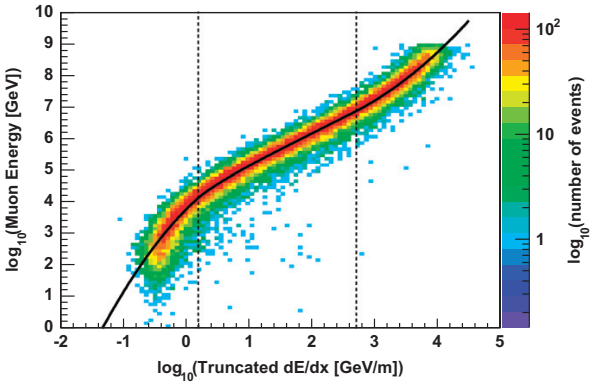

Fig. 8. Simulated E_μ vs. truncated dE/dx, using only the "hit" optical modules within the cylinder. The vertical dashed lines identify the ranges for the three fit equations (represented by the solid black line). At low dE/dx values, the curve drops off more steeply than in Fig. 4, which adversely affects the energy resolution in this range.

Fig. 8 shows the results from this alternate methodology combined with the truncated mean. The energy resolution for this "hit" technique was slightly better at the higher energies. However, at lower energies, the curve is much steeper than in the previous "all-sensor" truncated curve, and the energy resolution was significantly worse when using only the hit sensors in the dE/dx calculation. Thus, this "hit approach" was not used in the final truncated method. Instead, the data from the coincidence-hits (within the cylinder) were used for the actual photoelectron counts, and all the sensors (hit and unhit) in the cylinder were used for the calculation of expected photoelectrons.

3.4. DOMs method

An additional option was explored that diverged from the binning method, which was nicknamed the "DOMs method" after the digital optical modules in IceCube. In this option, instead of using 120 m bins, each optical module became a "bin" and was given its own dE/dx value by dividing the observed number of photoelectrons by the expected number of photoelectrons. The advantages of this method are (1) the track can be shorter (no minimum number of bins), (2) additional data will be used in the energy determination, and (3) the algorithm is slightly faster. The main disadvantage is that a large stochastic event would be recorded by many sensors, and thus there would be an undesirable correlation between sensors.

The technique was optimized (using similar procedures to those outlined above) to require a minimum of eight optical

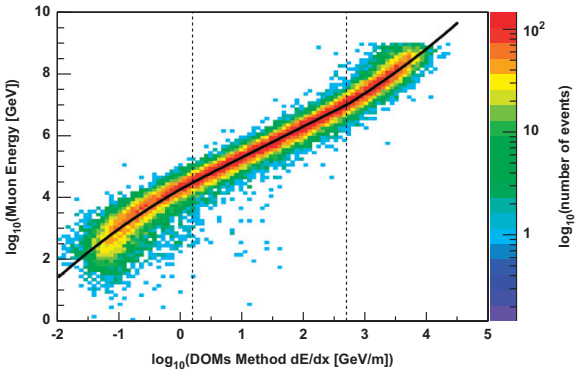

Fig. 9. Simulated E_μ vs. truncated dE/dx (DOMs method) at the center of the detector. The vertical dashed lines identify the ranges for the three fit equations (represented by the solid black line). The event distribution is much narrower than in Fig. 1 but similar to the binning method in Fig. 4.

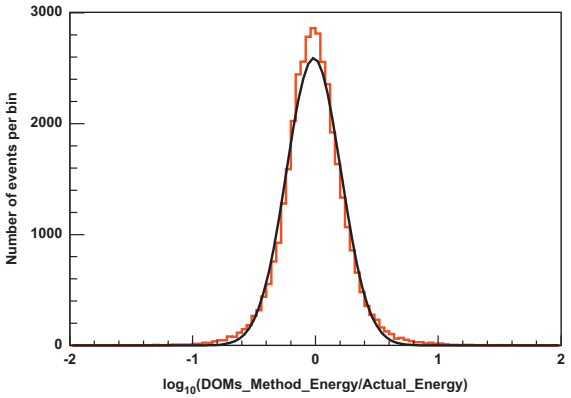

Fig. 10. Truncated muon energy resolution for the DOMs method, for muons with simulated energies between 1 TeV and 1 EeV, using the fit curve from Fig. 9. The number of events to the right of the Gaussian curve is much smaller than in Fig. 3. The resolution is very similar to that of the optimized binning method as shown in Fig. 6 ($\sigma = 0.22$ and RMS$=0.25$).

modules within 0–60 m of the reconstructed track for the event to qualify (versus 10–80 m for the bins method), and the optimal truncation was to omit the highest 50% of the optical modules (versus 40% of the bins). Then the dE/dx values for the remaining optical modules were averaged. This yielded an energy resolution and RMS improvement that was similar to that of the binning method ($\sigma = 0.22$ and RMS$=0.25$).

Figs. 9 and 10 show the results of this method. One or the other method may prove more useful in the various detector designs and is an option that can be explored. In this analysis, about 4% of the events would qualify for only one of the methods, while the remainder would qualify for both. Including the two approaches maximizes the capability of the truncated mean method.

3.5. Median method

One final option was to change from the truncated mean to the median of the bins. In this method, the truncation occurred at both the upper and lower ends of the ordered list of bins (or DOMs, in the case of the DOMs method), such that only one bin (DOM) remained. The dE/dx value for this bin (DOM) became the value for the event. For both the binning method and the DOMs method, which had separate optimizations, the energy resolution

and RMS were nearly unchanged for all muon energies when compared to the earlier truncated mean methods.

4. Results and conclusions

There is no apparent correlation between the energy calculation and the zenith angle (see Fig. 11). The distributions of the energy residuals are very similar in shape and width. There is also no apparent correlation between the energy calculation and azimuth angle, optical properties of the medium, or other parameters. Thus the truncation method is universally applicable to all particle track zenith and azimuth angles within the detector, with the proper bin size. The energy resolution improves with an increasing number of bins as expected, as shown in Fig. 12, but levels off at 0.18 in $\log_{10}(E_\mu)$.

Fig. 13 compares the RMS and Gaussian σ values of truncated and untruncated dE/dx for various muon energies, showing the improvement from using the truncated method.

Figs. 14 and 15 contrast the untruncated and truncated methods, respectively, for actual versus calculated muon energy. The improvement in energy resolution is fairly uniform over the energy range.

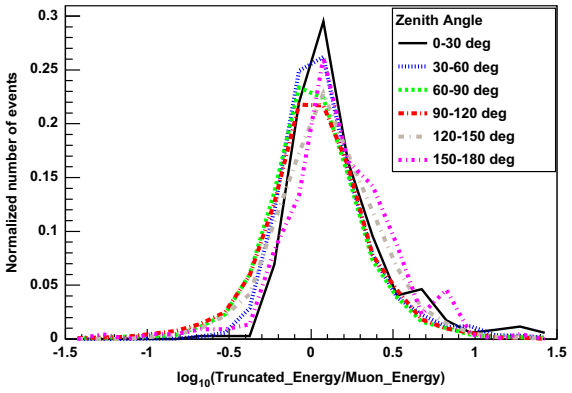

Fig. 11. Energy resolution (in $\log_{10}(E_\mu)$) for zenith angle bins of 30° for E_μ from 1 TeV to 100 TeV, using the truncated bins method. There is no visible correlation between zenith angle and energy resolution, for the energy range from 1 TeV to 1 EeV using an E_ν^{-1} spectrum.

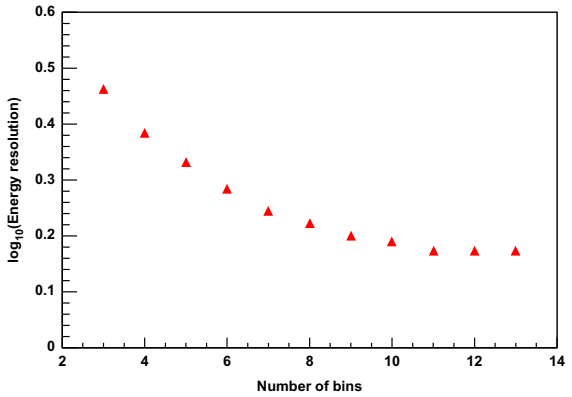

Fig. 12. Correlation between the number of bins and the average energy resolution (in $\log_{10}(E_\mu)$) of the muon events, using the optimized truncated mean method, for $E_\mu \gtrsim 10$ TeV.

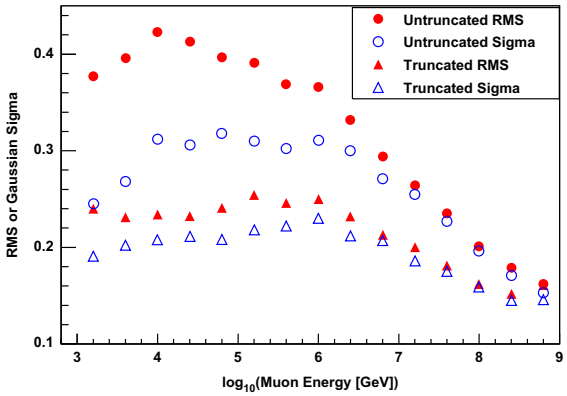

Fig. 13. Comparison of the RMS and Gaussian σ of untruncated and truncated dE/dx values vs. $\log_{10}(E_\mu)$, for simulated energies between 1 TeV and 1 EeV. The energy resolution for the truncated method is much improved over the untruncated method.

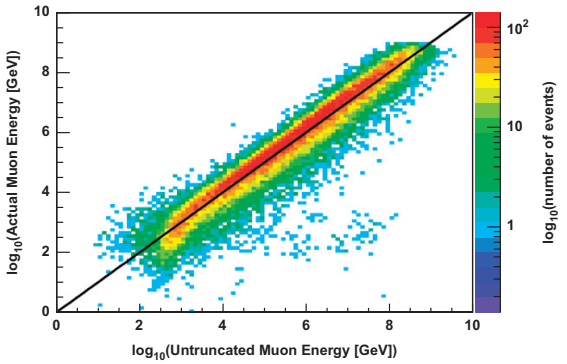

Fig. 14. Actual muon energy versus calculated muon energy for the untruncated method with the 3-equation fit. The black line is a perfect 1:1 correspondence.

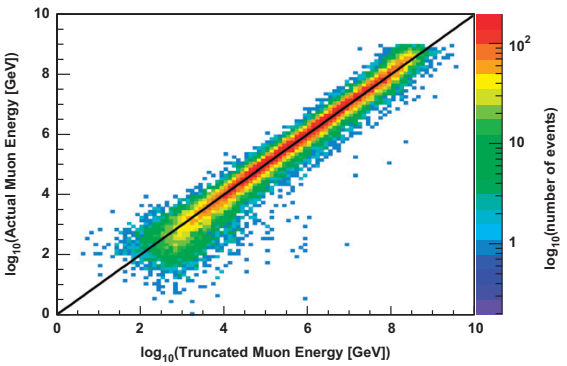

Fig. 15. Actual muon energy versus calculated muon energy for the truncated method (40% cuts with optimizations). The black line is a perfect 1:1 correspondence.

Fig. 16 compares the input muon energy spectrum to the spectrum of calculated energies from the truncated method. The agreement is quite good, with a slight shift in energy below 1 TeV due to the off-peak fit equation plus the spread in dE/dx at low energies. However, there are no glaring discontinuities in the calculated spectrum, which indicates that the truncated method gives back the original spectrum quite well.

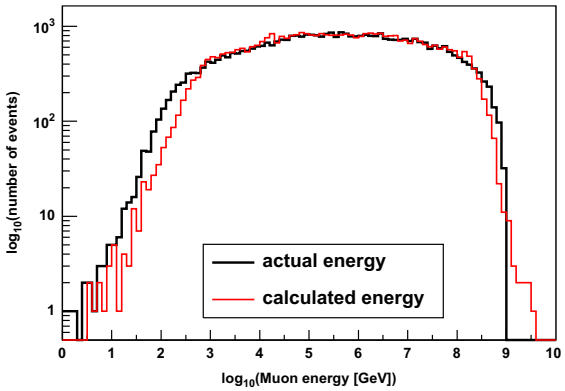

Fig. 16. Comparison of the truncated energy spectrum to the simulated E_ν^{-1} muon energy spectrum. The agreement is quite good between 1 TeV and 1 EeV, with a slight disagreement at low energy due to the large spread in dE/dx and off-peak fit equation to convert to E_μ.

By using the truncated mean method, the energy resolution is significantly improved. The best truncated method incorporated the following criteria: (1) only include the photoelectrons from optical modules within 10 to 80 m of the track, (2) truncate the highest 40% of the bins, (3) use both hit and unhit optical modules in the calculation, and (4) sum the remaining photoelectrons separately (observed and expected) to determine the new truncated dE/dx value. With these optimizations, the energy resolution was improved from 0.29 in $\log_{10}(E_\mu)$ to 0.22, for the energy range of 1 TeV to 1 EeV. This is a 26% improvement in the overall energy resolution, with better resolutions above 10 TeV. The technique is applicable to any detector that uses dE/dx as the primary means of the particle's energy determination.

Acknowledgments

We acknowledge the support from the following agencies: US National Science Foundation-Office of Polar Programs, US National Science Foundation—Physics Division, University of Wisconsin Alumni Research Foundation, the Grid Laboratory Of Wisconsin (GLOW) grid infrastructure at the University of Wisconsin—Madison, the Open Science Grid (OSG) grid infrastructure, US Department of Energy, National Energy Research Scientific Computing Center, the Louisiana Optical Network Initiative (LONI) Grid Computing Resources, the National Defense Science and Engineering Graduate (NDSEG) Fellowship Program; National Science and Engineering Research Council of Canada; Swedish Research Council, Swedish Polar Research Secretariat, Swedish National Infrastructure for Computing (SNIC), Knut and Alice Wallenberg Foundation, Sweden; German Ministry for Education and Research (BMBF), Deutsche Forschungsgemeinschaft (DFG), Research Department of Plasmas with Complex Interactions (Bochum), Germany; Fund for Scientific Research (FNRS-FWO), FWO Odysseus programme, Flanders Institute to encourage scientific and technological research in industry (IWT), Belgian Federal Science Policy Office (Belspo); University of Oxford, United Kingdom; Marsden Fund, New Zealand; Australian Research Council; Japan Society for Promotion of Science (JSPS); the Swiss National Science Foundation (SNSF), Switzerland.

References

[1] F. Halzen, S.R. Klein, Review of Scientific Instruments 81 (2010) 081101.
[2] R. Abbasi, et al., IceCube Collaboration, The Astrophysical Journal 744 (2012) 1.
[3] R. Abbasi, et al., IceCube Collaboration, The Astrophysical Journal 732 (2011) 18.
[4] C. Bogazzi, ANTARES Collaboration, 2011 arXiv:1112.0478.
[5] R. Abbasi, et al., IceCube Collaboration, Physical Review D 84 (2011) 082001.
[6] Zh.-A. Dzhilkibaev, et al., Baikal Collaboration, 2009 arXiv:0909.5562.
[7] R. Abbasi, et al., IceCube Collaboration, Physical Review D 82 (2010) 112003.
[8] P.S. Auchincloss, P. de Barbaro, A. Bodek, H.S. Budd, M. Pillai, F. Qun, W.K. Sakumoto, F.S. Merritt, et al., Nuclear Instruments and Methods in Physics Research Section A 343 (1994) 463.
[9] K. Mitsui, Physical Review D 45 (1992) 3051.
[10] M. Hauschild, Nuclear Instruments and Methods in Physics Research Section A 379 (1996) 436.
[11] H. Bichsel, Nuclear Instruments and Methods in Physics Research Section A 562 (2006) 154.
[12] M. Ageron, J.A. Aguilar, I. Al Samarai, A. Albert, F. Ameli, M. Andre, M. Anghinolf, G. Anton, et al., Nuclear Instruments and Methods in Physics Research Section A 656 (2011) 11.
[13] P. Sapienza, KM3NeT Collaboration, Nuclear Physics B—Proceedings Supplements 212–213 (2011) 134.
[14] L. Agostino, M. Buizza-Avanzini, M. Dracos, D. Duchesneau, M. Marafini, M. Mezzetto, L. Mosca, T. Patzak, et al., 2012 arXiv:1206.6665.
[15] K. Abe, T. Abe, H. Aihara, Y. Fukuda, Y. Hayato, K. Huang, A.K. Ichikawa, M. Ikeda, et al., 2011 arXiv:1109.3262.
[16] M. Wurm, et al., LENA Collaboration, Astroparticle Physics 35 (2012) 685.
[17] D. Barker, D.M. Mei, C. Zhang, 2012 arXiv:1202.5000.
[18] W.K. Sakumoto, P. de Barbaro, A. Bodek, H.S. Budd, B.J. Kim, F.S. Merritt, M.J. Oreglia, H. Schellman, et al., Physical Review D 45 (1992) 3042.
[19] K. Nakamura, et al., Particle Data Group Collaboration, Journal of Physics G: Nuclear and Particle Physics 37 (2010) 075021.
[20] D. Chirkin, W. Rhode, 2008 arXiv:hep-ph/0407075v2.
[21] D.E. Groom, N.V. Mokhov, S.I. Striganov, Atomic Data and Nuclear Data Tables 78 (2001) 183.
[22] P. Lipari, T. Stanev, Physical Review D 44 (1991) 3543.
[23] K. Daum, et al., Frejus Collaboration, Zeitschrift für Physik C 66 (1995) 417.
[24] R. Abbasi, et al., IceCube Collaboration, Physical Review D 83 (2011) 012001.
[25] R. Abbasi, et al., IceCube Collaboration, 2011 arXiv:1109.6096.
[26] A. Gazizov, M.P. Kowalski, Computer Physics Communications 172 (2005) 203.
[27] A.M. Dziewonski, D.L. Anderson, Physics of the Earth and Planetary Interiors 25 (1981) 297.
[28] S. Klein, Reviews of Modern Physics 71 (1999) 1501.
[29] J. Lundberg, P. Miocinovic, T. Burgess, J. Adams, S. Hundertmark, P. Desiati, K. Woschnagg, P. Niessen, Nuclear Instruments and Methods in Physics Research Section A 581 (2007) 619.
[30] J. Ahrens, et al., AMANDA Collaboration, Nuclear Instruments and Methods in Physics Research Section A 524 (2004) 169.
[31] D.J. Boersma, L. Gladstone, A. Karle, IceCube Collaboration, 2010 arXiv:1002.4900v2.
[32] A. Achterberg, et al., IceCube Collaboration, Astroparticle Physics 26 (2006) 155.
[33] M. Ackermann, et al., IceCube Collaboration, Journal of Geophysical Research 111 (2006) D13203.
[34] R. Abbasi, et al., IceCube Collaboration, Nuclear Instruments and Methods in Physics Research Section A 618 (2010) 139.
[35] V.A. Balkanov, I.A. Belolaptikov, L.B. Bezrukov, N.M. Budnev, A.G. Chensky, I.A. Danilchenko, J.-A.M. Dzhilkibaev, G.V. Domogatsky, et al., Applied Optics 33 (1999) 6818.
[36] J.A. Aguilar, et al., ANTARES Collaboration, Astroparticle Physics 23 (2005) 131.
[37] R. Abbasi, et al., IceCube Collaboration, Nuclear Instruments and Methods in Physics Research Section A 601 (2009) 294.